

University of London  
Imperial College of Science, Technology and Medicine  
Department of National Heart and Lung Institute

---

**Modelling the interaction between induced  
pluripotent stem cells derived cardiomyocytes  
patches and the recipient hearts**

---

***PhD Candidate:***

Damiano Fassina

***Supervisors:***

Sian E. Harding

Steven A. Niederer

**Imperial College  
London**

Submitted in part fulfilment of the requirements for the degree of  
Doctor of Philosophy in Life Science and Medicine of the University of London  
and the Diploma of Imperial College, July 2022



## Abstract

Cardiovascular diseases are the main cause of death worldwide. The single biggest killer is represented by ischemic heart disease. Myocardial infarction causes the formation of non-conductive and non-contractile, scar-like tissue in the heart, which can hamper the heart's physiological function and cause pathologies ranging from arrhythmias to heart failure. The heart can not recover the tissue lost due to myocardial infarction due to the myocardium's limited ability to regenerate. The only available treatment is heart transplant, which is limited by the number of donors and can elicit an adverse response from the recipients immune system. Recently, regenerative medicine has been proposed as an alternative approach to help post-myocardial infarction hearts recover their functionality. Among the various techniques, the application of cardiac patches of engineered heart tissue in combination with electroactive materials constitutes a promising technology. However, many challenges need to be faced in the development of this treatment. One of the main concerns is represented by the immature phenotype of the stem cells-derived cardiomyocytes used to fabricate the engineered heart tissue. Their electrophysiological differences with respect to the host myocardium may contribute to an increased arrhythmia risk. A large number of animal experiments are needed to optimize the patches' characteristics and to better understand the implications of the electrical interaction between patches and host myocardium. In this Thesis we leveraged cardiac computational modelling to simulate *in silico* electrical propagation in scarred heart tissue in the presence of a patch of engineered heart tissue and conductive polymer engrafted at the epicardium. This work is composed by two studies. In the first study we designed a tissue model with simplified geometry and used machine learning and global sensitivity analysis techniques to identify engineered heart tissue patch design variables that are important for restoring physiological electrophysiology in the host myocardium. Additionally, we showed how engineered heart tissue properties could be tuned to restore physiological activation while reducing arrhythmic risk. In the second study we moved to more realistic geometries and we devised a way to manipulate ventricle meshes obtained from magnetic resonance images to apply *in silico* engineered heart tissue epicardial patches. We then investigated how patches with different conduction velocity and action potential duration influence the host ventricle electrophysiology. Specifically, we showed that appropriately located patches can reduce the predisposition to anatomical isthmus mediated re-entry and that patches with a physiological action potential duration and higher conduction velocity were most effective in reducing this risk. We also demonstrated

that patches with conduction velocity and action potential duration typical of immature stem cells-derived cardiomyocytes were associated with the onset of sustained functional re-entry in an ischemic cardiomyopathy model with a large transmural scar. Finally, we demonstrated that patches electrically coupled to host myocardium reduce the likelihood of propagation of focal ectopic impulses. This Thesis demonstrates how computational modelling can be successfully applied to the field of regenerative medicine and constitutes the first step towards the creation of patient-specific models for developing and testing patches for cardiac regeneration.



## Acknowledgements

The work I have done for this Doctoral Thesis would not have been possible without the sapient guidance of my two supervisors Steven Niederer and Sian Harding, to whom go my deepest acknowledgments. I am particularly thankful to Steve for the almost daily supervision and the frank opinions, and to Sian for the fruitful dialogues despite the different scientific background. I would also like to thank Caroline Mendonca Costa for the technical and psychological support in the first half of my PhD, without her achieving all of this would have been much harder. My acknowledgments also go to every researcher of the Cardiac Electromechanics Research Group at King's College, for the team spirit and the availability showed throughout these three and a half years. Honorable mention for Stefano, Sofia, Marina(s), Adelisa, Cristobal, Hugh, Orod and Fernando who have been amazing colleagues and friends and supported me from day one, and to Charlie, Paul, Tiffany, Rosie and Hamed for bringing new energy towards the end of this journey. I would like to thank Francesco and Elias, for leaving me a lot of nice memories, despite the relatively brief interaction, and Chris Arthurs, who shared the house with me for two and a half years and made me grow as a researcher and as a person. I would like to thank my family: my parents for the economical support, my brother Martino for sharing his PhD experience with me and my partner, for the invaluable support provided and the never-ending patience. I am thankful towards all of the friends I have left in Italy, who have never left me, specially Enrico, Davide and Leonardo. I am also grateful towards the Imperial College volleyball club, SideOut and the Wimbledon five star beach volleyball club, for giving me the possibility to play my favourite sports and let off some steam after the long days in the office. I would also like to thank the British Heart Foundation, who sponsored this research project. Completing a PhD is notably challenging, and my experience has been made even more so by the Covid-19 pandemic. I am extremely thankful to have been surrounded by the people mentioned above, who have all contributed in making my journey throughout this PhD one to be remembered.



## **Dedication**

To my friends and family, and to everyone who loves me and believes in me.

‘When you stop learning, you start dying’

*Albert Einstein*

## **Statement of originality**

I hereby certify that the intellectual content of this Thesis is the result of my own work and that all the assistance received in preparing this Thesis and sources have been acknowledged and appropriately referenced.



## Copyright Declaration

The copyright of this thesis rests with the author. Unless otherwise indicated, its contents are licensed under a Creative Commons Attribution-Non Commercial 4.0 International Licence (CC BY-NC).

Under this licence, you may copy and redistribute the material in any medium or format. You may also create and distribute modified versions of the work. This is on the condition that: you credit the author and do not use it, or any derivative works, for a commercial purpose.

When reusing or sharing this work, ensure you make the licence terms clear to others by naming the licence and linking to the licence text. Where a work has been adapted, you should indicate that the work has been changed and describe those changes.

Please seek permission from the copyright holder for uses of this work that are not included in this licence or permitted under UK Copyright Law.





# Contents

<b>Abstract</b>	<b>1</b>
<b>Acknowledgements</b>	<b>3</b>
<b>1 Clinical Background</b>	<b>29</b>
1.1 Cardiac anatomy and physiology . . . . .	29
1.1.1 Anatomy . . . . .	29
1.1.2 Cell structure . . . . .	30
1.1.3 Electrical activation . . . . .	31
1.1.4 Action potential . . . . .	33
1.1.5 Excitation-contraction coupling . . . . .	35
1.1.6 Action potential transmission . . . . .	36
1.1.7 Cardiac cells refractoriness . . . . .	37
1.2 Cardiac arrhythmias . . . . .	38
1.2.1 Causes of arrhythmia . . . . .	40
1.3 Myocardial infarction . . . . .	40
1.3.1 General Pathophysiology . . . . .	41
1.3.2 Infarct scar formation . . . . .	42

1.3.3	Arrhythmias post-MI . . . . .	43
1.3.4	Current treatment options . . . . .	45
1.4	Regenerative medicine . . . . .	46
1.4.1	Cardiac regenerative medicine . . . . .	47
1.4.2	Stem cells in regenerative medicine . . . . .	47
1.4.3	Use of hiPSC-CMs in cardiac tissue engineering . . . . .	48
1.4.4	Conductive polymers in cardiac tissue engineering . . . . .	49
1.5	Open challenges in cardiac tissue engineering . . . . .	50
1.5.1	Stem cells derived cardiomyocytes immaturity . . . . .	52
1.5.2	Stem cell derived cardiomyocytes maturation techniques . . . . .	53
1.6	Motivation and Objectives . . . . .	55
1.6.1	Thesis Outline . . . . .	56
<b>2</b>	<b>Computational Methods</b>	<b>58</b>
2.1	Computational models of cardiac electrophysiology . . . . .	58
2.1.1	Cell scale: modelling ion channel kinetics and membrane potential . . . . .	59
2.1.2	Tissue scale: modelling the action potential propagation . . . . .	62
2.1.3	Numerical solvers for cell and tissue scale models equations . . . . .	66
2.2	Models of hiPSC-CMs electrophysiology . . . . .	67
2.3	Global Sensitivity Analysis . . . . .	68
2.3.1	Variance-based sensitivity analysis . . . . .	69
2.3.2	Gaussian processes emulators . . . . .	71

<b>3</b>	<b>Modelling the interaction between stem cells derived cardiomyocytes patches and host myocardium: a simple 3D model</b>	<b>74</b>
3.1	Introduction . . . . .	74
3.2	Methods . . . . .	76
3.2.1	From 3D geometry to a thin 3D idealized model . . . . .	76
3.2.2	Schematic tissue model description . . . . .	77
3.2.3	Simulating cardiac electrophysiology . . . . .	80
3.2.4	Conductive polymer modelling . . . . .	83
3.2.5	Stem cells-derived engineered heart tissue modelling . . . . .	86
3.2.6	Gaussian processes-based emulators . . . . .	87
3.2.7	Training set creation . . . . .	88
3.2.8	Global sensitivity analysis . . . . .	89
3.2.9	Parameters that match healthy activation times . . . . .	90
3.2.10	Arrhythmic behaviour . . . . .	90
3.2.11	Validation . . . . .	91
3.3	Results . . . . .	95
3.3.1	Model validation . . . . .	95
3.3.2	Do the effects of engineered heart tissue on activation depend on the species? . . . . .	96
3.3.3	Parameter values that match healthy electrophysiology . . . . .	100
3.3.4	Achieving physiological activation time with low arrhythmia risk . . . . .	101
3.4	Discussion . . . . .	108
3.4.1	Model validation . . . . .	108

3.4.2	Conductive polymer effects . . . . .	109
3.4.3	REAT as a biomarker . . . . .	109
3.4.4	From small animal models to human models . . . . .	110
3.4.5	Restoring healthy activation while minimizing arrhythmia risk . . . . .	111
3.5	Limitations . . . . .	114
3.6	Testing model assumptions and parameters choice . . . . .	116
3.7	Conclusions . . . . .	122
<b>4</b>	<b>Assessing the arrhythmogenic risk of engineered heart tissue patches through <i>in silico</i> application on infarcted ventricle models</b>	<b>123</b>
4.1	Introduction . . . . .	123
4.2	Methods . . . . .	125
4.2.1	Pipeline for <i>in silico</i> EHT patch application . . . . .	126
4.2.2	Models and parameters used . . . . .	129
4.2.3	Electrical propagation in ventricular models before and after EHT patch engraftment . . . . .	131
4.2.4	EHT patches and focal arrhythmia . . . . .	132
4.3	Results . . . . .	133
4.3.1	Programmed electrical stimulation in the control meshes . . . . .	133
4.3.2	EHT patches CV and APD determine anti or pro-arrhythmic behaviour .	133
4.3.3	Engraftment of EHT patches modifies the tissue's Rheobase-Cronaxie relation: . . . . .	141
4.4	Discussion . . . . .	141
4.4.1	EHT patches influence on structural arrhythmias . . . . .	144

4.4.2	Implications of EHT patch-host myocardium electrical coupling . . . . .	145
4.4.3	Heterogeneity in the EHT patch following electrical coupling can promote both sustained and non-sustained functional arrhythmias . . . . .	146
4.4.4	EHT patches influence on focal impulse propagation . . . . .	147
4.5	Limitations . . . . .	148
4.6	Conclusions . . . . .	149
<b>5</b>	<b>Discussion</b>	<b>151</b>
5.1	Simplified model Vs anatomically-detailed model: findings comparison . . . . .	151
5.1.1	Summary of studies findings . . . . .	151
5.1.2	Surviving tissue limits the influence of EHT patches on electrical propa- gation . . . . .	152
5.1.3	Anatomically-detailed model provides mechanistic explanation for ar- rhythmic behaviour . . . . .	153
5.1.4	EHT-related focal ectopies caused by hiPSC-CMs automaticity . . . . .	154
5.1.5	Tuning the EHT inward rectifying potassium current . . . . .	155
5.1.6	Design of engineered heart tissue patches: final remarks . . . . .	156
5.2	Machine learning and emulators in cardiac computational modelling . . . . .	158
5.2.1	Gaussian processes as cardiac models emulators . . . . .	159
5.2.2	Deep learning for cardiac models emulation . . . . .	159
5.3	Modelling the engineered heart tissue: assumptions and implications . . . . .	161
5.3.1	Uniformity of cells phenotype . . . . .	161
5.3.2	Isotropy . . . . .	162
5.3.3	Uniform coupling . . . . .	163

5.3.4	Comparison with other studies . . . . .	164
5.3.5	Engineered heart tissue multi-physics modelling . . . . .	164
5.4	Conclusions . . . . .	165

<b>Bibliography</b>		<b>167</b>
---------------------	--	------------

# List of Figures

1.1	Schematic representation of the heart anatomy and the blood circulation in the heart. . . . .	30
1.2	Schematic representation of the heart's electrical pathways . . . . .	32
1.3	Sample shape of a human ventricular cardiomyocyte action potential, color-coded according to each of the 4 phases of the action potential. Below, a schematic representation of the main ionic currents and pumps is reported. . . . .	34
1.4	Definition of activation time (AT), repolarisation time (RT) and action potential duration (APD) for a sample action potential shape. The AT corresponds to the depolarisation, i.e. to the action potential upstroke, while the RT corresponds to the time at which the action potential reaches 90% repolarisation. The APD is defined as the interval between AT and RT. . . . .	38
1.5	Different types of refractory periods in a sample of action potential shape . . . .	39
1.6	Schematic representation of an ideal re-entrant circuit. In panel A, a re-entrant wave with a small wavelength and a big excitable gap is reported, while in panel B is depicted a re-entrant wave with a large wavelength and a small excitable gap, less likely to represent a self-sustained re-entrant pattern. . . . .	44
1.7	Difference between AP shape of a adult human ventricular myocardium and a immature stem cell derived cardiomyocyte. . . . .	53
2.1	Schematic representation of the cable equation electrical circuits. . . . .	63

3.1	Schematic representation of our thin 3D tissue slab model along with the 10 design input parameters considered: Scar radius (SR), Scar depth (SD), Scar conductivity (SC), Engineered heart tissue thickness (EHTt), Engineered heart tissue conductivity (EHTc), Contact area (CA), Conductive polymer thickness (CPt), Conductive polymer conductivity (CPc), Internal bath thickness (IBT), Tissue thickness variation ( $\Delta_{tt}$ ). . . . .	77
3.2	From 3D geometry to our idealized thin 3D model. A) Human left ventricle anatomy model with transmural scar. B) Plane cutting transmurally through the ventricle wall. C) Extracted transmural section. D) Idealization of the geometry and application of an EHT patch mimicking experimental design. . . .	78
3.3	Value ranges of the 10 parameters (rows) used in the two versions of our model ( <i>epi-endo</i> , and <i>endo-epi</i> , 1 <sup>st</sup> and 2 <sup>nd</sup> columns respectively). The 3 sub-cases ( <i>transmural</i> , <i>block</i> and <i>fixed</i> ) are shown in the 3 <sup>rd</sup> , 4 <sup>th</sup> and 5 <sup>th</sup> columns. The table shows which parameters of the original model are fixed in order to derive each sub-case. The bottom row displays representations of each model version and sub-cases. . . . .	80
3.4	Representative AP traces from the 4 cell ionic models used to model rat, rabbit, human and hiPSC-CMs electrophysiology. . . . .	82
3.5	Visualization from 3 different angles of our model's fibers distribution. A: frontal view. B: angled view. C: Side view. Our slab model is made of a layer of tetrahedral elements. A vector determining fibre orientation is assigned to each element. Fibers are rotating from endocardium to epicardium. The EHT patch is assumed isotropic. . . . .	84
3.6	Spatial plots of the repolarization times for the human model ( <i>fixed</i> sub-case). .	91
3.7	The upper panel shows the repolarization gradient over the whole mesh at the 100th beat. In the lower panel, the blue rectangles indicate the areas considered for reporting the repolarization gradient. The values shown in Figure 3.15 are the repolarization gradients computed for the mesh nodes located in this area. .	92



- 3.8 Schematic representations of the models used in the validation step. The crosses indicate the nodes that were selected to extract the activation times and to compute the conduction velocities. . . . . 95
- 3.9 Results of the model validation. Experiments from 4 papers were compared to the model: Jackman et al (A), Thompson et al (B), Zimmermann et al (C) and Mawad et al (D-E). In panel A CV is evaluated in 3 different areas: on the patch, on the tissue far from the patch and on the tissue under the patch. In all 3 experiments, conduction velocity (CV) before (control) and after (graft) the attachment of the patch is compared. The CV measured experimentally (mean and standard deviation) are represented as black dots with error bars, with the p-values associated with each experiment. The simulated CV are displayed as red diamonds. . . . . 97
- 3.10 Upper panel: comparison of activation patterns in the model with the internal bath thickness set to 0.1 or 0 mm. Lower panel: table comparing the right epicardial activation time (REAT) for both internal bath thickness, for each of the 5 setups, in the rat model. . . . . 98
- 3.11 Cross-species comparison of the 500 simulations run to create the training datasets, classified as lower half, upper half or EHT, according to the propagation path (arrows in the left panel) followed by the stimulus. The colours on the right panel represent the arrows colours in the left one. Yellow, green and blue columns show the percentage of simulations classified as lower half, upper half or EHT, respectively. The percentage values are reported on each column. . . . . 99

- 3.12 Donut charts representing the total effect index from the GSA. The figure compares the total effect indices obtained from the rat, rabbit, and human models (rows), for the *epi-endo* and *endo-epi* versions of the model and the *transmural*, *block* and *fixed* model sub-cases (see section 3.2.2). The magnitude of the total effect indexes, represented by the size of the donut slices, shows how much each model parameter can influence the model output (the REAT). In other words, these charts show, for each species and each sub-case, which parameters most influence the electrical propagation in the model. For example, in the first row, first column, the parameter that influences propagation the most is the scar depth, while in the first row, last column, it is the EHT conductivity. . . . . 100
- 3.13 Sample activation pattern. Upper row: propagation in a healthy slab. Lower row: propagation in a sample simulation of the fixed setup, showing the delay in REAT activation. . . . . 101
- 3.14 Model output (REAT) vs EHT conductivity for the rat, rabbit and human model, in the fixed setup. Boxplots represent the distribution of REATs among the 500 LH simulations that had the EHT conductivity restricted to current experimental ranges. Diamonds represent REATs obtained by fixing all the other parameters and increasing EHT conductivity by multiplying the upper bound of the range used in the LH by 1.5, 2, 2.5, 3, 3.5, 4 and 4.5 folds. Dashed line indicates the healthy REAT estimated by our models. . . . . 102
- 3.15 Summary of the 4 cases tested for arrhythmic behavior. For the Baseline and High EHT cases, EHTc is set to 0.112 S/m (mid value in experimental range) and 1.008 S/m, respectively, and no modifications to ion channels' densities are made. When the density of the ion channels responsible for the fast Sodium current and the inward rectifier potassium current are increased, the EHTc is set to 0.112 S/m. The left panel shows which cases match estimated healthy REATs. The center panel shows the distribution of the mean repolarization gradients at the interface between myocardium and EHT (on 100 beats pacing protocol). The right panel shows the presence or absence of ectopic beats fired from the EHT. . 104

- 3.16 Results obtained by modifying the EHT  $g_{Na}$  and  $g_{K1}$  in the tissue (left) and cell (right) models. Left: the grid shows the REAT for the tissue model paced at 1 Hz. Values inside the blue contour are  $\leq$  the predicted healthy REAT and thus would restore pre-infarct activation. Green squares indicate no presence of ectopy, while grey squares indicate presence of ectopy. Right: the grid shows the self-activation frequency for the hiPSC-CM cell model, in a no-pacing protocol. Red squares show where the cell model self-activates with frequency  $< 1$  Hz (i.e., intrinsic-cycle length  $> 1000$  ms), while grey boxes show where the cell self-activates with frequency  $> 1$  Hz, thus causing the observed presence of ectopies in the tissue model. . . . . 105
- 3.17 AP traces from a mesh node in the EHT, with different values of  $g_{Na}$  and  $g_{K1}$ . The tissue model is paced at 1 Hz in all 3 cases. In the baseline case (grey trace) the EHT is activated every 1000 ms by the stimulus coming from the myocardium, which is paced at 1Hz. When increasing  $g_{Na}$  to 4 times the default value (blue trace), in order to increase the EHT CV, we observe a shortening in the intrinsic hiPSC-CM cycle length. Thus, the EHT self-activates at 800 ms, before being stimulated by the myocardium, causing an ectopic beat. Finally, when increasing  $g_{K1}$  to 1.4 times the default value, the intrinsic hiPSC-CM cycle length is brought back to values  $> 1000$  ms, allowing the EHT to be stimulated from the myocardium and thus eliminating the ectopy . . . . . 106
- 3.18 Snapshots from the tissue model showing the ectopic beat fired from the EHT. The snapshots are from the tissue simulation where  $g_{Na}$  in the hiPSC-CM model was multiplied by 4. The first two rows show the normal activation and repolarization caused by the stimulus from the myocardium. At  $t=500$  ms, the repolarization in both the myocardium and the EHT is completed (first snapshot, third row). Around  $t = 800$  ms, the ectopic beat is fired from the EHT (snapshot in the black rectangle). The ectopic beat can also be seen in the blue AP trace in the lower part of the figure, in contrast with the grey trace, representing the baseline (default  $g_{Na}$  and  $g_{K1}$ ), 1 Hz activation. . . . . 107

3.19	Comparison of AP traces from a myocardial node close to the EHT-tissue interface and the default myocardial AP (taken from a node far from the EHT-tissue interface). The black arrows indicate the increment in APD due to the electrotonic load exerted from the EHT on the tissue at the interface. A higher EHT conductivity causes a bigger increment in APD in neighboring host myocardium, resulting in turn in a higher repolarization gradient. . . . .	113
3.20	Comparison of sensitivity indices in the rat model (fixed sub-case) between the original model and models with REAT capped to 150, 175, and 200% of the predicted REAT without the scar. We observed a variation of 10, 1, and 3%, respectively. . . . .	117
3.21	Generation of the full 3D model (right) from the thin 3D model (left), for the human model (fixed sub-case). . . . .	117
3.22	Repolarization gradient for the full 3D model. The left panel shows the entire mesh. The right panel shows a transmural cross-section, for comparison with the repolarization gradient of the thin 3D model (Figure 3.7). . . . .	118
3.23	Total effect indices comparison between the original model and the model paced from the endocardium (rat model, <i>fixed</i> sub-case). . . . .	119
3.24	Total effect indices comparison between original model and model paced at 2 Hz (the original model was paced at 1 Hz) (rat model, <i>fixed</i> sub-case). . . . .	119
3.25	Comparison of the original model (left-hand side) and the model with a BZ (right-hand side). Panel A shows schematic representations of the original model and the BZ model. Panel B shows the total effect indices of both models, for the <i>fixed</i> setup of the rat model. . . . .	120
3.26	Schematic representations of the human model ( <i>fixed</i> sub-case) with transmural heterogeneity of adult ventricular cells included. The myocardium is divided into endocardium, mid-myocardium and epicardium, indicated in the figures by 3 different shades of blue, respectively from darker to lighter. . . . .	121
3.27	Total effect indices comparison between the original model and the model with transmural heterogeneities included (human model, fixed sub-case). . . . .	121

- 4.1 (A) The two left ventricle, heart failure models used in this study, from two different angles. In the top row the model with the isthmus scar is reported, while the model with the large lateral wall scar is reported in the bottom row. (B) The layer of viable tissue used as epicardial patch. (C) Ventricle models after the application of the EHT patch above the scarred area. . . . . 126
- 4.2 Pipeline for in silico EHT patch application. a) Starting mesh. b) Add surrounding bath elements. c) Select a plane parallel to the short axis just below the base. d) Use the selected plane to split the mesh in base, epicardial and endocardial surface. e) Run eikonal simulation to get elements distances from the epicardium. f) Tag elements to create EHT patch. g) Interpolate fibres from starting mesh. . . . . 128
- 4.3 Comparison of cell models AP traces from: 1 - the Paci model (used to model the EHT patch); 2 - the (unaltered) Ten Tusscher model (used to model the healthy myocardium); 3 – the modified Ten Tusscher model (used to model the BZ). Horizontal lines correspond to the APD90 of each trace, whose values are reported in the table. . . . . 130
- 4.4 Panel A) compares AP traces from the Paci model (used to model the EHT patch) for different values of  $g_{Kr}$  conductance (reported in table B). Horizontal lines in panel A) correspond to the APD90 of each trace, whose values are reported in table C). Table D) displays the conductivity values (of the bidomain model) and the  $g_{Na}$  conductance (relative to the default value in the Paci model) used to achieve the desired CV values in the EHT patch. . . . . 131
- 4.5 Onset of a re-entrant circuit after programmed electrical stimulation in the control mesh with an isthmus scar. Screenshots of the simulated transmembrane voltage ( $V_m$ ) are reported every 120 ms. The lightning symbols indicate ventricle pacing. The white arrows show the direction of the wavefront propagation. Arrows pointing to a line (second row) indicate the conduction block at the isthmus entrance. . . . . 134

4.6	Programmed electrical stimulation in the ventricle mesh with large lateral wall scar. Screenshots of the simulated transmembrane voltage ( $V_m$ ) are reported every 120 ms. The lighting symbols indicate ventricle pacing. No non-sustained or sustained re-entry is observed. . . . .	135
4.7	Programmed electrical stimulation in the isthmus scar model in the presence of the EHT patch. The table at the top displays which combinations of EHT patch characteristics (CV and APD) succeed in terminating the re-entrant circuit present in the control mesh. Below, an example of how the presence of the EHT patch can prevent the re-entry onset is reported. The second wavefront is slowed ( $t=540$ ms), but not blocked. Thus, it can enter the isthmus ( $t=660$ ms) and meet the wave entering the isthmus from above ( $t=720$ ms), preventing the onset of the re-entry. . . . .	137
4.8	Programmed electrical stimulation in the isthmus scar model in the presence of the EHT patch. The table at the top displays which combinations of EHT patch characteristics (CV and APD) succeed in terminating the re-entrant circuit present in the control mesh. Below, an example of how the presence of an EHT patch with long APD typical of hiPSC-CMs does not prevent the onset of the re-entry seen in the control case. The second electrical wave is prevented from entering the isthmus (straight white lines at $t=480$ ms and $t=600$ ms) and forced to travel around it ( $t=660$ ms). The wave is then free to travel through the isthmus ( $t=720$ ms), exit the isthmus ( $t=960$ ms) and excite again the whole ventricle ( $t=1020$ ms), maintaining the re-entrant circuit . . . . .	138
4.9	Endocardial view of the rapid pacing protocol in the isthmus scar model showed in Fig 6 in the Manuscript. Panel a) shows schematically the steps made to achieve this view, i.e. splitting the mesh along the long axis, adding transparency and removing the scar. Panel b) reports the screenshots at the same time steps showed in Fig 6 in the Manuscript. . . . .	139

4.10	Programmed electrical stimulation in the large lateral wall scar model in the presence of the EHT patch. The table at the top displays which combinations of EHT patch characteristics (CV and APD) promotes the onset of non-sustained (light red) or sustained (red) re-entries, which were not present in the control mesh. Below, an example of how the presence of the EHT patch can onset a sustained re-entry is reported. Screenshots of the simulated transmembrane voltage ( $V_m$ ) are reported every 120 ms. . . . .	142
4.11	Endocardial view of the rapid pacing protocol in the large scar model showed in Fig 7 in the Manuscript. Panel a) shows schematically the steps made to achieve this view, i.e. splitting the mesh along the long axis, adding transparency and removing the scar. Panel b) reports the screenshots at the same time steps showed in Fig 7 in the Manuscript. . . . .	143
4.12	The graph on top compares the Rheobase-Chronaxie relations fitted on simulations data from the model without EHT patch and the models with an EHT patch with CV equal to 50 and 100% of the healthy myocardial CV. The top row's screenshots show an ectopic impulse arising and propagating in the cube mesh extracted from the model without EHT. The bottom row's screenshots show an ecotpic impulse being dissipated by the presence of an EHT patch with sufficient CV. . . . .	144
5.1	Programmed electrical stimulation in the isthmus scar model with an EHT patch with 100% of the healthy CV value and 67% of the the reference hiPSC-CMs APD value. . . . .	156





# List of Acronyms

<b>RA</b>	right atrium
<b>RV</b>	right ventricle
<b>LV</b>	left ventricle
<b>LA</b>	left atrium
<b>CMs</b>	cardiomyocytes
<b>AP</b>	action potential
<b>MI</b>	myocardial infarction
<b>AF</b>	atria fibrillation
<b>VF</b>	ventricular fibrillation
<b>VT</b>	ventricular tachycardia
<b>HF</b>	Heart failure
<b>hiPSC-CMs</b>	human-induced pluripotent stem cells derived cardiomyocytes
<b>CV</b>	conduction velocity
<b>CP</b>	conductive polymers
<b>BZ</b>	border zone
<b>APD</b>	action potential duration
<b>ODEs</b>	ordinary differential equations

<b>PDEs</b>	partial differential equations
<b>GPs</b>	Gaussian processes
<b>EHT</b>	engineered heart tissue
<b>IBT</b>	internal bath thickness
<b>EHT<sub>t</sub></b>	engineered heart tissue thickness
<b>EHT<sub>c</sub></b>	engineered heart tissue conductivity
<b>CP<sub>t</sub></b>	conductive polymer thickness
<b>CP<sub>c</sub></b>	conductive polymer conductivity
<b>SR</b>	scar radius
<b>SD</b>	scar depth
<b>SC</b>	scar conductivity
<b>CA</b>	engineered heart tissue-slab tissue contact area
<b>REAT</b>	right epicardial activation time
<b>GSA</b>	global sensitivity analysis

# Chapter 1

## Clinical Background

In this thesis we investigate the use of engineered heart tissue patches. These patches find use in hearts in pathological conditions, namely infarcted hearts, which are characterized by the presence of scar tissue and are subject to arrhythmias. In this first Chapter, we provide the reader with the general (but nevertheless necessary) background knowledge on topics like heart anatomy and physiology, myocardial infarction and cardiac arrhythmias. These topics are propaedeutic to the last three sections of the Chapter, in which we introduce regenerative medicine and we describe the state-of-the-art, as well as the open challenges and main bottlenecks, that the field of cardiac tissue engineering is currently facing.

### 1.1 Cardiac anatomy and physiology

#### 1.1.1 Anatomy

The heart weighs approximately 350g and is roughly the size of an adult's clenched fist [1]. The whole heart is externally enclosed within the pericardium, which is attached to the diaphragm and to the sternum, anchoring the heart inside the thorax. The heart is composed of four chambers. The right atrium (RA) receives the blood rich in carbon dioxide from the rest of the body through the superior and inferior venae cavae. The blood is then passed to the right

ventricle (RV), through the tricuspid valve. The blood is then pumped to the lungs through the pulmonary artery. The blood, now rich in oxygen, flows back into the heart and into the left atrium (LA). From the LA the blood flows into the left ventricle (LV) across the mitral valve and is pumped to the rest of the body. The blood then flows back to the RA, where the loop starts again. A schematic representation of the heart anatomy and the blood circulation in the heart is reported in Figure 1.1

The heart tissue, named myocardium, is constituted of billions of hierarchically organised cardiac cells, termed cardiomyocytes (CMs). Collagen connects CMs into sheets, and binds the sheets together to make the myocardium. This multi-scale organization facilitates contraction allowing the heart to both shorten and twist as it pumps, and to efficiently and effectively pump blood out of the LV and around the body.

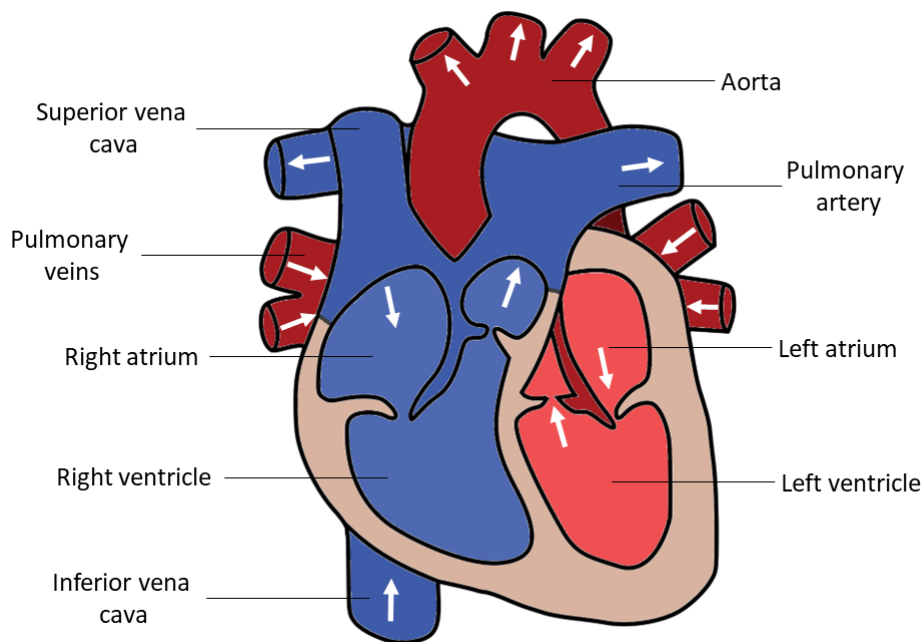


Figure 1.1: Schematic representation of the heart anatomy and the blood circulation in the heart.

### 1.1.2 Cell structure

The myocardium is a highly organized tissue, composed of several cell types, including smooth muscle cells, fibroblasts, and CMs. The fundamental contractile cell of the myocardium is the

**CMs.** Moving from the extracellular space to the intracellular space, the first structure encountered is the basement membrane. The basement membrane binds the cell to the collagen of the extracellular matrix, providing continuity between the myocyte and the extracellular space. After the basement membrane there is the sarcolemma, the structure normally referred to as the cell membrane. The sarcolemma is a lipid bilayer, containing hydrophilic heads and hydrophobic tails. Thanks to this organization, the sarcolemma can interact with both intracellular and extracellular spaces while being impermeable to charged molecules [2]. Molecules can move across the sarcolemma through membrane proteins such as pumps and channels. There are two main, specialized regions of the sarcolemma, the intercalated disks and the transverse tubular system. The intercalated disks consist in cell-to-cell junctions, linking adjacent **CMs** and providing a path of low resistance for rapid flow of ions. The transverse tubular system, or T-tubules, are invaginations of the sarcolemma which bring together in close proximity specific calcium ion channels and the sarcoplasmic reticulum, making the T-tubules an essential component in excitation-contraction coupling (see section 1.1.5). The sarcoplasmic reticulum is a **CMs** organelle, specialized in the regulation of calcium concentration in the cytoplasm. Specifically, it is the source of  $Ca^{2+}$  ions during excitation-contraction coupling. In **CMs**, the contractile apparatus is represented by the sarcomere. The sarcomere is composed of thin and thick intertwined filaments of proteins such as myosin, actin and tropomyosin. In order for the contraction to happen successfully, **CMs** require abundant quantities of ATP, which is produced in the mitochondria. Mitochondria occupy 40% of the cell volume, and are also known to play a role in handling  $Ca^{2+}$ , protecting **CMs** from  $Ca^{2+}$  overload [3].

### 1.1.3 Electrical activation

The heart works as a electromechanical pump, providing thousands of litres of oxygenated blood daily. A series of organized electrical events coordinates the contraction of the heart with each beat. The electrical pulse that initiates contraction is generated by the sinoatrial node, situated at the junction between the **RA** and the superior vena cava. This pulse excites the **RA**, travels through aligned myocardial strands connecting the **RA** and **LA** walls (the Bachmann's

bundle) and excites the [LA](#). The impulse travels through internodal pathways in the [RA](#), in order to reach the atrioventricular node, located in the lower back section of the interatrial septum, the wall of tissue separating the atria. There is no direct electrical connection between the atrial and ventricular chambers other than through the atrioventricular node, as fibrous, non-conducting tissue surrounds the tricuspid and mitral valves [\[4\]](#). From the atrioventricular node, the impulse then travels through the bundle of His and down the bundle branches, fibers specialized for rapid transmission of electrical impulses, on either side of the interventricular septum. The right bundle branch depolarizes the [RV](#), while the left bundle branch depolarizes the [LV](#). Both bundle branches terminate in Purkinje fibers, millions of small fibers projecting throughout the myocardium. After the bundle of His, the impulse first activates the papillary muscle (responsible for closing the mitral and tricuspid valves, separating the [LA](#) and [LV](#) and [RA](#) and [RV](#) respectively) prior to activating the ventricles, thereby preventing regurgitation of blood flow through the atrioventricular valves. A schematic representation of the heart's electrical pathways is reported in [Figure 1.2](#)

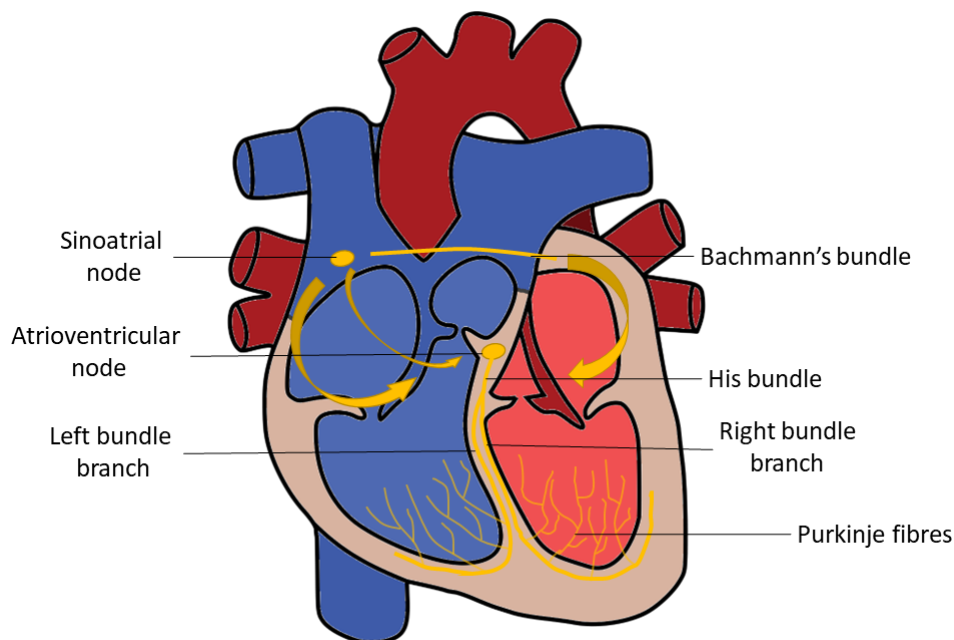


Figure 1.2: Schematic representation of the heart's electrical pathways

### 1.1.4 Action potential

At a cellular level, the propagation of the electric pulse initiates the propagation of the action potential (AP). The AP is an electrical stimulation created by a sequence of ion fluxes through specialized channels in the membrane of CMs, that leads to cardiac contraction. Two main forces drive ions across cell membranes: the chemical potential, i.e., an ion will move down its concentration gradient, and the electrical field created by net charge imbalance, which will drive ions away from regions with a similar net ion charge. The combination of these forces is named the electrochemical gradient. The net ionic gradient across the membrane gives rise to a potential, referred to as the transmembrane potential. When the electrical field exactly balances the diffusion, an equilibrium is reached. The potential difference across the cell membrane at equilibrium is termed *reversal* potential, which is different for each ion species. Ions can move across the cell membrane through channels, exchangers or pumps. Ion channels and exchanger are powered by one ion moving down its electrochemical gradient and are thus responsible for what is termed *passive* transport. Pumps use up energy from ATP molecules to move ions against their ionic concentrations gradients (*active* transport) maintaining charge differentials between the inside and outside of the CMs. The movement of ions across the cell membrane gives rise to the membrane currents, which can modify the transmembrane potential and trigger an AP. In a typical cardiomyocyte, an AP is composed of 5 phases (0-4), beginning and ending with phase 4. A sample shape of a human ventricular AP and its 4 phases are depicted in Figure 1.3.

Phase 4: *Resting phase*. The cell resting potential is maintained at approximately at -85 mV, close to the potassium reversal potential, because the cell membrane is relatively permeable to  $K^+$  ions. The intracellular concentration of potassium greatly exceeds the extracellular concentration. The high resting membrane potassium conductance means that potassium ions can diffuse out of the cell down their concentration gradient. However, as each potassium ion leaves the cell it causes the cell membrane potential to decrease. The resulting negative membrane potential attracts the positive potassium ions back into the cell. Eventually, the electric potential and diffusion forces driving potassium are balanced,

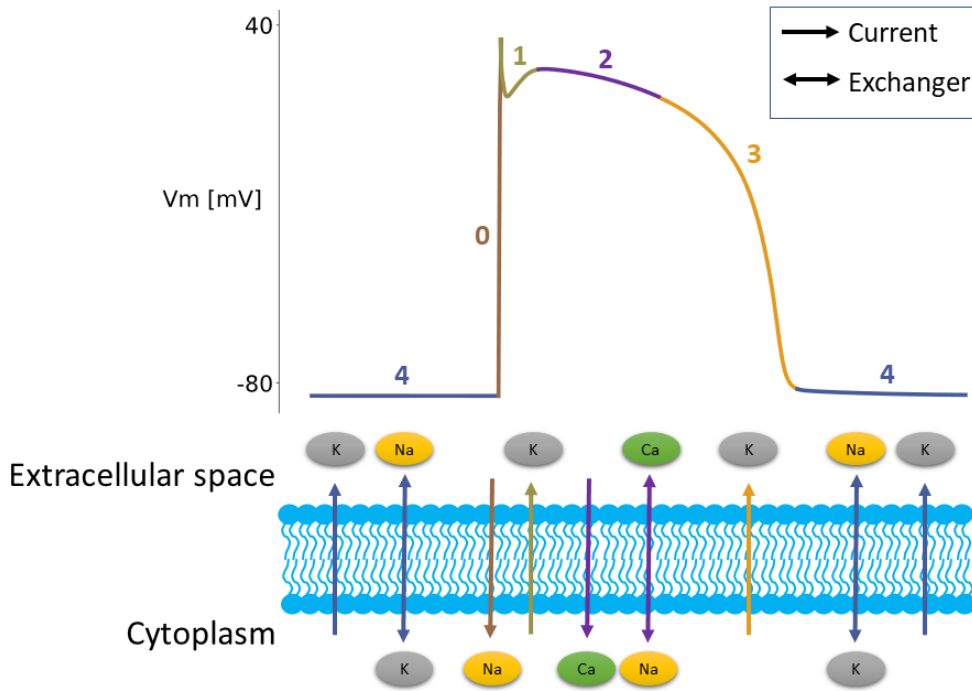


Figure 1.3: Sample shape of a human ventricular cardiomyocyte action potential, color-coded according to each of the 4 phases of the action potential. Below, a schematic representation of the main ionic currents and pumps is reported.

reaching the potassium reversal potential. The cell membrane resting potential is slightly more positive than the potassium reversal potential, due to the diffusion of positive sodium ions inside the cell, down their concentration gradient. The concentration gradient is maintained by the sodium-potassium pump, which consumes ATP molecules to extrude 3  $Na^+$  ions in exchange for 2  $K^+$  ions.

**Phase 0: Depolarisation.** After an electrical stimulus, the cell fast sodium channels open, allowing the rapid influx of  $Na^+$  into the cell (the fast sodium current  $I_{Na}$ ), depolarising the cell approximately to 35 mV.

**Phase 1: Early repolarisation.** After the AP upstroke, a short current termed transient outward current ( $I_{to}$ ) creates a  $K^+$  efflux from the cell. This causes the cell membrane potential to partially repolarise towards  $\approx 0-10$  mV and results in a spike at the start of the AP. However,  $I_{to}$  is not present in all species.

**Phase 2: Plateau phase.** During this phase the L-type calcium current ( $I_{CaL}$ ) opens, causing an



influx of  $Ca^{2+}$  ions. The sodium-calcium exchanger ( $I_{NaCa}$ ) transfers three sodium ions into the cell in exchange for one calcium ion flowing out, thus producing a net inward positive current. The transmembrane voltage is kept constant by the balance of ( $I_{NaCa}$ ) and the efflux of  $K^+$  through the slow-delayed rectifier potassium current ( $I_{Ks}$ ).

Phase 3: *Repolarisation*. In this phase the L-type calcium channels close and additional potassium channel are opened, creating the delayed rectifier potassium current ( $I_{Kr}$ ). The net efflux of positively charged potassium ions causes the cell to repolarise to its resting potential. Normal transmembrane ionic concentrations are restored by the  $Na^+$ - $Ca^{2+}$  exchanger and the  $Na^+$ - $K^+$  pump, which return  $Na^+$  and  $Ca^{2+}$  ions to the extracellular environment, and  $K^+$  ions to the cell interior.

### 1.1.5 Excitation-contraction coupling

Contraction is triggered in the cell through a process described as excitation-contraction coupling, where the electrical **AP** is first transmitted to a chemical signal, that in turn activates the contractile proteins to generate a contraction. Calcium is the mediator that couples electrical activation to physical contraction. During each **AP**,  $Ca^{2+}$  ions cycle in and out the cell's cytosol. The initial influx of  $Ca^{2+}$  into the cell through the L-type calcium channels during phase 2 of the **AP** is insufficient to trigger contraction of the myofilaments. The **CMs** cell membrane contains invaginations (T-tubules) that bring L-type  $Ca^{2+}$  channels into close contact with ryanodine receptors, specialized  $Ca^{2+}$  release receptors in the sarcoplasmic reticulum, an intra-cellular  $Ca^{2+}$  store. When  $Ca^{2+}$  enters the cells through L-type channels, ryanodine receptors change conformation and induce a larger release of  $Ca^{2+}$  from the sarcoplasmic reticulum. This mechanism is called calcium-induced calcium release. Following release of  $Ca^{2+}$  from the sarcoplasmic reticulum through the ryanodine receptors, the  $Ca^{2+}$  then binds to molecules of Troponin-C, one of the contractile proteins of the sarcomere, causing active sites between myosin heads and actin filaments to be exposed, in turn resulting in the activation of the myofilaments. Myofilaments are responsible for the generation of force and for the contraction of the cell. As the contraction ends, calcium ions unbind from the Troponin-C molecules and are

returned to the sarcoplasmic reticulum via the SERCA pump, while the  $Na^+-Ca^{2+}$  exchanger extrudes calcium ions back into the extra-cellular space [5].

### 1.1.6 Action potential transmission

The heart's synchronous contraction is possible thanks to the gap junctions, essentially pores in the myocytes cell membrane that directly connect the cytoplasm of neighbouring cells. They are formed by six membrane proteins called connexins, of which Connexin-43 is the predominant isoform in the ventricle. Gap junctions enable the CMs' electrical coupling, by providing a low resistance pathway for the passage of molecules and ions between adjacent cells [6]. This means that an AP in one cell will cause neighbouring cells to depolarize, causing the activation to propagate and activate the whole heart. This allows the heart chambers to act as a syncytium. That is the reason why the cell in the sinoatrial node, which have inherent pacemaker activity, are responsible for the setting the heart rate. When a cardiomyocyte is depolarised and its transmembrane potential is close to 0 mV, the potential difference between cells causes a flow of ions to enter the neighbouring cells through the gap junctions, starting in turn their depolarisation. The flow of ions causes the formation of a largely homogeneous propagation wavefront. Gap junctions are distributed through the sarcolemma, but are more dense at each end of myocytes. More dense gap junctions permit a stronger flow of ions, and that is why the CV of the propagation is faster along the direction in which CMs are aligned, i.e. the fibres direction, rather than in the direction transversal to the fibres. In other words, the distribution of the gap junctions is responsible for the myocardium anisotropy.

The flow of ions between neighbouring cells through the gap junctions is called *electrotonic current*. The electrotonic current is crucial for AP propagation, and concepts such as *source* and *sink* can explain a successful or failed propagation. The source is the flow of ions passing into a myocyte, i.e. the current that initiates the depolarisation. During AP propagation, an excited cell serves as a source of electrical charge for depolarizing adjacent unexcited cells [7]. The larger the current, or the volume of depolarised cells generating it, the more effective and faster the electrical propagation will be. The requirements of neighbouring resting cells to reach

the threshold to trigger an AP constitute an electrical sink (or load) for the excited cell [7]. In other words, the sink is the portion of tissue ready to be depolarised. For propagation to succeed, the excited cell must provide sufficient charge to bring the transmembrane potential of a cell in the sink from its resting value to the threshold. Once threshold is reached and an AP is triggered, the newly excited cell switches from being a sink to being a source for the downstream tissue, thus perpetuating AP propagation. The smaller the sink, the safer is for the electrical signal to propagate. On the other hand, a larger sink will cause a slower propagation and possible the termination of the wave [8].

### 1.1.7 Cardiac cells refractoriness

Once a CM has activated, there is a period of time where the CMs can not be activated again, referred to as refractory period. The refractory period of a myocyte is defined as the time from phase 0 (depolarisation) until the next possible depolarization. CMs have a longer refractory period than other muscle cells given the long plateau (phase 2). This is a physiological mechanism allowing sufficient time for the ventricles to empty and refill prior to the next contraction. The action potential duration (APD) is usually quantified as the time interval between the depolarisation (AP upstroke) and 90% repolarisation (Figure 1.4). During an AP, different degrees of refractoriness are encountered.

- *Absolute refractory period:* The CMs is completely unexcitable by a new stimulus.
- *Effective refractory period:* It is composed by the absolute refractory period and a short segment of phase 3, during which a stimulus may cause the CMs to depolarize minimally but will not result in a propagated action potential, i.e neighbouring cells will not depolarize.
- *Relative refractory period:* A greater than normal stimulus will depolarize the CMs and cause an action potential.
- *Supranormal period:* A period during which a weaker than normal stimulus will depolarize

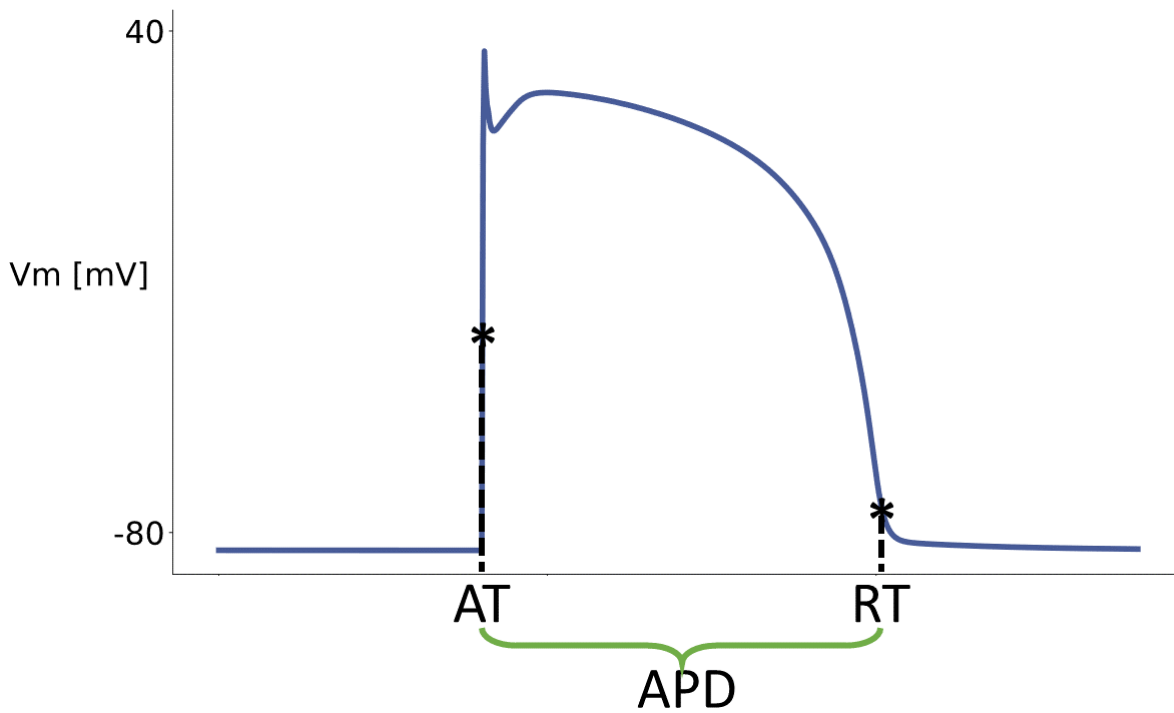


Figure 1.4: Definition of activation time (AT), repolarisation time (RT) and action potential duration (APD) for a sample action potential shape. The AT corresponds to the depolarisation, i.e. to the action potential upstroke, while the RT corresponds to the time at which the action potential reaches 90% repolarisation. The APD is defined as the interval between AT and RT.

the cells and cause an action potential. Cells in this phase are particularly susceptible to arrhythmias when exposed to an inappropriately timed stimulus.

In Figure 1.5 a sample AP shape with the different refractory periods is reported.

The concept of CMs being in an excitable or refractory state is considered crucial for the studies of abnormal heart rhythms (arrhythmias), as such areas of refractory cells could block the propagation of the electrical wavefront.

## 1.2 Cardiac arrhythmias

Cardiac arrhythmias happen when the electrical activation in the heart ceases to be synchronous and starts being rapid and/or chaotic. Rather than a compact and uniform wavefront, in the case of arrhythmia, the electrical propagation in the heart is characterised by the presence

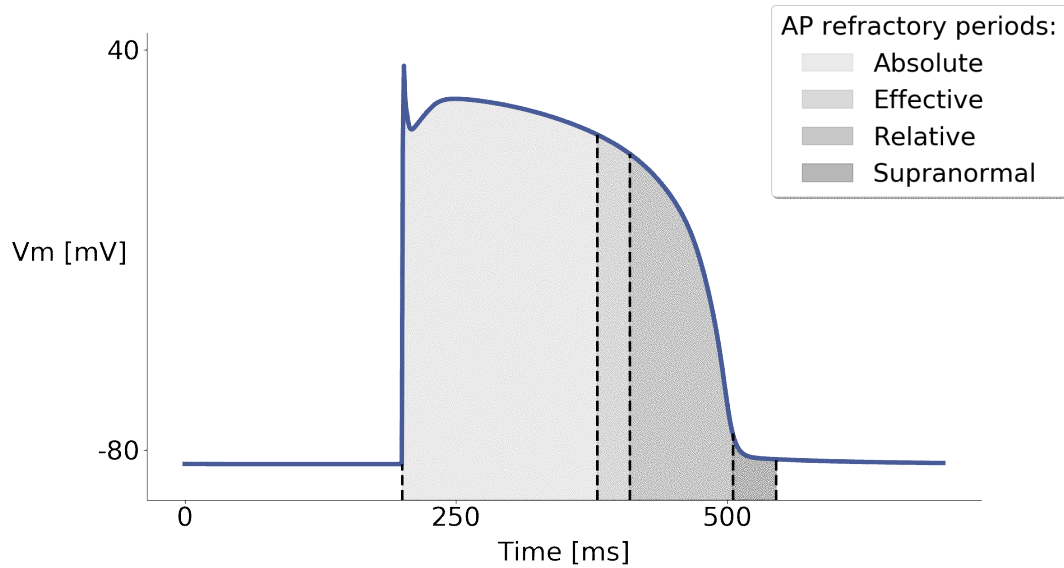


Figure 1.5: Different types of refractory periods in a sample of action potential shape

of disorganised, turbulent activation patterns. As the regular electrical activity is disrupted, coordinated cardiac contraction is also interrupted. The presence of small, out of synch areas of localised contractions can hamper the heart's ability to pump blood, thus representing a life-threatening hazard.

Arrhythmias can affect both atria and ventricles. Atrial arrhythmias are considered to be less dangerous, as the blood can still pass to the ventricles and be pumped around the body. Nevertheless, disruption in atrial synchronous contraction can cause blood pooling, which increases the probability of blood clots formations, in turn increasing the likelihood of strokes. Ventricular arrhythmias are considered life-threatening, as the ventricles pump blood to all of the other organs in the human body. During a ventricular arrhythmia pump function deteriorates or stops with severe consequences for the patient.

There are two types of ventricular arrhythmias: ventricular tachycardia (VT) and ventricular fibrillation (VF). During VT, rapid, non-physiological pattern of electrical propagation are present in the ventricle, but excitation is still fairly coordinated. As a result, contraction is impaired and the heart's pumping efficiency decreases. During VF, the electrical wave usually breaks up, resulting in multiple propagation wavefronts which cause small, isolated regions of the ventricle to activate and contract. In this case, the ventricle is not able to contract as a

whole. The cardiac output decreases to zero, rendering defibrillation via application of a strong electrical shock the only way to avoid death.

### 1.2.1 Causes of arrhythmia

Cardiac arrhythmia can have different causes. Irregular rhythms can be started by spurious, out of synch beats, that spontaneously occur in the myocardium. These ectopic beats can in turn arise from phenomena such as early or delayed-afterdepolarisations, where the CMs are depolarised following anomalous ion currents behaviour. Abnormal ion channel functioning can be caused by inherited genetic disorders or by the interaction with certain drugs. In addition, spurious beats can be due to diseased cells acquiring automaticity, i.e. the ability to self-stimulate, and thus generating additional activation waves, besides the physiological one from the sinoatrial node. However, most arrhythmias are due to the presence of regions of myocardium whose properties are different from the rest of tissue. These areas can include differences at the anatomical level (named *structural* differences) or at the electrophysiological level (named *functional* differences). When the propagating electrical wavefront comes in contact with these areas, it can be subject to break-up or can rotate around the obstacle, creating circuits or vortices-like waves, which lead to arrhythmias. The presence of areas of myocardium with different properties is often due to cardiovascular-related diseases such as myocardial infarction (MI).

## 1.3 Myocardial infarction

MI is defined as a tissue death (necrosis) as a result of prolonged ischemia, i.e. insufficient supply of oxygen and nutrition to an area of tissue due to a disruption in blood supply. The blood vessel supplying the affected area of tissue may be blocked due to an obstruction in the vessel, compression from structures outside the vessel or an external trauma could cause rupture of the vessel with consequent loss of blood pressure downstream of the rupture. Worldwide, in 2019, 197.2 milion people were estimated living with ischemic heart disease resulting from MI,

making MI one of the most expensive and prevalent conditions during inpatient hospitalizations [9].

### 1.3.1 General Pathophysiology

MI, commonly known as a heart attack, occurs when blood flow decreases or stops to a part of the heart for a prolonged period of time, causing damage to the myocardium. This is most commonly due to a blood clot that blocks one of the coronary arteries. Less frequently, a coronary artery blockage can also be due to a spasm or a tightening of the aforementioned artery. The coronary arteries are the blood vessels which supply oxygen-rich blood to the cells of the myocardium. In coronary artery diseases, the inside of a coronary artery is narrow and hardened, because of the build up of a fatty material, called plaque, decreasing the supply of blood to the heart. If the plaque breaks open, a blood clot can form on the surface of the plaque. The blood clot becomes a thrombus and can completely block the blood flow in the artery. Once the blood flow is blocked, this tissue becomes ischemic, leading to tissue damage, which will eventually form an infarct. After blood supply is interrupted, if the blockage is not treated and removed within a few hours, the damaged heart muscle will begin to die, and it will be replaced by fibrous scar tissue. The consequences of this can be severe: tissue death and myocardial scarring alter the normal conduction pathways of the heart and weaken affected areas. This creates a local risk of arrhythmia while globally decreasing the ability of the heart to pump blood. Depending on the size and location of the injury, a series of complications can arise. They may occur immediately following the infarction or may take time to develop. Disturbances of heart rhythms, including atria fibrillation (AF), VT, VF and heart block can arise as a result of ischemia and cardiac scarring. Stroke is also a risk, either as a result of clots or of disturbances in the heart's ability to pump effectively as a result of the infarction. If the infarction causes dysfunction of the papillary muscle, regurgitation of blood through the mitral valve may occur. The inability of the infarcted heart to pump blood in the correct way may also lead to rupture of the ventricular dividing wall or to cardiogenic shock. Heart failure (HF) may also develop as a long-term consequence, with an impaired ability of heart muscle to pump,

scarring, and increase in size of the existing muscle.

### 1.3.2 Infarct scar formation

The formation of fibrotic tissue is part of the heart's healing process after ischemia and subsequent necrosis of cardiac tissue. Fibroblasts and endothelial cells produce excess connective tissue, to provide structural support and to prevent further damage. However, the fibrotic tissue is profoundly different from the healthy myocardium. While in the acute stage fibroblasts have been shown to couple with surviving **CMs** and support (slow) electrical conduction [10], the chronic scar is not excitable (nor contractile) and thus can not conduct the electrical wave of activation. Around the fibrotic region (the core of the scar), a peripheral area of tissue is usually affected by less dramatic remodelling. This area is called the infarct border zone (**BZ**). Although the **BZ** remains excitable, it is affected by both structural and functional remodelling. There can be dispersed fibrosis, with loss of the original fibers orientation, due to fibers re-arrangement. In addition, gap junctions protein can be altered during the initial ischemic event, resulting in loss or repositioning of gap junctions in the infarct **BZ**, causing a reduction in **CV**, since current can flow less efficiently between cells. Moreover, protein subunits of ion channels can also be modified, often resulting in decreased ionic currents. Most notably, a reduction in the fast sodium current  $I_{Na}$  can lead to a slowing of the **AP** upstroke, which in turn delays the activation of the L-type calcium current ( $I_{CaL}$ ), resulting in a prolonged **AP**. Further remodelling can decrease the density of ion channels responsible for potassium handling, which also contributes to **APD** increment. A lengthening of the **APD** implies a delayed repolarisation and causes the tissue to be more refractory. These changes render the **BZ** heterogeneous, as it displays different properties with respect to the normal, healthy tissue.

Studies have shown that post-**MI VT** is often caused by the electrical wave exiting a circuitous pathway connecting two or more zones of surviving myocardium [11]. Presence of surviving myocardium are typically found at the endocardium, a phenomenon called endocardial sparing. More extensive areas of endocardial sparing have been linked with a higher likelihood of developing post-**MI VT** [12]. However, **VT** has been shown to arise also from the patchy spared



subepicardium over the infarct as well as intramurally [13].

All things considered, the scar resulting after a MI can be located anywhere in the heart and can have endless conformations. Moreover, the scar can be not completely fibrotic, as it happens when fibrotic regions are interspaced between bundles of surviving CMs. For these reasons, the resulting electrical propagation in a post-MI heart can be disrupted or follow unconventional paths or circuits that are created because of the presence of the scar. Under certain circumstances, this altered propagation can result in the onset of arrhythmias.

### 1.3.3 Arrhythmias post-MI

When the electrical activation wavefront interacts with scarred areas of the heart, it can break-up, travel around the scar, travel inside fibrotic tissue through bundles of surviving CMs, or travel through BZ areas with altered electrophysiology. The interaction of the electrical propagation waves with scarred regions often generates *reentrant arrhythmias*. Reentrant arrhythmias (or *re-entry*), indicate tortuous propagation, in which the electrical wave follows circling-like pathways, periodically re-exciting areas of myocardium. Reentries cause VT, because the reentrant frequency overcomes the normal heart rate imposed by the sinoatrial node. In case of wave fragmentation, VT can aggravate into life-threatening VF.

A necessary requisite for the onset of reentrant arrhythmias is a conduction block, meaning that the wave of electrical propagation is stopped. This can be caused by regions of non-conducting, fibrotic tissue, or by BZ areas. In the BZ, the APD is lengthened, thus the tissue will repolarise later. The following electrical wave could reach (depending on the stimulus rate) the BZ area still in its refractory period, thus being forced to bifurcate or to travel around the obstacle. Depending on the dimensions of the scar, by the time the wave travels around it, the BZ area that had caused the block can be fully repolarised and thus ready to be excited again, producing a reentrant circuit. An example of a reentrant circuit is reported in Figure 1.6. In certain circumstances, the reentrant wave can be self-sustained, meaning that it keeps looping through the reentrant circuit, without the need for pacemaking activity. The activation wavelength indicates the length of depolarised tissue at each time. The more

myocytes are active simultaneously, the greater the wavelength will be. The wavelength is defined by:  $\lambda = \text{APD} \times \text{CV}$ , where **APD** is the action potential duration and **CV** is the conduction velocity. Waves with low wavelength (i.e. low **CV** and short **APD**) are associated with self-sustained reentrant arrhythmias, because the excitable gap between wave head and tail is large (see Figure 1.6-A). Accordingly, higher values of wavelength are associated with non-sustained arrhythmias, because the excitable gap is reduced and the wave is more likely to terminate due to head-tail collision (see Figure 1.6-B).

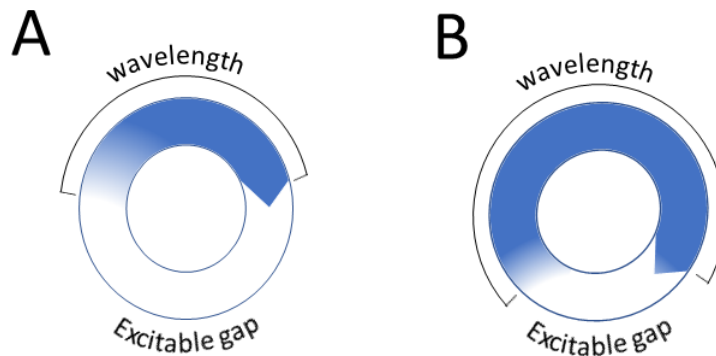


Figure 1.6: Schematic representation of an ideal re-entrant circuit. In panel A, a re-entrant wave with a small wavelength and a big excitable gap is reported, while in panel B is depicted a re-entrant wave with a large wavelength and a small excitable gap, less likely to represent a self-sustained re-entrant pattern.

Repolarisation dispersion is also known as a factor affecting conduction block [14], and it has thus been linked with promoting **VT** [15]. Repolarisation dispersion happens when regions of **CMs** repolarise at different time intervals, i.e. regional differences in **CMs APD** are present. Repolarisation dispersion can cause unidirectional block because a wavefront can not travel through late repolarising tissue, given its inexcitability, potentially also leading to the onset of re-entry. Additionally, an electrotonic current establishing from the tissue with late repolarisation to the tissue with early repolarisation can depolarise the latter, potentially initiating a premature beat if the threshold for activation is reached [15]. Besides being established that repolarisation gradients (i.e. alteration of repolarisation times along a specific axes) play an important role in **VT** arrhythmogenesis, a study from Chauhan et al [16] has also found more pronounced repolarisation heterogeneity in infarcted hearts of patients exhibiting **VT** with respect to those who did not exhibit **VT**, specifically linking repolarisation gradients to post-MI

**VT**. The Purkinje has also been linked to ventricular arrhythmias, whether as an initiator or maintainer [17]. 50% of deaths in patients with ischemic heart disease are attributed to lethal forms of **VT** or **VF** [18], with the currently available treatment options still far from optimal and a recent stagnation in the development of novel therapeutics for post-**MI** arrhythmias [19].

### 1.3.4 Current treatment options

At present, drug refractory recurrent **VT** is treated with catheter ablation. Although notable improvements have been made, patients who undertake catheter ablation still experience recurrence in 30% of cases [20]. A range of emergency therapies are instead available for the treatment of blood supply blockage to the myocardial tissue, to tackle **MI** in the early stages. The most frequent techniques adopted are angioplasty and coronary artery bypass graft. An angioplasty is a minimally invasive and endovascular surgical procedure to widen narrowed or obstructed blood vessels. Typically, a deflated balloon attached to a catheter is passed over a guide-wire into the narrowed vessel and then inflated to a fixed size. The balloon forces expansion of the blood vessel and the surrounding muscular wall, allowing an improved blood flow. A stent may be inserted at the time of ballooning to ensure the vessel remains open, and the balloon is then deflated and withdrawn. Angioplasty is a lower-risk option relative to surgery, but there still are risks and complications associated with it. For example, embolization, i.e. the launching of debris into the bloodstream, arterial rupture from over-inflation of a balloon catheter or the presence of a calcified target vessel or the formation of hematoma at the access site. Moreover, angioplasty may also provide a less durable treatment, as it can be more prone to restenosis, i.e. the recurrence of the blood vessel narrowing after the stent insertion, which can reach more than 50% of the original stenosis [21]. A different approach with respect to angioplasty is represented by the coronary artery bypass graft, which still aims to restore normal blood flow. This surgical procedure can be performed throughout two main approaches. In one, the left internal thoracic artery is diverted to the left anterior descending branch of the left coronary artery. In the other, a great saphenous vein is removed from a leg. One end of the vein is attached to the aorta or one of its major branches, and the other end is attached to

the obstructed artery immediately after the obstruction. Coronary artery bypass graft is also subject to complications, such as releases of debris during surgery, resulting in further blood flow blockages. Loss of mental function, particularly in elderly people, is also a complication of bypass surgery, however a neurocognitive decline over time has been associated with coronary artery disease regardless of the treatment.

Angioplasty and coronary artery bypass are emergency treatments, addressed to salvage threatened ischaemic myocardium, since patient survival after MI is largely dependent on infarct extent and residual cardiac function [21]. After the first emergency state, MI is treated with medications, including blood thinners, to improve blood flow, nitroglycerin to widen blood vessels and  $\beta$ -blockers to lower blood pressure and decrease heart activity. However, these measures do not free the patient from the risk of heart failure.

## 1.4 Regenerative medicine

Regenerative medicine is an umbrella term that indicates a branch of translational research and clinical applications focused on the repair, replacement or regeneration of cells, tissues or organs, to restore their normal function. Commonly used approaches in regenerative medicine include gene therapy, stem cells transplantation, tissue engineering and the reprogramming of cell and tissue types. This combination of several technological approaches moves regenerative medicine beyond traditional transplantation and replacement therapies. These regenerative medicine approaches can be focused on *repairing* or *regeneration*. While repairing an organ is associated with adaptation to loss of organ mass and restoration of the interrupted continuity by synthesis of scar tissue, regeneration indicates the process where lost specialized tissue is replaced by proliferation of undamaged, specialized cells. In other words, regeneration aims for both anatomical and functional restoration of tissue/organs at the anatomical site, while repair does not. This kind of process is already present in humans, but it is limited to a few organs, among which the heart is not present.

### 1.4.1 Cardiac regenerative medicine

MI causes irreversible damage to the myocardium because the adult human heart has minimal intrinsic ability to regenerate lost CMs. There are currently no treatment options to recover this lost tissue [22]. After the initial insult, fibroblasts and endothelial cells form a dense collagenous scar that maintains wall structure. However, the scar is stiff, non-contractile and non-conductive, thus it no longer contributes to myocardial contraction, potentially causing a critical loss in cardiac function that can lead to HF [23]. The most effective current therapy to restore heart function, cardiac transplantation, is limited by insufficient availability of donor organs and the requirement for lifelong immunosuppression. Electronic ventricular assist devices require invasive surgery and long-term anticoagulation therapy [24]. Recently regenerative medicine has been proposed as a promising approach to replace or augment the function of tissue lost to cardiac infarcts [25]. In addition to the potential of partially or fully restore cardiac function, cardiac tissue engineering can serve as surrogate human cardiac tissue for drug toxicity screening and personalized medicine, further enhancing the potential of this field.

### 1.4.2 Stem cells in regenerative medicine

The restoration of lost cardiac tissue is pursued through the transplantation of healthy CMs into the injured heart. This strategy entails many challenges, starting with the cell source to be utilized. Many potential cell sources have been investigated, such as bone marrow, stem cells, endothelial progenitor cells, skeletal myocytes, adult cardiac stem cells, and embryonic stem cells [26]. In the decade 1990-2000 bone marrow mesenchymal stem cells have been central to the development of cardiac regenerative medicine, because they were the first to be reported capable of differentiating into cardiac myocytes [27]. However, the results of the clinical trials performed using these kinds of cells have been unsatisfactory mostly because of the poor efficiency of differentiation into CMs [28]. Currently, the interest has changed and it is now focusing on human-induced pluripotent stem cells. They have the same properties of human embryonic stem cells, such as self-renewal and potency, but they bring some new advantages [29]. First, they do not raise ethical issues, since no human embryos are used. Second, they

allow the creation of a patient-specific stem cell culture, since they can be easily obtained from a patient, for example through a skin biopsy. This enables the creation of autologous tissues, which reduces the risk of rejection in case of transplant.

### 1.4.3 Use of hiPSC-CMs in cardiac tissue engineering

The first clinical experiments involved human-induced pluripotent stem cells derived cardiomyocytes ([hiPSC-CMs](#)) suspended in a liquid solution, directly injected into the infarcted area. However, this approach was hampered from the start by the poor retention rate of injected cells (1-5%) [30]. To overcome this problem, scaffolds have been developed. Beside enhancing cell retention, the presence of scaffolds can improve cell survival rate by creating a protective environment, promote integration with the host tissue, as well as provide mechanical support for the damaged tissue to prevent thinning and dilation of the infarct scar [31, 32, 33, 34]. The scaffolds are designed to recreate biomimetic micro-environments for cells to reach their full maturation [35]. A cardiac *patch* usually consists of a biocompatible scaffolding structure combined with [hiPSC-CMs](#) or other kinds of stem cells-derived [CMs](#). The term *graft* is instead used to indicate layers of [hiPSC-CMs](#) (without additional biomaterials) cultured as to form a patch-like structure. A graft of cardiac tissue created from stem cells derived [CMs](#) is also called engineered heart tissue ([EHT](#)).

Several experiments involving engraftment of patches of [hiPSC-CMs](#) have been performed, with studies outcomes spanning a wide range of different results. Two experiments from Gao et al showed that [CV](#) of [hiPSC-CMs](#) patches after 7 days of culturing are considerably lower than the values reported in literature for healthy myocardium ( $14 \pm 0.1$  and  $18.8 \pm 0.8$  cm/s compared to 65 cm/s) [36, 37]. Some studies have found limited to no coupling between engrafted patch and native myocardium. According to Jackman et al, despite the presence of vascularisation and electromechanical junctions, their patch did not couple with the recipient heart, because of the presence of a non-myocyte layer between the patch and the epicardium [38]. Another study [39] has found that post-MI transmural [CV](#) in areas far from the scar (and the patch) is higher in hearts with a [hiPSC-CMs](#) patch implanted, compared to hearts with a cell-free patch

(32 cm/s vs 22 cm/s).

Before the use of [hiPSC-CMs](#), neonatal rat cells, which also represent an immature cell phenotype, were used to create [EHTs](#). A famous study conducted by Zimmermann et al [40] in 2006 showed that thick (1-4mm) patches display evidence of electrical coupling with native myocardium. However, [CV](#) measurements were performed only on the host tissue, and reported a 20% decrement in [CV](#) between non-infarcted myocardium ( $69\pm6$  cm/s) and infarcted myocardium after implantation ( $55\pm16$  cm/s).

#### 1.4.4 Conductive polymers in cardiac tissue engineering

Desirable features for a scaffold used in cardiac tissue engineering include: electrical conductivity, biocompatibility and elasticity similar to the native myocardium [41].

While many different kinds of scaffolds have been tested, we focus on the use of scaffolds manufactured with electroactive materials. In fact, although injectable biomaterials benefit cardiac function by preventing ventricular dilation [32], the contraction and relaxation of the heart depends on the conduction of electric impulses through cardiac tissue, which is decreased after [MI](#) [42]. Among the wide variety of electroactive materials, conductive polymers ([CP](#)) have been extensively researched in recent years. [CP](#) are a class of  $\pi$ -conjugated polymers with loosely held electrons in their backbones [43]. Within the unsaturated backbone, the delocalized  $\pi$ -electrons can move freely to form an electrical pathway for mobile charge carriers. This feature, which makes the polymers conductive, is obtained by oxidizing or reducing the polymer through a process called doping [44]. Polyaniline(PANI), polypyrrole and polythiophene are largely used [CP](#) in conductive scaffold construction [43]. [CP](#) have widely been used in tissue engineering, trying to assist the recovery of the tissues which are responsive to electrical stimulation [45]. [CP](#) have also been specifically experimented in combination with human-induced stem cells. Findings by Borriello et al suggest that [CP](#) help human-induced pluripotent stem cells during the differentiation process in [CMs](#), while at the same time enhancing migration and proliferation of [hiPSC-CMs](#) [46].

Although several studies seem to confirm the benefits derived from implantation or injection of

CP from a histological point of view (preservation of cardiac function after MI), very few studies actually investigated how the electrical propagation of the stimulus is affected by the presence of the polymer. In a study from 2015, Mihic et al found that injection of chitosan conjugated with polypyrrole in infarcted rat hearts resulted in faster transverse conduction velocities along the border zone epicardial surface. This increment in CV could facilitate synchronous contraction and thus improve cardiac function [47]. The same combination of chitosan conjugated with polypyrrole was tested *in vitro* by a team in the University of Toronto. The biomaterial was used as a structure bridging two physically separated clusters of beating CMs and was found to improve synchronous contraction between the two clusters. The biomaterial was also grafted on ablation injury rat model, resulting in an increment in CV, although it is not clear how the latter was computed. More recently, application of a mussel-inspired cryogel patch was proven to reduce the infarct size and improve the cardiac function in MI rat models [48]. Bao et al conducted two studies on soft CP, injecting them, along with adipose tissue-derived stromal cells, into MI areas of rat hearts. Both studies resulted in an increase of the ejection fraction, reduced fibrotic tissue, and in an increment of Connexin-43, which suggest a promotion in electrical signal transmission [49, 50]. A recent (2020) study [51] tried to combine the use of conductive polymers and rat neonatal CMs, whose not-matured phenotype is similar to the hiPSC-CMs' one. 4 weeks after implantation on infarcted hearts, optical mapping measurements showed a CV of 55 cm/s in non-infarcted regions, and a CV of 40 cm/s on the infarcted regions, that are covered by the conductive patch. Hearts engrafted with conductive patches exhibited higher CV than the non-conductive ones (40 vs 20 cm/s). Interestingly, conductive patches with and without nested CMs showed the same CV (40cm/s). Finally, two recent studies have shown that constructs in polyaniline might synchronize the beating of isolated cardiomyocyte clusters grown on aligned conductive nanofibers and improve CV across fibrotic tissue [52, 53].

## 1.5 Open challenges in cardiac tissue engineering

Despite the huge steps forward in the past decades in the field of cardiac tissue engineering, creating a matured and fully functional tissue *in vitro* is still an open challenge. There are



several benchmarks that remain to be met before engineered heart tissues break into clinical application. The major requirements still to be met (relevant to electrophysiology) are: 1- electromechanical coupling (both between the stem cells-derived CMs in the graft, and between the graft and the host tissue); 2- avoid the development of arrhythmias; 3- stem cells-derived CMs maturation [54].

As introduced in section 1.3.3, lethal post-MI arrhythmias can arise from the patchy spared subepicardium over the infarct [13]. A treatment like EHT patches could significantly affect the propagation of the electrical impulse in these areas. For example, if a re-entrant arrhythmia is anchored to a fibrotic, non conducting-area, the presence of the patch could provide an alternative conducting path and avoid the initiation of the re-entry. In a similar fashion, in case of the presence of an isthmus, attachment of an EHT patch could short-circuit the re-entrant, figure-of-eight pattern, by providing a different conduction pathway. On the other hand, the introduction of an EHT patch could lead to the creation of new electrical pathways between areas of surviving CMs that would otherwise be isolated, ultimately resulting in the formation of new, pro-arrhythmic propagation circuits.

The considerations above take for granted a successful electromechanical coupling between the EHT patch and the host myocardium. However, little investigation has been performed on the communication between the EHT's and the host epicardium's gap junctions. Some studies have found electrical activity in the EHT to be synchronous with the pacing cycle length imposed on the myocardium, suggesting successful patch integration and gap junctions communications [39]. On the other hand, other studies have reported failed EHT-host electrical coupling following the presence of a fibrotic layer between the patch and the epicardium. More studies are needed to understand the implications of these phenomena, and to investigate the consequences of hybrid cases, such as incomplete/partial coupling. Moreover, little is known about the possible interaction (depending on the placement site) of EHT patches with layers of fat or with coronary arteries.

While animal studies have showed improvements in ventricular morphology and function, understanding how cardiac patches electrically interact with host tissues represents a crucial

bottleneck towards successful clinical application [55].

The first human clinical trial involving cardiac patches was performed by Menasche et al [56]. In this trial, fibrin patches with human embryonic stem cells-derived cardiovascular progenitors have been engrafted on infarcted left ventricles. Only a mild improvement in conditions was registered among patients, however, the safety profile was satisfactory, with no occurrence of arrhythmia and no detection of teratomas from residual pluripotency of the engrafted cells. The first clinical study (BioVAT-HF NCT04396899) involving transplantation of EHT containing hiPSC-CMs (embedded in bovine collagen) in patients with severe HF is reported, as of 2022, to be still in the recruiting phase [55].

### 1.5.1 Stem cells derived cardiomyocytes immaturity

From an electrophysiological point of view, one of the major challenges associated with human-induced pluripotent stem cells is the immaturity of the CMs derived from them. After differentiation in CMs, hiPSC-CMs are more similar to fetal CMs rather than adult CMs [57]. Adult CMs present a highly organised structure, optimized for contraction [58]. Specifically, adult CMs possess aligned sarcomeres, a vast network of T-Tubules, a longitudinal sarcoplasmic reticulum with terminal calcium reservoirs positioned near T-tubules to optimize calcium kinetics and a high density of mitochondria to improve ATP consumption from the contractile apparatus [59, 60]. hiPSC-CMs do not possess this level of complexity [61]. They can not equal the metabolic demand of adult CMs, necessary for generating the proper contractile force [62]. Moreover, hiPSC-CMs lacks of calcium handling, which is a key regulator of the electromechanical coupling. Specifically, hiPSC-CMs present an underdeveloped sarcoplasmic reticulum, a minor presence of proteins associated with calcium handling, such as the SERCA pump and the ryanodine receptor-2, as well as a lack of T-tubules, which co-localize L-type calcium channels and ryanodine receptors [63, 64].

hiPSC-CMs present different ion channels density with respect to adult CMs [65], and thus they display a distinct AP profile Figure 1.7. Unlike adult CMs, which are usually quiescent, hiPSC-CMs can self-excite, thus they possess a spontaneous beating rate [66]. hiPSC-CMs

AP profile also present a slower upstroke velocity, a longer APD and a less negative resting membrane potential [67, 68, 69]. These immature characteristics, combined with the lack of organized gap junctions, are responsible for a slowing in AP propagation.

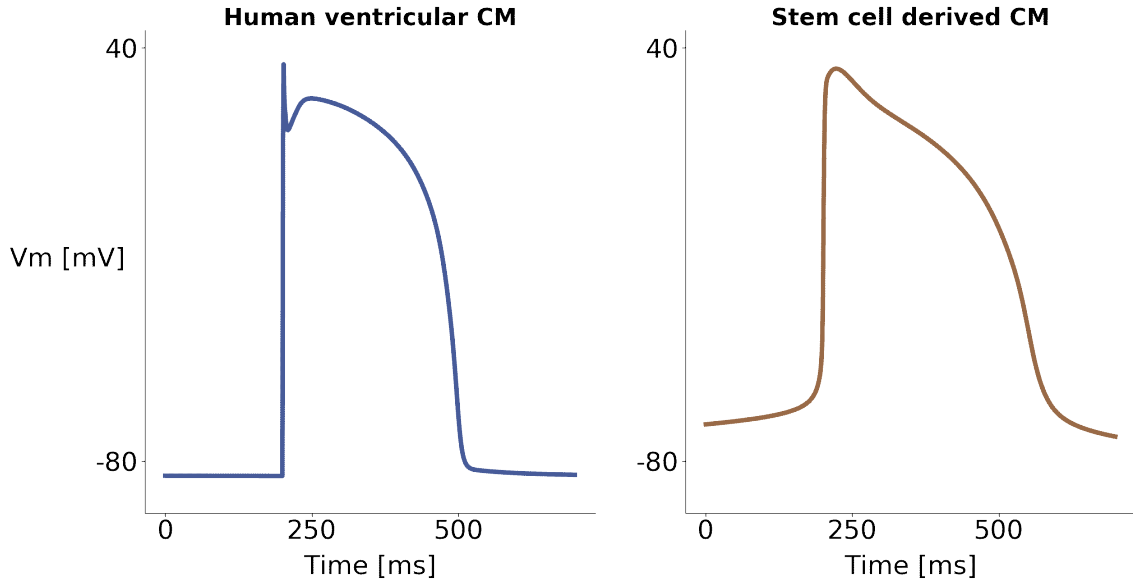


Figure 1.7: Difference between AP shape of a adult human ventricular myocardium and a immature stem cell derived cardiomyocyte.

Given the above listed differences in electrophysiology between hiPSC-CMs and adult CMs, the eventual electrical coupling between EHT with hiPSC-CMs and host myocardium intrinsically raises questions about safety, as introduction of electrical heterogeneities in the heart is generally regarded as pro-arrhythmic [70]. Recently, a considerable amount of effort has been put to investigate new maturation techniques for hiPSC-CMs.

### 1.5.2 Stem cell derived cardiomyocytes maturation techniques

Maturation is the process of cardiac development that turns fetal heart cells to adult CMs, capable to carry out their life-long pumping function [71]. The first approach to achieve hiPSC-CMs maturation consisted in prolonging culture time (up to several months). Despite helping maturation, hiPSC-CMs still showed fetal phenotype features [72]. This is possibly due to the fact that human CMs fully mature only years after birth [73]. However, early stages hiPSC-CMs transplanted in animal hearts have developed adult phenotype characteristics, proving that

hiPSC-CMs are able to mature, when the right environment is provided.

Several environmental factors contribute to cardiac development in humans [74]. Excitability and contractility are chief features in adult CMs. Thus, exogenous electrical and mechanical stimulation have been used to promote maturation. Experiments on neonatal rat CMs have shown that electrical stimulation at physiological frequency resulted in cell alignment and increment in connexin-43 and gap junctions [75]. Stimulation of hiPSC-CMs at frequencies higher than physiological ( $> 1\text{Hz}$ ) also promoted cell alignment, and improved sarcoplasmic reticulum function and the overall electrophysiological profile [76]. Mechanical stress protocols also encouraged hiPSC-CMs maturation, by improving sarcomeric organization and force development [77]. Since cardiac function is highly dependent on the myocardium anisotropic architecture, attempts to assemble hiPSC-CMs in 3D scaffolds have been proposed to promote maturation. 3D constructs with different architectures have been tested, such as cell sheets, spheroids and patches [78, 79, 80]. Growing hiPSC-CMs on 3D structures has been found to increase hiPSC-CMs contractile force and enhance general maturation [78]. Electrical and mechanical stimulation and structural support are often combined with other techniques such as biological factors and genetic regulation, to further enhance maturation. For instance, biological factors such as fatty acid can be used in hiPSC-CMs culturing to advance metabolic maturation, by supporting hiPSC-CMs metabolic shift from glycolysis to fatty acid oxidation [81]. Genetic manipulation is usually performed during the differentiation of pluripotent stem cells into CMs. With this approach, genes like *KCNJ2* and *CSQ2* can be overexpressed to, respectively, hyperpolarize the resting membrane potential [82] and improve calcium kinetics [83].

Despite the advances in hiPSC-CMs maturation techniques, a complete maturation has yet to be achieved [54], thus the possible effects of using not fully matured CMs for cardiac tissue engineering should be investigated.

## 1.6 Motivation and Objectives

The use of cardiac patches to alleviate the condition of post-MI hearts is currently still being tested on animal models. There are still several bottlenecks (see section 1.5) preventing this technology from making the leap to clinical trial and eventually to clinical application. The purpose of this Thesis is to leverage computational model of cardiac electrophysiology to try to address these limitations and, more generally, to investigate the impact of EHT patches on the recipient heart. To achieve this goal, we perform numerical simulation using state-of-the-art models representing ion channels kinetics at a tissue level and AP propagation at a tissue/organ level. We use *in silico* experiments to evaluate a range of different scenarios whose testing in laboratory experiments would otherwise be too expensive and time consuming. Moreover, we use computational models to explore the application of EHT patches in human hearts, which has yet to become reality.

Specifically, throughout this Thesis, we aim to:

- Create a geometrically simple model representing a scarred slab of tissue with an epicardial layer of hiPSC-CMs placed on top of the scar (representing the EHT patch), bridging the healthy tissue at the two ends of the scar.
- On the model outlined above, test how the presence of the EHT patch influences electrical propagation from one end to the other of the tissue slab. In order to do that, we will measure the time it took the electrical wave to reach the corner of the slab opposite to the stimulation area, after crossing the scar-EHT complex. This will give us an idea of whether the changes in model parameters are slowing or accelerating electrical propagation and enable the comparison of the activation time after the scar-EHT complex with the one of a healthy slab, to use as a benchmark for propagation in absence of a scar. The activation time in the corner opposite the stimulation area will also represent a scalar model output for our tissue model, which we will use as a target to train statistical emulators of our model. The differences in pathway followed by the electrical wave when moving from one side to the other of the tissue slab, through the scar-EHT complex, will also be

investigated.

- Create a version of the above model and compare the obtained results for 3 different species, namely rat, rabbit and human. This will be done to test whether/how much the results obtained experimentally on small mammals are translatable to humans. We have chosen rat and rabbit because they are the species most of the laboratory experiments are conducted on. And humans because it is the target species we are ultimately aiming to draw conclusions on.
- Create a more geometrically accurate model using left ventricle geometries reconstructed from magnetic resonance images of ischemic cardiomyopathy patients. We will devise a pipeline to simulate *in silico* the attachment of an epicardial EHT patch on infarcted left ventricle models.
- We will then use these models to test how the application of an EHT patch influences electrical propagation in more anatomically accurate scenarios. For example, we will test which electrical features render a patch able to prevent the onset of re-entrant arrhythmia in the presence of an isthmus-like scar pattern.

### 1.6.1 Thesis Outline

This Thesis is divided into 5 Chapters.

The first 2 Chapters provide the reader with the minimal background required to fully appreciate the work reported in later Chapters.

Specifically, this Chapter has provided the clinical context, laying out essential notions of cardiac anatomy and physiology and giving an overview on cardiac arrhythmias and myocardial infarction, two of the issues that motivate the existence of this work. In this Chapter we have also presented regenerative medicine as a possible solution to these issues and explained what are the open challenges that are hampering the progression to clinical applications.

Chapter 2 provides an overview of the state-of-the-art computational techniques and computational models for cardiac electrophysiology, used in this research to simulate *in silico* biophysical processes as the excitation of a cardiac cell and the propagation of the electrical stimulus in the cardiac tissue. A section on cell ionic models of stem cells derived cardiomyocytes is also given. Chapter 2 concludes with a brief overview of Gaussian Processes, a statistical model exploited in this study to emulate the complex biophysical models and ease their computational burden.

Chapter 3 reports our first study, where we modelled the interaction between a patch of engineered heart tissue and the host myocardium using a simple 3D model with an idealized geometry. We used the statistical tools described in Chapter 2 to do an in-depth investigation of the model behaviour, by performing a sensitivity analysis of the model. We then assessed which designed of the engineered heart tissue restored physiological activation and we assessed the related arrhythmic risk.

In Chapter 4 we built upon the work in Chapter 3, and moved to investigate the effects of engineered heart tissue on more realistic geometries. In this Chapter we describe how we manipulated left ventricle models from a cohort of heart failure patients to perform *in silico* the application of an engineered heart tissue patch. We then illustrates the effects on the left ventricle electrophysiology predicted by our simulations, based on the different engineered heart tissue patches design.

Finally, in Chapter 5 we discuss the overall findings, the implications and the limitations of the presented studies, we assess how the work presented in this Thesis fits in the literature and we draw the conclusions, considering eventual next steps.

# Chapter 2

## Computational Methods

This thesis makes extensive use of physics-based computational models to study the engineered heart tissues and its effects on the host myocardium electrophysiology. Computational models are an essential tool in engineering and have applications in a wide range of fields, from physics and chemistry to psychology and economics. In this work we use models applied to biology, specifically models designed to replicate human biophysical processes in a computer simulation (*in silico*). In this chapter we briefly present the models and computational techniques used in this thesis. Starting with an overview of models used in cardiac electrophysiology, from the cellular level to the tissue/organ level, we continue with a focus on models of hiPSC-CMs electrophysiology. We conclude with an introduction to sensitivity analysis and emulators for computational models, used in this thesis to investigate input-output model relations and tackle time-expensive computer simulations.

### 2.1 Computational models of cardiac electrophysiology

Over the past few decades, computational models of cardiac biophysical processes (electrophysiology, mechanics and fluid dynamics) have been developed, utilised, verified and validated [84]. Computational models represent a powerful tool to integrate and interpret empirical data, to gain quantitative insight on the mechanistic aspects behind biological processes. Computa-



tional models allow focused experimental measurements to be quantitatively interpreted in the context of wider physiological knowledge, encoded in a physics-based model, to identify underlying mechanisms in emergent systems. In computational models of the heart, the cell and tissue scale are routinely separated, both in terms of the modelling framework and in terms of the experimental data used to constrain the model parameters. At the level of the single cardiac myocyte, mathematical models made up of systems of ordinary differential equations (ODEs) represent the electrochemical processes happening inside a cardiac cell, i.e. the ion channels kinetics and the transmembrane potential. The parameters of these models are usually fitted from single cell voltage clamp experiments, in which single ion channels can be isolated for their behaviour to be studied. At the tissue level, the electrical excitation spreading across the heart is modelled as a reaction-diffusion process, treating the myocardium as a syncytium. The *reaction* part of these equations is represented by the processes happening within the single cell, while the *diffusion* part models the cell-to-cell electrical propagation. Reaction-diffusion mechanisms are modelled with partial differential equations (PDEs), which describe the propagation of the cardiac AP in space. The parameters of these models are fitted from experiments which record electrical propagation in cardiac tissue using techniques as micro-electrodes arrays or optical mapping with voltage-sensitive dyes.

### 2.1.1 Cell scale: modelling ion channel kinetics and membrane potential

The modelling of single cell electrophysiology lays its foundation on the work of Alan Hodgkin and Andrew Huxley, who first published in 1952 the mathematical formulation of the cell membrane [85]. The Hodgkin-Huxley model, initially designed to model the neuron AP, is also used as a starting model to develop models of cardiac cell AP, and throughout the decades has become one of the most successful mathematical models of a biological system. In the Hodgkin-Huxley framework, the cell membrane is modelled as a capacitor in parallel with a series of time-variant resistors and voltage generators, representing the ion channels. The current flowing through the membrane is usually defined as the sum of a capacitive component

( $I_m$ ) and a resistive component ( $I_{ion}$ ). The resistive component is defined as the sum of the transembrane ionic currents. We define the current across the cell membrane ( $I$ ) as

$$I = I_m + I_{ion}. \quad (2.1)$$

Expressing the capacitive current with the capacitor constitutive relation and the ionic currents through the Ohm law, we obtain:

$$I = C_m \frac{dV_m}{dt} + \sum g_{ion} (V_m - E_{ion}) \quad (2.2)$$

where  $g_{ion}$  are channel conductances for channels carrying the  $ion$  species,  $V_m$  is the transmembrane potential and  $E_{ion}$  is the Nernst or reversal potential for the  $ion$  species. The last term is repeated for each ion channel considered. In cardiac cell models, the main ions that are considered are sodium ( $Na^+$ ), responsible for depolarization, potassium ( $K^+$ ), involved in repolarization, and calcium ( $Ca^{2+}$ ), involved in electromechanical coupling. The Nernst or reversal potential for each ion ( $E_{ion}$ ) is computed as:

$$E_{ion} = \frac{RT}{zF} \ln \frac{[ion]_o}{[ion]_i} \quad (2.3)$$

where  $R$  is the ideal gas constant,  $T$  is the absolute temperature,  $z$  is the ion charge,  $F$  is the Faraday constant and  $[ion]_o$  and  $[ion]_i$  are the extracellular and intracellular ion concentrations, respectively.

The permeability of ion channels to a specific ion species is not constant, but rather controlled by a complex gating mechanism. In the Hodgkin-Huxley formulation, the conductance of each channel ( $g_{ion}$ ) is controlled by time- and voltage-dependent gating variables:

$$g_{ion} = x^a y^b G_{max} \quad (2.4)$$

where  $G_{max}$  is the maximum channel conductance and  $x(t, V_m)$  and  $y(t, V_m)$  are the activation

and inactivation gating variables. Essentially, the gating variables describe the fraction of open (and closed) gates for each channel, in fact their value range between 0 and 1. The amplitude of the current is proportional to the open gates in the channel. The generic gating variable  $x$  is described by the equation:

$$\frac{dx}{dt} = \alpha_x(V_m)(1 - x) - \beta_x(V_m)x \quad (2.5)$$

where  $\alpha_x$  and  $\beta_x$  are the voltage-dependent rate constants of the channel closing and opening, respectively. The activation rate thus increases monotonically with raising voltage, while the deactivation rate decreases monotonically with raising voltage. Imposing

$$\alpha_x = \frac{x_{inf}}{\tau_x} \quad (2.6)$$

and

$$\beta_x = \frac{1 - x_{inf}}{\tau_x} \quad (2.7)$$

equation 2.5 can be rewritten as:

$$\frac{dx}{dt} = \frac{x_{inf} - x}{\tau_x} \quad (2.8)$$

where  $x_{inf}$  is the steady-state, i.e. the value the gating variable tends at a certain transmembrane voltage and  $\tau_x$  is the gating variable time constant, which measures how fast the gating variable reaches the steady-state.  $x_{inf}$  is obtained by fitting experimental data with the following sigmoid function:

$$x_{inf} = \frac{1}{1 + \exp^{\frac{V_m - V_h}{K}}} \quad (2.9)$$

where  $V_h$  is the half activation voltage and  $K$  is the gradient of activation.

Although the Hodgkin-Huxley paradigm is still at the base of many models of membrane electrophysiology (including the ones used in this Thesis), more recent approaches have been developed, such as Markov-type models [86], in which the different configurations of the channel are represented by a discrete number of states.

### 2.1.2 Tissue scale: modelling the action potential propagation

At the tissue level, models of cardiac electrophysiology are written as PDEs describing the diffusion of the single cell AP in time in excitable tissue. The most common models are the monodomain and the bidomain models. The monodomain model can be derived as an extension of the cable equation of passive propagation. To provide the fundamental concepts behind the mono and bidomain models, in this section we derive the cable equation (in 1D, for simplicity) and show how it is modified to obtain the monodomain equation. Additionally, we outline the main assumptions of the bidomain model, briefly derive its equations and show how they relate with the equation of the monodomain model.

#### Deriving the cable equation

The cable equation in 1D can be derived as follows. We assume a length of cells acts as a cylindrical cable of infinite length. A schematic representation of the cable equation electrical components is reported in Figure 2.1

The transmembrane potential  $V_m$  is defined as:

$$V_m = \phi_i - \phi_e \quad (2.10)$$

where  $\phi_e$  and  $\phi_i$  are the extracellular and intracellular potential, respectively. The variation in  $V_m$  given a small variation in space  $\Delta x$  is given by:

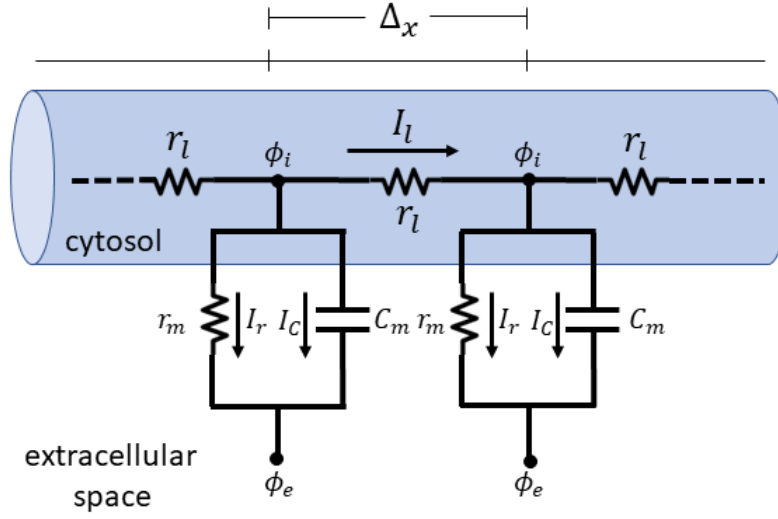


Figure 2.1: Schematic representation of the cable equation electrical circuits.

$$\Delta V_m = -I_l r_l \Delta x \quad (2.11)$$

where  $r_l$  is the cable resistance per unit length and  $I_l$  is the longitudinal current (along the cable main direction). For very small space intervals ( $\Delta x \rightarrow 0$ ), we obtain:

$$\frac{\partial V_m}{\partial x} = -I_l r_l \quad (2.12)$$

Given kirchoff's Law conservation of charge we have:

$$\Delta I_l = -I_m \Delta x \quad (2.13)$$

because charge can leave the cable only through the transmembrane current  $I_m$  in the small space interval  $\Delta x$ . Again, if  $\Delta x \rightarrow 0$ , we obtain:

$$\frac{\partial I_l}{\partial x} = -I_m \quad (2.14)$$

At each point  $x$  the transmembrane current  $I_m$  is a combination of a capacitive component  $I_c$  and a resistive component  $I_r$ . The capacitive component can be expressed with the constitutive relation for a capacitor:

$$I_c = C_m \frac{\partial V_m}{\partial t} \quad (2.15)$$

while the resistive component can be expressed by the Ohm's Law:

$$I_r = \frac{V_m}{R_m} \quad (2.16)$$

where  $R_m$  is the membrane resistance per unit length. Combining the two currents we can write the equation for the transmembrane current:

$$I_m = C_m \frac{\partial V_m}{\partial t} + \frac{V_m}{R_m} \quad (2.17)$$

Substituting 2.12 in 2.14, differentiating and equalling to equation 2.17, we obtain the passive cable equation:

$$\frac{\partial I_l}{\partial x} = \frac{\partial}{\partial x} \left( -\frac{1}{r_l} \frac{\partial V_m}{\partial x} \right) = -\frac{1}{r_l} \frac{\partial^2 V_m}{\partial x^2} = - \left( C_m \frac{\partial V_m}{\partial t} + \frac{V_m}{R_m} \right) \quad (2.18)$$

Rearranging, the cable equation in 1D can be written as follows:

$$\sigma_i \frac{\partial^2 V_m}{\partial x^2} = C_m \frac{\partial V_m}{\partial t} + \frac{V_m}{R_m} \quad (2.19)$$

where  $\sigma_i$  is the intracellular conductivity. The resistive component of the transmembrane current can be substituted with currents describing ion channels activity:

$$\sigma_i \frac{\partial^2 V_m}{\partial x^2} = C_m \frac{\partial V_m}{\partial t} + \sum I_{ion} \quad (2.20)$$

### From the 1D cable equation to the 1D monodomain equation

From the cable equation, the monodomain model can be derived by incorporating, in the reaction term in equation 2.20, the Hodgkin-Huxley formulation, which models the transmembrane potential locally. The 1D monodomain equation can thus be written as:

$$D \frac{\partial^2 V_m}{\partial x^2} = \frac{\partial V_m}{\partial t} + \frac{1}{C_m} I_{ion}(V_m, \nu) \quad (2.21)$$

where  $I_{ion}$  is the current flowing through the membrane ion channels, which depends on the transmembrane voltage  $V_m$  and other variables, summarized here with  $\nu$ .  $D$  is the diffusion coefficient, and it is defined as:

$$D = \frac{\sigma_i}{\beta C_m} \quad (2.22)$$

where  $\beta$  is the tissue surface to volume ratio. The diffusion coefficient  $D$  is an important parameter, as it models the gap junctions resistivity, which is assumed to be homogeneous over the length of the cell.

### Bidomain model

In the bidomain formulation, the syncytium is composed of two continuous and overlapping domains: the intracellular and the extracellular domains. They are separated by the cell membrane. Each domain is described by a generalization of Ohm's law, outlining the relationship between electrical potential ( $\phi$ ), current density ( $\mathbf{J}$ ) and conductivity (tensor  $\mathbf{G}$ ).

$$\mathbf{J}_e = -\mathbf{G}_e \nabla \phi_e$$

$$\mathbf{J}_i = -\mathbf{G}_i \nabla \phi_i$$

Considering the conservation of current and charge, assuming only membrane related sources in the intra- and extra-cellular space and writing the transmembrane current as a capacitive current plus an ionic current ( $I_{ion}$ ), we obtain the bidomain model equations:

$$\begin{aligned}\nabla \cdot (\mathbf{G}_e \nabla \phi_e) &= -\beta_m (C_m \frac{\partial V_m}{\partial t} + I_{ion}) \\ \nabla \cdot (\mathbf{G}_i \nabla \phi_i) &= \beta_m (C_m \frac{\partial V_m}{\partial t} + I_{ion})\end{aligned}$$

where  $\beta_m$  is the surface area-to-volume ratio of a cardiac cell,  $C_m$  the cell membrane capacitance,  $V_m$  the transmembrane voltage (given by equation 2.10) and  $I_{ion}$  is the sum of all ionic currents from the coupled cellular [AP](#) model.

When assuming that intracellular and extracellular conductivities have equal anisotropy ratio, the bidomain model can be reduced to the monodomain model:

$$\nabla \cdot \mathbf{G} \nabla V_m = \beta_m (C_m \frac{\partial V_m}{\partial t} + i_{ion}) \quad (2.23)$$

where  $\mathbf{G}$  is the effective conductivity, derived from the proportional conductivities assumption  $\mathbf{G}_e = \lambda \mathbf{G}_i$ . The bidomain model does not explicitly model the gap junctions conductances. Similarly to the monodomain model, it lumps together the cytoplasmic and the gap junctional resistances, homogenising the discrete cardiac tissue structure in a functional continuum.

### 2.1.3 Numerical solvers for cell and tissue scale models equations

The systems of [ODEs](#) which make up the models of cardiac [AP](#) can be numerically solved with standard integration methods such as Euler or Runge-Kutta. The mono and bidomain equations are solved using discretisation techniques, which transform the [PDEs](#) to linear systems of equations. These techniques include the Finite Difference Method and the Finite



Element Method, which divide the continuous domain into a grid of points and into a grid of small elements, respectively. The Finite Element Method is widely used in engineering to solve PDEs on complex geometries, and thus numerical packages implementing this method have been developed and made available by various research groups. In this Thesis, we use the Cardiac Arrhythmia Research Package (CARP), developed in the Medical University of Graz. CARP enables the user to simulate cardiac electrophysiology by providing optimized elliptic and parabolic solvers for the mono and bidomain equations, as well as implementation of optimized solvers for ODEs, such as the Rush-Larsen method, specifically developed for the solution of systems of ODEs in cardiac ionic models. Numerical solution can be further accelerated in CARP by using pragmatic techniques as look-up tables and exponential solutions for gating variables, which essentially pre-compute and store values of expensive functions such as exponentials and logarithms, which can then be retrieved from the look-up table instead of calculating the quantity directly.

## 2.2 Models of hiPSC-CMs electrophysiology

In the past decade, hiPSC-CMs started to appear as a new promising tool for *in vitro* drug models and for regenerative medicine purposes [87]. While several models of cell electrophysiology were produced, for different animal species (e.g. rabbit [88] and guinea pig [89]) as well as for different human cardiac phenotypes (e.g. ventricular [90] and atrial [91] CMs), a specific model of hiPSC-CMs electrophysiology was still missing. The firsts to fill this gap were Paci et al, which published the first hiPSC-CMs electrophysiology model in 2013 [92]. The same authors then built up on this work, producing other studies where they used their model to simulate LQT1 [93] and LQT3 [94] syndromes and compared the effects of different ion channel blockers in their hiPSC-CMs model against a model of adult CMs [95]. In 2018, Paci et al published a new version of their model, which is the model used in this study, with updated equations for handling calcium kinetics in hiPSC-CMs [96]. More recently, Kernik et al [97] developed a computational model of hiPSC-CMs electrophysiology incorporating experimental variability from multiple data sources and demonstrated the models capabilities in linking molecular

mechanisms to known cellular-level [hiPSC-CMs](#) phenotypes. Lastly, in 2022 Folkmanaitė et al [98] integrated a contractile element in a [hiPSC-CMs](#) model, publishing the first [hiPSC-CMs](#) electromechanical model. The authors coupled the Paci model with a model of human adult [CMs](#) contractile machinery. However, the model successfully reproduced the [hiPSC-CMs](#) contractile phenotype, exhibiting calcium transient and [AP](#) biomarkers within ranges established through experiments on [hiPSC-CMs](#).

The Paci [hiPSC-CMs](#) model used in this study follows the classical Hodgkin-Huxley formulation (see section 2.1.1), and describes the membrane potential as follows:

$$C_m \frac{dV_m}{dt} = -(I_{K1} + I_{to} + I_{Kr} + I_{Ks} + I_{CaL} + I_{NaK} + I_{Na} + I_{NaL} + I_{NaCa} + I_{bCa} + I_f + I_{bNa}) \quad (2.24)$$

where  $V_m$  is the transmembrane potential  $C_m$  is the cell capacitance and on the right term are listed all the modelled ion currents and pumps. All the ion currents are modelled according the Hodgkin-Huxley formulation, with time- and voltage-dependent gating variables (see section 2.1.1). In total, the model is composed by several dozens equations, containing around one hundred different parameters, such as ion concentrations in the modelled compartments (cytoplasm and sarcoplasmic reticulum) and ion channels conductances. All models equations and parameters values are provided in the supplementary material of the model publication [99].

## 2.3 Global Sensitivity Analysis

Existing guidelines from regulatory agencies [100] advocate for studies involving mathematical models to be accompanied by a sensitivity analysis. Sensitivity analysis is the study of how uncertainty in the outputs of a system or a model relate to the uncertainty in its inputs. A sensitivity analysis is considered *local* when one input at a time is varied by a small amount, while keeping the other inputs constant. The change in each output is then examined and related to the variation of the specific input to estimate the local derivative of the outputs with respect to each input parameter. While this process can give an idea of how the uncertainty in the model outputs distributes over the inputs, in complex and nonlinear models, inputs

interact with each others. For this reason, changing one input at a time can be inadequate [101]. A sensitivity analysis is considered *global* when all the inputs are varied simultaneously, over their entire range. This approach allows quantification of the impact of each input, as well as of inputs interactions, on the model output, providing a comprehensive view of the model input-output relation, rather than a local one. Various methods can be used to perform global sensitivity analysis (GSA), including regression methods and variance-based methods. Variance-based methods have proved well suited for this problem, and have been used widely by modellers and statisticians [102].

### 2.3.1 Variance-based sensitivity analysis

Variance-based techniques perform probabilistic sensitivity analysis, quantifying the sensitivity of the outputs to the model inputs in terms of changes in the outputs variance. The output variance is related to the input through the sensitivity indices, essentially a value from 0 to 1 computed and assigned to each input parameter. Two sets of sensitivity indices are usually computed: the *first order* effect and the *total* effect [103]. We can derive these two sets of sensitivity indexes by defining a model as a function  $Y = f(X_1, X_2, \dots, X_k)$ , where  $Y$  is a scalar output,  $k$  is the input space dimension and  $X_i$  is a generic input. The first order effect for a generic input  $X_i$  is defined as:

$$V_{X_i}(E_{\mathbf{X}_{\sim i}}(Y|X_i)) \quad (2.25)$$

where  $\mathbf{X}_{\sim i}$  denotes the matrix of all inputs but  $X_i$ . The mean of  $Y$  is computed over all possible values in  $\mathbf{X}_{\sim i}$ , while fixing  $X_i$ . The variance is then taken over all possible values of  $X_i$ . The sensitivity index associated with the first order effect is then computed by dividing the first order effect by the total variance:

$$S_i = \frac{V_{X_i}(E_{\mathbf{X}_{\sim i}}(Y|X_i))}{V(Y)} \quad (2.26)$$

$S_i$  is a normalized value, as the numerator varies between zero and  $V(Y)$ , and represents the first order effect of the input  $X_i$  on the model output. The total effect index is computed as:

$$S_{Ti} = 1 - \frac{V_{\mathbf{X}_{\sim i}}(E_{X_i}(Y|\mathbf{X}_{\sim i}))}{V(Y)} \quad (2.27)$$

The fraction numerator can be thought of as the first order effect of  $\mathbf{X}_{\sim i}$ , i.e. the first order effect of all inputs but  $X_i$ . Thus,  $V(Y)$  minus the fraction numerator will give the variance contribution of all terms that do include  $X_i$ . This variance contribution is named total effect, and it comprises the first and higher order effects, which include the interactions of the input  $X_i$  with the other inputs. In terms of reduction of variance,  $V_{X_i}(E_{\mathbf{X}_{\sim i}}(Y|X_i))$  is the expected reduction in variance if  $X_i$  could be fixed, while  $V_{\mathbf{X}_{\sim i}}(E_{X_i}(Y|\mathbf{X}_{\sim i}))$  is the expected reduction in variance if all the inputs but  $X_i$  could be fixed.

To compute the expected values and variances present in the sensitivity indices formulations (equations 2.26 and 2.27 above), integrals of the function  $Y = f(X_1, X_2, \dots, X_k)$  representing our model need to be computed. However, these integrals do not have a direct mathematical solution, thus estimators are needed to approximate their real values.

State-of-the-art estimators for these integrals have been developed by Saltelli [103]. According to Saltelli, the variance necessary to obtain the first-order effect  $S_i$  (equation 2.26), can be approximated as follows:

$$V_{X_i}(E_{\mathbf{X}_{\sim i}}(Y|X_i)) = \frac{1}{N} \sum_{j=1}^N f(\mathbf{A})_j (f(\mathbf{B}_A^{(i)})_j - f(\mathbf{B})_j) \quad (2.28)$$

where  $N$  is the number of model evaluations,  $f$  is the function representing our model and  $\mathbf{A}$  and  $\mathbf{B}$  are  $N \times k$  matrices of input factors, where  $k$  is the input space dimension. In other words, matrices  $\mathbf{A}$  and  $\mathbf{B}$  have on each row a combination of input parameters, sampled inside given parameter ranges.  $\mathbf{B}_A^{(i)}$  represents a matrix where column  $i$  comes from matrix  $\mathbf{A}$  and all other  $k - 1$  columns come from matrix  $\mathbf{B}$ . In this way, integral computations have been replaced with model evaluations on the input sequences stored in  $\mathbf{A}$  and  $\mathbf{B}$ .

These matrices are populated generating pseudo-random parameters sequences inside the input space (Monte Carlo approach) or low-discrepancy sequences (quasi-Monte Carlo approach). In this work we will use the quasi-random, low discrepancies Sobol sequences [104], because they have been shown to outperform crude Monte Carlo sampling in the estimation of multi-dimensional integrals [105]. These sequences are specifically designed to generate samples of  $X_1, X_2, \dots, X_k$  as uniformly as possible over the  $k$ -dimensional input space. Consecutive quasi-random points "know" about the position of points sampled previously and fill the gaps between them.  $\mathbf{A}$  and  $\mathbf{B}$  are then created from a quasi-random sequence of size  $N \times 2k$ , with  $\mathbf{A}$  being the left half of the sequence and  $\mathbf{B}$  the right part of it.

However, to obtain an accurate estimation of the integrals,  $N$  often results to be of the order of hundreds or thousands, i.e. hundreds or thousands of model evaluations are required (see terms  $f(\mathbf{A})$ ,  $f(\mathbf{B}_{\mathbf{A}}^{(i)})$  and  $f(\mathbf{B})$  in equation 2.28). Depending on the single model run time, the computation of the first order and total effect indices can quickly become very expensive. Techniques such as the use of emulators can be employed to reduce the computational burden.

### 2.3.2 Gaussian processes emulators

One drawback of the aforementioned cardiac tissue models is the computational burden associated with the numerical solvers necessary to solve the mono or bidomain equations. The computational time further increases when these models need to be solved multiple times, as happens when facing tasks like sensitivity analysis. Surrogate models (or *emulators*) can be used to learn a statistical representation of the model's input-output relationship. However, a series of model runs is still needed to obtain a set of outputs, i.e. the data on which to train the surrogate model. In this work we have used Gaussian processes (**GPs**) as surrogate to emulate our cardiac, tissue-level models.

**GPs** are stochastic processes, and can be thought of as a generalization of the Gaussian probability distribution. While probability distributions describe random variables, stochastic processes describe functions. **GPs** models are used in *supervised learning*, in which data are used to infer an input-output mapping. This problem is called regression or classification, depending

whether the output is continuous or discrete. In a regression problem, we need to find a function  $f$ , that maps the input to the available outputs and that will allow us to make predictions on new inputs. Essentially, we can find the target function  $f$  in two ways: we can choose a class of functions to consider, for example linear functions of the input, or we can follow a Bayesian approach. In the Bayesian approach, a *prior* probability is given to every possible target function. This probability distribution over target functions is specified by a Gaussian process. At this point, we can incorporate the information coming from the outputs (i.e. the available data). Observations will give us points in the output space, enabling us to favour functions that pass, or are close to, those points. Combining the prior with the available data (i.e. the model outputs) modifies the prior distribution, resulting in the *posterior* distribution over functions. The effect of data consists in scaling back in the posterior the functions that are incompatible with the data. In other words, the more data arrive, the less "flexible" our distribution of functions become.

The choice of the prior determines the properties of the functions used for inference. These properties can be modified by changing the *covariance function* of the Gaussian process. Covariance functions have adjustable parameters, which can be tuned according to the data. When using [GPs](#), the process of inferring the covariance functions parameters from the data is considered the learning step.

Since [GPs](#) enable us to approximate our model's input-output relationship with a function, they represent an ideal statistical tool to create *emulators*, i.e. surrogate models. More formally, our emulator can be defined as:

$$f(\mathbf{x}) := \mathbf{m}(\mathbf{x}) + \mathbf{g}(\mathbf{x}) \quad (2.29)$$

where  $\mathbf{m}(\mathbf{x})$  corresponds to the deterministic part, given by a linear regressor:

$$\mathbf{m}(\mathbf{x}) = \mathbf{h}(\mathbf{x})^T \beta \quad (2.30)$$

and  $\mathbf{g}(\mathbf{x})$  corresponds to the stochastic part, i.e. the Gaussian process, defined as:

$$\mathbf{g}(\mathbf{x}) \sim \mathcal{GP}(\mathbf{0}, k(\mathbf{x}, \mathbf{x}')) \quad (2.31)$$

As we can see in the equation above, the GP is characterized by zero mean and a covariance function, named *kernel*. The parameters of the linear regressor ( $\mathbf{h}$ ) in equation 2.30) are computed by minimizing the sum of the squared residuals between the data (the observations, or model runs, in our case) and the values predicted by the linear regressor. The GP's parameters are instead computed by maximizing the marginal likelihood function [106]:

$$p(\mathbf{y}|X) = \int p(\mathbf{y}|\mathbf{f}, X)p(\mathbf{f}|X)d\mathbf{f} \quad (2.32)$$

where  $p(\mathbf{y}|\mathbf{f}, X)$  is the likelihood and  $p(\mathbf{f}|X)$  is the prior. Under the Gaussian process model the prior and the likelihood are Gaussian, thus their product is also Gaussian, making possible to compute the analytical solution for the integral in equation (2.32) and ultimately computing the marginal likelihood. The GP's so called *hyperparameters* correspond to the *kernel* parameters. In this work we explored two anisotropic covariance functions, squared exponential and *Matern* [106]. The squared exponential has form:

$$k_{SE}(r) = \exp\left(-\frac{r^2}{2l^2}\right) \quad (2.33)$$

while the *Matern kernel* is defined as:

$$k_{Matern}(r) = \frac{2^{1-\nu}}{\Gamma(\nu)} \left(\frac{\sqrt{2\nu}r}{l}\right)^\nu K_\nu \frac{\sqrt{2\nu}r}{l} \quad (2.34)$$

In the equations above, the hyperparameters, which will be tuned according to the data, are  $l$  for the squared exponential and  $l$  and  $\nu$  for the *Matern* kernel.

A surrogate model mimics the behaviour of the simulated model, while being computationally cheaper to evaluate, as the numerical solving of the models equations is replaced by a simple function evaluation. The use of GPs emulators and the consequent reduction in computational burden permitted us to perform global sensitivity analysis on a cardiac tissue electrophysiology model.

## Chapter 3

# Modelling the interaction between stem cells derived cardiomyocytes patches and host myocardium: a simple 3D model

### 3.1 Introduction

MI hospitalizes 1 person every 5 minutes in the UK [107]. Although 7 persons out of 10 survive [108], their heart can be permanently compromised. Due to the lack of blood supply, MI can cause parts of the myocardium to become non-contraction and non-conductive, scar-like tissue. The presence of scar can have a severe impact on the heart, exposing patients to risks ranging from arrhythmias to impaired cardiac function.

The irreversible damage to the cardiac tissue caused by MI and the limited ability of the adult heart to regenerate lost CMs make cardiac transplantation or left ventricular assist devices the only treatments able to restore cardiac function. However, heart transplants are in limited supply and require life-long immuno-suppression [24], while left ventricular assist devices have approximately 80% complication rate [109]. Cardiac regenerative medicine has recently



been proposed as a promising alternative [24, 110, 111]. It comprises a wide spectrum of novel treatments, whose target is to replace or augment the function of tissue lost to cardiac infarcts. In this study we focus on the epicardial application of patches of stem cell-derived engineered heart tissue [112].

Many challenges need to be faced in the development of this treatment. A better understanding of the electrical interaction of the engineered and host heart tissue is crucial. While the presence of new engineered heart tissue can represent an alternative pathway for the electrical propagation in presence of scar tissue, the immaturity of the hiPSC-CMs can lead to different electrical propagation properties to the host that may contribute to an increased arrhythmia risk [38, 113, 114]. *In vitro* experiments involving patches have been conducted using many experimental setups with differences in pacing rates, engineered heart tissue dimensions and host species, making it hard to compare results and interpret results in the context of human physiology [115, 116, 117].

Computer simulations of the heart have advanced to a point where they are being used for interpreting and guiding clinical procedures [84]. Here we apply this approach to develop and validate a tissue-scale model to simulate *in silico* electrical propagation in a slab of scarred heart tissue in the presence of a patch of engineered heart tissue and CP engrafted at the epicardium.

This model is geometrically simple, does not resemble real heart anatomy and thus cannot be used to test potential creation of pro-arrhythmic circuits arising from the attachment of the EHT patch. However, the use of a ionic cell model reproducing the ion channels kinetics of hiPSC-CMs will enable us to test potential arrhythmic behaviour arising from the hiPSC-CMs automaticity. Moreover, we will test how the presence of the EHT patch influences electrical propagation from one end to the other of the tissue slab by recording the activation time in the corner of the slab opposite to the stimulation area, on the other side of the scar-EHT complex. We will use this measure to compare electrical propagation resulting from different model's parameters (such as EHT patch conductivity) combinations. The activation time in the corner opposite the stimulation area will also represent a scalar model output for our tissue model, which will enable us to use machine learning and global sensitivity analysis techniques

adapted to cardiac modelling to identify engineered heart tissue patch design variables that are important for restoring physiological electrophysiology in the host myocardium. We then test if these important variables are species dependent. Finally, we demonstrate how engineered heart tissues could be modified to recover physiological activation while reducing arrhythmic risk.

## 3.2 Methods

### 3.2.1 From 3D geometry to a thin 3D idealized model

To investigate the impact of patch design on activation properties we created a thin 3D slab model of the myocardium (Figure 3.1). The model structure was chosen to resemble current lab experiment designs. This model consists of a transmural cross section of host myocardium, an infarct region, a bath region (representing the Tyrode's solution the hearts are usually coated with during *ex-vivo* experiments in a Langendorff setup), an epicardial patch spanning the infarct region and a space between the patch (designated the internal bath area) and host myocardium capturing imperfect contact due to attaching the patch to the host only at the edges. The patch is modelled as a layer of hiPSC-CMs, which we refer to as EHT for brevity, combined with a layer of CP.

The model approximates a scar in the left ventricle wall. Figure 3.2 indicates how the model relates to a 3D experiment. As an example, we selected a human left ventricle anatomy model generated from cardiac magnetic resonance imaging [118]. To display how the thin 3D model relates to the cardiac anatomy. We have introduced a transmural scar (orange) into the human 3D left ventricle anatomy (A), we cut the ventricle to obtain a transmural section of the ventricular wall (B). We then focus on the infarcted area (C), where experimentally the EHT patch would be engrafted and indicate where the patch would be located relative to the scar (yellow). For our study, we have created a thin 3D model to provide a generalizable parametric representation of a patch over this transmural scar section (D). From this baseline thin 3D

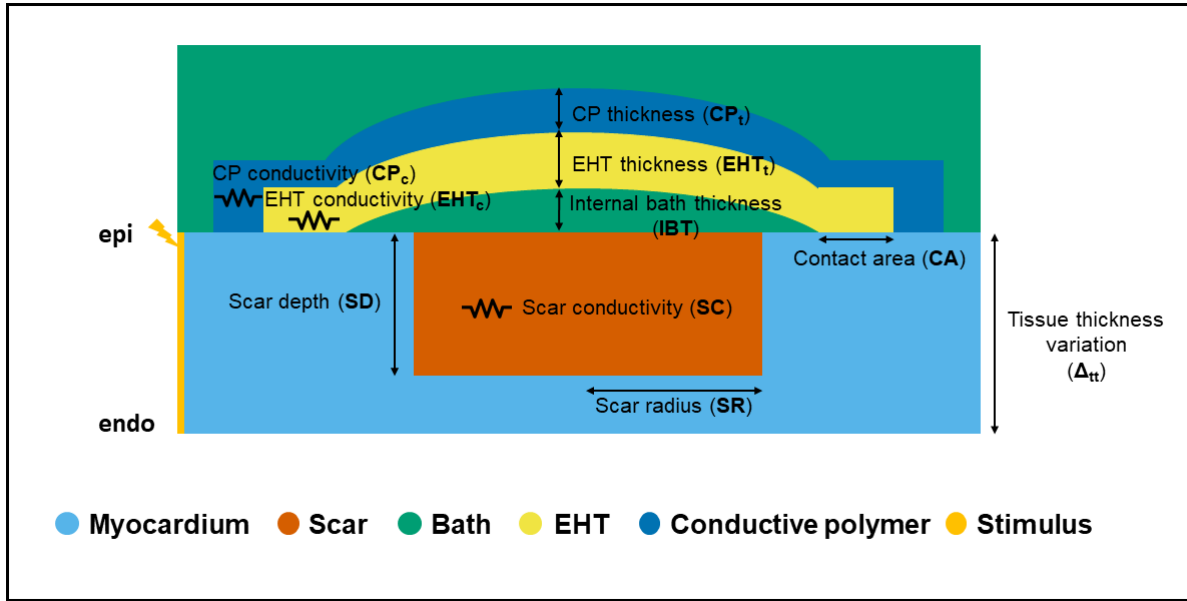


Figure 3.1: Schematic representation of our thin 3D tissue slab model along with the 10 design input parameters considered: Scar radius ( $SR$ ), Scar depth ( $SD$ ), Scar conductivity ( $SC$ ), Engineered heart tissue thickness ( $EHT_t$ ), Engineered heart tissue conductivity ( $EHT_c$ ), Contact area ( $CA$ ), Conductive polymer thickness ( $CP_t$ ), Conductive polymer conductivity ( $CP_c$ ), Internal bath thickness ( $IBT$ ), Tissue thickness variation ( $\Delta_{tt}$ ).

model, we vary the geometrical dimensions and conductivities of the different model components (scar, EHT, etc..) to predict the key design variables for determining the impact of EHT on the host-myocardium electrophysiology.

### 3.2.2 Schematic tissue model description

We consider 10 model input design parameters: tissue thickness ( $\Delta_{tt}$ ), internal bath thickness ( $IBT$ ), engineered heart tissue thickness ( $EHT_t$ ) and engineered heart tissue conductivity ( $EHT_c$ ), conductive polymer thickness ( $CP_t$ ) and conductive polymer conductivity ( $CP_c$ ), scar radius ( $SR$ ), scar depth ( $SD$ ) and scar conductivity ( $SC$ ) and width of the engineered heart tissue-slab tissue contact area ( $CA$ ). Physiologically plausible ranges for each parameter were defined from the literature (Table 3.1). The tissue thickness was chosen based on literature values for the rat, rabbit and human hearts ventricular wall [119, 120] (2, 4, and 6 mm, respectively), and variations from the reference value are encoded by the parameter  $\Delta_{tt}$ , ranging from -10 to +10% relative to the reference wall thickness value. To approximate the impact, if any,

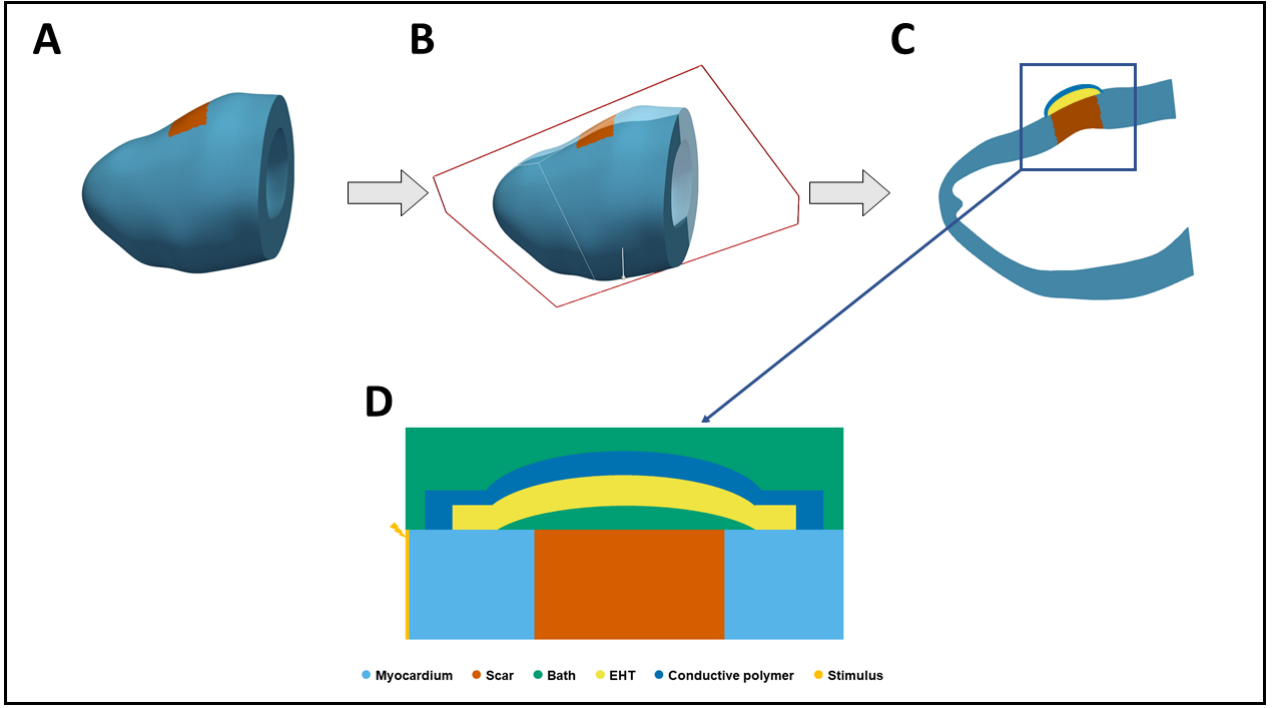


Figure 3.2: From 3D geometry to our idealized thin 3D model. A) Human left ventricle anatomy model with transmurular scar. B) Plane cutting transmurularly through the ventricle wall. C) Extracted transmurular section. D) Idealization of the geometry and application of an EHT patch mimicking experimental design.

of incomplete engraftment, we set the internal bath thickness between 0.1 and 1 mm, although we do not have literature values for this parameter. The values of the parameters related to the EHT patch (thickness, conductivity, and contact area) were chosen based on literature values from *in vitro* experiments where EHT patches had been engrafted onto the epicardium of infarcted hearts [110, 38, 121, 122, 123, 40]. The EHT thickness range is 0.5–2 mm and the range for EHT conductivity was taken as 10–80% of healthy myocardial conductivity. The scar depth was chosen between 10% and 100% of the tissue thickness [121, 124, 125] (100% thickness corresponds to a transmurular scar). The scar radius was set to between 0.7 and 6.6 mm. This allowed us to set the patch length to the average size of experimentally engrafted patches [124, 125], while still covering the scar. The scar conductivity was varied between 0 and 50% of the healthy host myocardium conductivity [126, 127, 128, 129]. The conductive polymer thickness was set to 0.5–2 mm and the conductivity values  $<18$  S/m. Both values were gathered from *in vitro* measurements performed on conductive polymer patches [53, 130, 131].

parameter label	parameter definition	range	units	references
SR	scar radius	0.7-6.6	mm	[38, 125]
SD	scar depth	0.2-6	mm	[121, 38, 125]
SC	scar conductivity	0-0.14	$\text{Sm}^{-1}$	[126, 127, 128, 129]
EHTt	engineered heart tissue thickness	0.5-2	mm	[38, 110]
EHTc	engineered heart tissue conductivity	0.028-0.224	$\text{Sm}^{-1}$	[121, 122]
CA	engineered heart tissue myocardium slab contact area	0.5-2	mm	[123, 40]
CPt	conductive polymer thickness	0.5-2	mm	[53, 130]
CPc	conductive polymer conductivity	0-18	$\text{Sm}^{-1}$	[53, 131]
IBT	internal bath thickness	0.1-1	mm	-
$\Delta_{tt}$	variation in slab thickness	0-10	% of tissue depth	[119, 120]

Table 3.1: Parameter ranges from literature for the 10 model input parameters.

We developed two versions of the model: one with the scar growing from the epicardium to the endocardium (labelled *epi-endo*), and one with the scar expanding from the endocardium to the epicardium (*endo-epi*). These two versions are described by the same 10 parameters. From these general models, we derived 3 sub-cases, progressively fixing the values of the 3 scar parameters (namely the scar depth, scar conductivity and scar radius). First, we set the scar depth equal to the tissue thickness, so that the scar is always transmural. This model was labelled *transmural*. Second, in addition to the scar depth being set equal to the tissue thickness, we also set the scar conductivity to 0, and we labelled this model *block*. Third, besides fixing the scar depth and conductivity, we also fixed the scar radius, setting it to 3.5 mm when modelling rat and rabbit myocardium and 5 mm when modelling human myocardium. We labelled this last sub-case *fixed*. Figure 3.3 below shows how the 3 sub-cases are derived from the two main versions of the model, as well as a schematic representation for each of them.

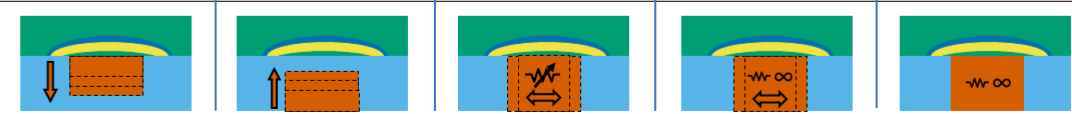
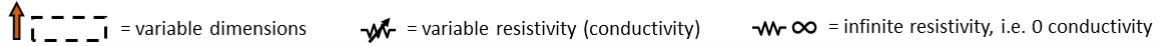
Parameters	Models		Sub-cases		
	Epi-endo (10 parameters)	Endo-epi (10 parameters)	Transmural (9 parameters)	Block (8 parameters)	Fixed (7 parameters)
1) SD [mm]	0.2 – 6	0.2 – 6	Equal to tissue thickness	Equal to tissue thickness	Equal to tissue thickness
2) SC [S/m]	0 – 0.14	0 – 0.14	0 – 0.14	0 (non-conductive)	0 (non-conductive)
3) SR [mm]	0.7 – 6.6	0.7 – 6.6	0.7 – 6.6	0.7 – 6.6	3.5 or 5
4) EHT <sub>t</sub> [mm]	0.5 – 2	0.5 – 2	0.5 – 2	0.5 – 2	0.5 – 2
5) EHT <sub>c</sub> [S/m]	0.028 – 0.224	0.028 – 0.224	0.028 – 0.224	0.028 – 0.224	0.028 – 0.224
6) CA [mm]	0.5 – 2	0.5 – 2	0.5 – 2	0.5 – 2	0.5 – 2
7) CP <sub>t</sub> [mm]	0.5 – 2	0.5 – 2	0.5 – 2	0.5 – 2	0.5 – 2
8) CP <sub>c</sub> [S/m]	0 – 18	0 – 18	0 – 18	0 – 18	0 – 18
9) IBT [mm]	0.1 – 1	0.1 – 1	0.1 – 1	0.1 – 1	0.1 – 1
10) Δ <sub>tt</sub> [%]	0 – 10	0 – 10	0 – 10	0 – 10	0 – 10
Schematic representations					
					

Figure 3.3: Value ranges of the 10 parameters (rows) used in the two versions of our model (*epi-endo*, and *endo-epi*, 1<sup>st</sup> and 2<sup>nd</sup> columns respectively). The 3 sub-cases (*transmural*, *block* and *fixed*) are shown in the 3<sup>rd</sup>, 4<sup>th</sup> and 5<sup>th</sup> columns. The table shows which parameters of the original model are fixed in order to derive each sub-case. The bottom row displays representations of each model version and sub-cases.

### 3.2.3 Simulating cardiac electrophysiology

As introduced in Chapter 3, cardiac electrophysiology is simulated using the bidomain model [132]. The bidomain equations model the cardiac tissue as a syncytium, composed by the intracellular and the extracellular domains. Intracellular ( $\phi_i$ ) and extracellular ( $\phi_e$ ) potential are linked through the transmembrane current  $I_m$ :

$$\nabla \cdot \mathbf{G}_e \nabla \phi_e = \beta_m I_m$$

$$\nabla \cdot \mathbf{G}_i \nabla \phi_i = -\beta_m I_m$$

Where  $\mathbf{G}_i$  and  $\mathbf{G}_e$  are the intracellular's and extracellular's conductivity tensors and  $\beta$  is the cardiac cells surface to volume ratio. The transmembrane current  $T_m$  is expressed as follows:

$$I_m = C_m \frac{\partial V_m}{\partial t} + I_{ion}(V_m, \nu) - I_{trans}$$

Where  $C_m$  is the membrane capacitance per unit area,  $V_m$  is the transmembrane voltage (defined as  $\phi_i - \phi_e$ ),  $I_{trans}$  is the transmembrane current density stimulus and  $I_{ion}$  is the current density flowing through the membrane ion channels, which depends on the transmembrane voltage  $V_m$  and other variables, summarized here with  $\nu$ . As described in Chapter 3, this represents the reaction term of the bidomain model PDEs. The equations describing the relations between ion channels and transmembrane potential depend on which cell ionic model one decides to couple with the bidomain equations. In this work, we aim to model a slab of myocardial tissue from different animal species, namely rat, rabbit and human. We thus chose 3 different ionic models, to represent each species' myocardium. We adopted the Mahajan model [88], the Terkildsen-Niederer-Crampin-Hunter-Smith model [133] and the Ten Tusscher model [90] for the rabbit, rat and human myocardium, respectively. For the EHT the model of hiPSC-CMs from Paci et al [96] was utilized. The model equations were solved using the Cardiac Arrhythmia Research Package (CARP) [134]. A representative AP trace for each cell model is shown in Figure 3.4. In the cardiac tissue, myocytes are arranged in fibre-like structures, with propagation faster parallel to the fiber orientation than perpendicular to it [135]. To capture this anisotropic behavior, we incorporated fibers in our model, transmurally rotating (from endocardium to epicardium) from a 40° angle to a -50° angle, with respect to the longitudinal direction [136]. Figure 3.5 serves as a visual aid for understanding fibres orientation in our thin 3D model. Our model is made of a layer of tetrahedral elements, and a vector determining the fibre orientation is assigned to each element. As can be seen in Figure 3.5, the fibres transmurally rotate (from endocardium to epicardium) from a 40° angle to a -50° angle, with respect to the longitudinal direction. This approach follows a previously validated method for assigning fibres to ventricular models [136]. The conductivities along the fibers' direction (longitudinal)

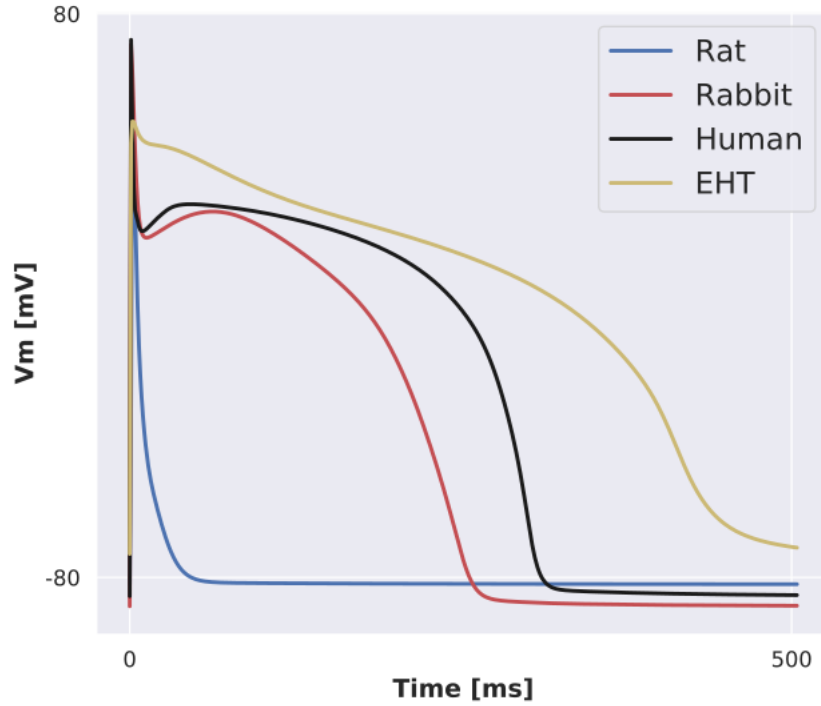


Figure 3.4: Representative AP traces from the 4 cell ionic models used to model rat, rabbit, human and hiPSC-CMs electrophysiology.

and perpendicular to the fibers' direction (transversal) are set according to Roberts and Scher [135], for both the intracellular and extracellular domains (Table 3.2), leading to conduction velocities of approximately 50 cm/s in the longitudinal direction and 20 cm/s in the transverse direction. For all simulations the bath conductivity was set to 1 S/m, to match Tyrode's solution conductivity [137, 138].

definition	value	units	reference
EHT ionic model	Paci	-	[96]
longitudinal tissue conductivity	0.28	$\text{Sm}^{-1}$	[135]
transversal tissue conductivity	0.026	$\text{Sm}^{-1}$	[135]
fibers orientation	rule-based	-	[136]
longitudinal extracellular conductivity	0.22	$\text{Sm}^{-1}$	[135]
transversal extracellular conductivity	0.13	$\text{Sm}^{-1}$	[135]
bath conductivity	1	$\text{Sm}^{-1}$	[137, 138]

Table 3.2: Model quantities kept fixed in all simulations: conductivity of the internal and external bath areas, ionic model used for the EHT (the model from Paci et al), conductivities and fiber orientations for the host myocardium.



We phenomenologically model the scar by decreasing the tissue conductivity [128]. No border zone between scar and healthy tissue or scar fibers remodeling were included in the model. The scar, **EHT** and **CP** conductivities are set for each simulation (ranges in Table 3.1). The scar conductivity range we set (0 to 50% of the healthy tissue conductivity) yields scar velocities between 10 and 40 cm/s, depending on the ionic model (rat, rabbit, or human). These settings allow our model to match the velocity range reported in the literature for propagation in scars, usually reported to be 50% or less than the healthy myocardial conduction velocity [70, 139, 140]. All models are created using thin 3D tetrahedral slab meshes with an edge length of 100  $\mu\text{m}$ . The reference cross section dimensions of the tissue simulations are 14x2, 14x4 and 20x6 mm for rat, rabbit and human, respectively, and are representative of the ventricular size and wall thickness in each species. Changes in wall thickness are encoded by a parameter ( $\Delta_{tt}$ ), representing the change in wall thickness from the reference value. For analysis of the effects of geometry, we consider variations in scar length and depth, internal bath thickness, **CP** and **EHT** thickness and **EHT**-tissue contact (Figure 3.1 and Table 3.1). The tissue is stimulated by injecting a transmembrane current (100  $\mu\text{A}/\text{cm}^2$ ) on the left side of the slab, across the whole slab section (Figure 3.1). We simulate 350 ms of propagation to ensure the whole tissue is activated. For all species, the tissue was modelled as having a 1 Hz pacing rate to match standard experimental conditions. To approximate a steady state, the cell model was paced with a 30  $\mu\text{A}/\text{cm}^2$  transmembrane current for 800 s at 1 Hz. The state variables were saved and were used for initializing the cell model in the tissue simulation.

### 3.2.4 Conductive polymer modelling

There are two main mechanisms for charge transport: diffusion and drift. The first is caused by concentration gradients while the second is caused by the presence of an electric field. In a conductive polymer, the electric field is caused by net charge, i.e. local imbalances between concentrations of positively and negatively charged species. Mathematically, under the use of a continuum assumption, charges movement in a conductive polymer can be modelled using **PDEs**. Poisson's equation is used to model the electrical field, relating its gradient to the

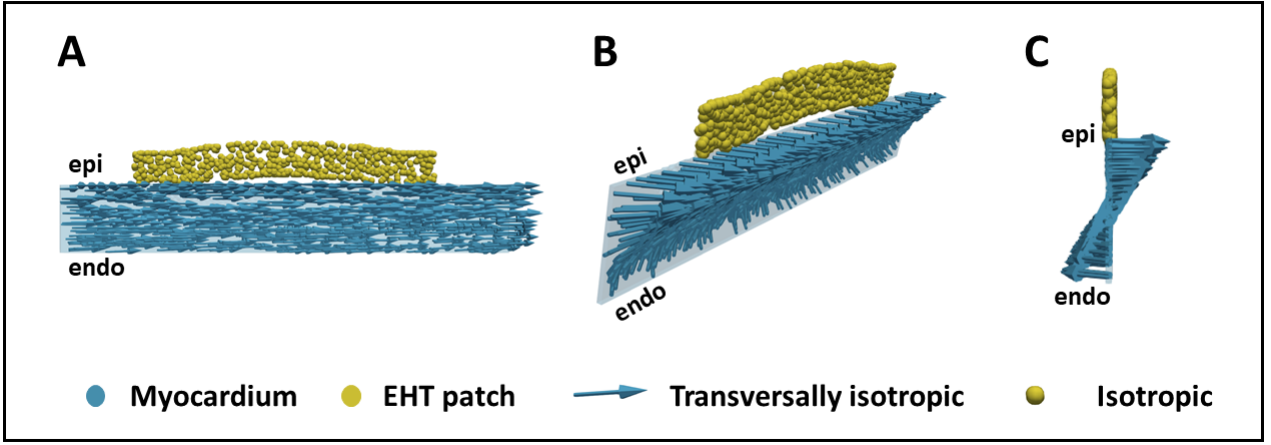


Figure 3.5: Visualization from 3 different angles of our model's fibers distribution. A: frontal view. B: angled view. C: Side view. Our slab model is made of a layer of tetrahedral elements. A vector determining fibre orientation is assigned to each element. Fibers are rotating from endocardium to epicardium. The EHT patch is assumed isotropic.

net charge inside the polymer. The Nernst-Planck equation models the ion current due to drift and diffusion. The two PDEs are coupled because of the intrinsic relation among ions concentrations, net charge, electric fields and ions drift. More in detail, the current density in a CP can be written as:

$$\mathbf{J}_i = \mathbf{J}_i^{diff} + \mathbf{J}_i^{drift}$$

where the two contributions, respectively from diffusion and drift, can be written as:

$$\mathbf{J}_i^{diff} = -\mathbf{D}_i \nabla C_i$$

$$\mathbf{J}_i^{drift} = z_i \mu_i C_i \mathbf{E}_i$$

where  $\mathbf{D}_i$  is the diffusion coefficient,  $C_i$  is the concentration of the species  $i$ ,  $z_i$  is the charge per species molecule,  $\mu_i$  is the mobility and  $\mathbf{E}_i$  is the electric fields, being  $\mathbf{E} = -\nabla\phi$ . The

concentration  $\mathbf{C}_i$  is expressed with the continuity equation:

$$\frac{\partial \mathbf{C}_i}{\partial t} = -\nabla \cdot \mathbf{J}_i$$

By substituting the formulation of the current density  $\mathbf{J}_i$ , we obtain the Nernst-Planck equation for the rate of change of the concentration of species  $i$ :

$$\frac{\partial \mathbf{C}_i}{\partial t} = -\nabla \cdot (-\mathbf{D}_i \nabla \mathbf{C}_i - z_i \mu_i \mathbf{C}_i \nabla \phi)$$

where species  $i$  can be ions or electrons. In the bidomain model adopted in this work, the extramyocardial domain is assumed Ohmic, and thus the potential propagation in this domain is described by a generalized Laplace equation. To reach this formulation, 3 assumptions have been made. First, we assumed charge movement to be carried by a single species:

$$\frac{\partial \mathbf{C}}{\partial t} = -\nabla \cdot (-\mathbf{D} \nabla \mathbf{C} - z \mu \mathbf{C} \nabla \phi)$$

Second, we assumed that the concentration of charge carriers does not change over time:

$$0 = -\nabla \cdot (-\mathbf{D} \nabla \mathbf{C} - z \mu \mathbf{C} \nabla \phi)$$

Third, we assume homogeneous charge concentration across the CP, so that the diffusive properties of the CP are homogeneous, bringing to 0 the diffusion term and enabling us to ignore the coefficients multiplying  $\nabla \phi$ :

$$0 = -\nabla \cdot (\nabla \phi)$$

We have thus reached the Laplace equation, used in this study for a simplified Ohmic conductor model of the CP. In previous works, charge transport in CP has been modelled using a continuum assumption and PDEs to describe the rate of change in concentration of charged particles [141, 142]. These studies aimed at describing the ions and holes movement in a small portion (nanometers) of CP. In this study we incorporate the CP in a myocardial slab model, modelling the CP on a larger scale (millimeters). To account for the effects of the conductive surface provided by the CP when in contact with the myocardium [130], we modelled the CP as an Ohmic conductor. This assumes that the charge concentration remains homogeneous across the CP, that the concentration of charge carriers remains constant over the duration of the simulation, that the diffusive properties of the CP are homogeneous, and that charge transport is governed by drift. The CP model is discussed further in the limitations section at the end of this Chapter. The conductive properties are varied by the range of values reported in the literature (Table 3.1).

### 3.2.5 Stem cells-derived engineered heart tissue modelling

The structure of the patch is shown in Figure 3.1. The patch consists of two layers: a CP (blue) and a layer of hiPSC-CMs (yellow) labeled as EHT. While the CP is modelled as an ohmic conductor, the EHT is modelled using the bidomain equations for cardiac tissue. The EHT connects the healthy myocardium at the two ends of the scar, effectively creating a new pathway for electrical propagation. The EHT is described by a hiPSC-CMs ionic model to include features of non mature cardiomyocyte phenotype, typical of hiPSC-CMs [96].

### 3.2.6 Gaussian processes-based emulators

The presence of MI scars creates regions of slow conduction in the heart, which can lead to arrhythmia [143]. To measure conduction delay caused by the patch, we computed the change in REAT in the model (measured as the time from stimulation to activation of the top right corner) and used this value to evaluate the impact of different parameters in our model. In such fashion, we can think of our model as a function  $\mathbf{X} \rightarrow \mathbf{Y}$  where  $\mathbf{X} = N \times D$  and  $\mathbf{Y} = 1 \times N$ . This function maps the matrix  $\mathbf{X}$ , whose rows corresponds to the  $N$  sets of parameters sampled from the  $D$ -dimensional parameter space, to the vector  $\mathbf{Y}$ , a column containing the REAT for each simulation. Fully exploring the 10-dimensional design space is computationally intractable with bidomain simulations. Thus, to reduce the computational time to evaluate the model for a given set of parameters we created a Gaussian Process-based emulator for the REAT as a function of the model's parameters (Table 3.1). In total, we trained 15 Gaussian Process emulators, one for each version of the model and one for each of the sub-cases, and for the 3 different species. The emulator is defined as  $f(\mathbf{x}) := \mathbf{m}(\mathbf{x}) + \mathbf{g}(\mathbf{x})$ , where  $\mathbf{m}(\mathbf{x})$  corresponds to the deterministic part, given by a linear regressor, and  $\mathbf{g}(\mathbf{x})$  corresponds to the stochastic part, given by a Gaussian Process. The linear regressor acts as a mean function, while the Gaussian Process is zero-mean and models the residuals. Two sets of parameters must be fitted, for such surrogate model to emulate the original model. We first fit the linear regressor parameters, by minimizing the sum of the squared residuals between the data ( $\mathbf{Y}$ ) and the values predicted by the linear regressor. The GPs' parameters are fitted to these residuals, i.e. to the data minus the predicted mean. The GPs are characterized by zero mean and a covariance function, called kernel. We fit on the residuals the kernel's parameter, termed the GPs' hyperparameters. The fit is made by maximizing the marginal likelihood function (see equation 2.30 in Rasmussen et al [106]). We used a first-degree polynomial as mean function for the linear regressor, and we tested 2 different anisotropic covariance functions for the kernel: squared exponential and Matern (see equations 4.9 and 4.14 in Rasmussen et al [106]). Two possible fitting strategies can be used. The linear regressor coefficients can be fitted separately, by minimizing the sum of the squared residuals with respect to the data, or concurrently with the GPs' hyperparameters, by maximal likelihood. We implemented the first strategy. In previous works it has been

shown that the two different strategies do not have a relevant impact on the GPs predictions [144]. Among the various metrics available, we choose the coefficient of determination, or R2, to measure the accuracy of our emulator. The R2 score has 1 as an upper bound, i.e. the best possible score, and it can be negative, although the score often lays between 0 and 1, since a constant model that always predicts the same value, disregarding the input, would get a 0 score. The R2 score is computed with a 5-fold cross validation. The emulators were built using routines from *scikit-learn* [145], a Python open-source machine learning library.

### 3.2.7 Training set creation

To train the GPs emulators we need a data set that maps from parameter values to the REAT value over the parameter space. For the 2 versions of the model (*epi-endo*, *endo-epi*), and each of the 3 sub-cases (*transmural*, *block*, *fixed* - see Section 3.2.2) we sampled 500 combinations of parameters from their  $D$ -dimensional parameter space using a Latin Hypercube, with  $D=10$ , 10, 9, 8, 7, respectively. At least 50 samples per parameter were considered. Simulations are performed for each parameter combination, leading to 7,500 simulations in total for training the GPs emulators.

We employed a 5-fold cross-validation with a train, validation, test split of 80-10-10. This means that 80% of the 500 data points were used for training, i.e. we tune the GPs hyperparameters to minimize the difference between the model predictions and those points. 10% of points are used for validation, i.e. we “hide” those data points during training. This is used to make sure the model is not overfitting, i.e. it is not learning “too much”, or too specifically, the patterns of the training set. The remaining 10% of data is used as a test set, to have a final assessment of how the model can perform on “new” data, i.e. on data that has never seen before. We performed a 5-fold cross validation, meaning that we repeated this process 5 times per training, randomly creating a different 80-10-10 partitioning of the dataset each time. We then took the mean of the emulators R2 scores, computed on each of the 5 test dataset, as a measure to summarise the accuracy of the emulators.

To post process the simulations, the activation times were computed from the transmembrane

voltage, as the instant in which it crosses (with positive derivative) the  $-10$  mV threshold. The AP propagation across the tissue slab was classified into 3 different paths. Bottom: the wave travels in the lower half of the tissue slab. Middle: the wave travels in the upper half of the tissue slab. Top: the wave travels through the EHT (see Figure 3.11).

### 3.2.8 Global sensitivity analysis

We performed a variance-based GSA [146] on each setup and sub-case of the defined tissue model. Specifically, we evaluate the total effect index, where the total effect for the  $i$ -th input parameter ( $ST_i$ ) consists of the sum of the  $i$ -th first order effect ( $S_i$ ) and the higher-order interactions. The first order effect is a normalized index that explains how much output variance is explained by the  $i$ -th parameter on its own. The higher-order interactions represent the contribution to the output variance from the interactions of the  $i$ -th parameter with all the other input parameters [103]. Trivially, in the case of a 2-dimensional parameters space, the total effects indexes can be written as:

$$ST_1 = S_1 + S_{12}$$

$$ST_2 = S_2 + S_{21}$$

where  $S_1$  and  $S_2$  are the first order effects and  $S_{12}$  and  $S_{21}$  are the higher-order interactions (in this case the only higher-order interaction present is the second-order one). To compute the Sobol sensitivity indexes we make use of the open-source Python library SALib [147], which implements the Saltelli method [103]. Since exact computation of the Sobol sensitivity indexes (see equations 2 and 4 in Saltelli et al [103]) requires solving integrals that are not analytically computable, the Saltelli method implements estimators (equations 16 and 19 in Saltelli et al [103]) that approximate the indexes real value. In turn, computing the estimators requires the evaluation of the model in a series of points, called the quasi-random, low discrepancies Sobol sequences [104]. Albeit the computational cost of our model is relatively cheap (from  $\approx 100$  s to

$\approx 200$  s depending on the slab dimensions in a 36 cores machine), a good approximation of the indexes real value needs at least  $N_s = 1000$  points in the Sobol sequences, which translates in  $N_s \times (D + 2)$  model evaluations [103]. Assuming  $N_s = 1000$ , computing the estimators for our 5 setups ( $D = 10, 10, 9, 8, 7$ ) requires  $1000 \times ((10 + 2) \times 2 + 9 + 2 + 8 + 2 + 7 + 2) = 54000$  model evaluations. Simulate the model 54000 times would require 112.5 days of simulation time. To overcome this, at the points belonging to the Sobol sequences, instead of running the model we evaluated the GPs emulator. As summarised in section 3.2.7, we used 500 simulations to train a GPs emulator for each model setup. This approach permitted us to run  $500 \times 5 = 2500$  simulations instead of 54000, sparing 51500 simulations. This is valid for each of the 3 species, thus, in total, emulating the model saved us  $51500 \times 3 = 154500$  simulations.

### 3.2.9 Parameters that match healthy activation times

GSA highlights which parameters play a key role in stimulus propagation in our model. We selected the most important parameters to tune to recover physiological activation times in the model. The healthy activation times are estimated by removing the scar, the EHT and the CP patch from our model, reducing it down to a slab representing a transmural slice of host myocardium. We repeated this procedure for the rat, rabbit and human models. We compared the REAT for different parameters values in the models with an EHT patch with the corresponding simulated healthy activation times for each species.

### 3.2.10 Arrhythmic behaviour

Finally, we focus on the human model and we assess whether the changes made to this model to match healthy electrophysiology led to pro-arrhythmic behavior. We chose to compute the repolarization gradients as a marker of arrhythmic activity. Early studies have established a close linking of repolarization heterogeneities and cardiac arrhythmogenesis [148, 149]. Additionally, the presence of an imbalance between the current available and the current needed for cell excitation (source-sink mismatch) and repolarization heterogeneities has been linked



with unidirectional block [150]. Since the engraftment of EHT patches is likely to introduce a source-sink mismatch (through the wavefront geometry and structural modifications), we considered the repolarization gradient to be, albeit approximately, a metric representative of the arrhythmic risk following EHT engraftment. To compute the repolarization gradients, we paced the model for 100 beats to reduce any transient effects. For the 100<sup>th</sup> beat only, we calculated the time to 80% repolarization at each node of the mesh. We then calculated the magnitude of the gradient of these repolarization times. We report repolarization gradients in the tissue slab, focusing on the interface between the EHT patch and the host myocardium. We focused on this area as it was the area with the highest gradients, it was the area most affected by the presence of the EHT and was close to the border of the scar, which is an area that is prone to ectopics [151]. Spatial plots of repolarization times and gradients can be seen in Figure 3.6 and Figure 3.7.

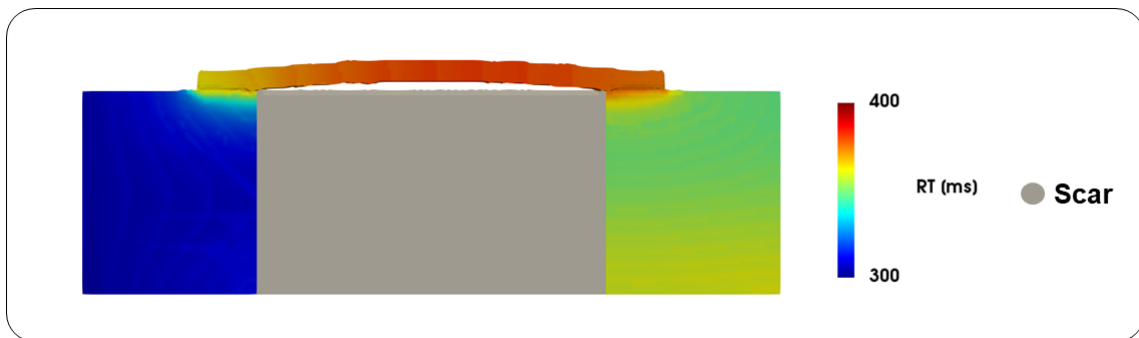


Figure 3.6: Spatial plots of the repolarization times for the human model (*fixed* sub-case).

### 3.2.11 Validation

To validate the model, we compared simulated changes in CV in the presence of non-native CMs engrafted on animal hearts in four optical mapping experiments [121, 40, 124, 53]. All simulations use the model structured as described above (Figure 3.1), which we will refer to as reference model, with modifications to match the specific experimental setups of the four different studies (Table 3.3).

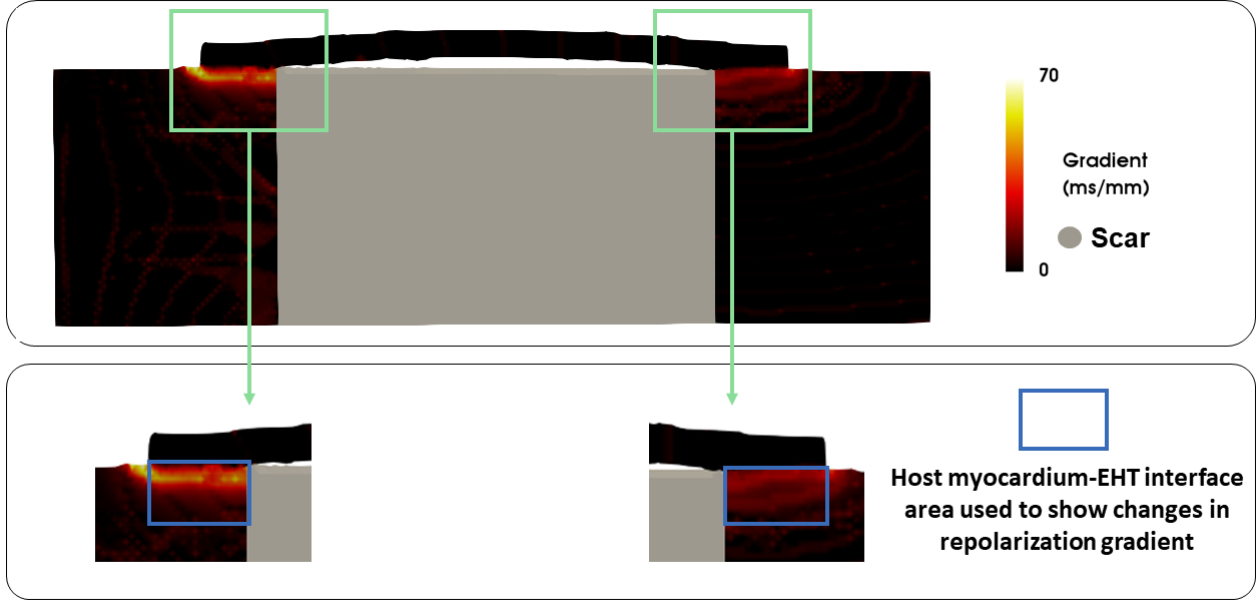


Figure 3.7: The upper panel shows the repolarization gradient over the whole mesh at the 100th beat. In the lower panel, the blue rectangles indicate the areas considered for reporting the repolarization gradient. The values shown in Figure 3.15 are the repolarization gradients computed for the mesh nodes located in this area.

Papers	Model parameters									
	SR [mm]	SD [mm]	SC [S/m]	EHTt [mm]	EHTc [S/m]	CA [mm]	CPt [mm]	CPc [S/m]	IBT [mm]	Tissue thickness [mm]
Range used in this study	0.7–6	0.2–6	0–0.14	0.5–2	0.028–0.224	0.5–2	0.5–2	0–18	0.1–1	1.8–6.6
Jackman et al [124]	-	-	-	1	0.224	0	-	-	0.1	3
Thompson et al [121]	-	-	-	0.2	0.224	30	-	-	0	0.2
Zimmermann et al [40]	5	3	0	3	0.224	2	-	-	0	3
Mawad et al [53]	3	2	0.06	-	-	-	0.5	16	0	2

Table 3.3: Modifications to model parameters to match the experimental studies setups. The first row reports the ranges used in our simulation study, while the rows below display the parameters values used to replicate each of the 3 experiments.

In Jackman et al [124], Langendorff rat hearts in a bath were engrafted with a 10 mm  $\times$  10 mm patch of neonatal rat cells. Prior to engraftment patches were paced at 1 Hz. Whole hearts were paced at 2 Hz. CV was measured before and after engraftment, in 3 different locations: on the patch, on the tissue underneath the patch and on the tissue far away from the patch. To simulate their experimental setup, we removed the scar and CP from our reference model. We also set the EHT-tissue contact area to 0 to match the presence of a thin layer devoid of CMs between the patch and the epicardium, as highlighted by the histological exam. The

remaining model parameters (second row in Table 3.3) were set based on their reference values (Table 3.1). We repeated the 1 Hz pacing protocol, first pacing the scar and then the tissue. We extracted activation times to compute CVs in the three locations where they were experimentally measured, i.e. patch, tissue under the patch and tissue far away from the patch. We use the Terkildsen-Niederer-Crampin-Hunter-Smith model [133] for rat electrophysiology and a neonatal rat cell ionic model [152] for the EHT.

In Thompson et al [121], rat neonatal cells monolayers are treated with transforming growth factor  $\beta$  and superimposed with monolayers of human embryonic stem cell-derived CMs. To replicate this setup, we removed scar and CP from the reference model, as done for the previous study, and set the tissue thickness to 0.2 mm, the internal bath thickness to 0 and the EHT-tissue contact area to 30 mm, i.e. the whole length of the monolayers (third row in Table 3.3). We set the bath conductivity to 0 S/m, since the monolayers were not perfused in a bath, but grown on fibronectin lines. We also reduced the tissue conductivity from 0.28 S/m to 0.123 S/m to match the 56% reduction in CV observed in the rat neonatal cells monolayers, following the treatment with growth factor  $\beta$ . The remaining parameters values were set as the mid values of the respective ranges, previously defined (Table 3.1). We used a neonatal rat cells ionic model [152] for the monolayers and the Paci model [96] for the stem cell-derived monolayers. We computed the rat neonatal cells monolayers CV before and after superimposing the stem cells-derived CMs layer, as was done experimentally.

In Zimmermann et al [40], left anterior descending artery ligation was performed on 8 Langendorff-perfused rat hearts, causing large transmural infarcts. The hearts were then engrafted with thick (15 mm  $\times$  15 mm  $\times$  2–3 mm) patches of neonatal rat cells. Myocardium CV was measured before and after engraftment through multi-electrode epicardial mapping. This system was modelled by removing the CP from the model and by setting the EHT thickness to 3 mm. Values belonging to the previously defined ranges were used for the remaining parameters (fourth row in Table 3.3). CV was again computed on the myocardial slab, before and after adding the EHT patch, and predicted changes in CV were compared against experimental observations. In Mawad et al [53], polyaniline patches were engrafted on both healthy and infarcted Langendorff-perfused rat hearts. CVs were computed through optical mapping data on healthy and infarcted

hearts, before and after patch implantation. The CP patches did not include CMs, for this reason we removed the EHT from our reference model. We then set the CP patch conductivity to 16 S/m, to match the one reported in the paper. We also removed the scar to model the healthy hearts, and we paced our model without (control) and with the CP patch. Finally, we added back the scar to the model, tuning the scar conductivity to match the decrement in CV observed in the ex-vivo hearts after infarction (fourth row Table 3.3). The resulting CV was taken as control. We then added the CP patch to the model with the scar, paced and measured the CV.

The exact nodes used to compute the CVs, as well as schematic representations of all the models used can be found in Figure 3.8. The CV between two nodes was computed by dividing their distance (difference in  $x$  coordinate, given that the nodes were selected with the same  $y$  coordinate) by the difference in the node activation times. Except when replicating the Jackman et al [124] experiment (Figure 3.8A), where the CV had to be measured at specific sites, we selected two epicardial nodes, one on the left side of the slab (before the scar) and one on the right side of the slab (after the scar), to compute a mean CV across the entire slab. The location of the selected nodes is reported below in Figure 3.8.

The internal bath thickness was set to 0 in the models used for the validation. However, in the range of parameters tested, it was always greater than 0, being the spanned interval 0.1 – 1 mm. We made this choice because: 1- we generated models automatically with dimensions described by scalars; 2- we wanted to have a consistent mesh discretization for running simulations; 3- We were concerned that meshes would fail to resolve a gap between 0 and 0.1 mm without a very high mesh resolution. For these reasons, we took a pragmatic decision and set 0.1 mm as the lower bound for the internal bath thickness with the intention of streamlining model generation and standardizing mesh generation without the need for model-specific mesh refinement.

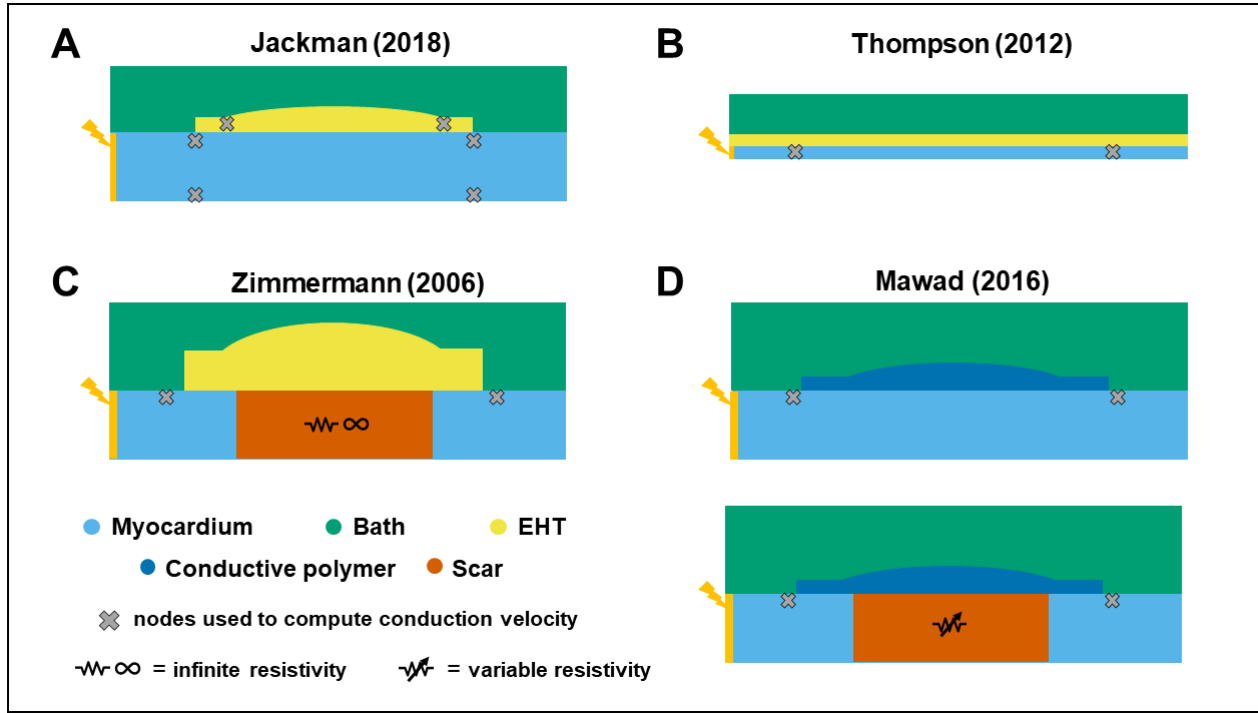


Figure 3.8: Schematic representations of the models used in the validation step. The crosses indicate the nodes that were selected to extract the activation times and to compute the conduction velocities.

## 3.3 Results

### 3.3.1 Model validation

One simulation run of our model took between 100 and 200 seconds of computational time. We do not report screenshot of the validation simulations, but we refer to Figure 3.8 for schematic representations of the models used in validation, and to Figure 3.13 for a sample of activation pattern in our model. We compared simulations results against four previously reported experimental studies [121, 40, 124, 53]. Consistent with Jackman’s finding of no significant change in the CV, our model predicts no change (Figure 3.9A). When replicating the experiment from Thompson et al (Figure 3.9B), our simulations predicted an increase in CV of 20%. This compares with a 110% increase in CV reported by Thompson et al. Our modelling framework captures this increase in CV qualitatively, if not quantitatively. This demonstrates that our modelling framework behaves as expected. However, a model calibrated for specific tissue

patches is likely to be necessary to achieve quantitative agreement with experimental results. For this reason, in subsequent analysis, we account for the potential uncertainty in the model parameters by performing a global sensitivity analysis over ranges of values, as opposed to specific parameter values. Zimmermann et al, reported that the host CV after patch implantation was 20% lower than in healthy hearts, this compares with a 22% decrement in CV in our simulations (Figure 3.9C). Mawad et al, reported a decrement in host CV after CP patches grafting. This observation was not matched by the model, that predicted a 10% increment of CV (Figure 3.9D). However, in a similar experiment in scarred tissue Mawad et al reported a 10% increment, that was matched by the simulations (Figure 3.9E).

In Figure 3.9, normalized CV means that the CV values are normalized to the control CV values. The experimental CV values, before and after engraftment (before=control, after=graft), coming from the considered papers are normalized to the control values mentioned in the papers. In the same fashion, the CV values from the simulations are normalized to the CV values coming from the control simulations. That is why the control CV values are always equal to 1 throughout Figure 3.9, because they are always divided by themselves.

To test if the 0.1 mm gap causes a meaningful difference in activation times relative to the 0 mm gap used in the validation simulations, we ran 5 additional simulations to compare models with IBT of 0.1 mm and 0 mm. We chose the rat model, and run simulations with a IBT of 0 mm for each sub-case (*epi-endo*, *endo-epi*, *transmural*, *block*, *fixed*), choosing one of the parameter combinations previously sampled, where IBT was 0.1 mm. As displayed in Figure 3.10, the electrical propagation and the REAT in the compared models are almost identical, showing that including an IBT of 0 mm in the parameter range is not likely to impact the results.

### 3.3.2 Do the effects of engineered heart tissue on activation depend on the species?

Current experiments for evaluating EHT in infarcted hearts use small animal models, predominantly rabbit and rat [115]. To test if specific patch design variables change with different

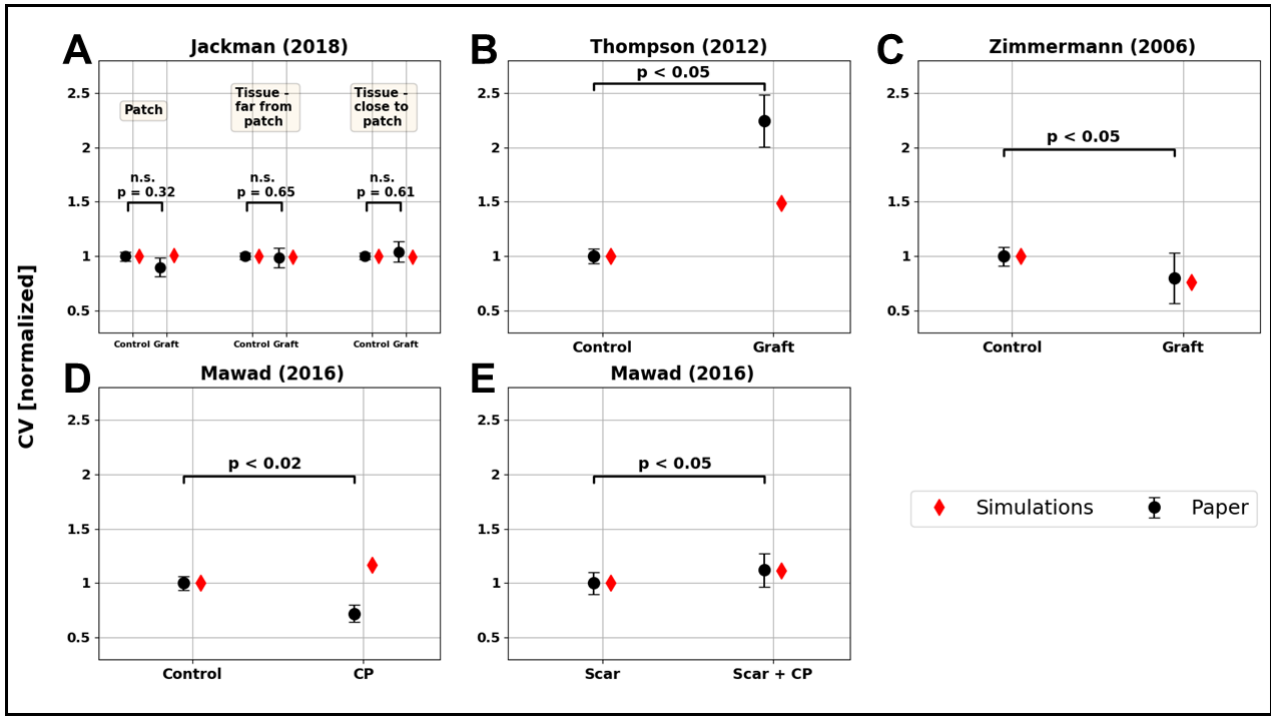


Figure 3.9: Results of the model validation. Experiments from 4 papers were compared to the model: Jackman et al (A), Thompson et al (B), Zimmermann et al (C) and Mawad et al (D-E). In panel A CV is evaluated in 3 different areas: on the patch, on the tissue far from the patch and on the tissue under the patch. In all 3 experiments, CV before (control) and after (graft) the attachment of the patch is compared. The CV measured experimentally (mean and standard deviation) are represented as black dots with error bars, with the p-values associated with each experiment. The simulated CV are displayed as red diamonds.

species, we compare the simulations in models with rat, rabbit and human host myocardium. We first consider the stimulus propagation paths. Secondly, we compute the GSA total effect indexes to highlight the most important parameters.

### Distribution of stimulus propagation paths

We assessed if the path of activation dynamics in the presence of a scar and patch are consistent across the 3 species. We classified the activation wave path across the model in all simulations (500 for each of the 5 model setups – see sections 3.2.2 and 3.2.7). The activation wave path is classified based on whether the stimulus propagated through the lower half of the slab, the upper half of the slab, or through the EHT (Figure 3.11). In rat, rabbit and human, in the *epi-endo* setup, the stimulus always reaches the right side of the slab propagating through its

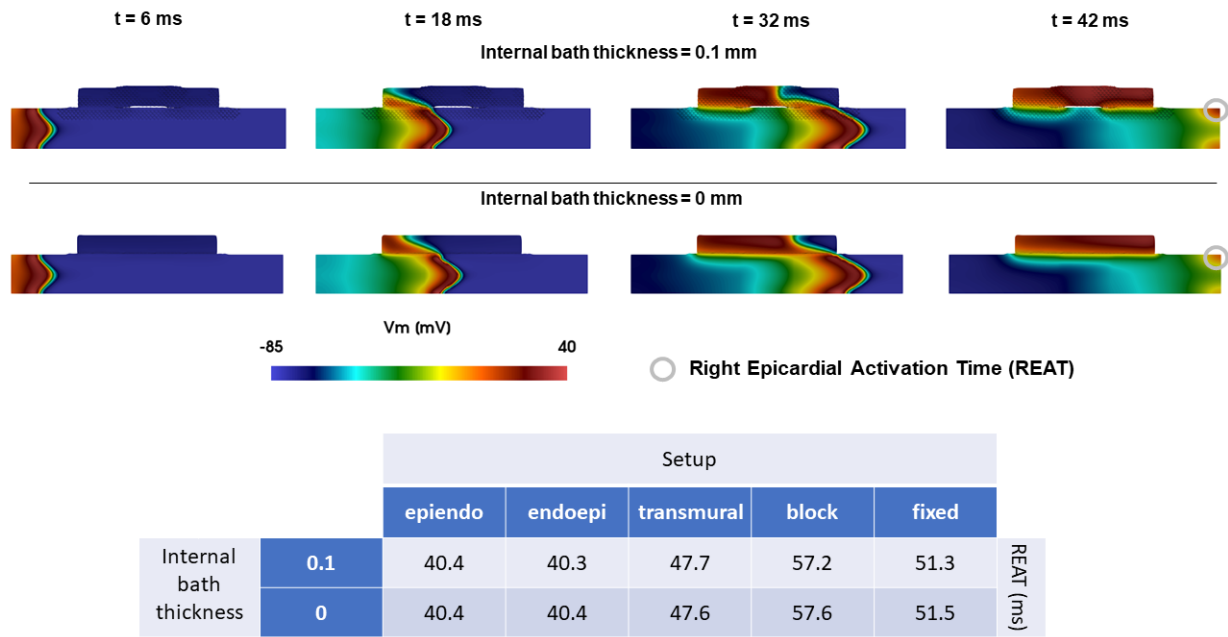


Figure 3.10: Upper panel: comparison of activation patterns in the model with the internal bath thickness set to 0.1 or 0 mm. Lower panel: table comparing the REAT for both internal bath thickness, for each of the 5 setups, in the rat model.

lower half. In the *endo-epi* setup, a decrement of cases classified as “lower half” is observed across all the 3 species, together with propagations both through the upper half and the EHT. In the *transmural* setup, stimulus spreading is divided between lower half and EHT in rat, rabbit, and human models. *Block* and *fixed* setup are not shown, as the stimulus is forced to travel through the EHT. This shows that, in our study, the dimensions and electrophysiology of each species does not impact the activation wave propagation path.

### Impact of model parameters on stimulus propagation

In Figure 3.12 the total effect indexes from the GSA for each of the 5 setups (see section 3.2.2) for the rat, rabbit, and human model are plotted. For all species, the indices indicate that in the first 3 setups (*epi-endo*, *endo-epi* and *transmural*) the stimulus propagation is mainly affected by the scar parameters. Specifically, in the first 2 setups (*epi-endo* and *endo-epi*) the scar depth and the scar conductivity have the highest index, explaining between 66–70% and 21–27% of the model output variance in the first setup and 65–69% and 20–25% in the second one. In the third setup (*transmural*), where the scar depth is fixed, the variance is mostly explained by



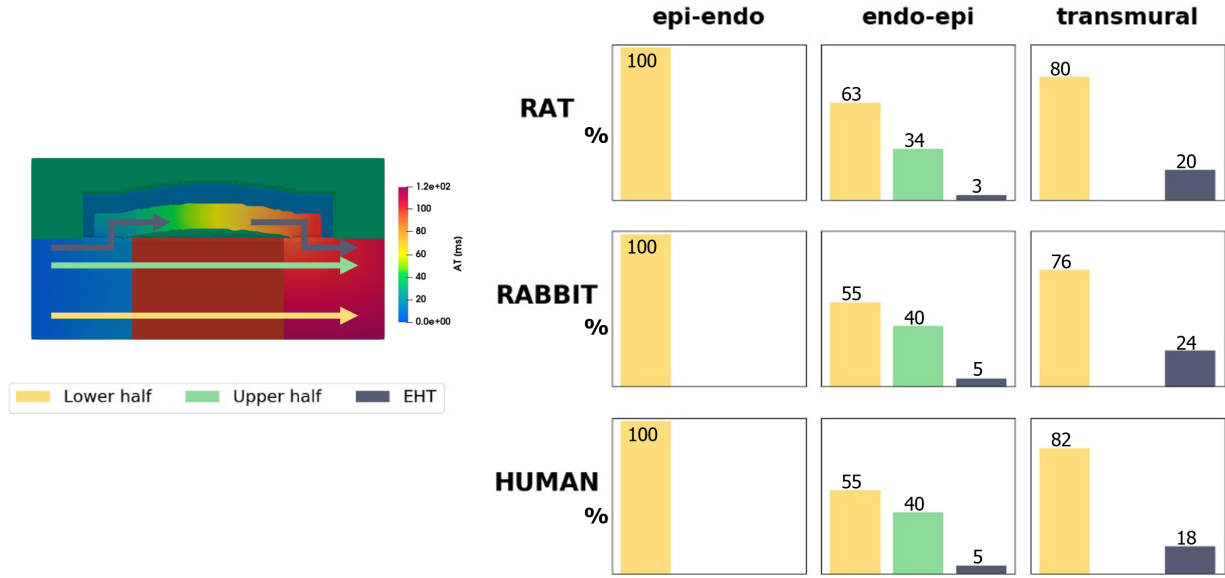


Figure 3.11: Cross-species comparison of the 500 simulations run to create the training datasets, classified as lower half, upper half or EHT, according to the propagation path (arrows in the left panel) followed by the stimulus. The colours on the right panel represent the arrows colours in the left one. Yellow, green and blue columns show the percentage of simulations classified as lower half, upper half or EHT, respectively. The percentage values are reported on each column.

the scar conductivity (76%). The EHT conductivity also starts to play a role. In the last two setups (*block* and *fixed*), when the activation wave is forced to propagate through the EHT, the sensitivity indexes indicate that the EHT conductivity explains 80% and 90% of the output variance in the *block* and *fixed* case, respectively. Comparing all 5 setups, we can observe that for all species the total effect index identifies the scar parameters as the most important for output variance in the *epi-endo*, *endo-epi*, and *transmural* setups. EHT conductivity is also confirmed in all species as the parameter explaining most output variance in the *block* and *fixed* cases. Finally, neither of the two CP quantities considered (thickness and conductivity) showed a high sensitivity index, despite the wide range of CP conductivities explored (Table 3.1).

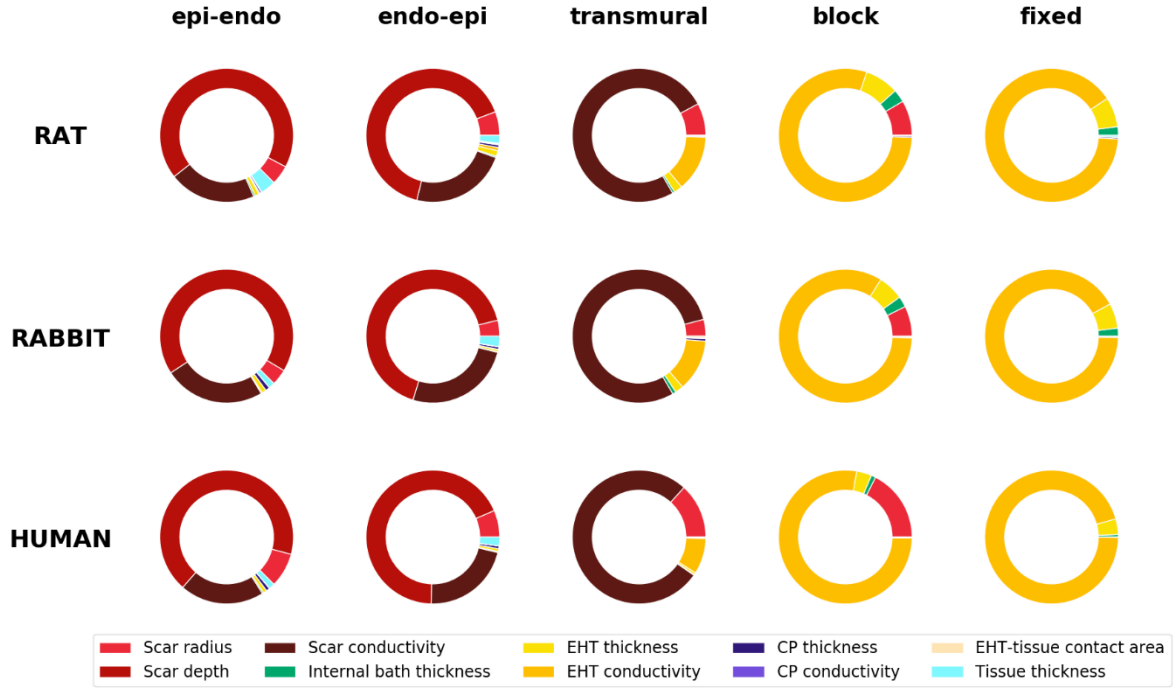


Figure 3.12: Donut charts representing the total effect index from the GSA. The figure compares the total effect indices obtained from the rat, rabbit, and human models (rows), for the *epi-endo* and *endo-epi* versions of the model and the *transmural*, *block* and *fixed* model sub-cases (see section 3.2.2). The magnitude of the total effect indexes, represented by the size of the donut slices, shows how much each model parameter can influence the model output (the REAT). In other words, these charts show, for each species and each sub-case, which parameters most influence the electrical propagation in the model. For example, in the first row, first column, the parameter that influences propagation the most is the scar depth, while in the first row, last column, it is the EHT conductivity.

### 3.3.3 Parameter values that match healthy electrophysiology

In models of the rat, rabbit, and human we simulated electrical activation in healthy myocardial slabs in the absence of scar or EHT. For the rat, rabbit and human models, the time for the activation to spread across the model tissue to the top right corner was 35.3, 34.9 and 45.8 ms, respectively. This provided our baseline target healthy REAT values (Figure 3.13).

In all simulations performed with scar, the presence of EHT did not lead to physiological activation times, considering an interval of  $\pm 10\%$  of the healthy target REATs (Figure 3.13). In the *blocked* and *fixed* models the GSA (Figure 3.12) identified EHT conductivity as the parameter explaining most of the variance in simulated activation times in all the 3 species. Following these

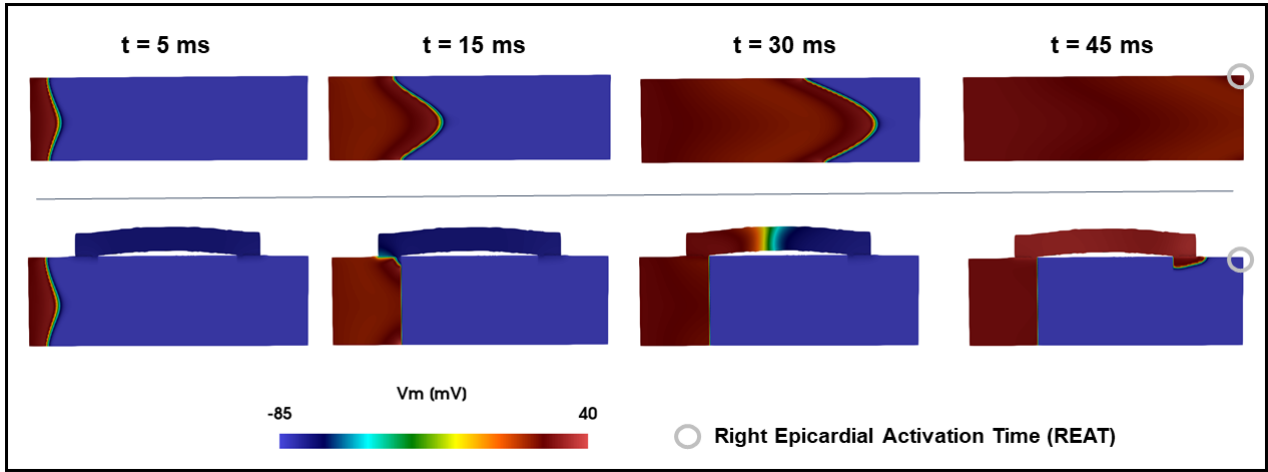


Figure 3.13: Sample activation pattern. Upper row: propagation in a healthy slab. Lower row: propagation in a sample simulation of the fixed setup, showing the delay in REAT activation.

results, we tested whether increasing [EHT](#) conductivity beyond reported experimental bounds could bring the activation time back to physiological values in the *fixed* model (Figure 3.14). For all species, the [EHT](#) conductivity was increased 1.5–5 fold, with respect to the upper limit for the reported experimental range chosen in the Latin Hypercube sampling (Table 3.1). For all the 3 species, a minimum 3-fold increase in the [EHT](#) conductivity (equal to 0.672 S/m) would be needed to bring the activation time to within  $\pm 10\%$  of the physiological value. The rat and human models achieved healthy activation times with [EHT](#) conductivity multiplied by a factor of 4.5 equal 1.008 S/m, while the rabbit model required the [EHT](#) conductivity to be multiplied by a factor of 5, equal to 1.12 S/m.

### 3.3.4 Achieving physiological activation time with low arrhythmia risk

Due to the [hiPSC-CMs](#) immature electrical properties, engraftment of [EHT](#) patches of [hiPSC-CMs](#) may induce arrhythmias [38, 113]. Thus, we investigated whether the proposed patch designs exhibit pro-arrhythmic behavior in the human model. Focusing on the *fixed* setup, as this had the smallest number of degrees of freedom, we considered repolarization gradients as a surrogate for arrhythmia marker [129]. To compute the repolarization gradients, we paced the model for

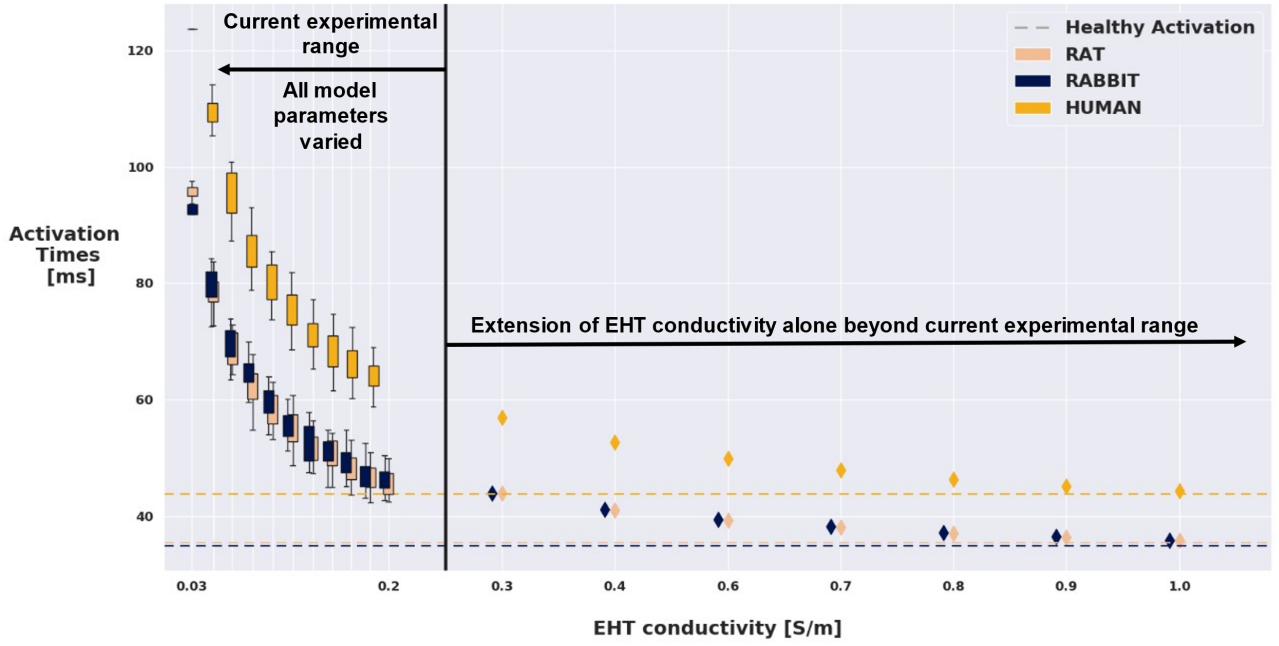


Figure 3.14: Model output (REAT) vs EHT conductivity for the rat, rabbit and human model, in the fixed setup. Boxplots represent the distribution of REATs among the 500 LH simulations that had the EHT conductivity restricted to current experimental ranges. Diamonds represent REATs obtained by fixing all the other parameters and increasing EHT conductivity by multiplying the upper bound of the range used in the LH by 1.5, 2, 2.5, 3, 3.5, 4 and 4.5 folds. Dashed line indicates the healthy REAT estimated by our models.

100 beats to reduce any transient effects. For the 100<sup>th</sup> beat only, we calculated the time to 80% repolarization at each node of the mesh. An example of repolarization times spatial plot is reported in Figure 3.6. We then calculated the magnitude of the gradient of these repolarization times. Figure 3.7 displays the repolarization gradients on the mesh and shows which nodes were considered when reporting the repolarization gradient. We considered the nodes located in the area depicted in the figure with a light green rectangle. The edge length of the rectangle base equals the EHT-myocardium contact area, while the rectangle height equals 1 mm, to focus on the myocardial area closer to the EHT. We focused on this area as it was the area with the highest gradients, it was the area most affected by the presence of the EHT and was close to the border of the scar, which is an area that is prone to ectopics [151]. Repolarization gradients can be used as a surrogate for arrhythmia marker because a high repolarisation gradient implies there is a greater chance of an ectopic beat generating arrhythmogenic unidirectional

block [150].

We considered the model with **EHT** conductivity equal to 0.112 S/m (the mid value in the experimental range) as the baseline case, where the propagation is slower than the physiological one. The baseline case exhibits a mean repolarization gradient of  $\approx 18$  ms/mm and no ectopic beats (Figure 3.15).

We then considered the case with **EHT** conductivity equal to 1.008 S/m, the value needed to match healthy activation time. In this case the mean repolarization gradients increased to  $\approx 50$  ms/mm but did not cause ectopic beats.

Our initial analysis (Figure 3.12) did not consider ion channels in the sensitivity analysis. To increase **CV** without increasing repolarization gradients, we increased  $Na^+$  channel density in the ionic model used to represent **hiPSC-CMs** in the **EHT** patch [99], while keeping the **EHT** tissue conductivity at the baseline value (0.112 S/m). This new model exhibited healthy activation times when the default  $Na^+$  channel density was increased by a factor of 4. The repolarization gradients were similar to the baseline value ( $\approx 18$  ms/mm). However, the increment in  $Na^+$  channel density caused a shortening of the **hiPSC-CMs** cycle length and resulted in ectopic beats within the **EHT** patch.

The inward rectifier potassium current ( $I_{K1}$ ) plays a key role in regulating **hiPSC-CMs** self-pacing behavior [153, 154]. We thus increased by a factor of 1.4 (from 28.2 nS / pF to 39.5 nS/pF) the density of the ion channels responsible for the potassium ions movement associated with the inward rectifier current. This resulted in **hiPSC-CMs** cycle-length lengthening, which successfully ended the **EHT**-generated ectopic beats. The repolarization gradients also decreased, exhibiting a value of  $\approx 4$  ms/mm, lower than the baseline case (Figure 3.15). The optimal multipliers reported above for the modelled ion channel densities are the results of a systematic analysis of the effects of different gNa and gK1 values in the **hiPSC-CMs** model, which is detailed below.

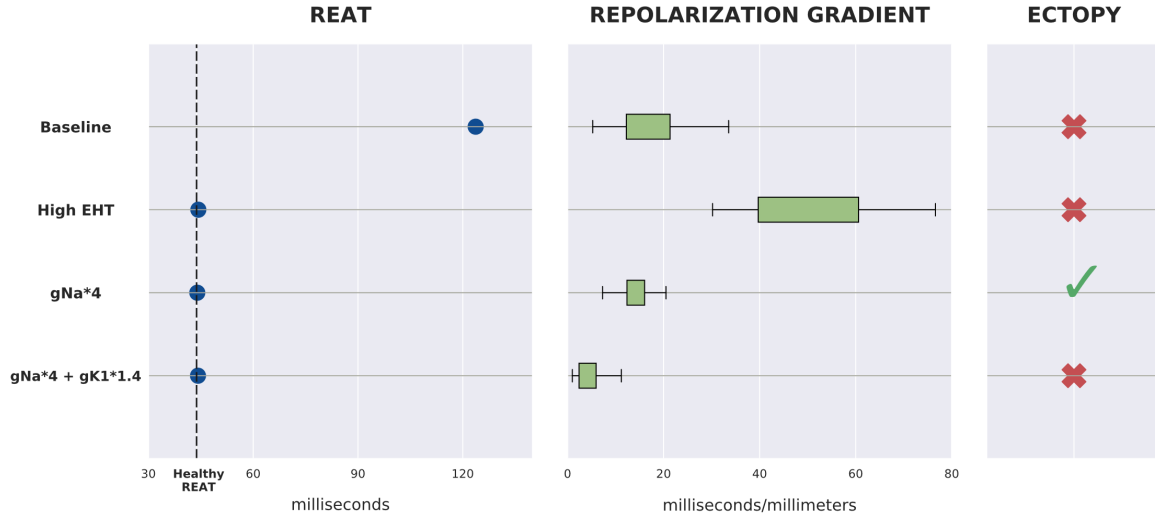


Figure 3.15: Summary of the 4 cases tested for arrhythmic behavior. For the Baseline and High EHT cases, EHTc is set to 0.112 S/m (mid value in experimental range) and 1.008 S/m, respectively, and no modifications to ion channels' densities are made. When the density of the ion channels responsible for the fast Sodium current and the inward rectifier potassium current are increased, the EHTc is set to 0.112 S/m. The left panel shows which cases match estimated healthy REATs. The center panel shows the distribution of the mean repolarization gradients at the interface between myocardium and EHT (on 100 beats pacing protocol). The right panel shows the presence or absence of ectopic beats fired from the EHT.

### How changing Paci model parameters (gNa and gK1) affects the EHT action potential and the presence of ectopies in the EHT

To increase the CV in the EHT without increasing the conductivity, we increased the Paci model parameter (gNa), which models the density of ion channels related to the fast sodium current. Although we succeeded in recovering a healthy REAT, increasing gNa resulted in a shortening of the intrinsic hiPSC-CMs cycle-length down to 806 ms (1.24 Hz), in turn causing the firing of ectopic beats from the EHT when the tissue was paced at 1 Hz.

Ectopies essentially arise because, in the hiPSC-CMs with increased gNa, the transmembrane potential increases more rapidly after repolarization, causing a more frequent repetition of the intrinsic activation cycle. To slow the intrinsic activation of the hiPSC-CMs and to allow the EHT to be activated by the myocardium, we increased the Paci model parameter (gK1) modeling the density of ion channels related to the inward rectifier potassium current.

After running our tissue model with 3, 3.25, 3.5, 3.75, 4 and 4.25 as multipliers for the default Paci model gNa, and 1.1, 1.2, 1.3, 1.4 and 1.5 as multipliers for the default Paci model gK1, we show (Figure 3.16 – left panel) that multipliers equal or greater than 4 and 1.4 (for gNa and for gK1, respectively) are needed to recover a healthy REAT while avoiding EHT-generated ectopies at 1 Hz pacing. We also ran single-cell simulations using the hiPSC-CMs ionic model (Paci model) and looked at the intrinsic single-cell activation rate for each parameter combination used in the tissue model. We found that the intrinsic activation frequency dropped below 1 Hz for the same parameter combinations for which no ectopies were observed in the tissue model simulations (paced at 1Hz).

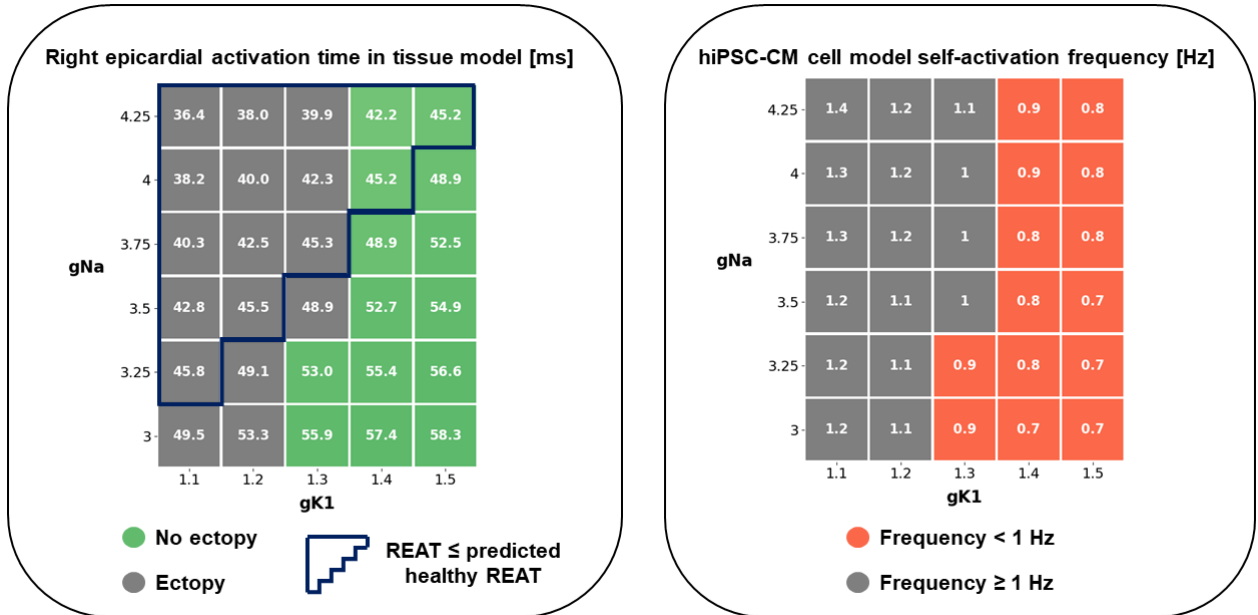


Figure 3.16: Results obtained by modifying the EHT gNa and gK1 in the tissue (left) and cell (right) models. Left: the grid shows the REAT for the tissue model paced at 1 Hz. Values inside the blue contour are  $\leq$  the predicted healthy REAT and thus would restore pre-infarct activation. Green squares indicate no presence of ectopy, while grey squares indicate presence of ectopy. Right: the grid shows the self-activation frequency for the hiPSC-CM cell model, in a no-pacing protocol. Red squares show where the cell model self-activates with frequency < 1 Hz (i.e., intrinsic-cycle length > 1000 ms), while grey boxes show where the cell self-activates with frequency > 1 Hz, thus causing the observed presence of ectopies in the tissue model.

The AP traces reported below in Fig Figure 3.17 serve as a visual aid for understanding how the EHT electrophysiology is affected when changing gNa and gK1. Increasing gNa produces an increase in the EHT AP upstroke, and thus in the CV in the EHT. However, increasing gNa

also shortens the intrinsic hiPSC-CMs cycle length, resulting in ectopic beats fired from the EHT when pacing tissue at 1 Hz (blue trace in Figure 3.17). Increasing gK1 slows down the intrinsic activation of the hiPSC-CMs and allows the EHT to be activated by the myocardium, paced at 1 Hz (orange trace in Figure 3.17).

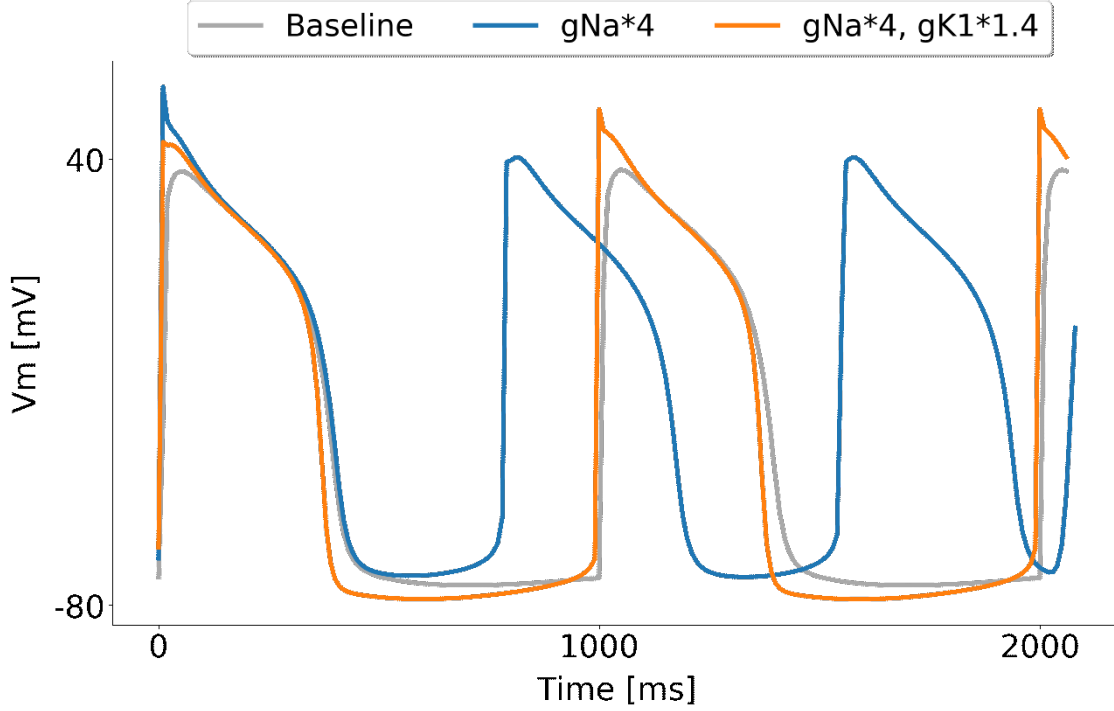


Figure 3.17: AP traces from a mesh node in the EHT, with different values of gNa and gK1. The tissue model is paced at 1 Hz in all 3 cases. In the baseline case (grey trace) the EHT is activated every 1000 ms by the stimulus coming from the myocardium, which is paced at 1Hz. When increasing gNa to 4 times the default value (blue trace), in order to increase the EHT CV, we observe a shortening in the intrinsic hiPSC-CM cycle length. Thus, the EHT self-activates at 800 ms, before being stimulated by the myocardium, causing an ectopic beat. Finally, when increasing gK1 to 1.4 times the default value, the intrinsic hiPSC-CM cycle length is brought back to values  $> 1000$  ms, allowing the EHT to be stimulated from the myocardium and thus eliminating the ectopy

We also provide in Fig Figure 3.18 below snapshots of the tissue model showing the ectopic beats firing from the EHT, and the corresponding AP traces for a mesh node in the EHT.



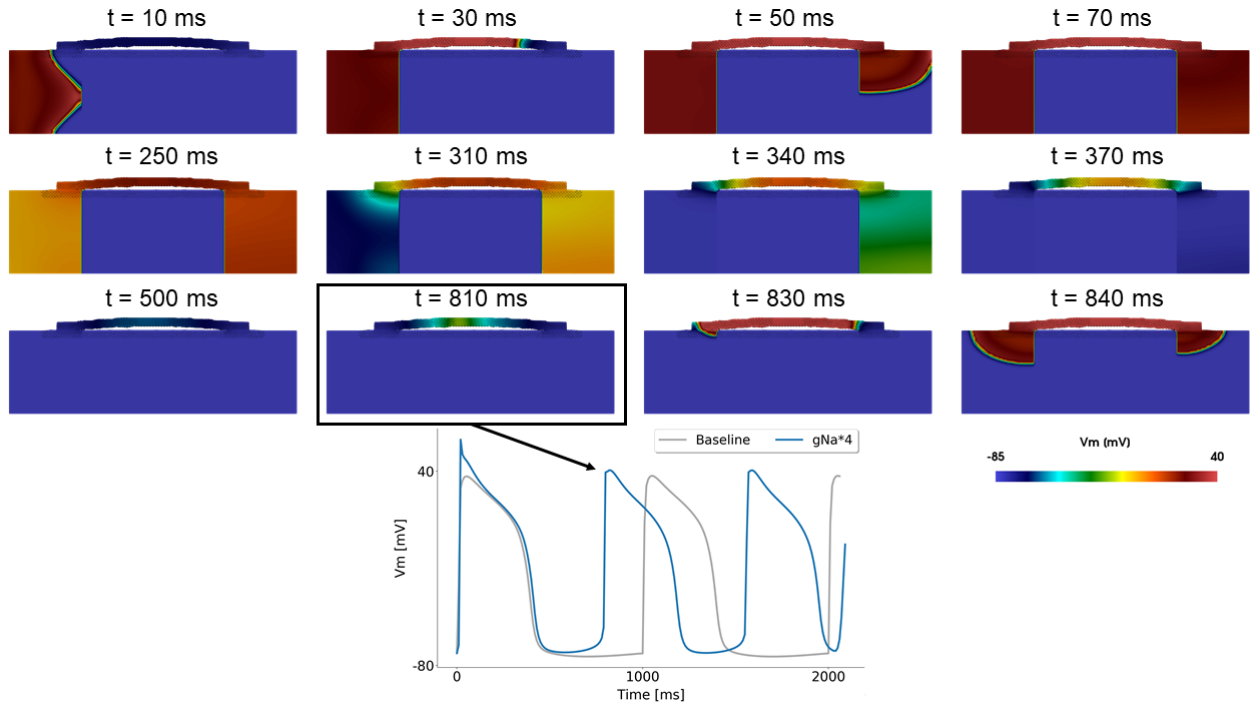


Figure 3.18: Snapshots from the tissue model showing the ectopic beat fired from the EHT. The snapshots are from the tissue simulation where  $gNa$  in the hiPSC-CM model was multiplied by 4. The first two rows show the normal activation and repolarization caused by the stimulus from the myocardium. At  $t=500$  ms, the repolarization in both the myocardium and the EHT is completed (first snapshot, third row). Around  $t = 800$  ms, the ectopic beat is fired from the EHT (snapshot in the black rectangle). The ectopic beat can also be seen in the blue AP trace in the lower part of the figure, in contrast with the grey trace, representing the baseline (default  $gNa$  and  $gK1$ ), 1 Hz activation.

## 3.4 Discussion

In this study we implemented an *in silico* cardiac electrophysiology model to investigate the impact of epicardial EHT patch design on the electrical propagation within infarcted myocardium. Tissue and patch geometrical dimensions and conductivities were incorporated through 10 modifiable model parameters (Figure 3.1). We demonstrated that our modeling framework could capture the interaction between host and EHT patches.

We found no difference in the impact of EHT on the REAT between the three different model species tested. The importance of different patch design values on modifying the REAT is also consistent across species, suggesting that, in the context of our model, the EHT has the same effect on electrical activation across species.

We demonstrated that only when the scar is transmural do EHT properties impact activation times. Finally, we predicted that increased sodium ( $I_{Na}$ ) and potassium ( $I_{K1}$ ) channel densities in the EHT properties will lead to recovery of activation times, no change in repolarization gradients and no ectopy. This provides a testable prediction for recovering host electrophysiology properties using EHT patches.

### 3.4.1 Model validation

In our validation study, the modeling framework was able to qualitatively match the changes in CV observed in all but one experiment in Mawad et al (Figure 3.9D), where our simulations predicted an increment in CV after engraftment, instead of a decrement, as reported in the study. Since we are modelling the CP as an ohmic conductor (see section 3.2.4), this increment in CV is expected and comes as a result of the bath loading effect [155]. Essentially, the presence of a conductive area around the tissue increases the extracellular conductivity for the tissue at the interface, supplying the current with a low-resistance pathway to flow in. This is an experimentally documented phenomenon [156], which is reproduced by the bidomain model. The bath loading effect may be responsible for the increment in CV in Mawad et al when the same CP patch was implanted on infarcted hearts (Figure 3.9E). Mawad et al also recorded

slowing in CV after engrafting CP patches on myocardial slices. Crucially, after the patch was removed, the myocardial slice did not recover to the CV observed before the engraftment, suggesting that epicardial or myocardial damage could potentially be involved in the observed CV slowing.

### 3.4.2 Conductive polymer effects

Attaching conductive polymer to EHT has been proposed as way to reduce arrhythmia risk [157]. The model captured the effects of the conductive polymer on infarcted hearts (Figure 3.9E). However, the GSA did not predict a role for the CP in impacting the REATs (Figure 3.12). While CP proved useful as a culturing surface, allowing pacing and synchronization of multiple cluster cells by propagating electrical stimuli [131], these experimental studies and our simulation results do not provide clear support for their role in increasing CV in EHT patches.

### 3.4.3 REAT as a biomarker

The choice of using only REAT as a biomarker was mainly dictated by the fact that we wanted to perform sensitivity analysis on our tissue model. By employing only one feature, we were able to consider our model as a function mapping a  $n$ -dimensional parameter space (where  $n=10,9,8$  or  $7$ ) to a scalar output. The presence of a scalar output meant that we could perform sensitivity analysis just by training one GPs emulator (which is trained to replicate the only available output). Otherwise we would have needed to train one GPs emulator for each additional feature (i.e. for each additional biomarker). We prioritized training multiple GPs emulators to emulate different species and different versions of our model, rather than keeping the same model, for the same species, and having different biomarkers. Thus, having to choose one biomarker to assess how the EHT patch affects the electrical activation, the time it took the stimulus to reach the other side of the slab, going through the scar-EHT complex, (i.e. the REAT) represents a solid choice, given also the simple geometry of our model.

### 3.4.4 From small animal models to human models

The species most commonly used in preclinical studies consist of small mammals such as rats and rabbits [158], which have distinct electrophysiology from humans [159]. Specifically, while some ionic currents such as  $I_{Na}$  and  $I_{K1}$  are conserved between species, other currents like the ones involved in the calcium handling ( $I_{CaL}$ ,  $I_{NaCa}$  and the Na-Ca exchanger) and the repolarizing currents ( $I_{Kr}$ ,  $I_{Ks}$ ) have found to be systematically different across species [159]. Current experiments for evaluating EHT in infarcted hearts are also mainly performed on small mammals. Testing whether findings in small animals models are transferrable to humans is a crucial step towards clinical application of EHT patches [115]. Consistent with previous simulation studies [160], we demonstrate that small animals provide a good model for replicating the qualitative effects of EHT patches on electrophysiology and that EHT design variables have similar importance and impact across species.

#### Distribution of stimulus propagation paths

The majority of simulations paths are classified as “lower half” (Figure 3.11). This is likely caused by the fiber distribution. The fibers angle ranges from  $40^\circ$  to  $-50^\circ$ , thus the longitudinal direction is more aligned with the conduction direction in the lower half of the slab. Our model also indicates that the distribution of stimulus paths is consistent across species. This result shows that the different electrophysiology of rat, rabbit and human CMs does not influence the electrical propagation in cardiac tissue in presence of a scar and an EHT patch. While some findings on small animal models, such as drugs effects, needs to take into account different between species at a cell level, such as ion channel expression [161], our results suggest that for electrical propagation the findings obtained on small animal models are transferrable to larger human models.

### Sensitivity indexes from GSA

Figure 3.12 indicates that the activation in the *epi-endo* and *endo-epi* setups is governed by the scar parameters (depth and conductivity), suggesting that the presence of EHT in our model does not have an impact when the scar is not transmural. In the transmural setup, however, the EHT conductivity starts to play a role. These findings are consistent with the stimulus path investigation (Figure 3.11), indicating the stimulus travelling almost exclusively through the slab in the *epi-endo* and *endo-epi* setups and travelling through the EHT in 18 to 24% of the simulations in the *transmural* setup. The sensitivity indexes are consistent across rat, rabbit and human, indicating that the parameters which mostly influence propagation are not species dependent. These findings highlight the translational potential of the small animal studies, while encouraging, where possible, the use of computer model to back/substitute experimental studies on animals.

### 3.4.5 Restoring healthy activation while minimizing arrhythmia risk

EHTs typically have a lower conduction than healthy tissue [162]. In our model, we saw that this was further exacerbated by the need for the activation wave to move up into the EHT and down into the viable tissue. This increases wavefront curvature, which can further slow activation [163]. We predicted that EHT conductivity in the human model needs to be increased to 1.008 S/m (corresponding to 4.5 times the healthy myocardial conductivity) to match physiological activation patterns. Improving conductivity in cardiac tissue is an area of active research, and can be accomplished through techniques such as preconditioning with insulin-like growth factor-1 [34], the delivery of the skeletal muscle  $Na^+$  channel through mesenchymal stem cells [164, 165] and the gene transfer of connexin-32 [166]. However, the lower conductivity of EHT is known to be caused by a combination of factors arising from the hiPSC-CMs immature phenotype [167, 168]. Specifically, hiPSC-CMs present a lower expression of gap junction proteins with respect to adult cells. Moreover, gap junctions in hiPSC-CMs are arranged in a more circumferential distribution, like that in fetal cardiac cells, rather than being abundant at the longitudinal ends of the cell, as it happens for mature CMs [169].

Improving hiPSC-CMs maturation could address these issues, provide hiPSC-CMs with more adult-like gap junctions and thus bring EHT conductivity close to the values proposed here. Experimentally, increasing the expression of gap junction proteins and development of parallel sarcomeres has been achieved through extending the culture time [170] and electrical [171] or mechanical [172] stimulations. Although this is a long and difficult process, latest studies have shown encouraging developments in hiPSC-CMs maturation techniques, on a molecular and metabolic level [167], as well as regarding structural and functional maturation of hiPSC-CMs derived tissues [173]. New culturing techniques are also being developed to be easily scalable, and being able to produce a large number of cells, required for tissue manufacturing and transplantation [168].

### **Increasing EHT conductivity promotes pro-arrhythmic behavior**

Our results indicate that increasing conductivity causes a rise in repolarization gradient at the myocardium-EHT interface (Figure 3.15). This can be explained by the increment in EHT electrotonic load on the tissue. The electrotonic load is due to diffusive currents flowing through the gap junctions of neighboring cells [174]. A large increment in conductivity, while restoring physiological activation times, could also exacerbate current diffusion between cells. Electrotonic currents are associated with changes in AP amplitude, AP repolarization and APD [174, 175]. In turn, heterogeneities in AP repolarization are linked to the formation of arrhythmogenic substrates [150]. Hence, our findings suggest that achieving the required CV through (large) augmentation of EHT gap junctions density may promote arrhythmic behavior at the myocardium-patch interface.

In our model, the electrotonic load brings the APD of the host myocardium ( $\approx 310$  ms) closer to the EHT APD ( $\approx 420$  ms). A higher EHT conductivity causes a higher electrotonic load, leading in turn to a more prominent lengthening of the host myocardium APD (Figure 3.19). Finally, a greater APD lengthening leads to higher repolarization gradients. Figure 3.19 shows how the AP of a myocardial node at the tissue-EHT interface changes when changing the conductivity in the EHT.

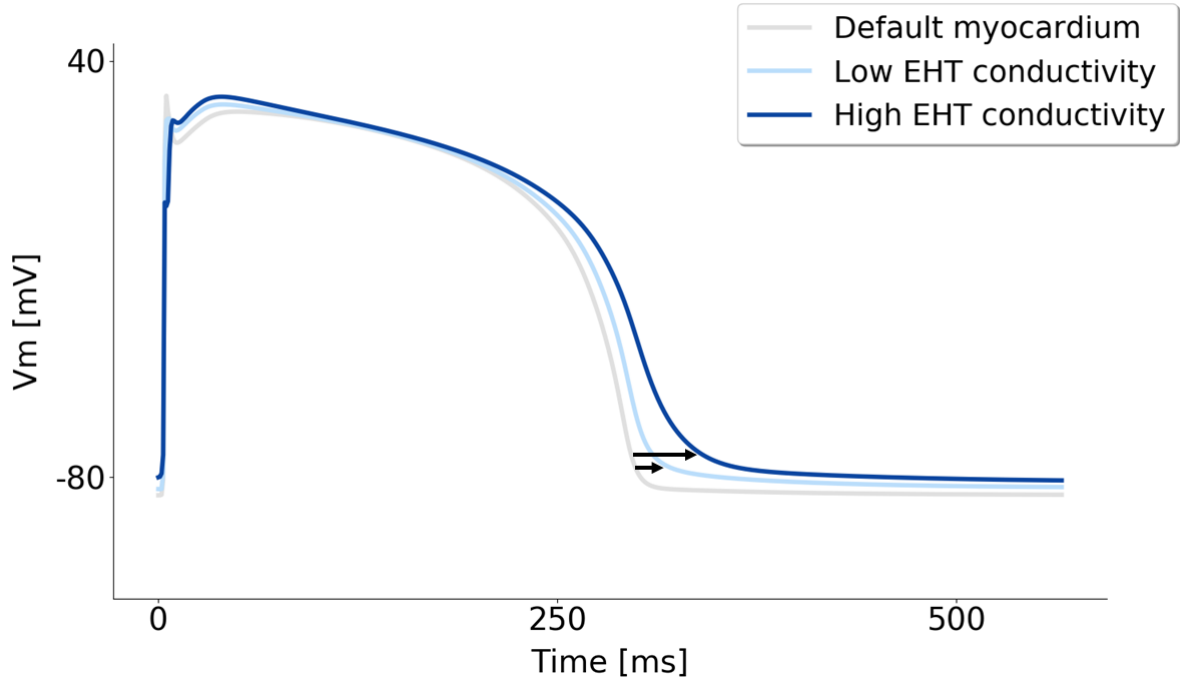


Figure 3.19: Comparison of AP traces from a myocardial node close to the EHT-tissue interface and the default myocardial AP (taken from a node far from the EHT-tissue interface). The black arrows indicate the increment in APD due to the electrotonic load exerted from the EHT on the tissue at the interface. A higher EHT conductivity causes a bigger increment in APD in neighboring host myocardium, resulting in turn in a higher repolarization gradient.

### Altering ion channel densities recovers healthy activation and has low arrhythmia-risk

Our model predicts that increased sodium ( $I_{Na}$ ) and potassium ( $I_{K1}$ ) channel densities in the [EHT](#) match the physiological activation patterns with no ectopy (Figure 3.15). Experimentally it has been shown that the immature phenotype causes [hiPSC-CMs](#) to have a lower [AP](#) upstroke velocity with respect to adult [CMs](#) [176]. This further hampers the possibility for [hiPSC-CMs](#) to reach [CV](#) values typical of adult [CMs](#). The [AP](#) upstroke velocity is known to be mainly regulated by the Na channel density [163]. Our model estimates a 4-fold increase in  $I_{Na}$  conductance in the Paci model (from 3.67 nS / pF [96] to 14.68 nS/pF) to be sufficient to match physiological activation. The augmented value is more in line with Na channels density values found in adult [CMs](#) [163]. This finding further highlights the importance of [hiPSC-CMs](#) maturity when it comes to successful electrical integration with host tissue. The low  $I_{Na}$  expression

also provides an additional explanation for the high values of EHT conductivity needed, according to our model (Figure 3.14), to match healthy activation. If the low Na channel density is retained, the EHT conductivity will have to be largely increased through gap junction density augmentation, which our model predicts to be pro-arrhythmic. We observed in our model that the increment in  $I_{Na}$  caused a shortening of the hiPSC-CMs cycle length, resulting in the EHT firing ectopic beats (Figure 3.18). This is consistent with a computational study from Paci et al where they found a decrement in cycle length when substituting the adult formulation of  $I_{Na}$  from the O'Hara model [177], which has higher  $I_{Na}$  conductance, in the first version of their hiPSC-CMs model [92]. In addition, our model exhibited ectopy termination when, beside  $I_{Na}$ , also  $I_{K1}$  was increased 1.4-fold, leading to physiological activation recovery, no increase in repolarization gradients and no ectopy. This is in agreement with earlier experimental works, which reported that introduction of adult-like  $I_{K1}$  eliminated hiPSC-CMs spontaneous activity [178] and brought hiPSC-CMs response to certain drugs closer to the one of adult CMs [179]. Low levels of the KCNJ2 gene in hiPSC-CMs is responsible for low  $I_{K1}$  expression and it is known to be one of the features that makes the hiPSC-CMs phenotype immature [180]. Thus, our findings place further emphasis on the importance of hiPSC-CMs maturation in the success of EHT patch engraftment.

## 3.5 Limitations

### Conductive Polymer Modelling

In this study we have used the Laplace equation for a simplified Ohmic conductor model of the CP. In more detailed modelling studies, Wang et al [142] matched experimental measures on CP by modelling drift and diffusion of charged species with Nernst-Planck equations. However, their results did not change when neglecting charges diffusion, concluding that the influence of diffusion in charge transport in CP is debatable. In another study, Cochrane et al [181] have measured the current/voltage (I/V) relationship in CP, and demonstrated that it becomes more linear (i.e. it follows the Ohm's law) as the conductive particle concentration (doping) increases.



Therefore, the modelling strategy adopted in this study (CP as an Ohmic conductor) empirically captures CP's bulk behavior, but it is not representative of the CP's charges mechanism at a molecular scale.

### Heterogeneity of hiPSC-CMs

We modeled the EHT as a homogenous syncytium. However, it is likely that EHTs contain stem-cell-derived cardiomyocytes exhibiting three phenotypes: atrial-like, ventricular-like, and nodal-like [182, 183]. We have not represented these distinct cell types explicitly and have assumed a single homogenized representation for the EHT. The need to explicitly represent different cell types depends on their relative number and their spatial organization. This is likely to depend on the EHT manufacturing process and could be modeled using the partitioned phenotypes or homogenized phenotype models for simulating electrical activation in tissue consisting of multiple cell types [184].

### Repolarization gradients as arrhythmia marker

We used repolarization gradients as an arrhythmia marker, however, Laurita et al [150] found that heterogeneities in AP repolarization are linked to the formation of arrhythmogenic substrates when an isthmus is present, which we did not explicitly include in our model. However, when the activation wave moves from the EHT and down into the viable tissue it will lead to enhanced wave curvature, which Laurita et al also listed as an alternate to an isthmus as a possible source of electrotonic load. Other studies have also shown that increased dispersion of repolarization enhances the occurrence of unidirectional blocks [129], highlighting that, alongside structural, also functional reentry may be possible. As a future/complementary work on our simulations data, other quantities such as the conduction safety factor or vulnerable windows could be computed to further quantify arrhythmic behaviour.

### 3.6 Testing model assumptions and parameters choice

In this study, we used an idealized thin 3D tissue model that does not include realistic whole-heart structure or geometry. Our model cannot therefore capture some phenomena arising from the 3D structure and complexity typical of the mammal ventricles (for example an electrical wave propagating around the scar rather than through the EHT patch). To test if tridimensionality could affect our results, we have run further tests and verified that the GSA sensitivity indices do not change when considering the possibility of activation around the scar, and that the repolarization gradients do not change in a full-3D slab model.

Additionally, when creating our model and conducting this study, we made a number of assumptions and parameters choice, as it happens for every modelling study. To test if these choices impacted our results, we have repeated our GSA using the rat model, *fixed* sub-case as a reference model. We have tested whether our results are affected by: 1- Pacing location; 2- Pacing frequency; 3- Presence of BZ; 4- Transmural heterogeneity of ventricle adult cardiomyocytes.

#### Impact of tridimensionality on sensitivity analysis

To test if activation waves travelling around the scar may impact our sensitivity analysis, we repeated the sensitivity analysis in the rat model (*fixed* sub-case), with the REAT capped to be less than 150, 175 or 200% of the predicted REAT when the scar was absent. We found a variation in the sensitivity indices of 10, 1, and 3%, when the REAT was capped, respectively, to 150, 175, and 200% of the predicted REAT without the scar (Figure 3.20). This suggests that the results of our study still hold when considering the possibility that the activation wave propagates around the scar.

#### Impact of tridimensionality on repolarization gradients

We used a thin 3D model in our primary analysis, which may not account for the impact on the repolarization gradients of different activation paths and scar morphologies typical of a 3D

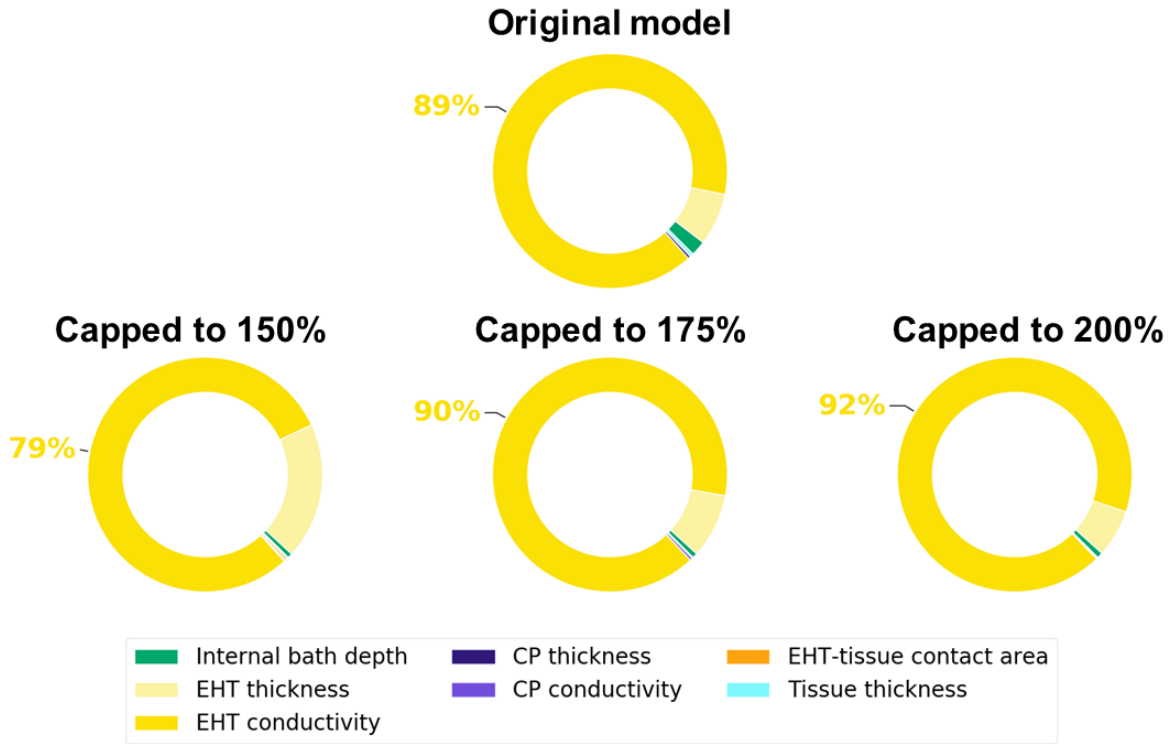


Figure 3.20: Comparison of sensitivity indices in the rat model (fixed sub-case) between the original model and models with REAT capped to 150, 175, and 200% of the predicted REAT without the scar. We observed a variation of 10, 1, and 3%, respectively.

environment. To investigate whether dimensionality could affect the repolarization gradient, we computed the repolarization gradient for propagation simulated in a full 3D version of our human model (*fixed* sub-case). The full 3D model was created by extending the current thin 3D model in the z-direction (Figure 3.21), i.e., the full 3D model featured multiple layers of elements in the z-direction, as opposed to only one layer of elements featured by the original, thin 3D model. Figure 3.22 shows the repolarization gradient in the full 3D model. Comparing it with

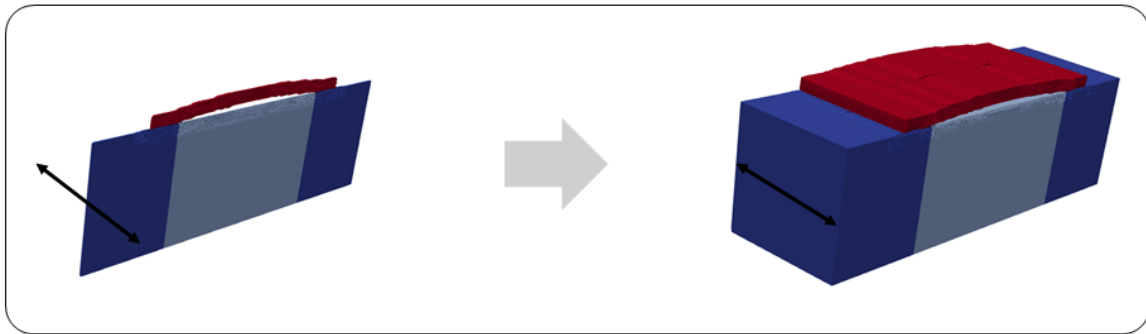


Figure 3.21: Generation of the full 3D model (right) from the thin 3D model (left), for the human model (fixed sub-case).

the repolarization gradient of the thin 3D model in Figure 3.7 reveals that their magnitudes are similar (maximum values  $\approx 70$  ms/mm in both cases) and that the spatial distributions are also comparable, with both exhibiting higher values at the tissue-EHT interface. Thus, dimensionality has a limited impact on our model.

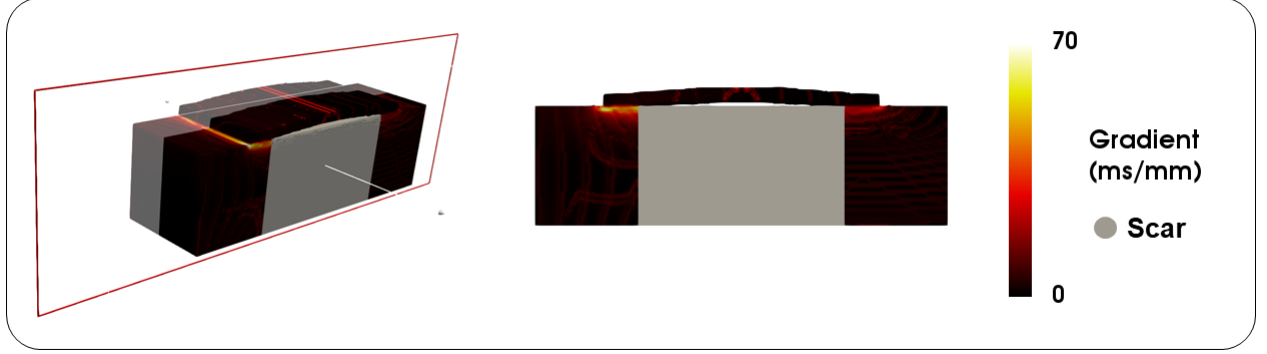


Figure 3.22: Repolarization gradient for the full 3D model. The left panel shows the entire mesh. The right panel shows a transmurular cross-section, for comparison with the repolarization gradient of the thin 3D model (Figure 3.7).

### Pacing location

The model aimed to represent the common experimental set up where the heart is often paced from an electrode placed on the ventricular epicardium. To test if the pacing protocol caused a large impact on the sensitivity analysis, we repeated the sensitivity analysis on the rat *fixed* sub-case, stimulated from a point on the endocardium. This caused a change in sensitivity of 2% (Figure 3.23).

### Pacing frequency

To test the output of our model at higher frequencies, we paced the TNCHS and Paci cell models with a  $30 \mu A/cm^2$  transmembrane current for 800 s at 2 Hz, and we used the state variables to initialize the cells model in the tissue simulation. We repeated the 500 simulations (with the same parameters combinations sampled previously) for the rat *fixed* model, and performed the

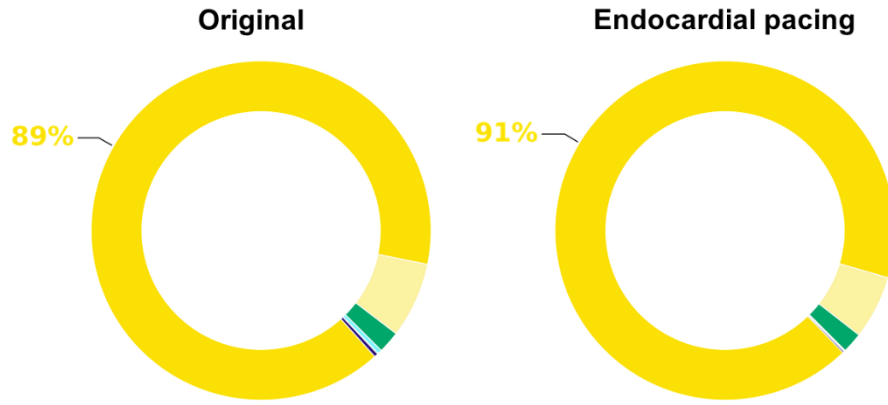


Figure 3.23: Total effect indices comparison between the original model and the model paced from the endocardium (rat model, *fixed* sub-case).

sensitivity analysis on the new simulation results. The comparison shows a 1% variation in the sensitivity indices, thus demonstrating that our results are not affected when pacing the model faster than 2 Hz.

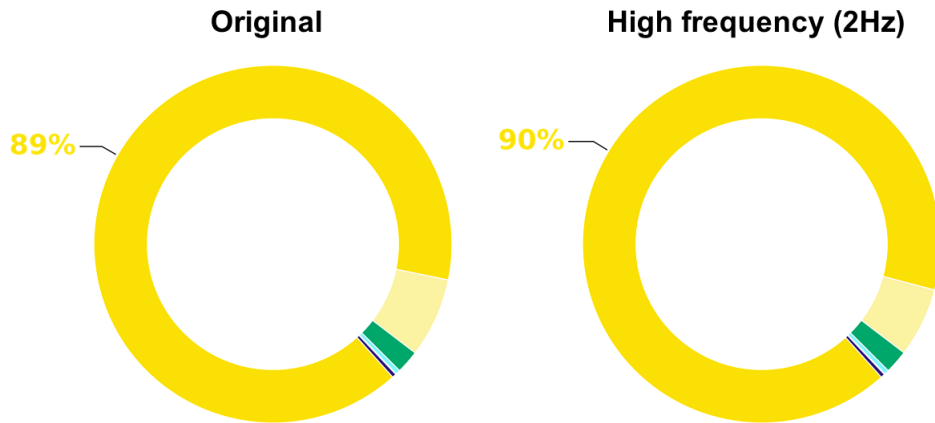


Figure 3.24: Total effect indices comparison between original model and model paced at 2 Hz (the original model was paced at 1 Hz) (rat model, *fixed* sub-case).

### Presence of border zone

In this section we create and test a version of our slab model featuring a **BZ** around the scar. The **BZ** replaces a portion of the scar in the original model. Specifically, the **BZ** thickness corresponds to 10% of the original scar width (see schematic representation in Figure 3.25A). For example, if the original scar width was 6 mm, a border of 0.6 mm thickness will be assigned

as the BZ. Isotropic tissue was assigned in the BZ, to account for structural remodeling and fibers disarray, with a conductivity set to 50% of the healthy transversal conductivities [128]. We repeated the 500 simulations (with the same parameters combinations sampled previously) for the fixed setups of the rat model. We also trained GPs emulators for both setups and performed the GSA. A comparison of the total effect indexes between the models without and with BZ is reported in Figure 3.25B, showing a 1% change.

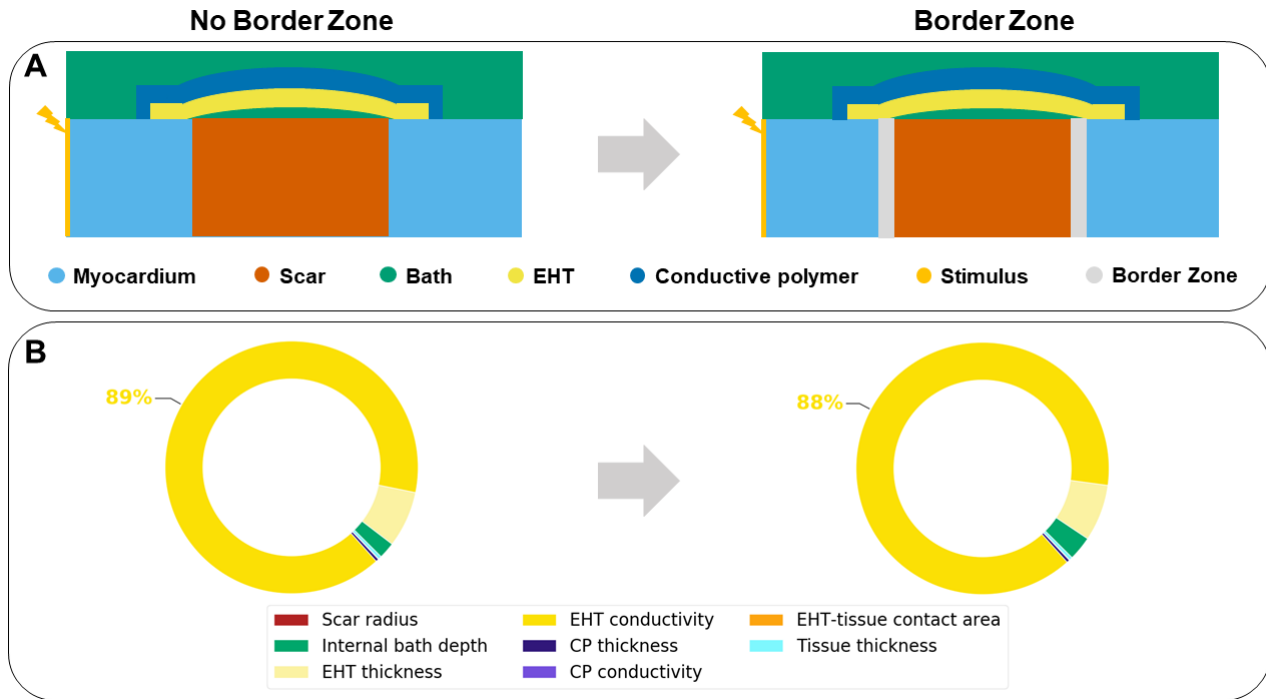


Figure 3.25: Comparison of the original model (left-hand side) and the model with a BZ (right-hand side). Panel A shows schematic representations of the original model and the BZ model. Panel B shows the total effect indices of both models, for the *fixed* setup of the rat model.

### Transmural heterogeneity of adult ventricular myocytes

Transmural heterogeneities of adult cells were not included in our tissue model. The rat cell model and the rabbit model that we used did not have transmural versions, and creating calibrated endo and epicardial versions of these models was outside the scope of this study. However, to estimate the impact of transmural heterogeneity on tissue activation, we developed

a version of the model where we defined three different transmural layers for endocardial, mid-myocardial and epicardial myocytes spanning 17, 41, and 42% of our model wall thickness, respectively (see Figure 3.26). These values were estimated from the data reported by several

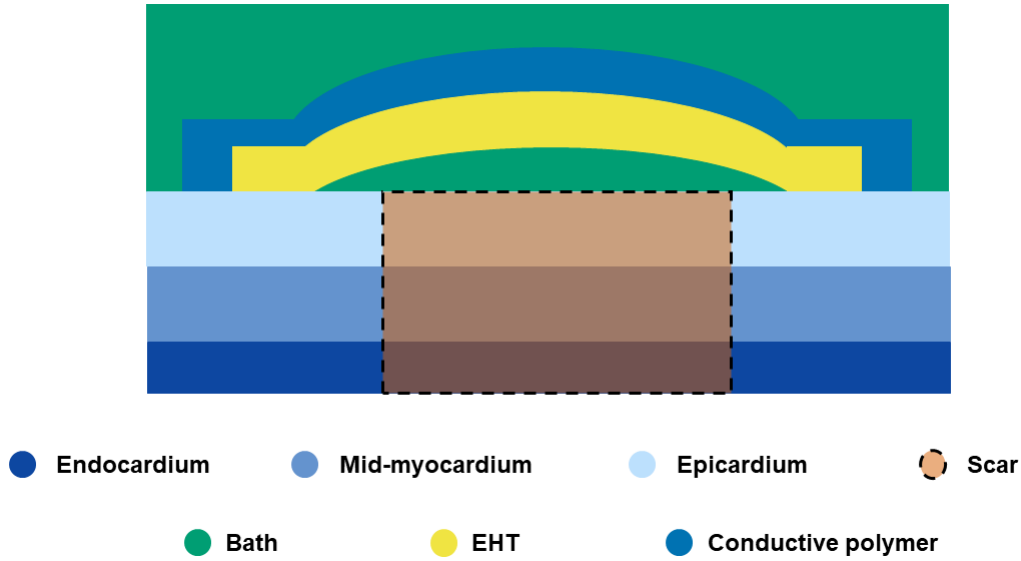


Figure 3.26: Schematic representations of the human model (*fixed* sub-case) with transmural heterogeneity of adult ventricular cells included. The myocardium is divided into endocardium, mid-myocardium and epicardium, indicated in the figures by 3 different shades of blue, respectively from darker to lighter.

experimental studies [185, 186, 187]. The layers were then assigned with the endocardial, mid-myocardial and epicardial version of the Ten Tusscher ionic model. Comparison of sensitivity indices for the human model (*fixed* sub-case) shows that including the transmural heterogeneity of adult human cells does not influence our results, causing a maximum change in sensitivity of 3% (Figure 3.27).

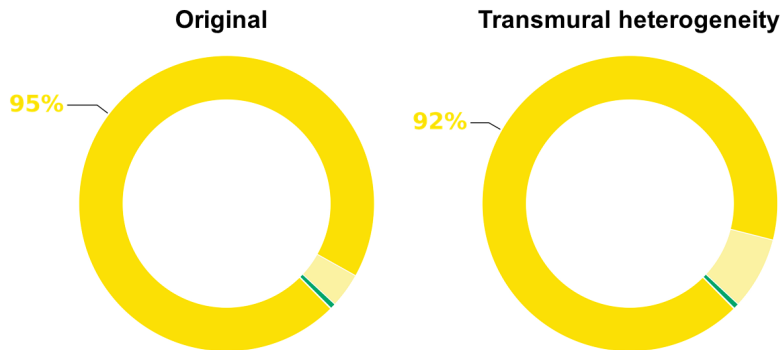


Figure 3.27: Total effect indices comparison between the original model and the model with transmural heterogeneities included (human model, *fixed* sub-case).

### 3.7 Conclusions

We have shown that our model can capture the interaction between host myocardium and EHT patches by validating it against independent experimental studies. We have found that engrafting an EHT patch on non-transmural scar has no effect on the REAT and offers a pathway for the electrical wave in less than 5% of the simulated cases (Figure 3.11), suggesting limited patch influence on electrical propagation. We have also found that, when the scar is transmural and non-conductive, the EHT patch conductivity is the main parameter influencing electrical propagation. Moreover, we demonstrated that EHT patches effects on host myocardium and EHT patch design variables are not species-dependent, providing further evidence that results in small animal model can be transferred to human models. Finally, our model indicated that, while it is possible to achieve physiological activation by tuning EHT conductivity, this approach may promote arrhythmic behavior. Instead, altering other immature characteristic of hiPSC-CMs, such as low AP upstroke velocity and lack of  $I_{K1}$ , may recover physiological activation while not increasing arrhythmia initiations.



## Chapter 4

# Assessing the arrhythmogenic risk of engineered heart tissue patches through *in silico* application on infarcted ventricle models

### 4.1 Introduction

Epicardial [EHT](#) patches manufactured from [hiPSC-CMs](#) have been studied in the past decade to tackle ischemic heart disease, the single biggest killer among cardiovascular diseases [188]. The successful differentiation of human-induced pluripotent stem cells in [CMs](#), unlocked a new source of autologous cardiac cells, free of ethic-related issues. This sparked the development of a new line of research on the feasibility of using [hiPSC-CMs](#) to aid infarcted hearts, by providing new, functioning tissue and, ultimately even replacing the fibrotic tissue present in the scar [24]. Initially [hiPSC-CMs](#) were injected at the infarct site as part of a liquid solution, but it became soon clear that a liquid solution was not an adequate vector to deliver the [hiPSC-CMs](#), exhibiting a retention rate around 5% [30]. These findings steered the research towards the use of scaffolds to give physical support to the [hiPSC-CMs](#), as well as trying to mimic the target

delivery environment, i.e. the myocardium.

Research on EHT patches ultimately aims to develop new and effective techniques for regenerating injured myocardium, or for correcting the post-MI defects that lead to further disease onset and progression [189]. Currently, the strategy to bridge the gap between clinical trials and clinical use, focuses on safe post-engraftment integration of the patch, which is to be achieved by overcoming several bottlenecks (see section 1.5). For example, avoiding infection or rejection post implantation [190], hiPSC-CMs acting as pacemaker cells causing arrhythmia, and the different speeds of AP propagation through the myocardium with or without graft or through the fibrotic interface between the host myocardium and the graft, which can also cause re-entries and arrhythmias [191].

Application of epicardial EHT patches manufactured from hiPSC-CMs to augment the function of lost cardiac tissue are currently being evaluated in the first in-patients clinical trials [192]. In recent years, various EHT engraftments have been performed *in vivo*. Most studies have been conducted on small animal models, namely mice, rats, guinea pigs and rabbits [39, 193, 36, 194, 195, 123, 196, 122], with a limited number of experiments performed in large animals (pigs) [37, 197, 198, 199] and primates [200]. The majority of these studies have found that engraftment of EHT patches helps scar remuscularization and improves LV ejection fraction. However, little data have been collected on electrical activity of the patches or host myocardium. This can be brought back to two main reasons: 1) *in-vivo* EHT patches were assessed exclusively using echocardiography or MRI, which do not provide any electrophysiologic information; 2) Some studies were designed to show technical feasibility and electrophysiologic data were not collected (mainly the case in large-animal studies).

Collecting experimental data on electrical activity would be crucial to shed light on the electrical coupling at the patch-host interface. While evidences of EHT-epicardium electrical coupling have been proven [39, 201], the exact mechanistic procedure behind is yet to be fully understood. It is generally agreed that hiPSC-CMs, despite possessing immature gap junctions, are able to establish communication and ion passage between them (and thus the EHT patch) and the host myocardium. However, how this new electrical interaction can affect signal propagation

and both the patch's and the host's APs is not yet clear.

In case of successful electrical coupling, the introduction of hiPSC-CMs into a human heart will lead to electrophysiological heterogeneity, that may contribute to increased arrhythmia risk. Yet scarce data are available on the impact of EHT patches on arrhythmia risk. Ye et al [198] did not observe any spontaneous arrhythmia during the 4-week follow-up period after the patch application in a porcine model. Previous studies in mice, rabbits, and guinea pigs have found limited evidence of increased arrhythmogenic risk with EHT patches [193, 122, 37, 199, 200]. In contrast, injection of hiPSC-CMs into scar caused an increased arrhythmic risk [202, 203]. These previous studies are in animals with shorter APD and smaller hearts than humans and extrapolating these results to patients may underestimate the risk.

As of now, the only study to evaluate the arrhythmogenic effect of patches in humans has been performed using stem cell-derived cardiovascular progenitors, while the arrhythmogenic effects of hiPSC-CMs-based patches have only been evaluated in animal models. It is known that large animals could retain potential arrhythmic complications not observable in small animal models, such as more extensive substrate available for re-entry [193, 204]. In this study, we aim to use human ventricle simulations to identify potential risks and properties of the EHT that can both exacerbate and mitigate arrhythmia risk. Specifically, we will investigate: (1) how patches can provide additional propagation pathways that can alter re-entrant dynamics in either pro- or anti-arrhythmic ways; (2) how EHT patch–host myocardium coupling affect propagation of ectopic impulses.

## 4.2 Methods

In this study we simulated electrical propagation on two left-ventricular models selected from a cohort of 24 ischemic heart failure models [118]. One heart was representative of a scar with an anatomical configuration that included a channel of viable tissue bordered on each side by scar, hypothesized to represent a possible isthmus for re-entry, and the other including a dense lateral wall scar (Figure 4.1-A). Briefly, the left ventricle geometry was segmented from cardiac

magnetic resonance with in-plane resolution of 0.6 x 0.6 - 1.37 x 1.37 mm and slice thickness of 8–20 mm, where the scar was identified with late gadolinium enhancement. The meshes include detailed representation of scar and border zone morphology. For all the details about the segmentation process the reader is referred to the publication by Costa et al [118].

For both meshes we introduced a 0.3 mm layer of viable myocardial tissue (Figure 4.1-B) over the area where the scar was visible on the epicardium and assigned a hiPSC-CMs cell model [96] to this region. This aimed to represent *in silico* the application of an epicardial EHT patch.

Pictures of the two resulting meshes are shown in Figure 4.1-C.

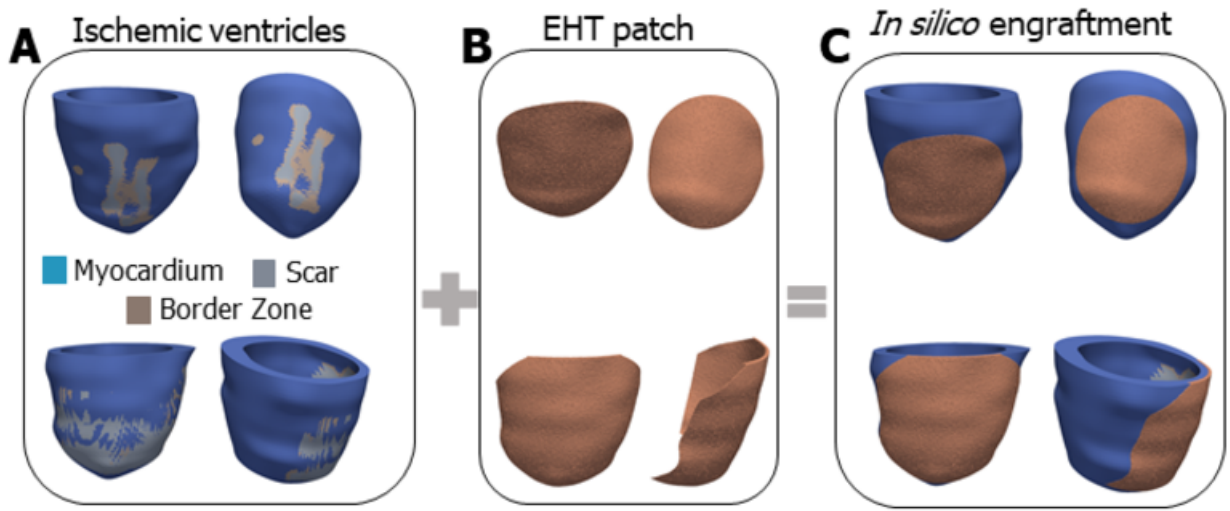


Figure 4.1: (A) The two left ventricle, heart failure models used in this study, from two different angles. In the top row the model with the isthmus scar is reported, while the model with the large lateral wall scar is reported in the bottom row. (B) The layer of viable tissue used as epicardial patch. (C) Ventricle models after the application of the EHT patch above the scarred area.

#### 4.2.1 Pipeline for *in silico* EHT patch application

A summary of the pipeline designed to apply the EHT patch on the ventricle meshes is shown in Figure 4.2. We started with the meshes published from Costa et al [118]. The mesh with the isthmus-like scar consisted of 221,852 nodes and 1,165,938 tetrahedral elements (Figure 4.2-a). The mesh with the large later wall scar consisted in 218,883 nodes and 1,134,099 tetrahedral elements. The meshes' initial resolution was  $\approx 0.8$ mm. The meshes' elements are tagged with

1, 3 or 4, depending on them being part of the myocardium, scar, or border zone, respectively. In the mesh with the isthmus-like scar the percentage of scar is 11.5% over the total volume, while in the mesh with the lateral wall scar, scar elements represent 16% of the mesh volume.

To create an electrophysiology simulation mesh we first define a bounding box around the ventricle and mesh it with tetrahedral elements of 2 mm edge length (Figure 4.2-b). This enables us to add elements to the mesh on the epicardial surface, which will be used later to define the EHT. We then define a plane parallel to the ventricle short axis, just below the ventricle base (Figure 4.2-c). We use this plane to split the mesh in base, endocardial and epicardial surface (Figure 4.2-d) and we run an eikonal simulation [205] imposing a velocity of 1 mm/s in all direction, so that we can obtain from the activation times the distance of each element from the epicardial surface (Figure 4.2-e). The eikonal equation is a partial differential equation used in problems involving a wave propagation. Briefly, the eikonal equation is used to simulate the cardiac AP propagation without simulating the AP at the cell level, which is traditionally done using ionic models. This approach idealizes the location of the AP front as a moving surface in the myocardial wall, and it has been validated against reaction-diffusion systems (such as the bidomain model) [206]. Since we are not computing an ionic model, the eikonal equation can be used on more coarsely resolved spatial grids, thus it helps saving computational time. We used the eikonal model to simulate wavefront propagation from the epicardium towards the outside of the ventricle. By specifying a propagation velocity of 1 mm/s, we were able to retrieve the distances of each element from the epicardial surface. In fact, since  $S = Vxt$ , where  $S$  is space,  $V$  is velocity and  $t$  is time, if  $V = 1$ , then  $t = S$ , in other words, activation time equals to the distance travelled from the wavefront, which is the distance from the epicardium. We then tag elements in order to create a circular EHT patch, centred in the middle of the scar and with  $\approx 0.3$  mm thickness (Figure 4.2-f) protruding from the epicardial surface. The EHT patch is modelled as isotropic, while the host myocardium mesh has rule-based fibres [136]. The resulting meshes have a final resolution of 0.3 mm in the myocardium and 2 mm in the bath. The isthmus-like scar mesh has 10,354,749 nodes while the large lateral wall scar mesh has 10,358,010 nodes. The bidomain simulations are performed on a High Performance Computing cluster and  $\approx 24$  hours are needed to simulate 5000 ms of

electrical activity using 512 cores.

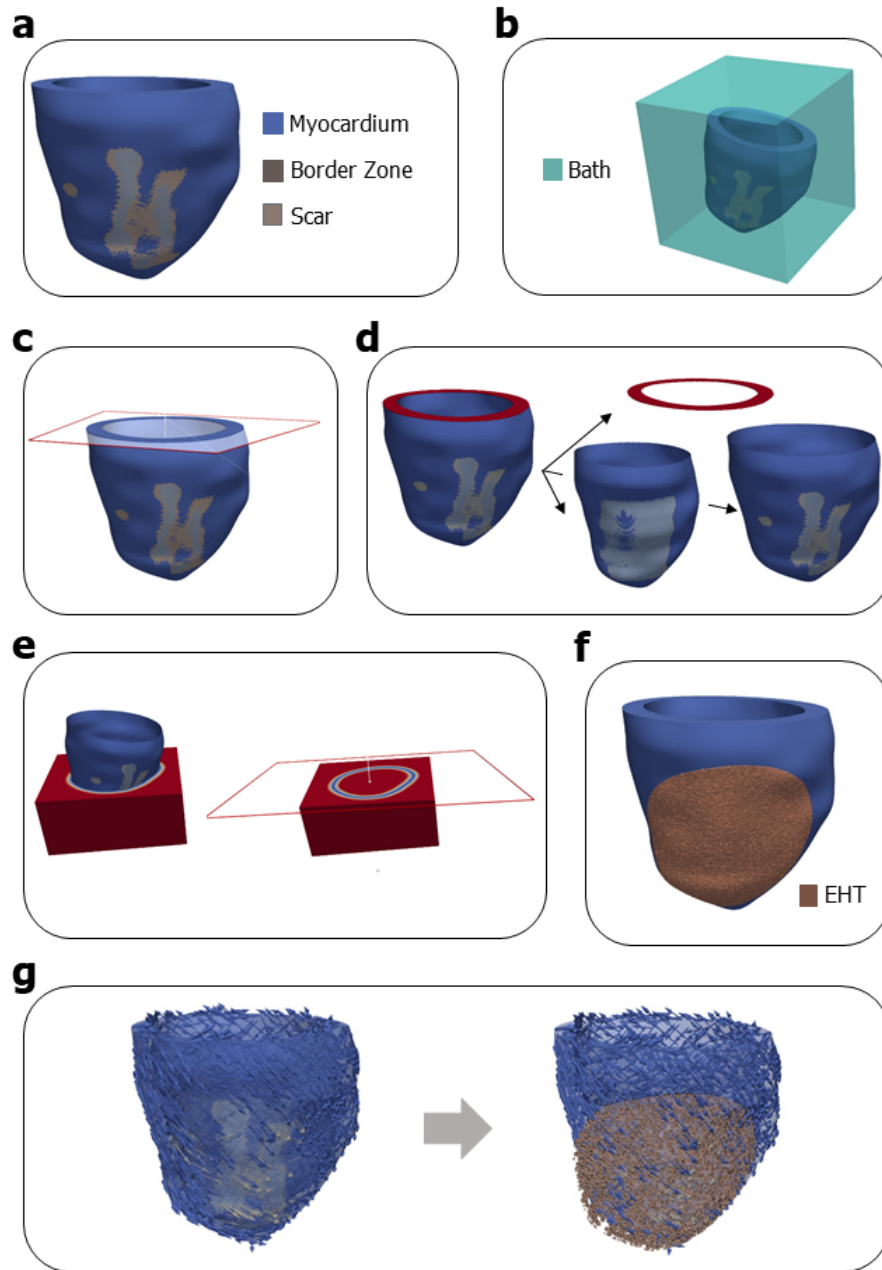


Figure 4.2: Pipeline for in silico EHT patch application. a) Starting mesh. b) Add surrounding bath elements. c) Select a plane parallel to the short axis just below the base. d) Use the selected plane to split the mesh in base, epicardial and endocardial surface. e) Run eikonal simulation to get elements distances from the epicardium. f) Tag elements to create EHT patch. g) Interpolate fibres from starting mesh.

### 4.2.2 Models and parameters used

Cardiac electrophysiology was simulated using the bidomain model [132]. The Ten Tusscher ionic cell model [90] was chosen to represent the ventricular myocardium (epicardial cell-type). For the EHT the model of hiPSC-CMs electrophysiology from Paci et al [96] was utilized. The model equations were solved using the Cardiac Arrhythmia Research Package [134]. To approximate a steady state, the myocardial and the hiPSC-CMs cell models were paced with a 30  $\mu\text{A}/\text{cm}^2$  transmembrane current for 800s at 1 Hz. The state variables were saved and were used for initializing the cell models in the ventricle simulation.

#### Ventricular parameters

The meshes had previously been assigned rule-based fibres [136]. We set conductivities along the fibre direction (longitudinal) and perpendicular to the fibre directions (transversal) to obtain CVs approximately of 65 cm/s and 35 cm/s, respectively, consistent with velocities reported for healthy ventricular myocardium [207]. To account for structural remodelling and fibre disarray, isotropic tissue conductivity was assigned in the BZ, leading to a CV approximately of 20 cm/s, corresponding to 55% the healthy transversal CV [139]. Moreover, further modifications were implemented to represent electrophysiological remodelling in the BZ, namely: reduction of fast sodium ( $I_{Na}$ ), L-type calcium ( $I_{CaL}$ ), rapid and slow delayed rectifier potassium currents ( $I_{Kr}$  and  $I_{Ks}$ ) conductance to 38%, 31%, 30% and 20% their control values, respectively [208]. These modifications led to an APD of 420 ms in the BZ, compared to 310 ms of the healthy myocardial APD (Figure 4.3). All modifications are summarised in Table 4.1. The scar was modelled as extracellular space with conductivity set to 0.01 S/m, to replicate experimental values of collagen conductivity [209].

#### EHT patches parameters

The CV and APD are two key parameters for determining re-entrant activation patterns [150, 214]. The rapid delayed rectifier potassium current ( $I_{Kr}$ ) is the most important for determining

ion current	% of default conductance value	reference
fast sodium ( $I_{Na}$ )	38%	[210]
L-type calcium ( $I_{CaL}$ )	31%	[211]
rapid delayed rectifier potassium current ( $I_{Kr}$ )	30%	[212]
slow delayed rectifier potassium current ( $I_{Ks}$ )	20%	[213]

Table 4.1: Ion channels alteration implemented in the Ten tusscher model to represent electrophysiological remodelling in the BZ

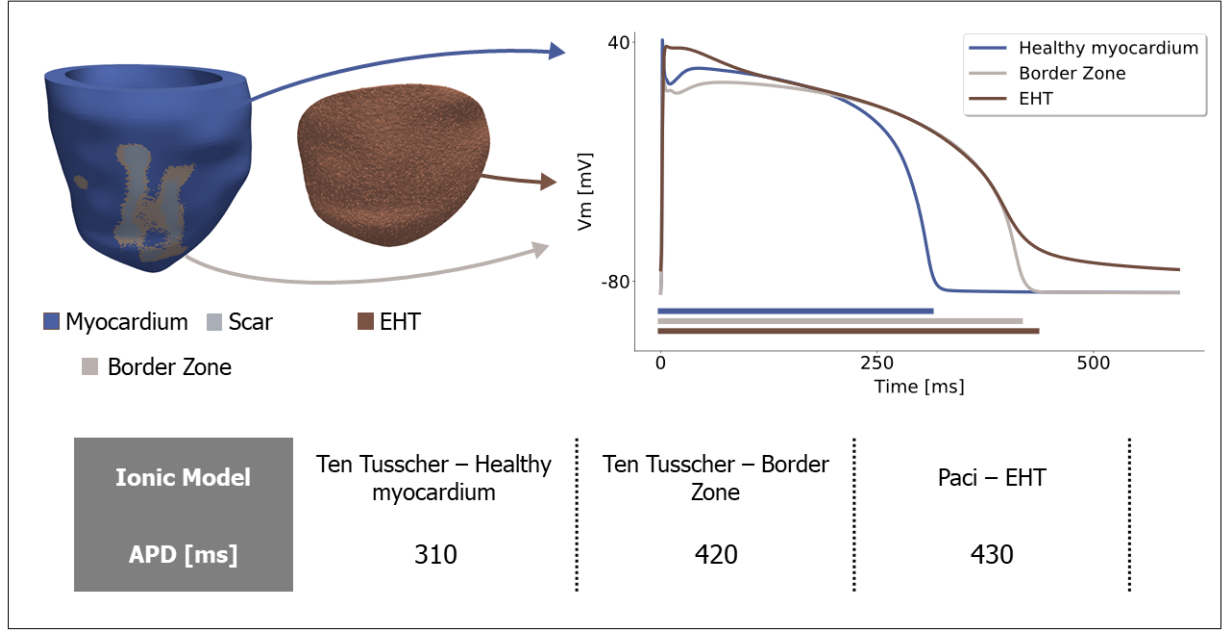


Figure 4.3: Comparison of cell models AP traces from: 1 - the Paci model (used to model the EHT patch); 2 - the (unaltered) Ten Tusscher model (used to model the healthy myocardium); 3 - the modified Ten Tusscher model (used to model the BZ). Horizontal lines correspond to the APD90 of each trace, whose values are reported in the table.

APD [215]. We have previously shown (Chapter 3 or [216]) that EHT conductivity is the most important EHT attribute for determining CV across the EHT. We have also shown that increasing CV in the EHT by altering EHT conductivity in combination with sodium channels density (to increase the hiPSC-CMs low AP upstroke velocity) is less pro-arrhythmic than increasing by a greater amount only EHT conductivity [216]. We thus modified the EHT patch conductivity and the EHT sodium channel density to obtain an EHT patch with CV equal to 10, 20, 50, 80 and 100% of healthy myocardial CV. We also modified the conductance of the ion channels responsible for  $I_{Kr}$  to 100, 150 and 200% of reference EHT cell model values.



Models with every permutation of change in conductivity and  $I_{Kr}$  were created, for a total of 15 models for each mesh. A summary of the resulting EHT patch CV and APD for each model is reported in Figure 4.4.

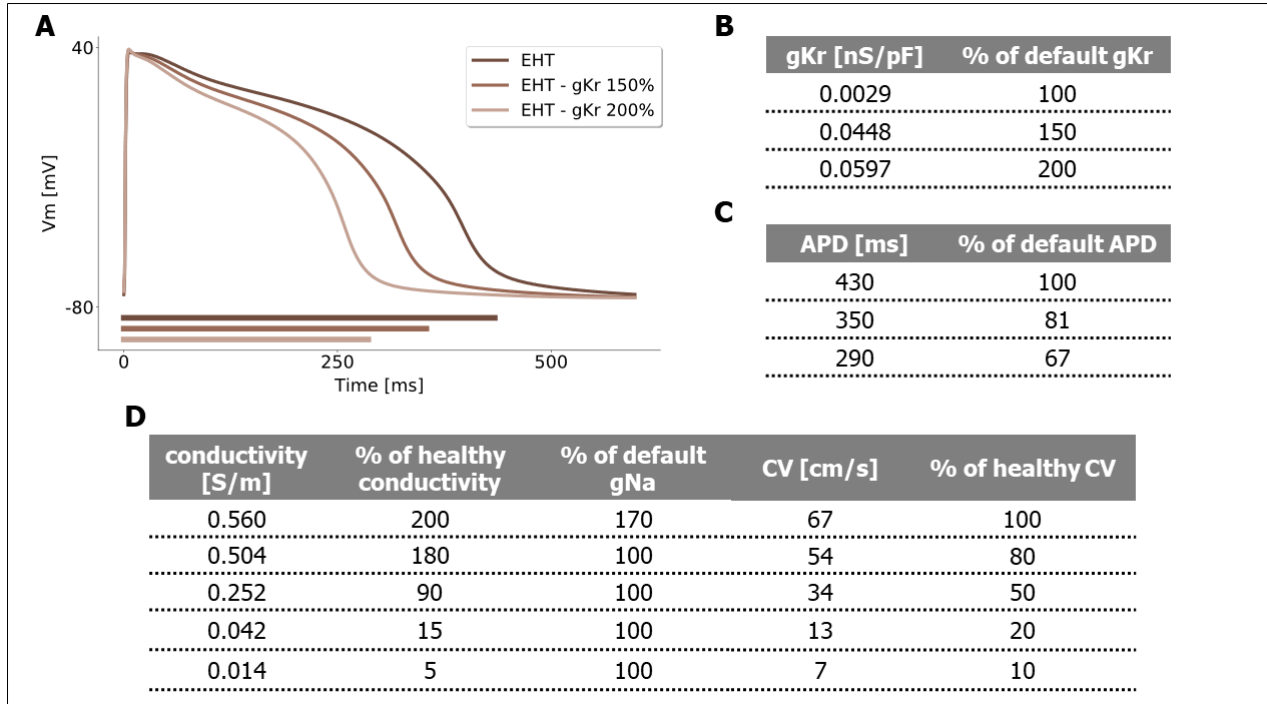


Figure 4.4: Panel A) compares AP traces from the Paci model (used to model the EHT patch) for different values of gKr conductance (reported in table B). Horizontal lines in panel A) correspond to the APD90 of each trace, whose values are reported in table C). Table D) displays the conductivity values (of the bidomain model) and the gNa conductance (relative to the default value in the Paci model) used to achieve the desired CV values in the EHT patch.

### 4.2.3 Electrical propagation in ventricular models before and after EHT patch engraftment

Electrical propagation was initiated in all the left ventricle models by applying an apical epicardial stimulus. We first created reference simulations by pacing the ventricle in the absence of the patch. We tested the impact of programmed electrical stimulation in both ventricles using an S1S2 protocol with an initialising S1 interval of 1000 ms and a S2 coupling interval of 420 ms. We simulated electrical activity for 5000 ms following the stimulation protocol, in the absence of the patch. The 420 ms interval was chosen as the smallest interval that avoided

refractoriness at the pacing site. For comparison with the control cases, we then repeated the same pacing protocol on each of the 15 models with the [EHT](#) patch (see section 4.2.2), to test how the different [EHT](#) patches parameters affected the presence of any sustained or non-sustained [VT](#).

#### 4.2.4 EHT patches and focal arrhythmia

Ectopic impulses represent an important cause of arrhythmia in ischemic cardiomyopathy, both intrinsically and as a trigger for re-entry [\[214\]](#). We hypothesized an [EHT](#) patch electrically coupled to the host myocardium would increase the electrotonic load on the epicardial cells, reducing the likelihood of propagation of an ectopic impulse. To test this hypothesis, we introduced simulations of ectopic impulses into our models. Ectopic impulses may be the result of delayed afterdepolarizations, which result from spurious calcium handling dynamics causing an inward transmembrane current that depolarizes the cell [\[217\]](#). To approximate this effect in our model, we simulated impulses by introducing an inward transmembrane current with varying magnitude and duration. Specifically, we varied the stimulus duration from 0.5 to 8 ms, and the stimulus strength from 10 to 220  $\mu\text{A}/\text{cm}^2$ . The minimum current amplitude necessary for ectopic impulse propagation was calculated for each impulse duration, to obtain the [BZ](#) Rheobase-Chronaxie relation [\[218\]](#), i.e. the relation between stimulus current amplitude and duration, representing a surrogate for the volume of tissue required to generate a propagating impulse. This was repeated for all 15 models (see section 4.2.2). We then compared the Rheobase-Chronaxie relation of each model to assess the impact of the [EHT](#) patch and its characteristics on likelihood of propagation of a focal impulse.

The current was applied in the [BZ](#), in close proximity to the scar, where ectopic impulses are more likely to happen [\[219\]](#). Since the purpose of this investigation was to test whether an ectopic impulse propagated or not, we focused our simulations on the area around the stimulus site, by extracting a cube of 2 cm edge from the original mesh (Figure [4.12](#)).

## 4.3 Results

### 4.3.1 Programmed electrical stimulation in the control meshes

We first applied the stimulation protocol to the two meshes in absence of a patch. In Figure 4.5 snapshots of the electrical propagation in the ventricle with the anatomic isthmus are reported. In this mesh, the pacing protocol resulted in sustained re-entry using the protected channel as the isthmus. The activation wave resulting from the S2 stimulation is blocked at the entrance of the isthmus (Figure 4.5 – ) while simultaneously proceeding around the scar. The excitation wave then enters the isthmus from above (Figure 4.5 – straight white arrows) and is thus able to travel towards the apex, exit the isthmus and excite the whole ventricle again, initiating sustained re-entry (Figure 4.5 – white curved arrows).

In Figure 4.6 snapshots of the electrical propagation following programmed electrical stimulation in the ventricle with the lateral scar are presented. In this model, programmed electrical stimulation with this protocol did not induce re-entry. The lateral scar in the anterior side of the ventricle blocks the electrical wave spreading from the apex. The myocardium above the scar is still excited by the signal propagating through the healthy tissue in the posterior side of the ventricle, but the wave is then terminated by the presence of the scar.

### 4.3.2 EHT patches CV and APD determine anti or pro-arrhythmic behaviour

We applied the same programmed electrical stimulation protocol to the models in the presence of the EHT patches with different CVs and APDs. As expected, increasing the rapid delayed rectifier potassium current ( $I_{Kr}$ ) in the Paci model caused a decrement in the EHT patch APD. The default APD of the Paci model is 430 ms, 120 ms longer than the viable myocardium APD (310 ms, from the Ten Tusscher model). The models with 150% of the default  $I_{Kr}$  exhibited an APD of 350 ms (81% of the reference value), while the models with 200% of the default  $I_{Kr}$  exhibited an APD of 290 ms (67% of the reference value). A comparison of the AP traces and

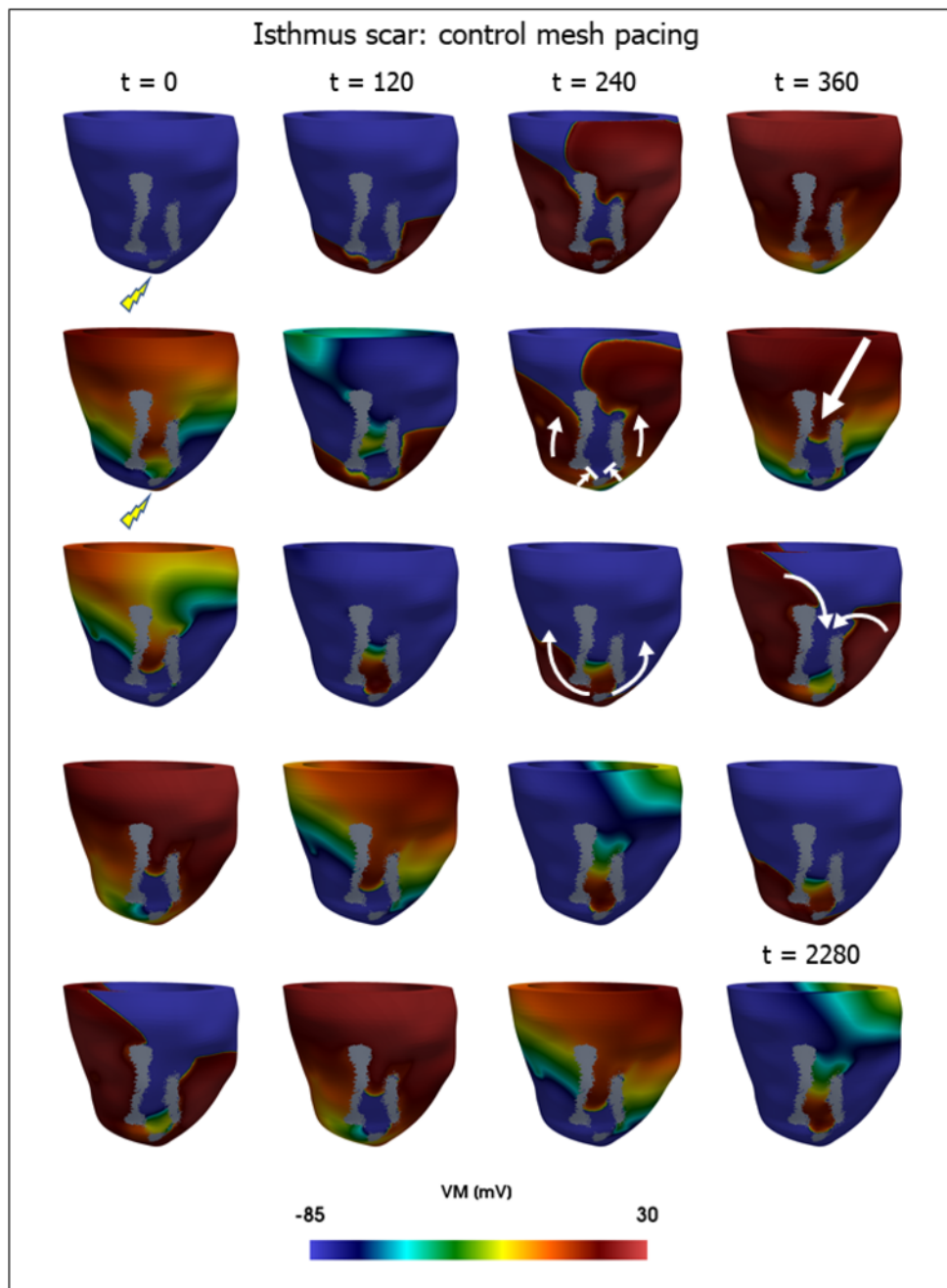


Figure 4.5: Onset of a re-entrant circuit after programmed electrical stimulation in the control mesh with an isthmus scar. Screenshots of the simulated transmembrane voltage ( $V_m$ ) are reported every 120 ms. The lighting symbols indicate ventricle pacing. The white arrows show the direction of the wavefront propagation. Arrows pointing to a line (second row) indicate the conduction block at the isthmus entrance.

respective [APD](#) values are displayed in [Figure 4.4](#).

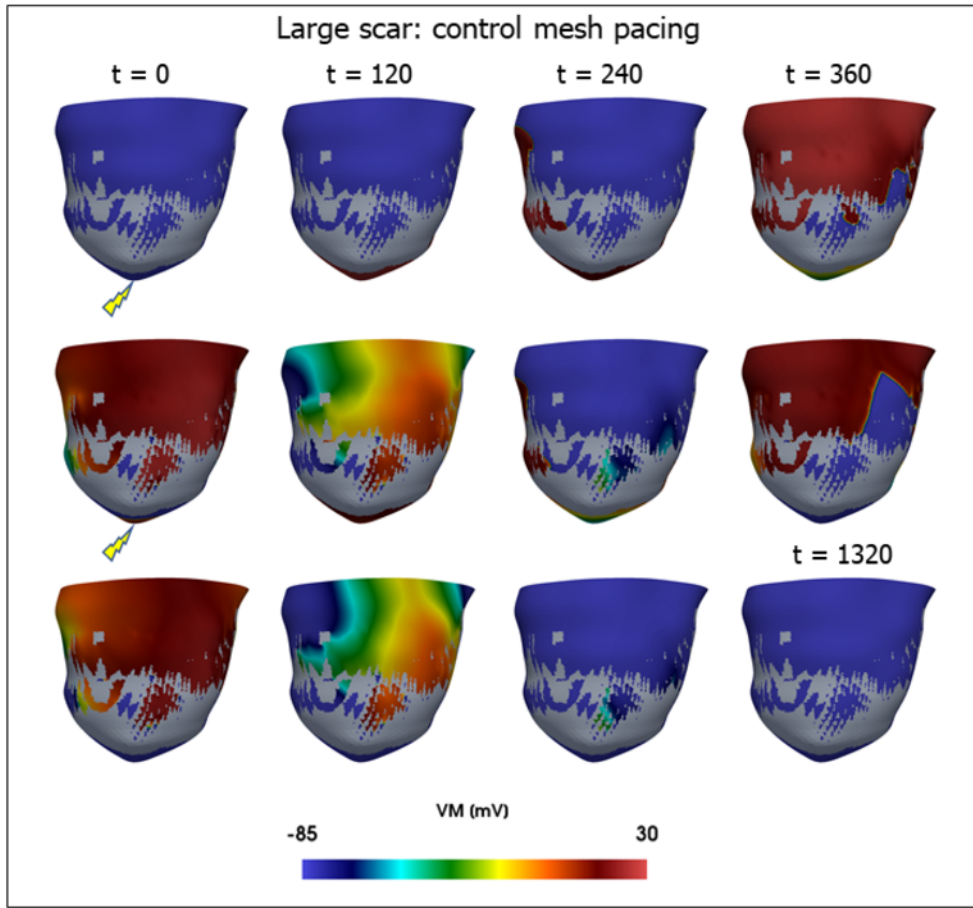


Figure 4.6: Programmed electrical stimulation in the ventricle mesh with large lateral wall scar. Screenshots of the simulated transmembrane voltage ( $V_m$ ) are reported every 120 ms. The lighting symbols indicate ventricle pacing. No non-sustained or sustained re-entry is observed.

### EHT patch can prevent sustained re-entry in model with apparent isthmus

In the isthmus mesh, which demonstrated sustained re-entry in the control case (Figure 4.5), we observed that the application of the EHT patch prevented the induction of re-entry in 8 out of 15 models (Figure 4.7). As evident from Figure 4.5, the re-entrant wave is dependent on propagation through an anatomically protected corridor of excitable myocardium. The EHT propagates the impulse across the entrance to the isthmus, preventing the development of unidirectional conduction block, and thereby removing a required condition for the initiation of re-entry (screenshots in Figure 4.7, first row). Specifically, no re-entry was observed in the models with an EHT patch with 100% of the healthy CV value, regardless of the patch APD. Similarly, no re-entry was observed when the EHT patch CV was equal to 50 and 80% of the healthy CV value and the EHT APD was 81% and 67% of the reference hiPSC-CMs

value. Figure 4.7 shows that as CV in the EHT decreases, the chance of re-entry increase. Specifically, re-entry was induced following programmed electrical stimulation when EHT CV was 10% of physiologic values with all EHT APD values. Similarly, longer APDs were more likely to retain the re-entrant mechanism observed in the control case. The EHT patch exerts its effect on the inducibility of sustained re-entry through differences in the likelihood of onset of unidirectional conduction block. With appropriate CV and APD values, the chance of development of unidirectional conduction block is reduced, with a concomitant reduction in the chance of initiation of re-entry, while lower CVs and higher APDs no longer mitigate the risk of unidirectional conduction block. This can be explained by the fact that the default EHT patch APD is similar to the BZ one (430 ms and 420 ms, respectively). Thus, in the presence of the default EHT, the isthmus entrance stays refractory to the second applied stimulus, similarly to the control case. However, when the EHT patch APD is reduced, the APD becomes significantly lower than the BZ APD (290 vs 420 ms). This reduces the refractory period after the first stimulus, and enables the second wavefront, albeit slowed down, to enter the isthmus, meet the wavefront coming from the upper entrance of the isthmus and prevent the onset of the re-entry (screenshots in Figure 4.7, second and third row). In the cases with the lowest EHT patch CV (10-20% of the default myocardial CV), the first wavefront (propagating more slowly) depolarizes the tissue at the entrance of the isthmus closer to the timing of the second stimulus, causing the tissue to be refractory to the second stimulus, despite the reduced APD. The re-entrant mechanism is thus retained (see screenshots in Figure 4.8). For an endocardial view of the electrical propagation across the model shown in Figure 4.7, see Figure 4.9.

### **Presence of functional arrhythmia following patch application in model with large lateral wall scar**

In contrast to the isthmus scar, a decreased APD was more pro-arrhythmic in the large scar case. After applying the EHT patch, healthy areas of myocardium on either side of the scar have a layer of conducting tissue between them. The specific conduction properties of this tissue will determine how it affects wavefront propagation. If the EHT patch CV is 50% or lower than the

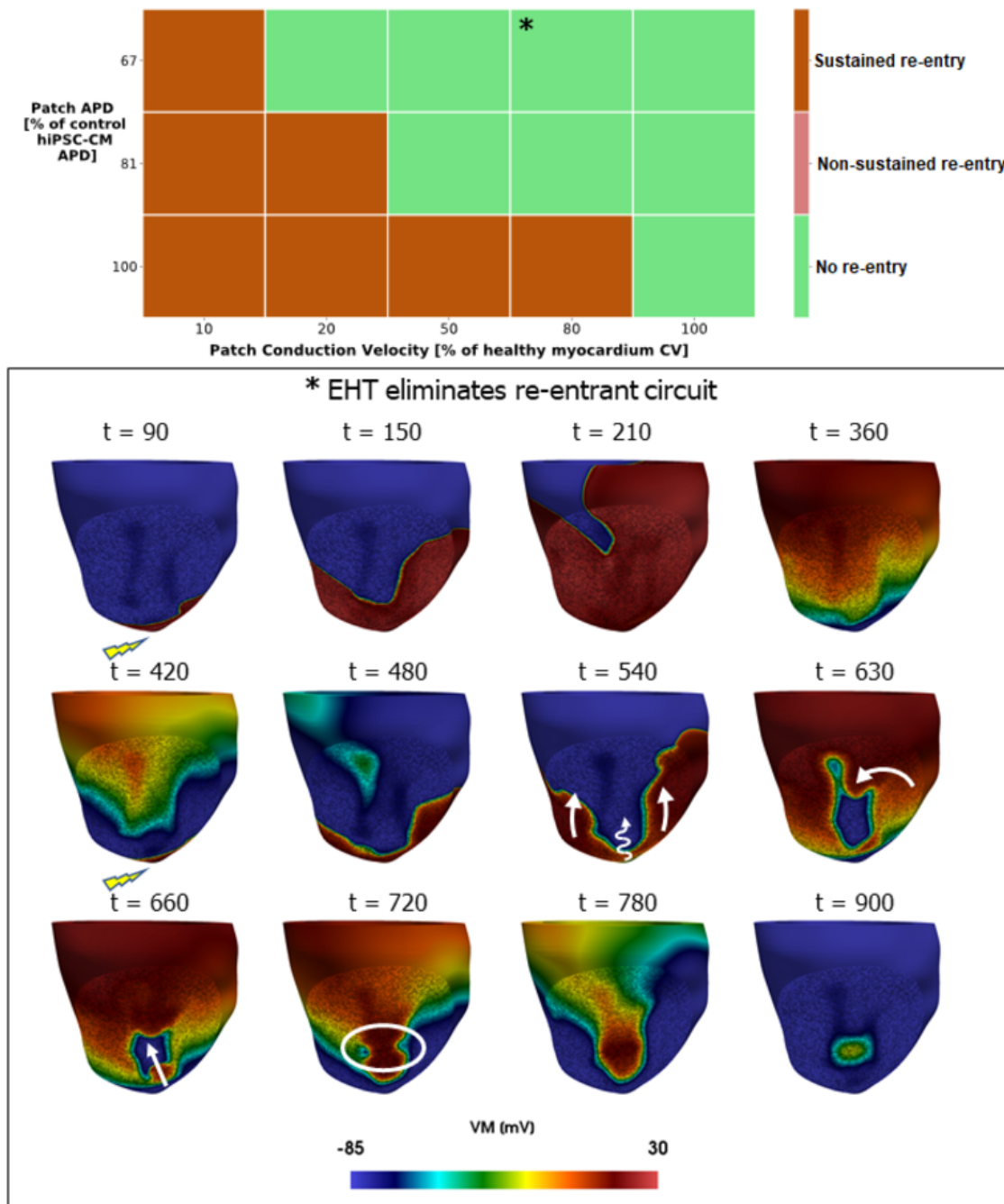


Figure 4.7: Programmed electrical stimulation in the isthmus scar model in the presence of the EHT patch. The table at the top displays which combinations of EHT patch characteristics (CV and APD) succeed in terminating the re-entrant circuit present in the control mesh. Below, an example of how the presence of the EHT patch can prevent the re-entry onset is reported. The second wavefront is slowed ( $t=540$  ms), but not blocked. Thus, it can enter the isthmus ( $t=660$  ms) and meet the wave entering the isthmus from above ( $t=720$  ms), preventing the onset of the re-entry.

healthy myocardium (screenshots in Figure 4.10), the wave will travel in the posterior side of the ventricle first (Figure 4.10 - first two rows - white arrows), as it did in absence of the patch.



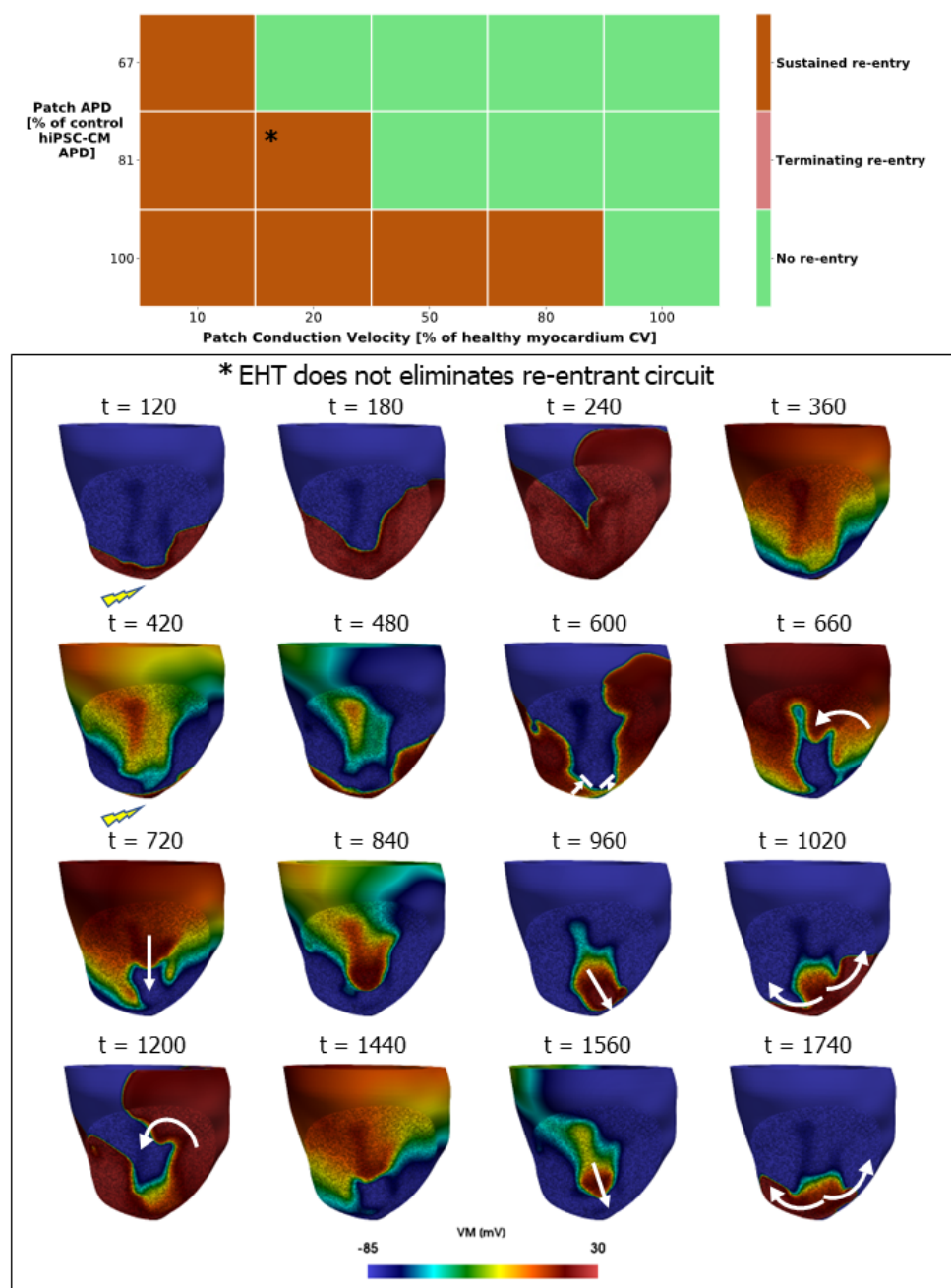


Figure 4.8: Programmed electrical stimulation in the isthmus scar model in the presence of the EHT patch. The table at the top displays which combinations of EHT patch characteristics (CV and APD) succeed in terminating the re-entrant circuit present in the control mesh. Below, an example of how the presence of an EHT patch with long APD typical of hiPSC-CMs does not prevent the onset of the re-entry seen in the control case. The second electrical wave is prevented from entering the isthmus (straight white lines at  $t=480$  ms and  $t=600$  ms) and forced to travel around it ( $t=660$  ms). The wave is then free to travel through the isthmus ( $t=720$  ms), exit the isthmus ( $t=960$  ms) and excite again the whole ventricle ( $t=1020$  ms), maintaining the re-entrant circuit



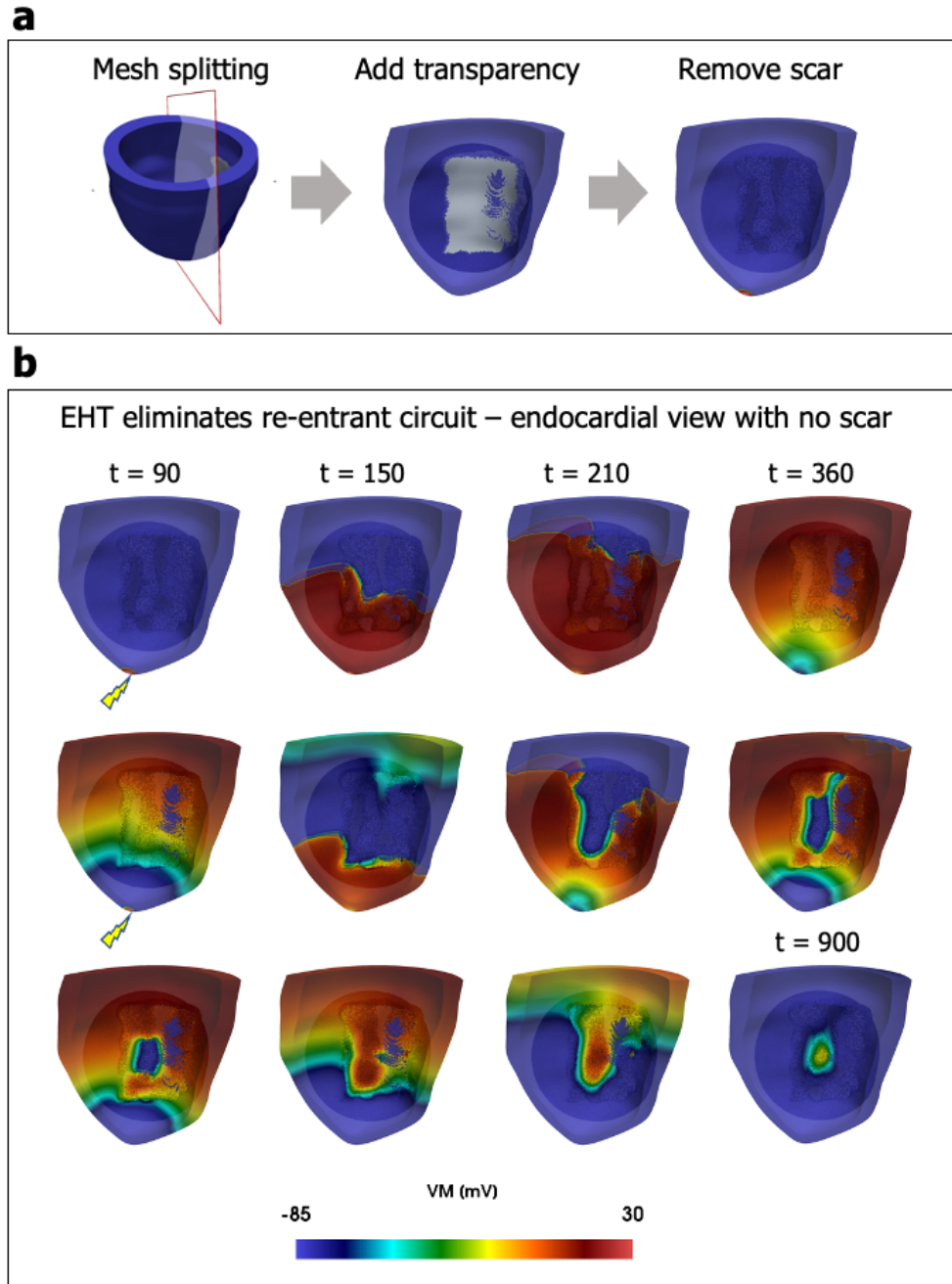


Figure 4.9: Endocardial view of the rapid pacing protocol in the isthmus scar model showed in Fig 6 in the Manuscript. Panel a) shows schematically the steps made to achieve this view, i.e. splitting the mesh along the long axis, adding transparency and removing the scar. Panel b) reports the screenshots at the same time steps showed in Fig 6 in the Manuscript.

In addition, the longer APD in the EHT patch will cause a late repolarization in the areas where the EHT is in contact with the scar (see Figure 4.10 – screenshots in second row, first column and third row, last column) and is less electrotonically coupled to the myocardium with its shorter APD. In the case of large scar, this will result in extensive areas of EHT patch over

scarred myocardium that will still be depolarized, in contact with regions of the patch that are already repolarized, because they are coupled with the viable myocardium that has a shorter APD. These early repolarised regions of the EHT patch can be depolarized again, creating the conditions for the onset of functional re-entry. The beginning of such a functional arrhythmia is indicated in Figure 4.10 with a black arrow. In our model, heterogeneity in the EHT patch electrical properties are responsible for the onset of sustained functional re-entry, in the form of two spiral waves. As can be seen in Figure 4.10, the clockwise rotating spiral wave is slower than the counter-clockwise rotating spiral wave, which spreads faster and it is also subject to breakup. This can be explained by the fact that, the counter-clockwise spiral wave travels through EHT in contact with healthy myocardium. The host myocardium has a lower resting membrane potential than the EHT. Electrotonic coupling will lower the EHT resting membrane potential and reduce the inactivation of sodium channels, causes a larger depolarising current and faster CV. In contrast the clockwise spiral wave travels through EHT in contact with scar, which maintains the EHT resting membrane potential and consequently has a slower CV. In the next stage, the activation then spreads to the rest of the healthy myocardium, making the counter-clockwise spiral wave subject to breakup. In the large scar model, which did not present re-entry in the control case (Figure 4.6), we observed no re-entry when an EHT patch with 80 or 100% of healthy myocardial CV was applied (Figure 4.10). Following engrafting of an EHT patch with 50% CV, non-sustained re-entry was observed when the APD was at the reference values for hiPSC-CMs, while no re-entry was observed when the APD was reduced to 81% and 67% the reference value. Following engraftment of an EHT patch with 20% healthy CV, non-sustained re-entry was observed in all cases, regardless of the patch APD. Finally, following engraftment of an EHT patch with 10% healthy CV, non-sustained re-entry was observed when APD was at the reference value, and sustained functional re-entry (Figure 4.10-screenshots) observed when the APD was reduced to 81 or 67% the reference values. The duration of the simulation was extended to 8000 ms to confirm that in these cases the induced arrhythmias were sustained for this period (i.e. the red squares in Figure 4.10, upper panel). An endocardial view of the electrical propagation across the model in Figure 4.10, is also available in Figure 4.11. Simulations have thus shown that adjusting the EHT patch CV and APD can

increase or decrease the susceptibility to different types of arrhythmias in the large lateral scar model.

### 4.3.3 Engraftment of EHT patches modifies the tissue's Rheobase-Chronaxie relation:

The simulations with varying stimulus duration and current amplitude on the control cube were used to fit a decay exponential curve and thus find the Rheobase-Chronaxie relation for the **BZ** (Figure 4.12), curve in lightest shade of blue). We then tested whether the relation changed after engraftment of **EHT** patches with different **CV** and **APD**. We found that, for the same stimulus duration, a higher stimulus current amplitude was needed to elicit propagation following engraftment of an **EHT** patch, resulting in an up-right shift of the Rheobase-Chronaxie curve (Figure 4.12 – black arrow). This was particularly noticeable when engrafting **EHT** patches with **CV** equal or greater than 50% of the healthy myocardial **CV**. The shift in the Rheobase-Chronaxie relation demonstrates that the coupling of an **EHT** patch with the infarct **BZ** in our model increases the source current required to generate a propagating impulse. This provides support for the hypothesis that the introduction of **EHT** patches with **CV** close to healthy myocardial **CV**, and electrically coupled with the epicardium, might reduce the likelihood of an ectopic impulse propagation.

## 4.4 Discussion

In this study we have used a validated **EHT** model virtually applied to patient-derived human scar models to show that: 1) application of **EHT** patches can reduce the likelihood of initiation of sustained re-entry through reducing the likelihood of development of unidirectional conduction block when applied across the susceptible area. In our model this was achieved by **EHT** patches with **CV** and **APD** values close to host myocardium values; 2) large **EHT** patches with low **CV** and long **APD**, typical of **hiPSC-CMs**, can create a heterogeneous substrate that predisposes the heart to functional re-entry; 3) application of **EHT** patches that are electrically coupled

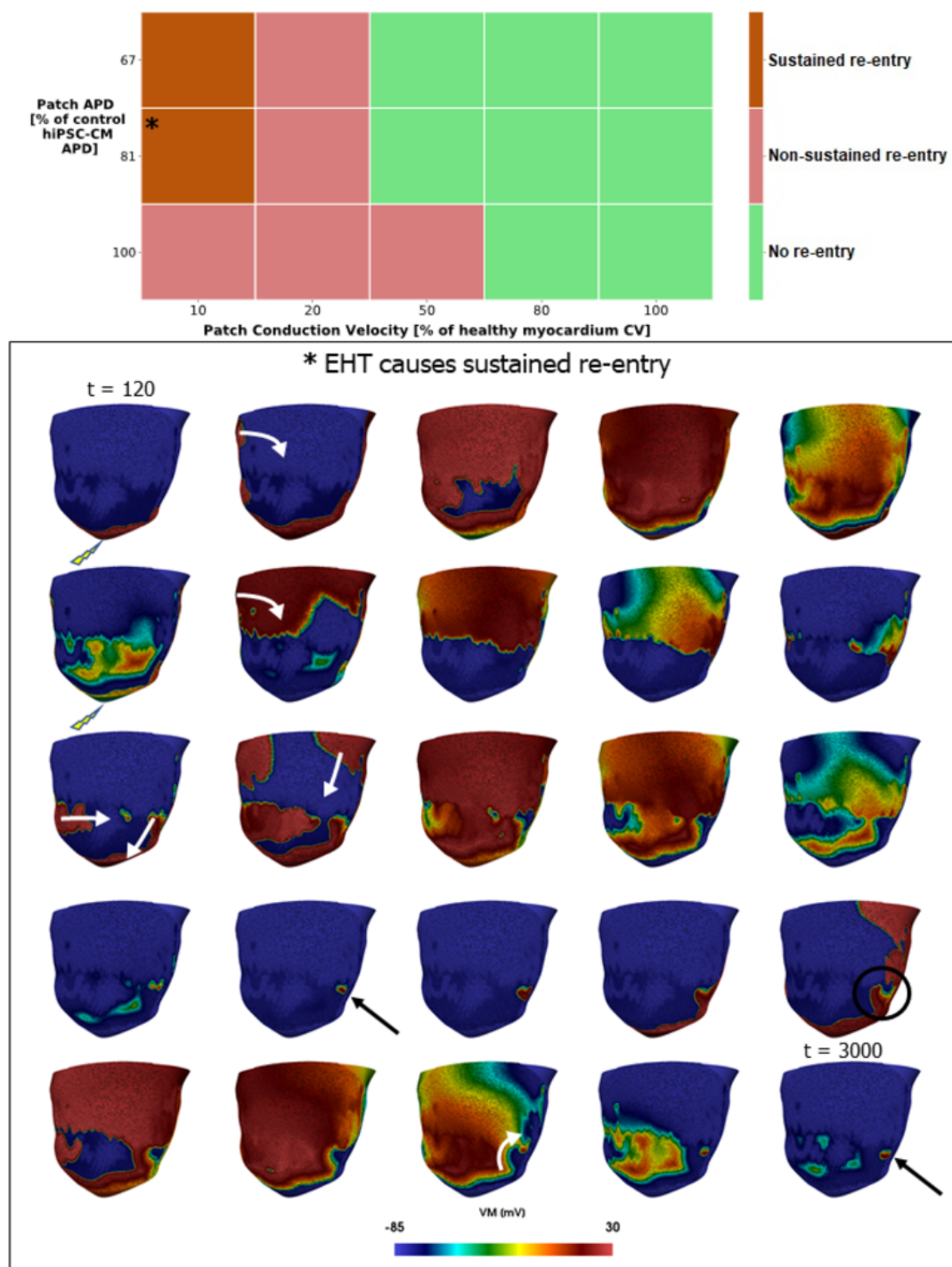


Figure 4.10: Programmed electrical stimulation in the large lateral wall scar model in the presence of the EHT patch. The table at the top displays which combinations of EHT patch characteristics (CV and APD) promotes the onset of non-sustained (light red) or sustained (red) re-entries, which were not present in the control mesh. Below, an example of how the presence of the EHT patch can onset a sustained re-entry is reported. Screenshots of the simulated transmembrane voltage (Vm) are reported every 120 ms.

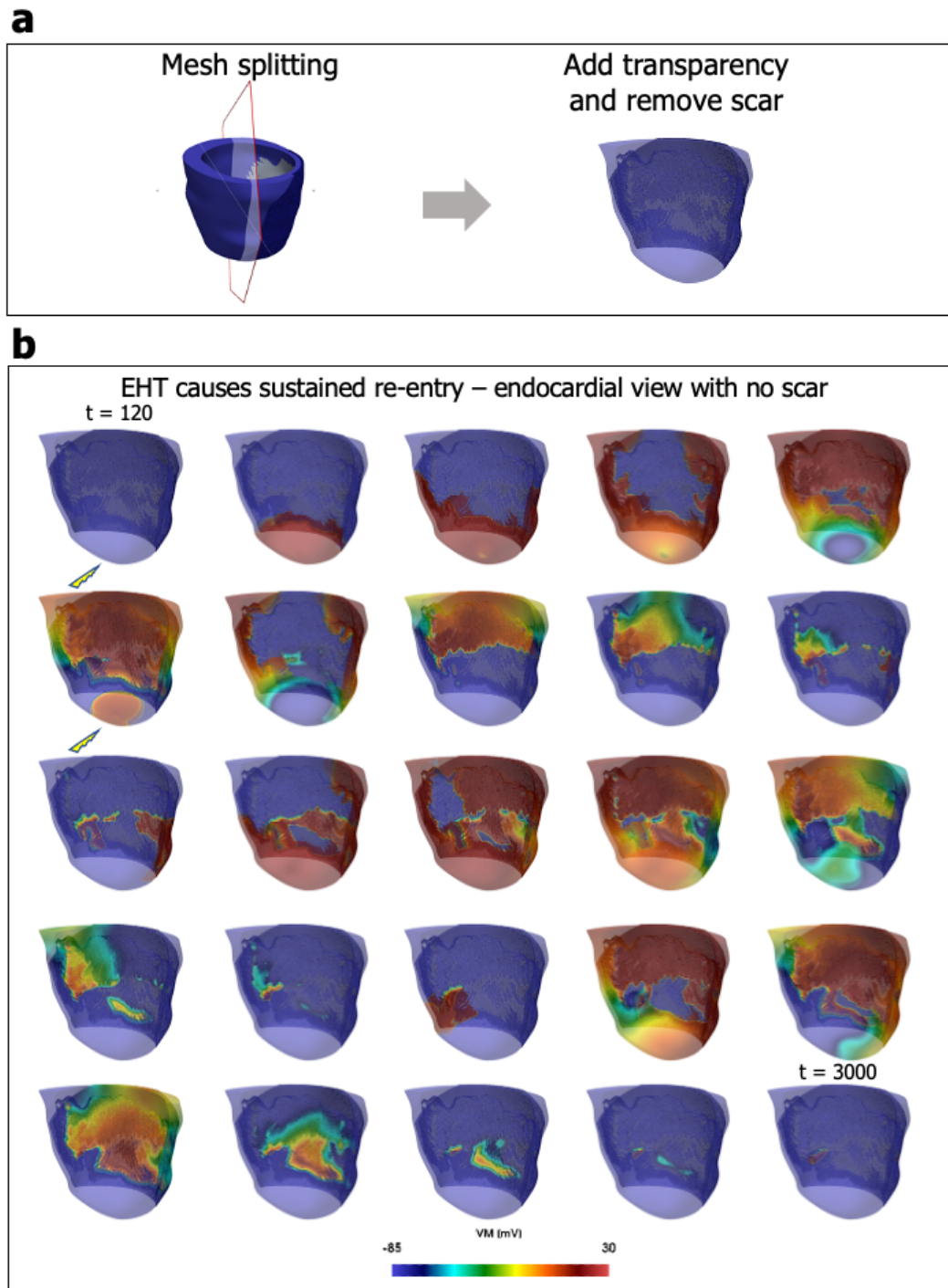


Figure 4.11: Endocardial view of the rapid pacing protocol in the large scar model showed in Fig 7 in the Manuscript. Panel a) shows schematically the steps made to achieve this view, i.e. splitting the mesh along the long axis, adding transparency and removing the scar. Panel b) reports the screenshots at the same time steps showed in Fig 7 in the Manuscript.

with host myocardium can reduce the chance of propagation of a focal impulse through changes in electrotonic loading of BZ tissue.



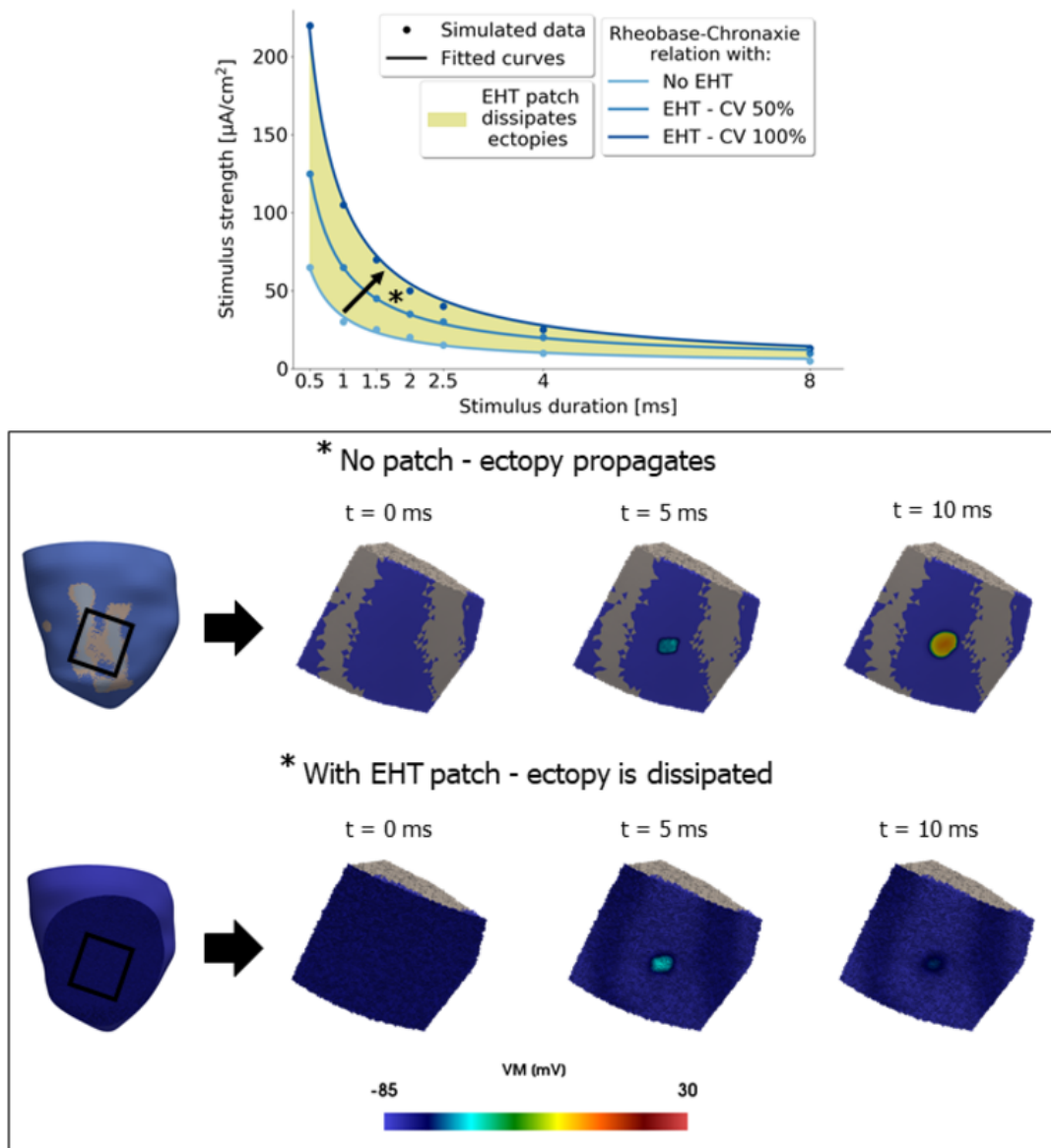


Figure 4.12: The graph on top compares the Rheobase-Chronaxie relations fitted on simulations data from the model without EHT patch and the models with an EHT patch with CV equal to 50 and 100% of the healthy myocardial CV. The top row's screenshots show an ectopic impulse arising and propagating in the cube mesh extracted from the model without EHT. The bottom row's screenshots show an ectopic impulse being dissipated by the presence of an EHT patch with sufficient CV.

#### 4.4.1 EHT patches influence on structural arrhythmias

Our simulations predicted that the engraftment of an [EHT](#) patch can prevent the induction of a sustained re-entry caused by an isthmus-like scar by reducing the likelihood of the development of unidirectional conduction block in a vulnerable isthmus, provided that the long [hiPSC-CMs](#) [APD](#) was reduced towards the [APD](#) of the host myocardium (Figure 4.7). A similar result

was observed experimentally by Li et al [194], whose engraftment of EHT patches on scarred myocardial sheets resulted in the coupling of disconnected cardiac regions and the suppression of re-entrant arrhythmias within the scarred area.

#### 4.4.2 Implications of EHT patch-host myocardium electrical coupling

Our simulations show that, where the EHT patch electrically couples with healthy myocardium, EHT activation and repolarization will be driven by the healthy myocardium. This is particularly noticeable at rest, where the electrotonic load in the EHTs, due to the electrical coupling with the healthy tissue, causes a drop in the hiPSC-CMs resting potential from  $\approx -70$  mV to a level closer to the adult myocardium level ( $\approx -85$  mV). However, this coupling does not occur where the EHT is in contact with the scar, as scar is non-excitabile and non-conductive tissue, and thus the EHT retains its intrinsic electrophysiological properties. The result is that this heterogeneity in the host myocardium tissue in contact with the EHT causes heterogeneity in the electrophysiological properties of the EHT, in turn responsible for the spiral waves observed in the model with the large scar. Experimentally, assessing electrical activity in engraftments has been proven to be a challenging task, particularly to discriminate between EHT, scar and remaining viable myocardium [39]. However, studies that have detected electrical coupling, report observations in line with our findings. Weinberg et al [39] have measured electrical activity in the EHT synchronous with the pacing cycle length imposed on the myocardium, suggesting that, following successful application and electrical coupling, host, healthy, myocardium can drive the EHT activation. More importantly, Shiba et al [204] identified differences in activity between EHT patches engrafted on intact myocardium and on scarred tissue, being the first faster and more uniform, and the second slower and more chaotic. This result seems consistent with the presence of scar contributing to the formation of heterogeneities in the EHT electrophysiology.

### 4.4.3 Heterogeneity in the EHT patch following electrical coupling can promote both sustained and non-sustained functional arrhythmias

In addition to reducing the propensity to the induction of anatomic isthmus-mediated re-entry, our simulations predicted that EHT patches can predispose to the initiation of functional re-entries (Figure 4.10). In the patient model with a large lateral wall scar we did not observe re-entry in the control simulations (Figure 4.6). However, the engraftment of the EHT patch, which couples with the viable tissue but not the scar, introduces extensive areas of heterogeneity in the EHT, which is well recognized as a risk factor for arrhythmia. Interestingly, despite all cases of EHT patch with CV lower than 50% healthy myocardial CV exhibiting re-entry, re-entry was only sustained in the cases with lowest EHT CV and shortest APD. This observation could reflect differences in the wavelength of the re-entrant waves. The wavelength measures the spatial extension of a propagating wave [220], i.e. of all the depolarized cells, and it is computed as the product of refractory period (or APD) and CV. The models displaying sustained, functional re-entry, are the ones with lowest CV and shortest APD, and thus the ones with the smallest wavelength. A decrement in wavelength is associated with enhanced re-entry sustenance, as the re-entrant wave is less likely to collide with its tail of refractoriness and extinguish itself [221].

Transplantation of either cells or patches resulting in isolated cardiomyocyte that are separated from the host myocardium have been reported experimentally and identified as possible anatomical pathways for re-entry mechanisms [39, 193, 204]. Yamazaki et al [222] observed initiation of both VT and VF due to islands of enhanced refractoriness and APD dispersion, showing *in vitro* a similar mechanism to the one we report in our study. Bursac et al [114] found spiral waves in EHT patches even pre-engraftment, due to anatomic heterogeneities. The hazards of introducing heterogeneities are well known, yet experiments on small animals have so far not linked EHT application with increased arrhythmic risk [193, 122, 37, 199]. However, our simulations on human heart failure ventricles show that these heterogeneities can be responsible for the onset of life-threatening, sustained arrhythmias, suggesting that the impact



of heterogeneities in small animals in experiments might have been underestimated, possibly due to the smaller heart volume [193].

#### 4.4.4 EHT patches influence on focal impulse propagation

Our models indicated that application of electrically coupled patches with CV 50% or greater than viable myocardium reduced the chance of ectopic impulse propagation. Ectopic impulse propagation is inhibited because of the increased electrotonic load in the host tissue, resulting in an increase in the source current required to depolarize the adjacent coupled tissue. Ectopic impulses can be caused by spurious calcium handling dynamics which in turn causes a transmembrane current that depolarizes the cell. In the absence of the patch, the spurious current is enough to depolarize a group of cells above threshold and thus trigger an AP (Figure 4.12 – first row of screenshots). In the presence of the patch, the cells that were previously depolarized are now electrically coupled with EHT patch CMs, which increase the electrotonic sink. Some of the spurious current is now distributed to the EHT patch CMs (Figure 4.12 – second row of screenshots), but since the same current is distributed across a larger volume of tissue, the change in transmembrane voltage in each cell is lower, such that none of the cells now reach threshold to trigger an AP. Hence, no AP is triggered and the ectopic impulse does not propagate. In these simulations, patches with 20 or 10% viable myocardium CV were predicted to have a limited impact on likelihood of ectopic impulse propagation. An EHT patch with low CV might have less (and less organized) gap junctions [223], leading to a less efficient electrical coupling and ultimately to a lower electrotonic load applied to the host myocardium [163]. For this reason, the EHT patch might not dissipate enough current to avoid the triggering of AP and the consequent propagation of the ectopic impulse.

Ectopic impulses have been observed both experimentally [224] and in simulations [225, 143] around infarcted regions. In addition, ectopic impulses were reported consistently after intramural injection of hiPSC-CMs [202]. Experimental data collected after EHT patch engraftment report both absence [193, 37, 199] and presence [122, 200] of ventricular ectopies. However, in the two studies reporting ventricular ectopies, it was not clear whether the ectopic activation

was generating from the remodelled tissue around the infarct or from the patch itself, due to the hiPSC-CMs automaticity. Liu et al [200] study was conducted on macaques, which have a lower heart than other small mammals. A heart rate lower than the intrinsic hiPSC-CMs activation rate could render the recipient heart vulnerable to ectopic activation from the engrafted EHT patch [216]. The absence of ectopies generated from the remodelled tissue are in accordance with the mechanism unveiled by our simulations, suggesting that EHT patches application might help decrease the incidence of ectopic beats related to the ischemic tissue. However, the possibility of ectopies deriving from hiPSC-CMs intrinsic automaticity should still be considered.

## 4.5 Limitations

Our models included detailed scar and BZ morphology, as well as structural and ionic remodelling typical of scar and BZ (see Methods). However, the myocardium not affected by ischemia was modelled as healthy tissue. This will not represent the heart failure phenotype, in which the non-ischemic tissue can also undergo electrophysiological remodelling [226]. However, while the quantitative CV and APD values may change, the observed mechanisms of sustained and terminating VT with an EHT patch, are still plausible with a heart failure phenotype.

In our simulations we assume that the EHT is electrically connected to the host tissue. While electrical coupling has been observed experimentally [193, 122, 37, 199, 200, 204], a full patch-host electrical integration in an experimental set up might be prevented due to incomplete adhesion or presence of a fibrotic layer between patch and host tissue [39, 124]. If the patch remains electrically uncoupled from the host myocardium, its direct impact on arrhythmogenesis will be limited.

We modeled the EHT as a homogenous syncytium. However, it is likely that EHTs contain stem-cell-derived cardiomyocytes exhibiting three phenotypes: atrial-like, ventricular-like, and nodal-like [183]. We have not represented these distinct cell types explicitly and have assumed a single homogenized representation for the EHT. The need to explicitly represent different cell

types depends on their relative number and their spatial organization. This is likely to depend on the [EHT](#) manufacturing process and could be modeled using the partitioned phenotypes or homogenized phenotype models for simulating electrical activation in tissue consisting of multiple cell types [184].

In this study we have used the epicardial version of the Ten tusscher ionic cell model to simulate the cell-level electrophysiology of the ventricular myocardium. However, it is known that transmural repolarization gradients are present in animal's ventricles, namely, longer [APD](#) is reported in the endocardium with respect to the epicardium. Since repolarization times are strictly linked with refractoriness, changes in this property may impact our results. However, we are simulating the effect of an epicardial [EHT](#) patch, which, by definition, predominantly impacts the epicardium. Since we used the epicardial version of the Ten tusscher cell model, our simulations capture the correct local tissue electrophysiology. We also showed in previous studies (Chapter 3 or [216]) that ventricular transmural heterogeneity had a limited impact on activation patterns and local repolarisation gradients near the patch in a simplified ventricular wall model.

Specific values derived from these models are not generalizable beyond the specific anatomic and functional configurations assessed, however the results do indicate some generalizable observations about potentially important mechanisms by which [EHT](#) patch engraftment will affect predisposition to arrhythmia.

Finally, our models do not capture paracrine and autocrine effects, which have been linked with angiogenesis and improved cardiac function observed *ex-vivo* in infarcted hearts after [EHT](#) patches application [196, 198, 199].

## 4.6 Conclusions

We have shown that appropriately located [EHT](#) patches can reduce the predisposition to anatomical isthmus mediated re-entry in a model of ischemic cardiomyopathy, through a reduction in the likelihood of development of unidirectional conduction block. In these models,

EHT patches with a physiological APD and higher CV were most effective in reducing this risk. We have also demonstrated that EHT patches with CV and APD typical of hiPSC-CMs were associated with the onset of sustained functional re-entry in an ischemic cardiomyopathy model with a large transmural scar. Finally, we have demonstrated EHT patches electrically coupled to host myocardium reduce the likelihood of propagation of focal ectopic impulses, an effect that was most evident with higher CV within the patch. These results indicate that engrafting immature EHT patches and specifically those with lower CV than the host myocardium, may have little impact on anatomically defined and promote functional re-entry. hiPSC-CMs maturation may be important to minimize the arrhythmic risk when transplanting EHT patches in human ischemic hearts.

# Chapter 5

## Discussion

### 5.1 Simplified model Vs anatomically-detailed model: findings comparison

#### 5.1.1 Summary of studies findings

In Chapter 3 and 4 we presented the creation and application of computational cardiac models to study pre-clinical and clinical [EHT](#) grafts.

In our first study (Chapter 3) we used a simple model with an idealized geometry and we found that the [EHT](#) patch had an effect on electrical propagation only when the scar was both transmural and non-conductive. Moreover, we found that [EHT](#) patches design variables were not species-dependent and that it is possible to recover physiological activation times by tuning the [EHT](#) conductivity. Our simulations finally predicted that a large increment in [EHT](#) conductivity might be pro-arrhythmic and that altering other immature features of [hiPSC-CMs](#) may recover physiological activation while not increasing the risk of arrhythmia.

In the second study (Chapter 4), we moved from an idealized geometry to a realistic one, by simulating electrical propagation in left ventricle models obtained from magnetic resonance images from patients with ischemic cardiomyopathy. Our simulations showed that [EHT](#) patches with

physiological APD and higher CV can reduce the occurrence of anatomical isthmus mediated re-entries, by preventing conduction block at the isthmus entrance. We also showed that EHT patches with CV and APD typical of hiPSC-CMs can onset functional re-entry in an a model with a large transmural scar. Finally, we demonstrated that EHT patches electrically coupled with the host myocardium reduce the likelihood of propagation of focal ectopic impulses.

### 5.1.2 Surviving tissue limits the influence of EHT patches on electrical propagation

In the simplified model used in the first study, we modelled the scar with varying transmurality and conductivity, and found that the EHT patch had an effect on electrical propagation only when the scar was both transmural and non-conductive. This was confirmed both by the sensitivity indices from the GSA (Figure 3.11) and from the propagation paths examination (Figure 3.12). In our model, this is explained by the fact that the stimulus (in most cases) propagates more quickly in the myocardium, thus the top right corner of the slab is excited by an electrical wave coming from the myocardium, despite the stimulus also travelling through the EHT. This is due to the EHT's lower CV, with respect to the healthy tissue, and the need for the activation wave to move up into the EHT patch and down into the viable tissue. Thus, when the scar is not transmural and some viable tissue is still present, our model predicts the viable tissue to have a primary role in propagation. A similar phenomenon can be observed in the models with more realistic geometries used in our second study. The layer of hiPSC-CMs we designed as an EHT patch was placed over the scar, based on where the scar was visible from the epicardium, as it is commonly done in wet lab experiments. However, being as the EHT patch was modelled as circle-shaped and the scar irregularly shaped, part of the EHT patch was in direct contact with healthy tissue, as well as BZ and scar tissue. Focusing on the areas where the patch is in contact with healthy tissue, it is possible to notice that the activation is always driven by the healthy tissue, with the activation in the EHT patch "trailing", i.e. the EHT activates in response to the activation of the healthy tissue underneath, thus never guiding the electrical propagation. Hence, activation not being influenced by the EHT when

viable tissue is present underneath is a feature that is retained when going from a geometrically simple model to one with a realistic geometry.

### 5.1.3 Anatomically-detailed model provides mechanistic explanation for arrhythmic behaviour

The simple model also predicted that design variables are not species-dependent. Using different ionic cell models we represented rat, rabbit and human myocardium, and we varied the geometrical dimensions of the slab to mimic the myocardial wall thickness of each of the 3 species. By comparing the electrical propagation paths (Figure 3.11) and the sensitivity indices from the GSA (Figure 3.12), we observed that the influence of the EHT patch on the electrical propagation was similar regardless of the species. In other words, differences at a cellular level did not seem to influence the effects of the patch on the tissue-level propagation. This finding is encouraging, as it supports the translatability in humans of results from animal experiments. Many experiments on small mammals did not link EHT patches with an increment in arrhythmia incidence [193, 122, 37, 199, 200]. However, when moving to a more complex and close to reality geometry, our simulations found that EHT patches can be responsible for the initiation of focal re-entrant arrhythmias (Figure 4.10). It thus appears that translatability in humans of the results regarding arrhythmic risk may depend on the scar complexity, but not on the specific cellular physiology. As suggested in the literature [193, 227], experiments in small mammals are likely to underestimate the arrhythmic risk, due to the smaller dimensions of rat and rabbit's hearts with respect to human's. This is due to the fact that hearts of greater dimension offer more area for re-entrant patterns to arise [193]. Our simulations showed that, in our models, the creation of an arrhythmogenic substrate after attachment of an EHT patch was due to the heterogeneity of the scar translating in heterogeneity in the EHT patch. The immature phenotype typical of hiPSC-CMs causes them to have a higher resting membrane potential with respect to adult CMs [67, 68, 69]. Thus, the EHT patch will have a higher resting membrane potential compared to the host myocardium. When coupling with healthy tissue, the EHT patch high resting membrane potential is lowered by the electrotonic load exerted

on the patch from the healthy tissue. This lowers the inactivation of the sodium channels, causing in turn a larger depolarising current and a larger CV when the EHT over viable host myocardium is activated. However, this does not happen where the EHT patch is in contact with the scar tissue. The scar is non-conducting, and thus acts as an insulator, not causing any electrotonic load on the patch. The EHT patch hence retains the immature phenotype and its features, notably the lower CV. Under this conditions, the EHT patch represents a heterogeneous substrate for the electrical wave to propagate through, and heterogeneities in the propagation substrate are known to be pro-arrhythmic [228].

This mechanism had not been initially uncovered when using the simpler model (Chapter 3). When using the simple model we quantified the repolarisation gradient on the host tissue at the patch-tissue interface. While focusing on the electrotonic load that the EHT patch exerts on the host tissue enabled us to find an increment in repolarization gradients in the host tissue, the models based on real geometries revealed that it is actually the electrotonic load that the host tissue exerts on the EHT patch (or the lack of it from the scar tissue) that causes the most evident arrhythmia-related issues.

#### 5.1.4 EHT-related focal ectopies caused by hiPSC-CMs automaticity

In the first study (Chapter 3) we recovered the estimated physiological activation time by increasing the sodium channel density of the EHT patch instead of the gap junctions conductivity, to avoid increasing the electrotonic load and thus the repolarisation gradient (see section 3.4.4). We used this finding in our second study, while tuning the EHT patch CV. To find the parameters combinations needed to create models of EHT patches with different CV, we simulated electrical propagation on a tissue slab, using the ionic model for hiPSC-CMs [96] utilized in the EHT patches. We performed a grid search on two parameters, gap junctions conductivity and sodium channels density. We investigated CV for every simulation by collecting the activation times at a fixed distances, and we kept the combinations of sodium channels density and gap junctions conductivity which enabled us to match our target CV values (10, 20, 50, 80 and



100% of healthy myocardial CV values, i.e. 67 cm/s).

In the first study, we had noticed how increasing the sodium channels density caused a shortening in the hiPSC-CMs intrinsic cycle length and resulted in ectopic beats fired from the EHT patch (see section 3.3.4), when the model was paced at 1 Hz frequency. Despite increasing the sodium channels density, we did not incur ectopic beats fired from the EHT in the second study, because the models were stimulated with a higher frequency pacing protocol (2.4 Hz), thus overriding the hiPSC-CMs self-pacing frequency. However, the simulations where no re-entry was observed (green squares in Figure 4.7) run all the same until 5000 ms of simulation time, and no ectopy generated from spontaneous beating of the EHT patch was observed. This suggests that the myocardium could act as a strong electrotonic sink to suppress the hiPSC-CMs intrinsic automaticity.

### 5.1.5 Tuning the EHT inward rectifying potassium current

In the first study we increased the inward rectifier potassium channels density to bring back the hiPSC-CMs intrinsic cycle length to values below 1 Hz (see section 3.3.4). This was not needed in the second study, in such the maximum sodium channel density multiplier used in the second study was 2, while being 4 in the first study (because the gap junctions conductivity value was not increased together with the sodium channels density, as it was in the second study). Consequently, the shortening in the hiPSC-CMs intrinsic cycle length was less pronounced in the second study, and an increment of the inward rectifier potassium channels density was not needed.

However, by looking at the electrical propagation in the isthmus mesh of Chapter 4 when the EHT patch CV was equal to the myocardial CV (Figure 5.1), we can see that the electrical wave deriving from the first apical stimulation propagates in the patch with uniform velocity, while the electrical wave from the second stimulation slows down in correspondence of the patch areas in contact with the scar. This happens despite the EHT patch also having APD smaller than the host myocardium's (290 ms vs 310 ms).

Tuning **CV** of the **EHT** patch was performed with one stimulation, so slowing of **CV** in a rapid pacing protocol was not taken into account in the initial process of **CV** tuning. The **CV** slowing during the second propagation may be related to the **hiPSC-CMs** high resting membrane potential, hence increasing the inward rectifier potassium current might restore uniform velocity through the **EHT** for all the electrical waves elicited by the rapid pacing protocol, thus improving the **EHT** patch performance.

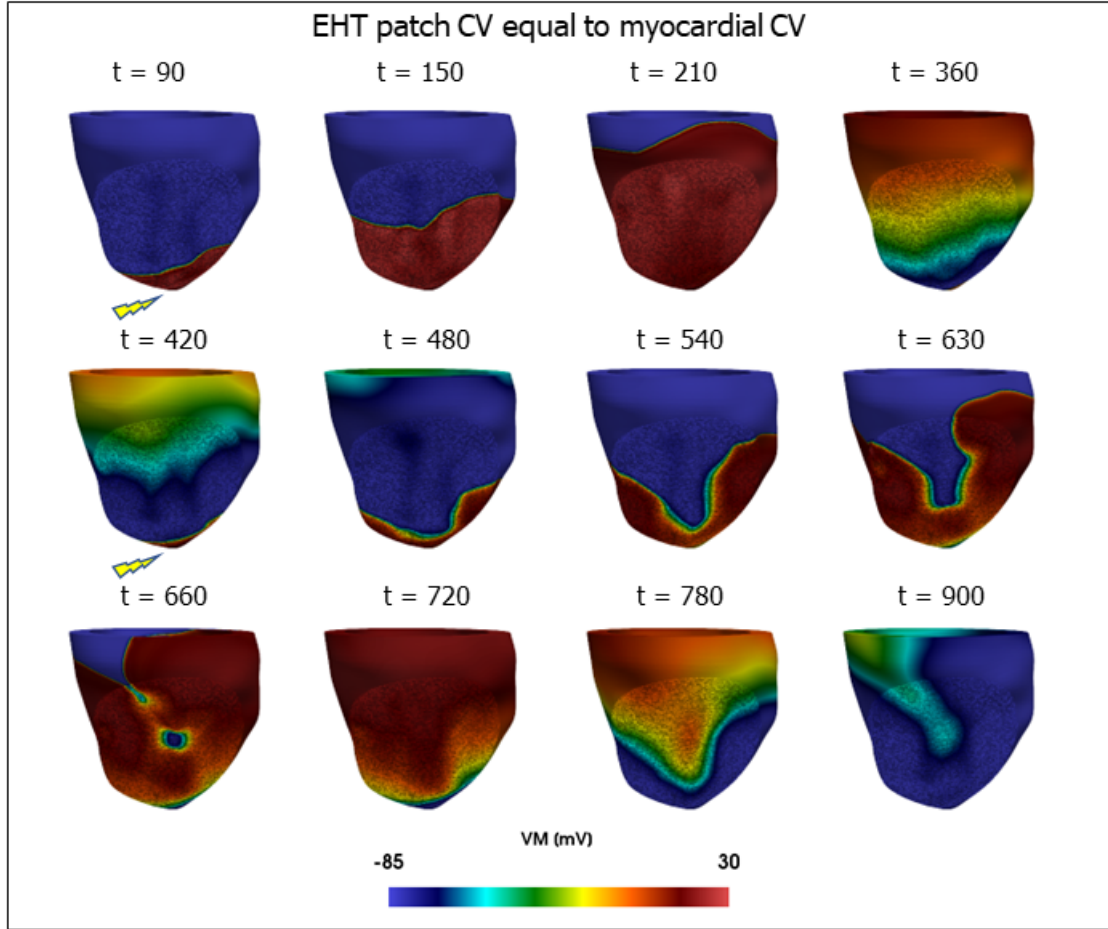


Figure 5.1: Programmed electrical stimulation in the isthmus scar model with an EHT patch with 100% of the healthy CV value and 67% of the the reference hiPSC-CMs APD value.

### 5.1.6 Design of engineered heart tissue patches: final remarks

Our simulation studies point towards **hiPSC-CMs** maturity as paramount for limiting **EHT** patches arrhythmic risk. Specifically, by leveraging the flexibility of computational models, we

were able to identify specific features that should be taken into account when designing EHT patches. While the EHT CV should be as close as possible to the host myocardium's CV, our model showed that obtaining so by exclusively augmenting gap junctions density in the EHT does not constitute a safe approach, in such it promotes an increment in repolarisation gradients in the host tissue. Our simulations instead predict that addressing the lack of hiPSC-CMs fast sodium current (i.e. tackling the hiPSC-CMs slow AP upstroke) represents a safer way to increase CV in EHT constructs. Another known immature feature of hiPSC-CMs is the lack/underexpression of inward rectifying potassium current [180]. While the main concern regarding the lack of inward rectifying potassium current is linked to hiPSC-CMs automaticity, our simulations found that the hiPSC-CMs automaticity is likely to be overridden by the physiological activation frequency, and that the hiPSC-CMs automaticity might be suppressed by the electrotonic load exerted from the host myocardium on the EHT patch. Nevertheless, we found that ensuring the presence of an adult-like inward rectifying potassium current in the EHT patch could help lowering the high resting membrane potential typical of the hiPSC-CMs, in turn reducing the inactivation of sodium channels and ultimately resulting in a larger EHT CV.

CPs have been recently used as biomaterials to create cardiac patches [53, 229]. In our first study (Chapter 3) we simulated the presence of a layer of CP, paired with a layer of EHT derived from hiPSC-CMs. The results of the GSA in our model did not indicate the CP's properties (i.e. conductivity and thickness) as significant in increasing the EHT CV. For this reason, we did not include the CP in the *in silico* EHT application in Chapter 4.

The exact interaction at the myocardium-CP interface still needs to be elucidated [181]. However, the capability to transport ions is believed to be crucial in CPs for cardiac applications (see Figure 1 in [181]). The actual mode of conductivity and interfacial charging is known to differently affect biological processes [230]. Langer et al [231] found that stimulation through a CP using electronic conductivity, or just the presence of the electric field, did not elicit a cellular response, while a quantifiable cellular response could be obtained only using polypyrrole, a mixed (ions and electrons) conductor. Our model is partially able to replicate this effect, in such the presence of the CP around the tissue increases the extracellular conductivity for

the tissue at the interface, supplying the current (i.e. the moving ions) with a low-resistance pathway to flow in. However, modelling techniques more specific to the field of material engineering, such as density functional theory [232], could be used to model charges movement and investigate how ions involved in the cardiac AP can interact with the CP surface.

While CP constructs have been extensively investigated *in vitro*, there are still some challenges hampering the application of CP constructs *in vivo*, such as the conductivity decrement in physiological environment and the possible immune reaction or chronic inflammatory responses [233]. A complete understanding of the long-term toxicity of CPs *in vivo* and their interaction with the immune system constitutes a requirement towards the CPs becoming a standard therapy alongside EHTs in cardiac tissue engineering.

## 5.2 Machine learning and emulators in cardiac computational modelling

In the study presented in Chapter 3, we opted for a computationally friendly model, with an idealized geometry (see Figure 3.1). Despite the relative simplicity of the model, when it came to perform sensitivity analysis, tens of thousands of model runs were required, rendering the problem intractable.

The computational burden of tissue and organ level models of cardiac electrophysiology is well known [234]. The recent surge of patient-specific modelling, and the attempt to bring personalized models into the clinic, has driven the development of scalable code to handle organ-scale simulations [84]. However, when such complex models must be solved multiple times, they become quickly unaffordable [235]. Complex models need to be solved multiple times in a variety of situations, specifically when facing tasks as sensitivity analysis and uncertainty quantification. In these cases, surrogate models are leveraged to achieve computational feasibility.

### 5.2.1 Gaussian processes as cardiac models emulators

Different kinds of surrogate models (or *emulators*) are available, such as lower-fidelity models, which consist in introducing modelling simplifications, reduced order models and emulators obtained via [GPs](#) regression. In this work, we used GP-based emulators to replace the computationally expensive model, enabling us to rapidly predict the model's output and thus perform the [GSA](#). In the past years, GP-based emulators have been used to perform models parameters constraining via Bayesian History Matching in an array of different applications, such as in models of galaxy formation [\[236\]](#) and infectious disease modelling [\[237\]](#). More recently, GP emulators have been used as a surrogate of cardiac models. Coveney et al [\[238\]](#) used emulators to fit models of human atrial [CMs](#). Longobardi et al [\[144\]](#) employed GP-based surrogates to fit a multi-scale bi-ventricular model of rat heart contraction and to perform [GSA](#) on the model. Another work from Karabelas et al [\[239\]](#) employed [GPs](#) to emulate and carry out [GSA](#) on one of the first 4 chamber heart hemodynamics models, where [GPs](#) demonstrated good performance also with computational fluid dynamics models.

### 5.2.2 Deep learning for cardiac models emulation

Various machine learning techniques can be used in cardiac electrophysiology [\[240\]](#). One of the main areas where the application of machine learning has become widespread is electrocardiogram analysis, electrocardiogram being largely available and obtainable through non-invasive measurements [\[240\]](#). Specifically, several *shallow* learning algorithms (in contrast with *deep* learning, i.e. neural networks), such as decision trees [\[241\]](#) and support vector machines [\[242\]](#), have been used for electrocardiograms classification. As a result, these algorithms are trained to automatically distinguished between healthy phenotypes and abnormal ones (e.g. affected by [AF](#)).

## Neural networks-based reduced order models

Recently, machine learning techniques have also begun to be used in combination with computational models of cardiac electrophysiology. The aim consists in reducing the computational burden regarding both predictive modelling, i.e. extrapolating the state of the modelled biophysical system forward in time, and parameters inference, i.e. estimating the model parameters underlying an observation of the system's behaviour. Specifically, Cantwell et al [234] have shown how neural networks can be used to predict the output (in 2 dimensions) of the monodomain model (see section 2.1.2), and thus predict correctly the diffusion of the AP in excitable cardiac tissue. In the last 2 years, more pioneering work on this topic has been performed by Fresca et al [235], which used neural networks to create deep learning-based reduced order models of the monodomain model. These new models provide solutions to parametrized electrophysiology problems, in a more efficient way than regular reduced order models. Regazzoni et al [243] extended the concept of deep learning-based reduced order models to simulations of cardiac electromechanics. The authors show how reduced order models based on neural networks can be used to model active force generation at a sub-cellular level, in lieu of complex sarcomere models. In the context of simulating multiscale cardiac electromechanics, the authors reported how using the deep learning-based reduced models enabled a one order of magnitude decrease in computational time and only introduced a small error in the main cardiac biomarkers of clinical interest. The same authors extended this work by creating a deep learning-based reduced order models that approximates a 3D electromechanical model of a human ventricle [244]. Besides good accuracy with respect to the full-order model, the machine learning-based model was shown to speed-up numerical simulations by three orders of magnitude, thus enabling the performance of GSA and parameter Bayesian estimation, which would normally be unaffordable on the full-blown ventricular model of cardiac electromechanics.

## Physics-informed neural networks

The approaches just described [234, 235, 243, 244] leverage deep learning to cut the computational time of numerically solving system of ordinary and partial differential equations. They

do so by employing neural networks within a *black-box* approach, i.e. the neural networks learn the dynamics of the model from input-output pairs generated by the complete model. Recently, a new kind of approach has been developed, consisting in embedding the modelled physics into machine learning. This is done through neural networks that can be trained from additional information acquired by enforcing the physical laws [245], termed physics-informed neural networks (*PINNs*). A recent work by Martin et al [246] has used *PINNs* to characterise cardiac electrophysiology. The authors have used *PINNs* to successfully predict the spatio-temporal evolution of the [AP](#), for parameters estimation, as well as to identify heterogeneities in electrophysiological properties.

In summary, we used a statistical tool to emulate our model following an approach already used in combination with computational models [236, 237] and more specific with cardiac models [144, 238]. While incorporating machine learning in cardiac computational modelling is still in its infancy, the potential speed-up in computational time, with consequent faster models parametrisation, could unlock several applications in personalised medicine and bring cardiac modelling closer to direct clinical application.

## 5.3 Modelling the engineered heart tissue: assumptions and implications

As for every modelling study, we made a series of assumptions when devising this work.

### 5.3.1 Uniformity of cells phenotype

One of the main assumptions derives from the use of the bidomain model, according to which the myocardium is modelled as a syncytium. We used the bidomain model coupled with a ionic model representing [hiPSC-CMs](#) electrophysiology [96] to replicate electrical propagation in the [EHT](#). In doing so, we assumed that the [EHT](#) is a homogeneous syncytium. However, it is plausible [EHTs](#) will contain different stem-cell derived [CMs](#) phenotypes, such as atrial-

or ventricular-like [182]. Even with recently developed techniques promoting differentiation efficiency and purity, the heterogeneity of cellular population after differentiation in CMs is still present [247]. The resulting heterogeneity in the electrophysiological properties of the EHT may have an impact on its effect on the infarcted myocardium.

Novel modelling technique could be adopted to capture this heterogeneity in the EHT. Bowler et al developed a partitioned phenotypes models to simulate electrical activation in tissue with cells of multiple types [184]. The authors specifically tested the model against experimental data from 2D hiPSC-CMs sheets, and were able to match experimental features like CV and self-pacing frequency. In the foreseeable future, new algorithms able to tackle simulations of electrical propagation in tissues with cell-level discretization could become an additional tool to tackle this limitation [248]. Such algorithms are however likely to require the use of supercomputers more powerful than the current ones.

### 5.3.2 Isotropy

In our simulations we assumed the EHT patch to be isotropic. In other words, the components of the conductivity tensor of the bidomain model were all set to the same value. It is possible to model cardiac tissue anisotropy using a vector field representing cardiac fibers [136]. We used this approach to model the cardiac fibers in the myocardium of both the simple model (Chapter 3) and the ventricle models (Chapter 4). Introducing fibers orientation, i.e. anisotropy, when modelling the EHT patch could have an impact in the study where we performed *in silico* patch engraftment (Chapter 4). If considering anisotropy of the EHT patch, the orientation of engraftment needs also to be taken into account, as the fibres orientation should match the direction of electrical propagation, which in simulations can depend on the pacing location. Since the target of our second study was to assess how EHT patches with different CV and APD affected the host ventricle electrophysiology, we kept the EHT patch as isotropic, in order not to introduce further variability in the study.

However, depending on the method utilized to fabricate the patch, the newly-differentiated cardiac cells will either randomly agglomerate, and thus support isotropic propagation, or grow,



for example, along the fibers of a pre-oriented scaffold [114]. It is now accepted that anisotropy represents a requirement for EHTs, in such that promotes both electrical [249] and mechanical [250] maturity of the hiPSC-CMs composing the EHT patch. *In silico* patch engraftment considering EHT anisotropy could thus be performed, exploiting the models to assess the effect of different fibres orientation and levels of anisotropy on the host electrophysiology.

### 5.3.3 Uniform coupling

When performing *in silico* EHT patch engraftment (Chapter 4) we assumed uniform coupling between the EHT patch and the host myocardium. In other words, we assumed all of the areas of the patch successfully adhere to the epicardium and that the outermost layer of epicardial CMs and the hiPSC-CMs, composing the EHT, electrically couple, i.e. electrical currents, in the form of ions, can readily pass from one cell to another. Electrical coupling between EHT patches and host tissue has been observed several times [193, 122, 37, 199, 200, 204]. However, incomplete adhesion between patch and host tissue due to the presence of a fibrotic layer has also been reported [39, 124]. Since the goal of our work was to evaluate the effects of different EHT patch CV and APD on the host electrophysiology, we assumed the presence of (full) electrical coupling. If coupling is completely prevented from the presence of a fibrotic layer interposed between EHT patch and host myocardium, activation from the epicardium will not cause activation in the patch [124]. Between the two extreme cases of full coupling and no coupling, the possibility of partial coupling is also present. The EHT patch could couple in a non-uniform way with the host tissue, resulting in extensive areas of the patch not electrically connected with the host myocardium. While this could be modelled and implications of partial coupling could be investigated *in silico*, based on the results from Chapter 4, where we observed the partial coupling caused by the scar to be pro-arrhythmic, it seems likely that a partial coupling between host myocardium and EHT patch would further exacerbate heterogeneities in the EHT, in turn increasing the arrhythmia risk.

### 5.3.4 Comparison with other studies

In this Thesis, we leveraged computational models of cardiac electrophysiology to investigate the interaction between EHT patches manufactured using hiPSC-CMs and the host myocardium. We initially used a model with simplified geometry, representing a section of scarred myocardial tissue, as well as a section of EHT patch placed in contact with the epicardium, in correspondence of the scar. We then moved to geometries obtained from magnetic resonance images of left ventricle with ischemic cardiomyopathy, and we devised a way to manipulate the mesh to add an additional layer of tissue, in correspondence with the epicardial scar. In such fashion, we replicated *in silico* the engraftment of EHT patches on infarcted ventricles.

To the best of our knowledge, beside the work presented in this Thesis, the only other attempt to model EHT patches and their interaction with infarcted myocardial tissue was published by Yu et al [251]. Using a framework similar to the one presented in Chapter 4, the authors found that arrhythmogenicity was sensitive to the patient-specific fibrotic substrate, to the patch engraftment site and that transplanting patches composed by more mature hiPSC-CMs could alleviate the EHT patches VT burden. The findings are aligned with what we reported in Chapter 4, and further stress the importance of hiPSC-CMs maturation. Moreover, given the dependance of VT inducibility and recurrence on the patient-specific scar substrate, both our and Yu et al's work highlight the requirement of patient-specific EHT patches optimization to achieve clinical safety.

### 5.3.5 Engineered heart tissue multi-physics modelling

In this work we used state-of-the-art modelling techniques to replicate electrical propagation in cardiac tissue. The bidomain model has in fact been validated against experimental data [252] and it is widely used in the modelling community (coupled with cell models for ion kinetics) to model cardiac electrophysiology [163]. However, the overall heart function is regulated by a more complex interaction of different biophysical processes [253]. As mentioned in section 1.1.5, the electrical activity of the heart is fundamentally linked to the heart contraction, through the

excitation-contraction coupling. Alongside successful electrical coupling, of equal importance will be the ability of the EHT patch to contract effectively and in sync with the host tissue. It is for instance well-known that immature hiPSC-CMs are incapable to develop the same tension as an adult CMs. EHT patches with different mechanical properties are likely to have an impact on the remuscularisation process and affect the characteristic and function of the post-engraftment host tissue. This will necessarily introduce additional variables to optimise in the design of EHT patches. In the same way computational modelling as shown in this Thesis can help assessing the safety and effectiveness of EHT patches from an electrophysiological point of view, mathematical models could also be used to aid the design of the EHT patches mechanical properties.

Briefly, cellular tension models give a mathematical description of the sub-cellular tension development, and provide a quantitative description of the CMs' active tension. The active tension is then incorporated in the equations modelling the cardiac tissue deformation [254]. However, the highly non-linear nature of the constitutive equations render the cardiac mechanics models more complex to handle than electrophysiology models [254]. Given this complexity, in the literature there is less freely available code implementing numerical methods to solve problems of cardiac mechanics. Moreover, the instability associated with the numerical solvers makes it harder to perform tasks such as parameter fitting. While modelling of post-MI fibrotic ventricles electromechanics has recently been performed [255, 256], there are currently, to the best of our knowledge, no published studies involving modelling of EHT patches mechanics.

## 5.4 Conclusions

MI represents one of the major causes of hospitalization in the modern world and one of the major factors burdening on national healthy systems of developed countries. Advances in stem cells technology, namely the ability to differentiate pluripotent cells in the cell phenotype of choice, has made possible the creation of EHT constructs. The ultimate goal of regenerative medicine consists in successfully delivering the newly, lab-created cardiac tissue, in post-MI

hearts, to relieve the hearts from the burdensome presence of scar tissue and improve the overall cardiac function. Assessing how the difference in electrophysiological properties between the EHTs and the host tissue affects the electrical activity of the host heart is of paramount importance for ensuring safety and represents a necessary step towards clinical application.

*In vitro* optimization of EHT patches parameters is hampered by the high amount of time and economic cost required to design and perform lab experiments. In this Thesis we address this issue leveraging computational models of cardiac electrophysiology to perform *in silico* experiments, targeted to assess the effects of EHT patches with different electrical properties. In Chapter 3, by performing global sensitivity analysis on a model with simplified geometry, we investigated how the most commonly varied EHT design parameters influence the electrical activity in the host tissue. Inspired by recent studies, we developed a machine learning framework to create a surrogate of our model, to overcome the computational burden derived from multiple model runs required to explore the multi-dimensional parameter space.

Encouraging results have been obtained so far from *ex vivo* implantation of EHT patches. However, these experiments have all been performed on small mammals. It is thus crucial to evaluate whether such experimental outcomes can be translatable to humans. In Chapter 3 we exploited the versatility of computational models to replicate cellular kinetics and electrical propagation of different animal species (namely rat, rabbit and human) and to perform a cross-species comparison of the effects of EHT patches.

Extensive research in the field of cardiac modelling has been carried out in the past decades [257]. Cardiac models have also reached clinical application, as in the case of catheter ablation [208] and cardiac resynchronization therapy [258]. However, regenerative medicine represents a novel topic of application of cardiac modelling. In Chapter 4 we developed the first pipelines for manipulating ventricle meshes with the target of replicating *in silico* the engraftment of an epicardial patch. Moreover, we performed state-of-the-art bidomain simulations in two patient-derived ventricle models, exploring the impact of EHT patches with different CV and APD on the host electrophysiology. This work represents a framework that can be used in synergy with laboratory experiments to both guide the experiments design and shed light on the mechanistic

aspects behind experimental observations.

The future clinical application of EHT patches, as for many other biomedical technologies [259], falls into the field of personalised medicine, as each patient is likely to need a tailored treatment. Computational modelling is of crucial importance to achieve this goal [260]. The modelling work done in this Thesis demonstrates how computer models can be successfully applied to the field of regenerative medicine. Additionally, the studies reported in this Thesis constitutes the first step towards the creation of patient-specific models for developing and testing EHT patches for cardiac regeneration.

# Bibliography

- [1] Anthony J. Weinhaus. Anatomy of the human heart. *Handbook of Cardiac Anatomy, Physiology, and Devices, Third Edition*, pages 61–88, 2015.
- [2] Elizabeth A. Woodcock and Scot J. Matkovich. Cardiomyocytes structure, function and associated pathologies. *International Journal of Biochemistry and Cell Biology*, 37(9):1746–1751, 2005.
- [3] Laura D. Osellame, Thomas S. Blacker, and Michael R. Duchon. Cellular and molecular mechanisms of mitochondrial function. *Best Practice and Research: Clinical Endocrinology and Metabolism*, 26(6):711–723, 2012.
- [4] Diane M. Bosen. Atrio-ventricular nodal reentry tachycardia. *Dimensions of Critical Care Nursing*, 21(4):134–139, 2002.
- [5] M. Donald Bers. Cardiac excitation–contraction coupling. *Nature*, 415(January):198–205, 2002.
- [6] Stephan Rohr. Role of gap junctions in the propagation of the cardiac action potential. *Cardiovascular Research*, 62(2):309–322, 2004.
- [7] Ziad F. Issa, John M. Miller, and Douglas P. Zipes. Molecular Mechanisms of Cardiac Electrical Activity. *Clinical Arrhythmology and Electrophysiology*, pages 1–14, 2019.
- [8] Stephan Rohr, Jan P. Kucera, Vladimir G. Fast, and André G. Kléber. Paradoxical improvement of impulse conduction in cardiac tissue by partial cellular uncoupling. *Science*, 275(5301):841–844, 1997.

- [9] American Heart Association. Heart Disease and Stroke Statistics-2021 Update A Report from the American Heart Association, 2021.
- [10] Luka Nicin, Julian U.G. Wagner, Guillermo Luxán, and Stefanie Dimmeler. Fibroblast-mediated intercellular crosstalk in the healthy and diseased heart. *FEBS Letters*, 596(5):638–654, 2022.
- [11] Rights Desk, Lippincott Williams, and Kluwer Health. PATHOPHYSIOLOGY AND NATURAL HISTORY Quantitative analysis of myocardial infarct structure in patients with ventricular tachycardia. *Library*, 2010.
- [12] Jacques M.T. de Baker, Ruben Coronel, Sara Tasseron, Arthur A.M. Wilde, Tobias Opthof, Michiel J. Janse, Frans J.L. van Capelle, Anton E. Becker, and George Jambroes. Ventricular tachyrdia in the infarcted, Langendorff-perfused human heart: Role of the arrangement of surviving cardiac fibers. *Journal of the American College of Cardiology*, 15(7):1594–1607, 1990.
- [13] J. M.T. De Bakker, F. J.L. Van Capelle, M. J. Janse, A. A.M. Wilde, R. Coronel, A. E. Becker, K. P. Dingemans, N. M. Van Hemel, and R. N.W. Hauer. Reentry as a cause of ventricular tachycardia in patients with chronic ischemic heart disease: Electrophysiology and anatomic correlation. *Circulation*, 77(3):589–606, 1988.
- [14] J. HAN and G. K. MOE. NONUNIFORM RECOVERY OF EXCITABILITY IN VENTRICULAR MUSCLE. *Circulation research*, 14:44–60, 1964.
- [15] Ruben Coronel, Francien J.G. Wilms-Schopman, Tobias Opthof, and Michiel J. Janse. Dispersion of repolarization and arrhythmogenesis. *Heart Rhythm*, 6(4):537–543, 4 2009.
- [16] Vijay S. Chauhan, Eugene Downar, Kumaraswamy Nanthakumar, John D. Parker, Heather J. Ross, Wilson Chan, and Peter Picton. Increased ventricular repolarization heterogeneity in patients with ventricular arrhythmia vulnerability and cardiomyopathy: a human in vivo study. *American journal of physiology. Heart and circulatory physiology*, 290(1), 1 2006.

- [17] Edward J. Vigmond and Bruno D. Stuyvers. Modeling our understanding of the His-Purkinje system. *Progress in Biophysics and Molecular Biology*, 120(1-3):179–188, 2016.
- [18] Corina Grey, Rod Jackson, Morten Schmidt, Majid Ezzati, Perviz Asaria, Daniel J. Exeter, and Andrew J. Kerr. One in four major ischaemic heart disease events are fatal and 60% are pre-hospital deaths: A national data-linkage study (ANZACS-QI 8). *European Heart Journal*, 38(3):172–180, 2017.
- [19] Matthew Amoni, Eef Dries, Sebastian Ingelaere, Dylan Vermoortele, H. Llewelyn Roderrick, Piet Claus, Rik Willems, and Karin R. Sipido. Ventricular arrhythmias in ischemic cardiomyopathy—New avenues for mechanism-guided treatment. *Cells*, 10(10):1–29, 2021.
- [20] Francis E. Marchlinski, Charles I. Haffajee, John F. Beshai, Timm Michael L. Dickfeld, Mario D. Gonzalez, Henry H. Hsia, Claudio D. Schuger, Karen J. Beckman, Frank M. Bogun, Scott J. Pollak, and Anil K. Bhandari. Long-Term Success of Irrigated Radiofrequency Catheter Ablation of Sustained Ventricular Tachycardia: Post-Approval THERMOCOOL VT Trial. *Journal of the American College of Cardiology*, 67(6):674–683, 2016.
- [21] Terrence D. Welch, Eric H. Yang, Guy S. Reeder, and Bernard J. Gersh. Modern Management of Acute Myocardial Infarction. *Current Problems in Cardiology*, 37(7):237–310, 2012.
- [22] Keith A. Webster. Mitochondrial Death Channels. *American scientist*, 97(5):384, 9 2009.
- [23] Thygesen K, Alpert JS, Jaffe AS, Simoons ML, Chaitman BR, White HD, Thygesen K, Alpert JS, White HD, Jaffe AS, Katus HA, Apple FS, Lindahl B, Morrow DA, Chaitman BR, Clemmensen PM, Johanson P, Hod H, Underwood R, Bax JJ, Bonow JJ, Pinto F, Gibbons RJ, Fox KA, Atar D, Newby LK, Galvani M, Hamm CW, Uretsky BF, Steg PG, Wijns W, Bassand JP, Menasche P, Ravkilde J, Ohman EM, Antman EM, Wallentin LC, Armstrong PW, Simoons ML, Januzzi JL, Nieminen MS, Gheorghiade M, Filippatos G, Luepker RV, Fortmann SP, Rosamond WD, Levy D, Wood D, Smith SC, Hu D,



- Lopez-Sendon JL, Robertson RM, Weaver D, Tendera M, Bove AA, Parkhomenko AN, Vasilieva EJ, Mendis S, Bax JJ, Baumgartner H, Ceconi C, Dean V, Deaton C, Fagard R, Funck-Brentano C, Hasdai D, Hoes A, Kirchhof P, Knuuti J, Kolh P, McDonagh T, Moulin C, Popescu BA, Reiner Z, Sechtem U, Sirnes PA, Tendera M, Torbicki A, Vahanian A, Windecker S, Morais J, Aguiar C, Almahmeed W, Arnar DO, Barili F, Bloch KD, Bolger AF, Botker HE, Bozkurt B, Bugiardini R, Cannon C, de Lemos J, Eberli FR, Escobar E, Hlatky M, James S, Kern KB, Moliterno DJ, Mueller C, Neskovic AN, Pieske BM, Schulman SP, Storey RF, Taubert KA, Vranckx P, and Wagner DR. Third universal definition of myocardial infarction. *Journal of the American College of Cardiology*, 60(16):1581–1598, 10 2012.
- [24] Yimu Zhao, Nicole T. Feric, Nimalan Thavandiran, Sara S. Nunes, and Milica Radisic. The Role of Tissue Engineering and Biomaterials in Cardiac Regenerative Medicine. *Canadian Journal of Cardiology*, 30(11):1307–1322, 2014.
- [25] Peter Paul Zwetsloot, Anna Maria Dorothea Végh, Sanne Johanna Jansen Of Lorkeers, Gerardus P.J. Van Hout, Gillian L. Currie, Emily S. Sena, Hendrik Gremmels, Jan Willem Buikema, Marie Jose Goumans, Malcolm R. Macleod, Pieter A. Doevendans, Steven A.J. Chamuleau, and Joost P.G. Sluijter. Cardiac stem cell treatment in myocardial infarction: A systematic review and meta-analysis of preclinical studies. *Circulation Research*, 118(8):1223–1232, 4 2016.
- [26] Mei Li, Hao Wu, Yuehui Yuan, Benhui Hu, and Ning Gu. Recent fabrications and applications of cardiac patch in myocardial infarction treatment. *View*, 3(April):20200153, 2021.
- [27] Donald Orlic, Jan Kajstura, Stefano Chimenti, Igor Jakoniuk, Stacie M. Anderson, Baosheng Li, James Pickel, Ronald McKay, Bernardo Nadal-Ginard, David M. Bodine, Annarosa Leri, and Piero Anversa. Bone marrow cells regenerate infarcted myocardium. *Nature*, 410(6829):701–705, 4 2001.
- [28] Wenjie Wang, Keiji Itaka, Shinsuke Ohba, Nobuhiro Nishiyama, Ung il Chung, Yuichi Yamasaki, and Kazunori Kataoka. 3D spheroid culture system on micropatterned substrates

- for improved differentiation efficiency of multipotent mesenchymal stem cells. *Biomaterials*, 30(14):2705–2715, 5 2009.
- [29] Brian Liao, Nicolas Christoforou, Kam W. Leong, and Nenad Bursac. Pluripotent stem cell-derived cardiac tissue patch with advanced structure and function. *Biomaterials*, 32(35):9180–9187, 2011.
- [30] Andre Chow, Daniel J. Stuckey, Emaddin Kidher, Mark Rocco, Richard J. Jabbour, Catherine A. Mansfield, Ara Darzi, Sian E. Harding, Molly M. Stevens, and Thanos Athanasiou. Human Induced Pluripotent Stem Cell-Derived Cardiomyocyte Encapsulating Bioactive Hydrogels Improve Rat Heart Function Post Myocardial Infarction. *Stem Cell Reports*, 9(5):1415–1422, 2017.
- [31] Elsie S. Place, Nicholas D. Evans, and Molly M. Stevens. Complexity in biomaterials for tissue engineering. *Nature Materials*, 8(6):457–470, 2009.
- [32] Jun Wu, Faquan Zeng, Xi Ping Huang, Jennifer C.Y. Chung, Filip Konecny, Richard D. Weisel, and Ren Ke Li. Infarct stabilization and cardiac repair with a VEGF-conjugated, injectable hydrogel. *Biomaterials*, 32(2):579–586, 2011.
- [33] Karen L. Christman, Andrew J. Vardanian, Qizhi Fang, Richard E. Sievers, Hubert H. Fok, and Randall J. Lee. Injectable Fibrin Scaffold Improves Cell Transplant Survival, Reduces Infarct Expansion, and Induces Neovasculature Formation in Ischemic Myocardium. *Journal of the American College of Cardiology*, 44(3):654–660, 8 2004.
- [34] Gang Lu, Husnain K. Haider, Shujia Jiang, and Muhammad Ashraf. Sca-1 + stem cell survival and engraftment in the infarcted heart: Dual role for preconditioning-induced connexin-43. *Circulation*, 119(19):2587–2596, 2009.
- [35] Khadijeh Ashtari, Hojjatollah Nazari, Hyojin Ko, Peyton Tebon, Masoud Akhshik, Mohsen Akbari, Sanaz Naghavi Alhosseini, Masoud Mozafari, Bitra Mehravi, Masoud Soleimani, Reza Ardehali, Majid Ebrahimi Warkiani, Samad Ahadian, and Ali Khademhosseini. Electrically conductive nanomaterials for cardiac tissue engineering. *Advanced Drug Delivery Reviews*, 144:162–179, 2019.

- [36] Ling Gao, Molly E. Kupfer, Jangwook P. Jung, Libang Yang, Patrick Zhang, Yong Da Sie, Quyen Tran, Visar Ajeti, Brian T. Freeman, Vladimir G. Fast, Paul J. Campagnola, Brenda M. Ogle, and Jianyi Zhang. Myocardial Tissue Engineering with Cells Derived from Human-Induced Pluripotent Stem Cells and a Native-Like, High-Resolution, 3-Dimensionally Printed Scaffold. *Circulation Research*, 120(8):1318–1325, 2017.
- [37] Ling Gao, Zachery R. Gregorich, Wuqiang Zhu, Saidulu Mattapally, Yasin Oduk, Xi Lou, Ramaswamy Kannappan, Anton V. Borovjagin, Gregory P. Walcott, Andrew E. Pollard, Vladimir G. Fast, Xinyang Hu, Steven G. Lloyd, Ying Ge, and Jianyi Zhang. Large cardiac muscle patches engineered from human induced-pluripotent stem cell-derived cardiac cells improve recovery from myocardial infarction in swine. *Circulation*, 137(16):1712–1730, 2018.
- [38] Christopher Jackman, Hanjun Li, and Nenad Bursac. Long-term contractile activity and thyroid hormone supplementation produce engineered rat myocardium with adult-like structure and function. *Acta Biomaterialia*, 78:98–110, 2018.
- [39] Florian Weinberger, Kaja Breckwoldt, Simon Pecha, Allen Kelly, Birgit Geertz, Jutta Starbatty, Timur Yorgan, Kai Hung Cheng, Katrin Lessmann, Tomas Stolen, Scherrer Crosbie Marielle, Godfrey Smith, Hermann Reichenspurner, Arne Hansen, and Thomas Eschenhagen. Cardiac repair in Guinea pigs with human engineered heart tissue from induced pluripotent stem cells. *Science Translational Medicine*, 8(363):1–13, 2016.
- [40] Wolfram Hubertus Zimmermann, Ivan Melnychenko, Gerald Wasmeier, Michael Didié, Hiroshi Naito, Uwe Nixdorff, Andreas Hess, Lubos Budinsky, Kay Brune, Bjela Michaelis, Stefan Dhein, Alexander Schwoerer, Heimo Ehmke, and Thomas Eschenhagen. Engineered heart tissue grafts improve systolic and diastolic function in infarcted rat hearts. *Nature Medicine*, 12(4):452–458, 2006.
- [41] Robert Maidhof, Nina Tandon, Eun Jung Lee, Jianwen Luo, Yi Duan, Keith Yeager, Elisa Konofagou, and Gordana Vunjak-Novakovic. Biomimetic perfusion and electrical stimulation applied in concert improved the assembly of engineered cardiac tissue. *Journal of Tissue Engineering and Regenerative Medicine*, 6(10):1–21, 2012.

- [42] Sally L. Rutherford, Mark L. Trew, Gregory B. Sands, Ian J. Legrice, and Bruce H. Smaill. High-resolution 3-dimensional reconstruction of the infarct border zone: Impact of structural remodeling on electrical activation. *Circulation Research*, 111(3):301–311, 2012.
- [43] Manju.Gerard, Ashab.Choubey, and B.D.Malhotra. Review: Application of Conducting Polymer to Biosensors. *Biosensors & Bioelectronics*, 17:345–359, 2001.
- [44] Guorui Jin and Kai Li. The electrically conductive scaffold as the skeleton of stem cell niche in regenerative medicine. *Materials Science and Engineering C*, 45:671–681, 2015.
- [45] Nathalie K. Guimard, Natalia Gomez, and Christine E. Schmidt. Conducting polymers in biomedical engineering. *Progress in Polymer Science (Oxford)*, 32(8-9):876–921, 2007.
- [46] A. Borriello, V. Guarino, L. Schiavo, M. A. Alvarez-Perez, and L. Ambrosio. Optimizing PANi doped electroactive substrates as patches for the regeneration of cardiac muscle. *Journal of Materials Science: Materials in Medicine*, 22(4):1053–1062, 2011.
- [47] Anton Mihic, Zhi Cui, Jun Wu, Goran Vlacic, Yasuo Miyagi, Shu Hong Li, Sun Lu, Hsing Wen Sung, Richard D. Weisel, and Ren Ke Li. A conductive polymer hydrogel supports cell electrical signaling and improves cardiac function after implantation into myocardial infarct. *Circulation*, 132(8):772–784, 8 2015.
- [48] Leyu Wang, Junzi Jiang, Wenxi Hua, Ali Darabi, Xiaoping Song, Chen Song, Wen Zhong, Malcolm M.Q. Xing, and Xiaozhong Qiu. Mussel-Inspired Conductive Cryogel as Cardiac Tissue Patch to Repair Myocardial Infarction by Migration of Conductive Nanoparticles. *Advanced Functional Materials*, 26(24):4293–4305, 6 2016.
- [49] Rui Bao, Baoyu Tan, Shuang Liang, Ning Zhang, Wei Wang, and Wenguang Liu. A  $\pi$ - $\pi$  conjugation-containing soft and conductive injectable polymer hydrogel highly efficiently rebuilds cardiac function after myocardial infarction. *Biomaterials*, 122:63–71, 4 2017.
- [50] Wei Wang, Baoyu Tan, Jingrui Chen, Rui Bao, Xuran Zhang, Shuang Liang, Yingying Shang, Wei Liang, Yuanlu Cui, Guanwei Fan, Huizhen Jia, and Wenguang Liu. An

- injectable conductive hydrogel encapsulating plasmid DNA-eNOs and ADSCs for treating myocardial infarction. *Biomaterials*, 160:69–81, 4 2018.
- [51] Shanglin Chen, Meng Hsuan Hsieh, Shu Hong Li, Jun Wu, Richard D. Weisel, Yen Chang, Hsing Wen Sung, and Ren Ke Li. A conductive cell-delivery construct as a bioengineered patch that can improve electrical propagation and synchronize cardiomyocyte contraction for heart repair. *Journal of Controlled Release*, 320:73–82, 4 2020.
- [52] Chun Wen Hsiao, Meng Yi Bai, Yen Chang, Min Fan Chung, Ting Yin Lee, Cheng Tse Wu, Barnali Maiti, Zi Xian Liao, Ren Ke Li, and Hsing Wen Sung. Electrical coupling of isolated cardiomyocyte clusters grown on aligned conductive nanofibrous meshes for their synchronized beating. *Biomaterials*, 34(4):1063–1072, 2013.
- [53] Damia Mawad, Catherine Mansfield, Antonio Lauto, Filippo Perbellini, Geoffrey W. Nelson, Joanne Tonkin, Sean O. Bello, Damon J. Carrad, Adam P. Micolich, Mohd M. Mahat, Jennifer Furman, David J. Payne, Alexander R. Lyon, J. Justin Gooding, Sian E. Harding, Cesare M. Terracciano, and Molly M. Stevens. A Conducting polymer with enhanced electronic stability applied in cardiac models. *Science Advances*, 2(11), 2016.
- [54] Miguel F. Tenreiro, Ana F. Louro, Paula M. Alves, and Margarida Serra. Next generation of heart regenerative therapies: progress and promise of cardiac tissue engineering. *npj Regenerative Medicine*, 6(1), 2021.
- [55] Timm Häneke and Makoto Sahara. Progress in Bioengineering Strategies for Heart Regenerative Medicine. *International Journal of Molecular Sciences 2022, Vol. 23, Page 3482*, 23(7):3482, 3 2022.
- [56] Philippe Menasché, Valérie Vanneaux, Albert Hagège, Alain Bel, Bernard Cholley, Alexandre Parouchev, Isabelle Cacciapuoti, Reem Al-Daccak, Nadine Benhamouda, Hélène Blons, Onnik Agbulut, Lucie Tosca, Jean Hugues Trouvin, Jean Roch Fabreguettes, Valérie Bellamy, Dominique Charron, Eric Tartour, Gérard Tachdjian, Michel Desnos, and Jérôme Larghero. Transplantation of Human Embryonic Stem Cell-Derived

- Cardiovascular Progenitors for Severe Ischemic Left Ventricular Dysfunction. *Journal of the American College of Cardiology*, 71(4):429–438, 1 2018.
- [57] Eric K.N. Gähwiler, Sarah E. Motta, Marcy Martin, Bramasta Nugraha, Simon P. Høerstrup, and Maximilian Y. Emmert. Human iPSCs and Genome Editing Technologies for Precision Cardiovascular Tissue Engineering. *Frontiers in Cell and Developmental Biology*, 9, 6 2021.
- [58] John M. Squire. Architecture and function in the muscle sarcomere. *Current Opinion in Structural Biology*, 1997.
- [59] George A. Porter, Jennifer R. Hom, David L. Hoffman, Rodrigo A. Quintanilla, Karen L. de Mesy Bentley, and Shey Shing Sheu. Bioenergetics, mitochondria, and cardiac myocyte differentiation. *Progress in Pediatric Cardiology*, 2011.
- [60] Christian Pinali, Hayley Bennett, J. Bernard Davenport, Andrew W. Trafford, and Ashraf Kitmitto. Three-dimensional reconstruction of cardiac sarcoplasmic reticulum reveals a continuous network linking transverse-tubules: This organization is perturbed in heart failure. *Circulation Research*, 2013.
- [61] Scott D. Lundy, Wei Zhong Zhu, Michael Regnier, and Michael A. Laflamme. Structural and functional maturation of cardiomyocytes derived from human pluripotent stem cells. *Stem Cells and Development*, 2013.
- [62] Gary D. Lopaschuk and Jagdip S. Jaswal. Energy metabolic phenotype of the cardiomyocyte during development, differentiation, and postnatal maturation. In *Journal of Cardiovascular Pharmacology*, 2010.
- [63] Jing Liu, Ji Dong Fu, Chung Wah Siu, and Ronald A. Li. Functional Sarcoplasmic Reticulum for Calcium Handling of Human Embryonic Stem Cell-Derived Cardiomyocytes: Insights for Driven Maturation. *Stem Cells*, 2007.
- [64] Deborah K. Lieu, Jing Liu, Chung Wah Siu, Gregory P. McNerney, Hung Fat Tse, Amir Abu-Khalil, Thomas Huser, and Ronald A. Li. Absence of transverse tubules contributes

- to non-uniform  $\text{Ca}^{2+}$  wavefronts in mouse and human embryonic stem cell-derived cardiomyocytes. *Stem Cells and Development*, 2009.
- [65] Charles Antzelevitch and Alexander Burashnikov. Overview of Basic Mechanisms of Cardiac Arrhythmia, 2011.
- [66] Jonathan Satin, Izhak Kehat, Oren Caspi, Irit Huber, Gil Arbel, Ilanit Itzhaki, Janos Magyar, Elizabeth A. Schroder, Ido Perlman, and Lior Gepstein. Mechanism of spontaneous excitability in human embryonic stem cell derived cardiomyocytes. *Journal of Physiology*, 559(2):479–496, 2004.
- [67] Christine Mummery, Dorien Ward-van Oostwaard, Pieter Doevendans, Rene Spijker, Stieneke Van den Brink, Rutger Hassink, Marcel Van der Heyden, Tobias Opthof, Martin Pera, Aart Brutel de la Riviere, Robert Passier, and Leon Tertoolen. Differentiation of human embryonic stem cells to cardiomyocytes: Role of coculture with visceral endoderm-like cells. *Circulation*, 2003.
- [68] Marcelo C. Ribeiro, Leon G. Tertoolen, Juan A. Guadix, Milena Bellin, Georgios Kosmidis, Cristina D’Aniello, Jantine Monshouwer-Kloots, Marie Jose Goumans, Yu li Wang, Adam W. Feinberg, Christine L. Mummery, and Robert Passier. Functional maturation of human pluripotent stem cell derived cardiomyocytes invitro - Correlation between contraction force and electrophysiology. *Biomaterials*, 2015.
- [69] Olaf Scheel, Stefanie Frech, Bogdan Amuzescu, Jörg Eisfeld, Kun Han Lin, and Thomas Knott. Action potential characterization of human induced pluripotent stem cell-derived cardiomyocytes using automated patch-clamp technology. *Assay and Drug Development Technologies*, 2014.
- [70] Candido Cabo, Jianan Yao, Penelope A. Boyden, Shan Chen, Wajid Hussain, Heather S. Duffy, Edward J. Ciaccio, Nicholas S. Peters, and Andrew L. Wit. Heterogeneous gap junction remodeling in reentrant circuits in the epicardial border zone of the healing canine infarct. *Cardiovascular Research*, 72(2):241–249, 2006.

- [71] Suraj Kannan and Chulan Kwon. Regulation of cardiomyocyte maturation during critical perinatal window. In *Journal of Physiology*, 2020.
- [72] Antje Ebert, Amit U. Joshi, Sandra Andorf, Yuanyuan Dai, Shrivatsan Sampathkumar, Haodong Chen, Yingxin Li, Priyanka Garg, Karl Toischer, Gerd Hasenfuss, Daria Mochly-Rosen, and Joseph C. Wu. Proteasome-dependent regulation of distinct metabolic states during long-term culture of human iPSC-derived cardiomyocytes. *Circulation Research*, 2019.
- [73] Nicholas S. Peters, Nicholas J. Severs, Stephen M. Rothery, Christopher Lincoln, Magdi H. Yacoub, and Colin R. Green. Spatiotemporal relation between gap junctions and fascia adherens junctions during postnatal development of human ventricular myocardium. *Circulation*, 1994.
- [74] Gaetano J. Scuderi and Jonathan Butcher. Naturally engineered maturation of cardiomyocytes, 2017.
- [75] Nina Tandon, Christopher Cannizzaro, Pen Hsiu Grace Chao, Robert Maidhof, Anna Marsano, Hoi Ting Heidi Au, Milica Radisic, and Gordana Vunjak-Novakovic. Electrical stimulation systems for cardiac tissue engineering. *Nature Protocols*, 2009.
- [76] Sara S. Nunes, Jason W. Miklas, Jie Liu, Roozbeh Aschar-Sobbi, Yun Xiao, Boyang Zhang, Jiahua Jiang, Stéphane Massé, Mark Gagliardi, Anne Hsieh, Nimalan Thavandiran, Michael A. Laflamme, Kumaraswamy Nanthakumar, Gil J. Gross, Peter H. Backx, Gordon Keller, and Milica Radisic. Biowire: A platform for maturation of human pluripotent stem cell-derived cardiomyocytes. *Nature Methods*, 2013.
- [77] Ingra Mannhardt, Kaja Breckwoldt, David Letuffe-Brenière, Sebastian Schaaf, Herbert Schulz, Christiane Neuber, Anika Benzin, Tessa Werner, Alexandra Eder, Thomas Schulze, Birgit Klampe, Torsten Christ, Marc N. Hirt, Norbert Huebner, Alessandra Moretti, Thomas Eschenhagen, and Arne Hansen. Human Engineered Heart Tissue: Analysis of Contractile Force. *Stem Cell Reports*, 2016.



- [78] Tatsuya Shimizu, Masayuki Yamato, Yuki Isoi, Takumitsu Akutsu, Takeshi Setomaru, Kazuhiko Abe, Akihiko Kikuchi, Mitsuo Umezu, and Teruo Okano. Fabrication of pulsatile cardiac tissue grafts using a novel 3-dimensional cell sheet manipulation technique and temperature-responsive cell culture surfaces. *Circulation research*, 2002.
- [79] Cláudia Correia, Alexey Koshkin, Patrícia Duarte, Dongjian Hu, Madalena Carido, Maria J. Sebastião, Patrícia Gomes-Alves, David A. Elliott, Ibrahim J. Domian, Ana P. Teixeira, Paula M. Alves, and Margarida Serra. 3D aggregate culture improves metabolic maturation of human pluripotent stem cell derived cardiomyocytes. *Biotechnology and Bioengineering*, 2018.
- [80] Weining Bian, Nima Badie, Herman D. Himel, and Nenad Bursac. Robust T-tubulation and maturation of cardiomyocytes using tissue-engineered epicardial mimetics. *Biomaterials*, 2014.
- [81] Cláudia Correia, Alexey Koshkin, Patrícia Duarte, Dongjian Hu, Ana Teixeira, Ibrahim Domian, Margarida Serra, and Paula M. Alves. Distinct carbon sources affect structural and functional maturation of cardiomyocytes derived from human pluripotent stem cells. *Scientific Reports*, 2017.
- [82] Deborah K. Lieu, Ji Dong Fu, Nipavan Chiamvimonvat, Kelvin Chan Tung, Gregory P. McNerney, Thomas Huser, Gordon Keller, Chi Wing Kong, and Ronald A. Li. Mechanism-based facilitated maturation of human pluripotent stem cell-derived cardiomyocytes. *Circulation: Arrhythmia and Electrophysiology*, 2013.
- [83] Jing Liu, Deborah K. Lieu, Chung Wah Siu, Ji Dong Fu, Hung Fat Tse, and Ronald A. Li. Facilitated maturation of Ca<sup>2+</sup> handling properties of human embryonic stem cell-derived cardiomyocytes by calsequestrin expression. *American Journal of Physiology - Cell Physiology*, 2009.
- [84] Steven A. Niederer, Joost Lumens, and Natalia A. Trayanova. Computational models in cardiology. *Nature Reviews Cardiology*, 16(2):100–111, 2019.
- [85] A L Hodgkin and A F Huxley. 1952) I I7. *J. Physiol*, pages 500–544, 1952.

- [86] Martin Fink and Denis Noble. Markov models for ion channels: versatility versus identifiability and speed. *Philosophical Transactions of the Royal Society A: Mathematical, Physical and Engineering Sciences*, 367(1896):2161–2179, 6 2009.
- [87] Ivan Kopljar, Hua Rong Lu, Karel Van Ammel, Martin Otava, Fetene Tekle, Ard Teisman, and David J. Gallacher. Development of a Human iPSC Cardiomyocyte-Based Scoring System for Cardiac Hazard Identification in Early Drug Safety De-risking. *Stem cell reports*, 11(6):1365–1377, 12 2018.
- [88] Aman Mahajan, Yohannes Shiferaw, Daisuke Sato, Ali Baher, Riccardo Olcese, Lai Hua Xie, Ming Jim Yang, Peng Sheng Chen, Juan G. Restrepo, Alain Karma, Alan Garfinkel, Zhilin Qu, and James N. Weiss. A rabbit ventricular action potential model replicating cardiac dynamics at rapid heart rates. *Biophysical Journal*, 94(2):392–410, 2008.
- [89] Gregory M. Faber and Yoram Rudy. Action potential and contractility changes in [Na(+)](i) overloaded cardiac myocytes: a simulation study. *Biophysical journal*, 78(5):2392–2404, 2000.
- [90] K. H.W.J. Ten Tusscher, D. Noble, P. J. Noble, and A. V. Panfilov. A model for human ventricular tissue. *American Journal of Physiology - Heart and Circulatory Physiology*, 286(4 55-4):1573–1589, 2004.
- [91] Eleonora Grandi, Sandeep V. Pandit, Niels Voigt, Antony J. Workman, Dobromir Dobrev, José Jalife, and Donald M. Bers. Human atrial action potential and Ca<sup>2+</sup> model: sinus rhythm and chronic atrial fibrillation. *Circulation research*, 109(9):1055–1066, 10 2011.
- [92] Michelangelo Paci, Jari Hyttinen, Katriina Aalto-Setälä, and Stefano Severi. Computational models of ventricular-and atrial-like human induced pluripotent stem cell derived cardiomyocytes. *Annals of Biomedical Engineering*, 41(11):2334–2348, 2013.
- [93] Michelangelo Paci, Jari Hyttinen, and Stefano Severi. Computational modelling of LQT1 in human induced pluripotent stem cell derived cardiomyocytes. *Computing in Cardiology*, 40:1239–1242, 2013.

- [94] Michelangelo Paci, Stefano Severi, and Jari Hyttinen. Computational modeling supports induced pluripotent stem cell-derived cardiomyocytes reliability as a model for human LQT3. In *Computing in Cardiology*, volume 41, pages 69–72. IEEE Computer Society, 2014.
- [95] M. Paci, J. Hyttinen, B. Rodriguez, and S. Severi. Human induced pluripotent stem cell-derived versus adult cardiomyocytes: An in silico electrophysiological study on effects of ionic current block. *British Journal of Pharmacology*, 172(21):5147–5160, 2015.
- [96] Michelangelo Paci, Risto Pekka Pölönen, Dario Cori, Kirsi Penttinen, Katriina Aalto-Setälä, Stefano Severi, and Jari Hyttinen. Automatic optimization of an in silico model of human iPSC derived cardiomyocytes recapitulating calcium handling abnormalities. *Frontiers in Physiology*, 9(JUN):1–14, 2018.
- [97] Divya C. Kernik, Stefano Morotti, Hao Di Wu, Priyanka Garg, Henry J. Duff, Junko Kurokawa, José Jalife, Joseph C. Wu, Eleonora Grandi, and Colleen E. Clancy. A computational model of induced pluripotent stem-cell derived cardiomyocytes incorporating experimental variability from multiple data sources. *The Journal of physiology*, 597(17):4533–4564, 9 2019.
- [98] M Folkmanaite, X Zhou, F Margara, M Zaccolo, and B Rodriguez. Modelling and in silico simulation of human induced pluripotent stem cell derived cardiomyocyte electro-mechanical properties. *Cardiovascular Research*, 118(Supplement\_1), 6 2022.
- [99] Michelangelo Paci, Elisa Passini, Aleksandra Klimas, Stefano Severi, Jari Hyttinen, Blanca Rodriguez, and Emilia Entcheva. In Silico Populations Optimized on Optogenetic Recordings Predict Drug Effects in Human Induced Pluripotent Stem Cell-Derived Cardiomyocytes. *Computing in Cardiology*, 2018-Sept:10–13, 2018.
- [100] DG DG COMM Communication. European Commission SEC(2005) 791 IMPACT ASSESSMENT GUIDELINES \*. Technical report, European Commission, 2005.
- [101] Andrea Saltelli and Paola Annoni. How to avoid a perfunctory sensitivity analysis. *Environmental Modelling & Software*, 25(12):1508–1517, 12 2010.

- [102] Andrea Saltelli, Marco Ratto, Terry Andres, Francesca Campolongo, Jessica Cariboni, Debora Gatelli, Michaela Saisana, and Stefano Tarantola. *Global sensitivity analysis: The primer*. John Wiley & Sons Ltd, 2008.
- [103] Andrea Saltelli, Paola Annoni, Ivano Azzini, Francesca Campolongo, Marco Ratto, and Stefano Tarantola. Variance based sensitivity analysis of model output. Design and estimator for the total sensitivity index. *Computer Physics Communications*, 181(2):259–270, 2010.
- [104] I M Sobol. UNIFORMLY DISTRIBUTED SEQUENCES WITH AN ADDITIONAL PROPERTY. *Zhurnal Vychislitel'noi Matematiki i Matematicheskoi Fiziki*, 16(5):1332–1337, 1976.
- [105] I. M. Sobol and S. S. Kucherenko. On Global sensitivity analysis of quasi-Monte Carlo algorithms. *Monte Carlo Methods and Applications*, 11(1):83–92, 2005.
- [106] C. E. Rasmussen & C. K. I. Williams. *Gaussian Processes for Machine Learning*, volume 7. The MIT Press, 2006.
- [107] British Heart Foundation. Global Heart & Circulatory Diseases Factsheet. Technical Report July, British Heart Foundation, 2021.
- [108] Kate Smolina, F. Lucy Wright, Mike Rayner, and Michael J. Goldacre. Determinants of the decline in mortality from acute myocardial infarction in England between 2002 and 2010: Linked national database study. *BMJ (Online)*, 344(7842):1–9, 2012.
- [109] Leslie W. Miller and Joseph G. Rogers. Evolution of left ventricular assist device therapy for advanced heart failure: A review. *JAMA Cardiology*, 3(7):650–658, 2018.
- [110] Brian Liao, Donghui Zhang, and Nenad Bursac. Functional cardiac tissue engineering (CONDUÇÃO ELÉTRICA?). *Regenerative Medicine*, 7(2):187–206, 2012.
- [111] Kaveh Roshanbinfar, Tilman U Esser, and Felix B Engel. Stem Cells and Their Cardiac Derivatives for Cardiac Tissue Engineering and Regenerative Medicine, 2021.

- [112] Rui Guo, Masatoshi Morimatsu, Tian Feng, Feng Lan, Dehua Chang, Feng Wan, and Yunpeng Ling. Stem cell-derived cell sheet transplantation for heart tissue repair in myocardial infarction. *Stem Cell Research and Therapy*, 11(1):1–13, 2020.
- [113] Chin Siang Ong, Takuma Fukunishi, Huaitao Zhang, Chen Yu Huang, Andrew Nashed, Adriana Blazeski, Deborah Disilvestre, Luca Vricella, John Conte, Leslie Tung, Gordon F. Tomaselli, and Narutoshi Hibino. Biomaterial-Free Three-Dimensional Bioprinting of Cardiac Tissue using Human Induced Pluripotent Stem Cell Derived Cardiomyocytes. *Scientific Reports*, 7(1):2–12, 2017.
- [114] Nenad Bursac, Yihua Loo, Kam Leong, and Leslie Tung. Novel anisotropic engineered cardiac tissues: Studies of electrical propagation. *Biochemical and Biophysical Research Communications*, 361(4):847–853, 2007.
- [115] Ngan F. Huang, Vahid Serpooshan, Viola B. Morris, Nazish Sayed, Gaspard Pardon, Oscar J. Abilez, Karina H. Nakayama, Beth L. Pruitt, Sean M. Wu, Young sup Yoon, Jianyi Zhang, and Joseph C. Wu. Big bottlenecks in cardiovascular tissue engineering. *Communications Biology*, 1(1):8–11, 2018.
- [116] John P.A. Ioannidis. Extrapolating from animals to humans, 2012.
- [117] Jesus Egido, Carlos Zaragoza, Carmen Gomez-Guerrero, Jose Luis Martin-Ventura, Luis Blanco-Colio, Begoa Lavin, Beat Mallavia, Carlos Tarin, Sebastian Mas, and Alberto Ortiz. Animal models of cardiovascular diseases, 2011.
- [118] Mendonca Costa C, Neic A, Kerfoot E, Gillette K, Porter B, Sieniewicz B, Gould J, Sidhu B, Chen Z, Elliott M, Mehta V, Plank G, Rinaldi A, Bishop M, and Niederer S. A Virtual Cohort of Twenty-four Left-ventricular Models of Ischemic Cardiomyopathy Patients. *Heart Rhythm*, 2020.
- [119] Rock Ukaha and Jessica Iloh. Measurement of Heart Size in the Rabbit (*Oryctolagus cuniculus*) by Vertebral Scale System. *Journal of Scientific Research and Reports*, 2018.

- [120] B. Korecky and K. Rakusan. Normal and hypertrophic growth of the rat heart: Changes in cell dimensions and number. *American Journal of Physiology - Heart and Circulatory Physiology*, 1978.
- [121] Susan A. Thompson, Paul W. Burridge, Elizabeth A. Lipke, Michael Shambloott, Elias T. Zambidis, and Leslie Tung. Engraftment of human embryonic stem cell derived cardiomyocytes improves conduction in an arrhythmogenic in vitro model. *Journal of Molecular and Cellular Cardiology*, 53(1):15–23, 2012.
- [122] Richard J. Jabbour, Thomas J. Owen, Pragati Pandey, Marina Reinsch, Brian Wang, Oisín King, Liam Steven Couch, Dafni Pantou, David S. Pitcher, Rasheda A. Chowdhury, Fotios G. Pitoulis, Balvinder S. Handa, Worrapong Kit-Anan, Filippo Perbellini, Rachel C. Myles, Daniel J. Stuckey, Michael Dunne, Mayooraan Shanmuganathan, Nicholas S. Peters, Fu Siong Ng, Florian Weinberger, Cesare M. Terracciano, Godfrey L. Smith, Thomas Eschenhagen, and Sian E. Harding. In vivo grafting of large engineered heart tissue patches for cardiac repair. *JCI Insight*, 6(15):1–13, 2021.
- [123] Johannes Riegler, Malte Tiburcy, Antje Ebert, Evangeline Tzatzalos, Uwe Raaz, Oscar J. Abilez, Qi Shen, Nigel G. Kooreman, Evgenios Neofytou, Vincent C. Chen, Mouer Wang, Tim Meyer, Philip S. Tsao, Andrew J. Connolly, Larry A. Couture, Joseph D. Gold, Wolfram H. Zimmermann, and Joseph C. Wu. Human engineered heart muscles engraft and survive long term in a rodent myocardial infarction model. *Circulation Research*, 117(8):720–730, 2015.
- [124] Christopher P. Jackman. Engineered cardiac tissue patch maintains structural and electrical properties after epicardial implantation. *Physiology & behavior*, 176(3):139–148, 2017.
- [125] David Simpson, Hong Liu, Tai-Hwang Michael Fan, Robert Nerem, and Samuel C. Dudley. A Tissue Engineering Approach to Progenitor Cell Delivery Results in Significant Cell Engraftment and Improved Myocardial Remodeling. *STEM CELLS*, 2007.

- [126] Adam J. Connolly and Martin J. Bishop. Computational Representations of Myocardial Infarct Scars and Implications for Arrhythmogenesis. *Clinical Medicine Insights: Cardiology*, 10s1:27–40, 2016.
- [127] P. Colli-Franzone, V. Gionti, L. F. Pavarino, S. Scacchi, and C. Storti. Role of infarct scar dimensions, border zone repolarization properties and anisotropy in the origin and maintenance of cardiac reentry. *Mathematical Biosciences*, 315(October 2018):108228, 2019.
- [128] Caroline Mendonca Costa, Gernot Plank, Christopher A. Rinaldi, Steven A. Niederer, and Martin J. Bishop. Modeling the electrophysiological properties of the infarct border zone. *Frontiers in Physiology*, 9(APR):1–14, 2018.
- [129] Caroline Mendonca Costa, Aurel Neic, Eric Kerfoot, Bradley Porter, Benjamin Sieniewicz, Justin Gould, Baldeep Sidhu, Zhong Chen, Gernot Plank, Christopher A. Rinaldi, Martin J. Bishop, and Steven A. Niederer. Pacing in proximity to scar during cardiac resynchronization therapy increases local dispersion of repolarization and susceptibility to ventricular arrhythmogenesis. *Heart Rhythm*, 16(10):1475–1483, 2019.
- [130] Kristina Fidanovski and Damia Mawad. Conjugated Polymers in Bioelectronics: Addressing the Interface Challenge. *Advanced Healthcare Materials*, 8(10):1–9, 2019.
- [131] Zhi Cui, Nathan C. Ni, Jun Wu, Guo Qing Du, Sheng He, Terrence M. Yau, Richard D. Weisel, Hsing Wen Sung, and Ren Ke Li. Polypyrrole-chitosan conductive biomaterial synchronizes cardiomyocyte contraction and improves myocardial electrical impulse propagation. *Theranostics*, 8(10):2752–2764, 2018.
- [132] C.S. Henriquez and A.A. Papazoglou. Conduction in a 3D bidomain representation of cardiac tissue with unequal anisotropy. In *Proceedings of the 15th Annual International Conference of the IEEE Engineering in Medicine and Biology Societ*, pages 748–749. IEEE, 1993.

- [133] Jonna R. Terkildsen, Steven Niederer, Edmund J. Crampin, Peter Hunter, and Nicolas P. Smith. Using Physiome standards to couple cellular functions for rat cardiac excitation-contraction. *Experimental Physiology*, 93(7):919–929, 2008.
- [134] E. J. Vigmond, R. Weber dos Santos, A. J. Prassl, M. Deo, and G. Plank. Solvers for the cardiac bidomain equations. *Progress in Biophysics and Molecular Biology*, 96(1-3):3–18, 2008.
- [135] D. E. Roberts, L. T. Hersh, and A. M. Scher. Influence of cardiac fiber orientation on wavefront voltage, conduction velocity, and tissue resistivity in the dog. *Circulation Research*, 44(5):701–712, 1979.
- [136] J. D. Bayer, R. C. Blake, G. Plank, and N. A. Trayanova. A novel rule-based algorithm for assigning myocardial fiber orientation to computational heart models. *Annals of Biomedical Engineering*, 40(10):2243–2254, 2012.
- [137] S. Mashima, K. Harumi, and S. Murao. The magnitude of the electromotive force of canine ventricular myocardium. *Circulation Research*, 42(6):757–763, 1978.
- [138] P. Steendijk, E. T. van der Velde, and J. Baan. Dependence of anisotropic myocardial electrical resistivity on cardiac phase and excitation frequency. *Basic Research in Cardiology*, 89(5):411–426, 1994.
- [139] P. C. Ursell, P. I. Gardner, A. Albala, J. J. Fenoglio, and A. L. Wit. Structural and electrophysiological changes in the epicardial border zone of canine myocardial infarcts during infarct healing. *Circulation Research*, 56(3):436–451, 1985.
- [140] P. I. Gardner, P. C. Ursell, J. J. Fenoglio, and A. L. Wit. Electrophysiologic and anatomic basis for fractionated electrograms recorded from healed myocardial infarcts. *Circulation*, 72(3):596–611, 1985.
- [141] Eleni Stavrinidou, Pierre Leleux, Harizo Rajaona, Michel Fiocchi, Sébastien Sanaur, and George G. Malliaras. A simple model for ion injection and transport in conducting polymers. *Journal of Applied Physics*, 2013.



- [142] Xuezheng Wang, Benjamin Shapiro, and Elisabeth Smela. Development of a model for charge transport in conjugated polymers. *Journal of Physical Chemistry C*, pages 382–401, 2009.
- [143] Hector Martinez-Navarro, Xin Zhou, Alfonso Bueno-Orovio, and Blanca Rodriguez. Electrophysiological and anatomical factors determine arrhythmic risk in acute myocardial ischaemia and its modulation by sodium current availability: Sodium current, arrhythmia and ischemia. *Interface Focus*, 11(1), 2021.
- [144] S. Longobardi, A. Lewalle, S. Coveney, I. Sjaastad, E. K.S. Espe, W. E. Louch, C. J. Musante, A. Sher, and S. A. Niederer. Predicting left ventricular contractile function via Gaussian process emulation in aortic-banded rats: Aortic banded rat heart simulations. *Philosophical Transactions of the Royal Society A: Mathematical, Physical and Engineering Sciences*, 378(2173), 2020.
- [145] G. Varoquaux, L. Buitinck, G. Louppe, O. Grisel, F. Pedregosa, and A. Mueller. Scikit-learn. *GetMobile: Mobile Computing and Communications*, 19(1):29–33, 2015.
- [146] I. M. Sobol. Global sensitivity indices for nonlinear mathematical models and their Monte Carlo estimates. *Mathematics and Computers in Simulation*, 55(1-3):271–280, 2001.
- [147] Jon Herman and Will Usher. SALib : Sensitivity Analysis Library in Python ( Numpy ). Contains Sobol , SALib : An open-source Python library for Sensitivity Analysis. *The Journal of Open Source Software*, 41(April):2015–2017, 2018.
- [148] Mahshid Assadi, Mark Restivo, William B. Gough, and Nabil El-Sherif. Reentrant ventricular arrhythmias in the late myocardial infarction period: 17. Correlation of activation patterns of sinus and reentrant ventricular tachycardia. *American Heart Journal*, 119(5):1014–1024, 1990.
- [149] M. A. Allesie, F. I.M. Bonke, and F. J.G. Schopman. Circus movement in rabbit atrial muscle as a mechanism of tachycardia. III. The 'leading circle' concept: a new model of circus movement in cardiac tissue without the involvement of an anatomical obstacle. *Circulation Research*, 41(1):9–18, 1977.

- [150] Kenneth R. Laurita and David S. Rosenbaum. Interdependence of modulated dispersion and tissue structure in the mechanism of unidirectional block. *Circulation Research*, 87(10):922–928, 2000.
- [151] Nassir F. Marrouche, Atul Verma, Oussama Wazni, Robert Schweikert, David O. Martin, Walid Saliba, Fethi Kilicaslan, Jennifer Cummings, J. David Burkhardt, Mandeep Bhargava, Dianna Bash, Johannes Brachmann, Jens Guenther, Steven Hao, Salwa Beheiry, Antonio Rossillo, Antonio Raviele, Sakis Themistoclakis, and Andrea Natale. Mode of initiation and ablation of ventricular fibrillation storms in patients with ischemic cardiomyopathy. *Journal of the American College of Cardiology*, 43(9):1715–1720, 2004.
- [152] Topi Korhonen, Sandra L. Hänninen, and Pasi Tavi. Model of excitation-contraction coupling of rat neonatal ventricular myocytes. *Biophysical Journal*, 96(3):1189–1209, 2009.
- [153] Laura Sartiani, Esther Bettiol, Francesca Stillitano, Alessandro Mugelli, Elisabetta Cerbai, and Marisa E. Jaconi. Developmental Changes in Cardiomyocytes Differentiated from Human Embryonic Stem Cells: A Molecular and Electrophysiological Approach. *Stem Cells*, 25(5):1136–1144, 2007.
- [154] Alan Fabbri, Birgit Goversen, Marc A. Vos, Toon A.B. van Veen, and Teun P. de Boer. Required GK1 to Suppress Automaticity of iPSC-CMs Depends Strongly on IK1 Model Structure. *Biophysical Journal*, 117(12):2303–2315, 2019.
- [155] Martin J. Bishop and Gernot Plank. Representing cardiac bidomain bath-loading effects by an augmented monodomain approach: Application to complex ventricular models. *IEEE Transactions on Biomedical Engineering*, 58(4):1066–1075, 2011.
- [156] R. Plonsey, C. Henriquez, and N. Trayanova. Extracellular (volume conductor) effect on adjoining cardiac muscle electrophysiology. *Medical & Biological Engineering & Computing*, 26(2):126–129, 1988.
- [157] Andre Chow, Daniel J. Stuckey, Emaddin Kidher, Mark Rocco, Richard J. Jabbour, Catherine A. Mansfield, Ara Darzi, Sian E. Harding, Molly M. Stevens, and Thanos

- Athanasidou. Human Induced Pluripotent Stem Cell-Derived Cardiomyocyte Encapsulating Bioactive Hydrogels Improve Rat Heart Function Post Myocardial Infarction. *Stem Cell Reports*, 9(5):1415–1422, 11 2017.
- [158] Christian Riehle and Johann Bauersachs. Small animal models of heart failure, 2019.
- [159] Andrew G. Edwards and William E. Louch. Species-dependent mechanisms of cardiac arrhythmia: A cellular focus. *Clinical Medicine Insights: Cardiology*, 11, 2017.
- [160] M. Fernandez-Chas, M. J. Curtis, and S. A. Niederer. Mechanism of doxorubicin cardiotoxicity evaluated by integrating multiple molecular effects into a biophysical model. *British Journal of Pharmacology*, 175(5):763–781, 2018.
- [161] Stefano Morotti, Caroline Liu, Bence Hegyi, Haibo Ni, Alex Fogli Iseppe, Lianguo Wang, Crystal M Ripplinger, Donald M Bers, Andrew G Edwards, and Eleonora Grandi. Quantitative cross-species translators of cardiac myocyte electrophysiology: model training, experimental validation, and applications. *bioRxiv*, 2020.
- [162] Deok Ho Kim, Elizabeth A. Lipke, Pilnam Kim, Raymond Cheong, Susan Thompson, Michael Delannoy, Kahp Yang Suh, Leslie Tung, and Andre Levchenko. Nanoscale cues regulate the structure and function of macroscopic cardiac tissue constructs. *Proceedings of the National Academy of Sciences of the United States of America*, 107(2):565–570, 2010.
- [163] R. H. Clayton, O. Bernus, E. M. Cherry, H. Dierckx, F. H. Fenton, L. Mirabella, A. V. Panfilov, F. B. Sachse, G. Seemann, and H. Zhang. Models of cardiac tissue electrophysiology: Progress, challenges and open questions. *Progress in Biophysics and Molecular Biology*, 104(1-3):22–48, 2011.
- [164] Gerard J.J. Boink, David H. Lau, Iryna N. Shlapakova, Eugene A. Sosunov, Evgeny P. Anyukhovskiy, Helen E. Driessen, Wen Dun, Ming Chen, Peter Danilo, Tove S. Rosen, Nazira Zgen, Heather S. Duffy, Yelena Kryukova, Penelope A. Boyden, Richard B. Robinson, Peter R. Brink, Ira S. Cohen, and Michael R. Rosen. SkM1 and Cx32 improve con-

- duction in canine myocardial infarcts yet only SkM1 is antiarrhythmic. *Cardiovascular Research*, 94(3):450–459, 2012.
- [165] Lev Protas, Wen Dun, Zhiheng Jia, Jia Lu, Annalisa Bucchi, Sindhu Kumari, Ming Chen, Ira S. Cohen, Michael R. Rosen, Emilia Entcheva, and Richard B. Robinson. Expression of skeletal but not cardiac Na<sup>+</sup> channel isoform preserves normal conduction in a depolarized cardiac syncytium. *Cardiovascular Research*, 81(3):528–535, 2009.
- [166] Jia Lu, Hong Zhan Wang, Zhiheng Jia, Joan Zuckerman, Zhongju Lu, Yuanjian Guo, Gerard J.J. Boink, Peter R. Brink, Richard B. Robinson, Emilia Entcheva, and Ira S. Cohen. Improving cardiac conduction with a skeletal muscle sodium channel by gene and cell therapy. *Journal of Cardiovascular Pharmacology*, 60(1):88, 7 2012.
- [167] Kacey Ronaldson-Bouchard, Stephen P. Ma, Keith Yeager, Timothy Chen, Lou Jin Song, Dario Sirabella, Kumi Morikawa, Diogo Teles, Masayuki Yazawa, and Gordana Vunjak-Novakovic. Advanced maturation of human cardiac tissue grown from pluripotent stem cells. *Nature*, 556(7700):239–243, 2018.
- [168] Shunsuke Funakoshi, Ian Fernandes, Olya Mastikhina, Dan Wilkinson, Thinh Tran, Wahiba Dhahri, Amine Mazine, Donghe Yang, Benjamin Burnett, Jeehoon Lee, Stephanie Protze, Gary D. Bader, Sara S. Nunes, Michael Laflamme, and Gordon Keller. Generation of mature compact ventricular cardiomyocytes from human pluripotent stem cells. *Nature Communications*, 12(1), 2021.
- [169] Kazutoshi Takahashi and Shinya Yamanaka. Induction of Pluripotent Stem Cells from Mouse Embryonic and Adult Fibroblast Cultures by Defined Factors. *Cell*, 2006.
- [170] Tsukasa Kamakura, Takeru Makiyama, Kenichi Sasaki, Yoshinori Yoshida, Yimin Wuriyanghai, Jiarong Chen, Tetsuhisa Hattori, Seiko Ohno, Toru Kita, Minoru Horie, Shinya Yamanaka, and Takeshi Kimura. Ultrastructural maturation of human-induced pluripotent stem cell-derived cardiomyocytes in a long-term culture. *Circulation Journal*, 2013.

- [171] George Eng, Benjamin W. Lee, Lev Protas, Mark Gagliardi, Kristy Brown, Robert S. Kass, Gordon Keller, Richard B. Robinson, and Gordana Vunjak-Novakovic. Autonomous beating rate adaptation in human stem cell-derived cardiomyocytes. *Nature Communications*, 2016.
- [172] Anton Mihic, Jiao Li, Yasuo Miyagi, Mark Gagliardi, Shu Hong Li, Jean Zu, Richard D. Weisel, Gordon Keller, and Ren Ke Li. The effect of cyclic stretch on maturation and 3D tissue formation of human embryonic stem cell-derived cardiomyocytes. *Biomaterials*, 2014.
- [173] Yimu Zhao, Naimeh Rafatian, Nicole T. Feric, Brian J. Cox, Roozbeh Aschar-Sobbi, Erika Yan Wang, Praful Aggarwal, Boyang Zhang, Genevieve Conant, Kacey Ronaldson-Bouchard, Aric Pahnke, Stephanie Protze, Jee Hoon Lee, Locke Davenport Huyer, Danica Jekic, Anastasia Wickeler, Hani E. Naguib, Gordon M. Keller, Gordana Vunjak-Novakovic, Ulrich Broeckel, Peter H. Backx, and Milica Radisic. A Platform for Generation of Chamber-Specific Cardiac Tissues and Disease Modeling. *Cell*, 176(4):913–927, 2019.
- [174] Madison S. Spach, J. Francis Heidlage, Paul C. Dolber, and Roger C. Barr. Electrophysiological effects of remodeling cardiac gap junctions and cell size. Experimental and model studies of normal cardiac growth. *Circulation Research*, 86(3):302–311, 2000.
- [175] Ben Hanson, Peter Sutton, Nasser Elameri, Marcus Gray, Hugo Critchley, Jaswinder S. Gill, and Peter Taggart. Interaction of activation-repolarization coupling and restitution properties in humans. *Circulation: Arrhythmia and Electrophysiology*, 2(2):162–170, 2009.
- [176] WESLEY C. LABARGE. *QUEST TOWARDS THE DEVELOPMENT OF HUMAN CARDIAC TISSUE EQUIVALENTS MADE FROM HUMAN INDUCED PLURIPOTENT STEM CELL DERIVED CARDIAC CELLS* by WESLEY C. LABARGE JIANYI ZHANG, COMMITTEE CHAIR Submitted to the graduate faculty of The University of Alabama at Bi. PhD thesis, The University of Alabama, 2020.

- [177] Thomas O'Hara, László Virág, András Varró, and Yoram Rudy. Simulation of the undiseased human cardiac ventricular action potential: Model formulation and experimental validation. *PLoS Computational Biology*, 7(5), 2011.
- [178] Arie O. Verkerk, Christiaan C. Veerman, Jan G. Zegers, Isabella Mengarelli, Connie R. Bezzina, and Ronald Wilders. Patch-clamp recording from human induced pluripotent stemcell-derived cardiomyocytes: Improving action potential characteristics throughdynamic clamp. *International Journal of Molecular Sciences*, 18(9), 2017.
- [179] Glenna C.L. Bett, Aaron D. Kaplan, Agnieszka Lis, Thomas R. Cimato, Emmanuel S. Tzanakakis, Qinlian Zhou, Michael J. Morales, and Randall L. Rasmusson. Electronic "expression" of the inward rectifier in cardiocytes derived from human-induced pluripotent stem cells. *Heart Rhythm*, 10(12):1903–1910, 2013.
- [180] Birgit Goversen, Marcel A.G. van der Heyden, Toon A.B. van Veen, and Teun P. de Boer. The immature electrophysiological phenotype of iPSC-CMs still hampers in vitro drug screening: Special focus on IK1. *Pharmacology and Therapeutics*, 183(October 2017):127–136, 2018.
- [181] Cedric Cochrane, Maryline Lewandowski, Koncar Vladan, and Claude Dufour. Design and Development of a Flexible Strain Sensor. *Sensors*, 7:473–492, 2007.
- [182] Junyi Ma, Liang Guo, Steve J. Fiene, Blake D. Anson, James A. Thomson, Timothy J. Kamp, Kyle L. Kolaja, Bradley J. Swanson, and Craig T. January. High purity human-induced pluripotent stem cell-derived cardiomyocytes: Electrophysiological properties of action potentials and ionic currents. *American Journal of Physiology - Heart and Circulatory Physiology*, 301(5):2006–2017, 2011.
- [183] Jianhua Zhang, Gisela F. Wilson, Andrew G. Soerens, Chad H. Koonce, Junying Yu, Sean P. Palecek, James A. Thomson, and Timothy J. Kamp. Functional cardiomyocytes derived from human induced pluripotent stem cells. *Circulation Research*, 104(4):30–41, 2009.

- [184] Louise A. Bowler, David J. Gavaghan, Gary R. Mirams, and Jonathan P. Whiteley. Representation of Multiple Cellular Phenotypes Within Tissue-Level Simulations of Cardiac Electrophysiology. *Bulletin of Mathematical Biology*, 81(1):7–38, 2019.
- [185] Gan Xin Yan, Wataru Shimizu, and Charles Antzelevitch. Characteristics and distribution of M cells in arterially perfused canine left ventricular wedge preparations. *Circulation*, 98(18):1921–1927, 1998.
- [186] Charles Antzelevitch, Serge Sicouri, Silvio H Litovsky, Anton Lukas, Subramaniam C Krishnan, Jose M Di Diego, Gary A Gintant, and Da-wei Liu. Heterogeneity Within the Ventricular Wall. *Circulation Research*, 69(6):1427–1449, 1991.
- [187] SERGE SICOURI, JEFFREY FISH, and CHARLES ANTZELEVITCH. Distribution of M Cells in the Canine Ventricle. *Journal of Cardiovascular Electrophysiology*, 5(10):824–837, 1994.
- [188] British Heart Foundation. UK Factsheet. Technical Report January, British Heart Foundation, 2020.
- [189] Jianyi Zhang, Wuqiang Zhu, Milica Radisic, and Gordana Vunjak-Novakovic. Can we engineer a human cardiac patch for therapy? *Circulation Research*, 123(2):244–265, 2018.
- [190] Jacqueline S. Wendel, Lei Ye, Pengyuan Zhang, Robert T. Tranquillo, and Jianyi Jay Zhang. Functional consequences of a tissue-engineered myocardial patch for cardiac repair in a rat infarct model. *Tissue Engineering - Part A*, 20(7-8):1325–1335, 2014.
- [191] Yuedan Li and Xiaozhong Qiu. Bioelectricity-coupling patches for repairing impaired myocardium. *Wiley Interdisciplinary Reviews: Nanomedicine and Nanobiotechnology*, 14(4):1–24, 2022.
- [192] Wolfram Hubertus Zimmermann. Tissue engineered heart repair from preclinical models to first-in-patient studies. *Current Opinion in Physiology*, 14:70–77, 2020.

- [193] Simon Pecha, Kaja Yorgan, Matti Röhl, Birgit Geertz, Arne Hansen, Florian Weinberger, Susanne Sehner, Heimo Ehmke, Hermann Reichenspurner, Thomas Eschenhagen, and Alexander Peter Schwoerer. Human iPS cell-derived engineered heart tissue does not affect ventricular arrhythmias in a guinea pig cryo-injury model. *Scientific Reports*, 9(1):1–12, 2019.
- [194] Junjun Li, Itsunari Minami, Motoko Shiozaki, Leqian Yu, Shin Yajima, Shigeru Miyagawa, Yuji Shiba, Nobuhiro Morone, Satsuki Fukushima, Momoko Yoshioka, Sisi Li, Jing Qiao, Xin Li, Lin Wang, Hidetoshi Kotera, Norio Nakatsuji, Yoshiki Sawa, Yong Chen, and Li Liu. Human Pluripotent Stem Cell-Derived Cardiac Tissue-like Constructs for Repairing the Infarcted Myocardium. *Stem Cell Reports*, 9(5):1546–1559, 2017.
- [195] Shigeru Miyagawa, Yoshiki Sawa, Satoru Sakakida, Satoshi Taketani, Haruhiko Kondoh, Imran Ahmed Memon, Yukiko Imanishi, Tatsuya Shimizu, Teruo Okano, and Hikaru Matsuda. Tissue cardiomyoplasty using bioengineered contractile cardiomyocyte sheets to repair damaged myocardium: Their integration with recipient myocardium. *Transplantation*, 80(11):1586–1595, 2005.
- [196] Kenji Miki, Hisazumi Uenaka, Atsuhiko Saito, Shigeru Miyagawa, Taichi Sakaguchi, Takahiro Higuchi, Tatsuya Shimizu, Teruo Okano, Shinya Yamanaka, and Yoshiki Sawa. Bioengineered Myocardium Derived from Induced Pluripotent Stem Cells Improves Cardiac Function and Attenuates Cardiac Remodeling Following Chronic Myocardial Infarction in Rats. *STEM CELLS Translational Medicine*, 1(5):430–437, 2012.
- [197] Eva Querdel, Marina Reinsch, Liesa Castro, Deniz Köse, Andrea Bähr, Svenja Reich, Birgit Geertz, Bärbel Ulmer, Mirja Schulze, Marc D. Lemoine, Tobias Krause, Marta Lemme, Jascha Sani, Aya Shibamiya, Tim Stüdemann, Maria Köhne, Constantin von Bibra, Nadja Hornaschewitz, Simon Pecha, Yusuf Nejajsie, Ingra Mannhardt, Torsten Christ, Hermann Reichenspurner, Arne Hansen, Nikolai Klymiuk, M. Krane, C. Kupatt, Thomas Eschenhagen, and Florian Weinberger. Human Engineered Heart Tissue Patches Remuscularize the Injured Heart in a Dose-Dependent Manner. *Circulation*, pages 1991–2006, 2021.



- [198] Lei Ye, Ying Hua Chang, Qiang Xiong, Pengyuan Zhang, Liying Zhang, Porur Somasundaram, Mike Lepley, Cory Swingen, Liping Su, Jacqueline S. Wendel, Jing Guo, Albert Jang, Daniel Rosenbush, Lucas Greder, James R. Dutton, Jianhua Zhang, Timothy J. Kamp, Dan S. Kaufman, Ying Ge, and Jianyi Zhang. Cardiac repair in a porcine model of acute myocardial infarction with human induced pluripotent stem cell-derived cardiovascular cells. *Cell Stem Cell*, 15(6):750–761, 2014.
- [199] Masashi Kawamura, Shigeru Miyagawa, Kenji Miki, Atsuhiko Saito, Satsuki Fukushima, Takahiro Higuchi, Takuji Kawamura, Toru Kuratani, Takashi Daimon, Tatsuya Shimizu, Teruo Okano, and Yoshiki Sawa. Feasibility, safety, and therapeutic efficacy of human induced pluripotent stem cell-derived cardiomyocyte sheets in a porcine ischemic cardiomyopathy model. *Circulation*, 126(11 SUPPL.1):29–37, 2012.
- [200] Yen Wen Liu, Billy Chen, Xiulan Yang, James A. Fugate, Faith A. Kalucki, Akiko Futakuchi-Tsuchida, Larry Couture, Keith W. Vogel, Clifford A. Astley, Audrey Baldessari, Jason Ogle, Creighton W. Don, Zachary L. Steinberg, Stephen P. Seslar, Stephanie A. Tuck, Hiroshi Tsuchida, Anna V. Naumova, Sarah K. Dupras, Milly S. Lyu, James Lee, Dale W. Hailey, Hans Reinecke, Lil Pabon, Benjamin H. Fryer, W. Robb MacLellan, R. Scott Thies, and Charles E. Murry. Human embryonic stem cell-derived cardiomyocytes restore function in infarcted hearts of non-human primates. *Nature Biotechnology*, 36(7):597–605, 2018.
- [201] Yuji Shiba, Toshihito Gomibuchi, Tatsuichiro Seto, Yuko Wada, Hajime Ichimura, Yuki Tanaka, Tatsuki Ogasawara, Kenji Okada, Naoko Shiba, Kengo Sakamoto, Daisuke Ido, Takashi Shiina, Masamichi Ohkura, Junichi Nakai, Narumi Uno, Yasuhiro Kazuki, Mitsuo Oshimura, Itsunari Minami, and Uichi Ikeda. Allogeneic transplantation of iPS cell-derived cardiomyocytes regenerates primate hearts. *Nature*, 538(7625):388–391, 2016.
- [202] James J.H. Chong, Xiulan Yang, Creighton W. Don, Elina Minami, Yen Wen Liu, Jill J. Weyers, William M. Mahoney, Benjamin Van Biber, Savannah M. Cook, Nathan J. Palpant, Jay A. Gantz, James A. Fugate, Veronica Muskheli, G. Michael Gough, Keith W. Vogel, Cliff A. Astley, Charlotte E. Hotchkiss, Audrey Baldessari, Lil Pabon, Hans Rei-

- necke, Edward A. Gill, Veronica Nelson, Hans Peter Kiem, Michael A. Laflamme, and Charles E. Murry. Human embryonic-stem-cell-derived cardiomyocytes regenerate non-human primate hearts. *Nature*, 510(7504):273–277, 2014.
- [203] Rocco Romagnuolo, Hassan Masoudpour, Andreu Porta-Sánchez, Beiping Qiang, Jennifer Barry, Andrew Laskary, Xiuling Qi, Stéphane Massé, Karl Magtibay, Hiroyuki Kawajiri, Jun Wu, Tamilla Valdman Sadikov, Janet Rothberg, Krishna M. Panchalingam, Emily Titus, Ren Ke Li, Peter W. Zandstra, Graham A. Wright, Kumaraswamy Nanthakumar, Nilesh R. Ghugre, Gordon Keller, and Michael A. Laflamme. Human Embryonic Stem Cell-Derived Cardiomyocytes Regenerate the Infarcted Pig Heart but Induce Ventricular Tachyarrhythmias. *Stem Cell Reports*, 12(5):967–981, 2019.
- [204] Yuji Shiba, Sarah Fernandes, Wei Zhong Zhu, Dominic Filice, Veronica Muskheli, Jonathan Kim, Nathan J. Palpant, Jay Gantz, Kara White Moyes, Hans Reinecke, Benjamin Van Biber, Todd Dardas, John L. Mignone, Atsushi Izawa, Ramy Hanna, Mohan Viswanathan, Joseph D. Gold, Michael I. Kotlikoff, Narine Sarvazyan, Matthew W. Kay, Charles E. Murry, and Michael A. Laflamme. Human ES-cell-derived cardiomyocytes electrically couple and suppress arrhythmias in injured hearts. *Nature*, 489(7415):322–325, 2012.
- [205] James P. Keener. An eikonal-curvature equation for action potential propagation in myocardium. *Journal of Mathematical Biology*, 29(7):629–651, 1991.
- [206] Piero Colli Franzone and Luciano Guerri. Spreading of excitation in 3-d models of the anisotropic cardiac tissue. I. validation of the eikonal model. *Mathematical Biosciences*, 113(2):145–209, 1993.
- [207] Bryan J. Caldwell, Mark L. Trew, Gregory B. Sands, Darren A. Hooks, Ian J. LeGrice, and Bruce H. Smaill. Three distinct directions of intramural activation reveal nonuniform side-to-side electrical coupling of ventricular myocytes. *Circulation: Arrhythmia and Electrophysiology*, 2(4):433–440, 2009.

- [208] Fernando O. Campos, Aurel Neic, Caroline Mendonca Costa, John Whitaker, Mark D. O'Neill, Reza Rezavi, Christopher Aldo Rinaldi, Daniel Scherr, Steven Alexander Niederer, Gernot Plank, and Martin J. Bishop. An automated near-real time computational method for induction and treatment of scar-related ventricular tachycardias. *Med Image Anal*, pages 1–31, 2021.
- [209] Martin J Bishop. UKPMC Funders Group Author Manuscript Modelling the Role of the Coronary Vasculature During External Field Stimulation. *IEEE Trans Biomed Eng*, 57(10):2335–2345, 2010.
- [210] Hermenegild J. Arevalo, Fijoy Vadakkumpadan, Eliseo Guallar, Alexander Jebb, Peter Malamas, Katherine C. Wu, and Natalia A. Trayanova. Arrhythmia risk stratification of patients after myocardial infarction using personalized heart models. *Nature Communications*, 7(May), 2016.
- [211] Keith F. Decker and Yoram Rudy. Ionic mechanisms of electrophysiological heterogeneity and conduction block in the infarct border zone. *American Journal of Physiology - Heart and Circulatory Physiology*, 299(5):1588–1597, 2010.
- [212] Wen Dun, Shigeo Baba, Takuya Yagi, and Penelope A. Boyden. Dynamic remodeling of  $K^+$  and  $Ca^{2+}$  currents in cells that survived in the epicardial border zone of canine healed infarcted heart. *American Journal of Physiology - Heart and Circulatory Physiology*, 287(3 56-3):1046–1054, 2004.
- [213] Min Jiang, Candido Cabo, Jian An Yao, Penelope A. Boyden, and Gea Ny Tseng. Delayed rectifier K currents have reduced amplitudes and altered kinetics in myocytes from infarcted canine ventricle. *Cardiovascular Research*, 48(1):34–43, 2000.
- [214] Stanley Nattel, Brett Burstein, and Dobromir Dobrev. Atrial remodeling and atrial fibrillation: mechanisms and implications. *Circulation. Arrhythmia and electrophysiology*, 1(1):62–73, 2008.
- [215] Simon M. Bryant, Xiaoping Wan, S. Jane Shipsey, and George Hart. Regional differences in the delayed rectifier current ( $I(Kr)$  and  $I(Ks)$ ) contribute to the differences in

- action potential duration in basal left ventricular myocytes in guinea-pig. *Cardiovascular Research*, 40(2):322–331, 1998.
- [216] Damiano Fassina, Caroline M. Costa, Stefano Longobardi, Elias Karabelas, Gernot Plank, Sian E. Harding, and Steven A. Niederer. Modelling the interaction between stem cells derived cardiomyocytes patches and host myocardium to aid non-arrhythmic engineered heart tissue design. *PLOS Computational Biology*, 18(4):e1010030, 4 2022.
- [217] Klaus Schlotthauer and Donald M. Bers. Sarcoplasmic Reticulum  $\text{Ca}^{2+}$  Release Causes Myocyte Depolarization. *Circulation Research*, 87(9):774–780, 2000.
- [218] Leslie A. Geddes. Accuracy Limitations of Chronaxie Values. *IEEE Transactions on Biomedical Engineering*, 51(1):176–181, 2004.
- [219] Ara Arutunyan, Luther M. Swift, and Narine Sarvazyan. Initiation and propagation of ectopic waves: Insights from an in vitro model of ischemia-reperfusion injury. *American Journal of Physiology - Heart and Circulatory Physiology*, 283(2 52-2):741–749, 2002.
- [220] Faramarz H. Samie and José Jalife. Mechanisms underlying ventricular tachycardia and its transition to ventricular fibrillation in the structurally normal heart. *Cardiovascular Research*, 50(2):242–250, 2001.
- [221] Steven D. Girouard and David S. Rosenbaum. Role of wavelength adaptation in the initiation, maintenance, and pharmacologic suppression of reentry. *Journal of Cardiovascular Electrophysiology*, 12(6):697–707, 2001.
- [222] Masatoshi Yamazaki, Naoki Tomii, Koichi Tsuneyama, Hiroki Takanari, Ryoko Niwa, Haruo Honjo, Itsuo Kodama, Tatsuhiko Arafune, Naomasa Makita, Ichiro Sakuma, Dobromir Dobrev, Stanley Nattel, and Yukio Tsuji. Rotors anchored by refractory islands drive torsades de pointes in an experimental model of electrical storm. *Heart Rhythm*, 19(2):318–329, 2022.
- [223] Valentin Sottas, Carl Mattheis Wahl, Mihnea C. Trache, Michael Bartolf-Kopp, Sidney Cambridge, Markus Hecker, and Nina D. Ullrich. Improving electrical properties of

- iPSC-cardiomyocytes by enhancing Cx43 expression. *Journal of molecular and cellular cardiology*, 120:31–41, 7 2018.
- [224] Chung Chuan Chou, Shengmei Zhou, Hideki Hayashi, Motoki Nihei, Yen Bin Liu, Ming Shien Wen, San Jou Yeh, Michael C. Fishbein, James N. Weiss, Shien Fong Lin, Delon Wu, and Peng Sheng Chen. Remodelling of action potential and intracellular calcium cycling dynamics during subacute myocardial infarction promotes ventricular arrhythmias in Langendorff-perfused rabbit hearts. *Journal of Physiology*, 580(3):895–906, 2007.
- [225] Fernando O. Campos, Yohannes Shiferaw, Rodrigo Weber dos Santos, Gernot Plank, and Martin J. Bishop. Microscopic isthmuses and fibrosis within the border zone of infarcted hearts promote calcium-mediated ectopy and conduction block. *Frontiers in Physics*, 6(JUN):1–14, 2018.
- [226] Takeshi Aiba and Gordon F. Tomaselli. Electrical Remodeling in the Failing Heart Takeshi. *Current Opinion in Cardiology*, 23(1):1–7, 2014.
- [227] M. J. Janse and A. L. Wit. Electrophysiological mechanisms of ventricular arrhythmias resulting from myocardial ischemia and infarction. <https://doi.org/10.1152/physrev.1989.69.4.1049>, 69(4):1049–1169, 1989.
- [228] Nicholas J. Severs, Emmanuel Dupont, Steven R. Coppen, Deborah Halliday, Edward Inett, Daniel Baylis, and Stephen Rothery. Remodelling of gap junctions and connexin expression in heart disease. *Biochimica et Biophysica Acta (BBA) - Biomembranes*, 1662(1-2):138–148, 3 2004.
- [229] Michaela Kapnisi, Catherine Mansfield, Camille Marijon, Anne Geraldine Guex, Filippo Perbellini, Ifigeneia Bardi, Eleanor J. Humphrey, Jennifer L. Puetzer, Damia Mawad, Demosthenes C. Koutsogeorgis, Daniel J. Stuckey, Cesare M. Terracciano, Sian E. Harding, and Molly M. Stevens. Auxetic Cardiac Patches with Tunable Mechanical and Conductive Properties toward Treating Myocardial Infarction. *Advanced Functional Materials*, 28(21), 2018.

- [230] Anthony J. Petty, Rebecca L. Keate, Bin Jiang, Guillermo A. Ameer, and Jonathan Rivnay. Conducting Polymers for Tissue Regeneration in Vivo. *Chemistry of Materials*, 32(10):4095–4115, 2020.
- [231] Christine E. Schmidt, Venkatram R. Shastri, Joseph P. Vacanti, and Robert Langer. Stimulation of neurite outgrowth using an electrically conducting polymer. *Proceedings of the National Academy of Sciences of the United States of America*, 94(17):8948–8953, 1997.
- [232] Theresa M. McCormick, Colin R. Bridges, Elisa I. Carrera, Paul M. Dicarmine, Gregory L. Gibson, Jon Hollinger, Lisa M. Kozycz, and Dwight S. Seferos. Conjugated polymers: Evaluating DFT methods for more accurate orbital energy modeling. *Macromolecules*, 46(10):3879–3886, 2013.
- [233] Matteo Solazzo, Fergal J. O’Brien, Valeria Nicolosi, and Michael G. Monaghan. The rationale and emergence of electroconductive biomaterial scaffolds in cardiac tissue engineering. *APL Bioengineering*, 3(4), 2019.
- [234] Chris D. Cantwell, Yumnah Mohamied, Konstantinos N. Tzortzis, Stef Garasto, Charles Houston, Rasheda A. Chowdhury, Fu Siong Ng, Anil A. Bharath, and Nicholas S. Peters. Rethinking multiscale cardiac electrophysiology with machine learning and predictive modelling. *Computers in Biology and Medicine*, 104:339–351, 1 2019.
- [235] Stefania Fresca, Andrea Manzoni, Luca Dedè, and Alfio Quarteroni. Deep learning-based reduced order models in cardiac electrophysiology. *PLOS ONE*, 15(10):e0239416, 10 2020.
- [236] Ian Vernon, Michael Goldsteiny, and Richard G. Bowerz. Galaxy formation: A Bayesian uncertainty analysis. *Bayesian Analysis*, 5(4):619–670, 2010.
- [237] Ioannis Andrianakis, Ian R. Vernon, Nicky McCreesh, Trevelyan J. McKinley, Jeremy E. Oakley, Rebecca N. Nsubuga, Michael Goldstein, and Richard G. White. Bayesian History Matching of Complex Infectious Disease Models Using Emulation: A Tutorial and a Case Study on HIV in Uganda. *PLOS Computational Biology*, 11(1):e1003968, 1 2015.

- [238] Sam Coveney and Richard H. Clayton. Fitting two human atrial cell models to experimental data using Bayesian history matching. *Progress in Biophysics and Molecular Biology*, 139:43–58, 11 2018.
- [239] Elias Karabelas, Stefano Longobardi, Jana Fuchsberger, Orod Razeghi, Cristobal Rodero, Marina Strocchi, Ronak Rajani, Gundolf Haase, Gernot Plank, and Steven Niederer. Global Sensitivity Analysis of Four Chamber Heart Hemodynamics Using Surrogate Models. *IEEE transactions on bio-medical engineering*, PP, 2022.
- [240] Rahul G. Muthalaly and Robert M. Evans. Applications of Machine Learning in Cardiac Electrophysiology. *Arrhythmia & Electrophysiology Review*, 9(2):71, 6 2020.
- [241] Christopher Schilling, Matthias Keller, Daniel Scherr, Tobias Oesterlein, Michel Haïssaguerre, Claus Schmitt, Olaf Dössel, and Armin Luik. Fuzzy decision tree to classify complex fractionated atrial electrograms. *Biomedizinische Technik*, 60(3):245–255, 6 2015.
- [242] Shadnaz Asgari, Alireza Mehrnia, and Maryam Moussavi. Automatic detection of atrial fibrillation using stationary wavelet transform and support vector machine. *Computers in Biology and Medicine*, 60:132–142, 5 2015.
- [243] F. Regazzoni, L. Dedè, and A. Quarteroni. Machine learning of multiscale active force generation models for the efficient simulation of cardiac electromechanics. *Computer Methods in Applied Mechanics and Engineering*, 370:113268, 10 2020.
- [244] F. Regazzoni, M. Salvador, L. Dede, and A. Quarteroni. A machine learning method for real-time numerical simulations of cardiac electromechanics. *Computer Methods in Applied Mechanics and Engineering*, 393:114825, 4 2022.
- [245] George Em Karniadakis, Ioannis G. Kevrekidis, Lu Lu, Paris Perdikaris, Sifan Wang, and Liu Yang. Physics-informed machine learning. *Nature Reviews Physics* 2021 3:6, 3(6):422–440, 5 2021.
- [246] Clara Herrero Martin, Alon Oved, Rasheda A. Chowdhury, Elisabeth Ullmann, Nicholas S. Peters, Anil A. Bharath, and Marta Varela. EP-PINNs: Cardiac Electro-

- physiology Characterisation Using Physics-Informed Neural Networks. *Frontiers in Cardiovascular Medicine*, 8:2179, 2 2022.
- [247] Xiao Ni, Ke Xu, Yunfei Zhao, Jingyan Li, Linli Wang, Fengxu Yu, and Guang Li. Single-cell analysis reveals the purification and maturation effects of glucose starvation in hiPSC-CMs. *Biochemical and Biophysical Research Communications*, 534:367–373, 1 2021.
- [248] Omer Berenfeld, Valentina D.A. Corino, Axel Loewe, Juan Pablo Martínez, and Jose F. Rodriguez Matas. Editorial: Atrial Fibrillation: Technology for Diagnosis, Monitoring, and Treatment. *Frontiers in Physiology*, 13, 2 2022.
- [249] Kevin D. Costa, Eun Jung Lee, and Jeffrey W. Holmes. Creating Alignment and Anisotropy in Engineered Heart Tissue: Role of Boundary Conditions in a Model Three-Dimensional Culture System. <https://home.liebertpub.com/ten>, 9(4):567–577, 7 2004.
- [250] Weining Bian, Christopher P. Jackman, and Nenad Bursac. Controlling the structural and functional anisotropy of engineered cardiac tissues. *Biofabrication*, 6(2), 2014.
- [251] Joseph K. Yu, Jialiu A. Liang, William H. Franceschi, Qinwen Huang, Farhad Pashakhanloo, Eric Sung, Patrick M. Boyle, and Natalia A. Trayanova. Assessment of arrhythmia mechanism and burden of the infarcted ventricles following remuscularization with pluripotent stem cell-derived cardiomyocyte patches using patient-derived models. *Cardiovascular Research*, 118(5):1247–1261, 3 2022.
- [252] V. G. Fast and A. G. Kleber. Microscopic conduction in cultured strands of neonatal rat heart cells measured with voltage-sensitive dyes. *Circulation research*, 73(5):914–925, 1993.
- [253] Steven A. Niederer, Kenneth S. Campbell, and Stuart G. Campbell. A short history of the development of mathematical models of cardiac mechanics. *Journal of Molecular and Cellular Cardiology*, 127:11–19, 2 2019.
- [254] D. A. Nordsletten, S. A. Niederer, M. P. Nash, P. J. Hunter, and N. P. Smith. Coupling multi-physics models to cardiac mechanics. *Progress in Biophysics and Molecular Biology*, 104(1-3):77–88, 1 2011.



- [255] Matteo Salvador, Marco Fedele, Pasquale Claudio Africa, Eric Sung, Luca Dede', Adityo Prakosa, Jonathan Chrispin, Natalia Trayanova, and Alfio Quarteroni. Electromechanical modeling of human ventricles with ischemic cardiomyopathy: numerical simulations in sinus rhythm and under arrhythmia. *Computers in Biology and Medicine*, 136:104674, 9 2021.
- [256] Matteo Salvador, Francesco Regazzoni, Stefano Pagani, Luca Dede', Natalia Trayanova, and Alfio Quarteroni. The role of mechano-electric feedbacks and hemodynamic coupling in scar-related ventricular tachycardia. *Computers in Biology and Medicine*, 142:105203, 3 2022.
- [257] Alejandro Lopez-Perez, Rafael Sebastian, and Jose M. Ferrero. Three-dimensional cardiac computational modelling: methods, features and applications. *BioMedical Engineering OnLine* 2015 14:1, 14(1):1–31, 4 2015.
- [258] Angela W.C. Lee, Caroline Mendonca Costa, Marina Strocchi, Christopher A. Rinaldi, and Steven A. Niederer. Computational Modeling for Cardiac Resynchronization Therapy. *Journal of cardiovascular translational research*, 11(2):92–108, 1 2018.
- [259] Albert Van Den Berg, Christine L. Mummery, Robert Passier, and Andries D. Van der Meer. Personalised organs-on-chips: functional testing for precision medicine. *Lab on a Chip*, 19(2):198–205, 1 2019.
- [260] Jorge Corral-Acero, Francesca Margara, Maciej Marciniak, Cristobal Roderio, Filip Loncaric, Yingjing Feng, Andrew Gilbert, Joao F. Fernandes, Hassaan A. Bukhari, Ali Wajdan, Manuel Villegas Martinez, Mariana Sousa Santos, Mehrdad Shamohammdi, Hongxing Luo, Philip Westphal, Paul Leeson, Paolo DiAchille, Viatcheslav Gurev, Manuel Mayr, Liesbet Geris, Pras Pathmanathan, Tina Morrison, Richard Cornelussen, Frits Prinzen, Tammo Delhaas, Ada Doltra, Marta Sitges, Edward J. Vigmond, Ernesto Zacur, Vicente Grau, Blanca Rodriguez, Espen W. Remme, Steven Niederer, Peter Mortier, Kristin McLeod, Mark Potse, Esther Pueyo, Alfonso Bueno-Orovio, and Pablo Lamata. The 'Digital Twin' to enable the vision of precision cardiology. *European Heart Journal*, 41(48):4556–4564, 12 2020.